Modeling and power control of a marine current turbine system with energy storage devices

Zhibin Zhou

université de bretagne occidentale

THÈSE / UNIVERSITÉ DE BRETAGNE OCCIDENTALE
sous le sceau de l'Université européenne de Bretagne

pour obtenir le titre de
DOCTEUR DE L'UNIVERSITÉ DE BRETAGNE OCCIDENTALE
Mention : Science pour l'Ingénieur
École Doctorale EDSM

présentée par
Zhibin ZHOU
Préparée au sein de l'EA 3634 IRENav
et de l'EA 4325 LBMS

Modeling and power control of a marine current turbine system with energy storage devices

This Project has received financial support from Brest Métropole Océane

Thèse soutenue le 17 octobre 2014
devant le jury composé de :

Maria DAVID
Professeur, Institut National Polytechnique de Toulouse / *rapporteur*

Seddik BACHA
Professeur, Université Joseph Fourier, Grenoble / *rapporteur*

Seifeddine BENELGHALI
Maître de Conférences, Aix-Marseille Université / *examinateur*

Mohamed MACHMOUM
Professeur, Polytech'Nantes, Saint-Nazaire / *président*

Tianhao TANG
Professeur, Shanghai Maritime University, Shanghai / *examinateur*

Mohamed BENBOUZID
Professeur, Université de Bretagne Occidentale / *directeur de thèse*

Jean Frédéric CHARPENTIER
Maître de Conférences, HDR, Ecole Navale / *co-directeur de thèse*

Franck SCUILLER
Maître de Conférences, Ecole Navale / *co-encadrant*

Acknowledgments

This work has been carried out at French Naval Academy Research Institute (EA 3436 IRENav) and at the Laboratoire Brestois de Mécanique et des Systèmes (EA 4325 LBMS) of the University of Brest. The financial support provided by Brest Métropole Océane (BMO) is gratefully acknowledged.

I wish to express my gratitude to my main supervisor ***Prof. Mohamed BENBOUZID*** for the consistently inspiration, encouragement and guidance throughout this work. I also wish to thank my supervisors ***Dr. Jean Frédéric CHARPENTIER*** and ***Dr. Franck SCUILLER*** for their valuable comments, suggestions and discussions related to this thesis and the published papers.

I wish to thank the pre-examiners ***Prof. Maria PIETRZAK-DAVID*** from National Polytechnic Institute of Toulouse and ***Prof. Seddik BACHA*** from the Polytechnic Institute of Grenoble for their valuable comments and corrections. I am also grateful to my PhD thesis defense committee members: ***Prof. Mohamed MACHMOUM*** from Polytech'Nantes, ***Dr. Seifeddine BENELGHALI*** from the University of Aix-Marseille and ***Prof. Tianhao TANG*** from Shanghai Maritime University, China.

Special thanks are due to ***Prof. Tianhao TANG*** for his suggestions in this PhD work as well as for encouraging me to apply for this research position in 2011.

I also wish to thank my friends ***Elhoussin***, ***Dieudonné***, ***Imad***, ***Ousmane***, ***Jingang HAN***, ***Yang YI***, ***Jing WU***, ***Clément***, ***Emerry***, ***Dhafar***, ***Sébastien***, ***Ali***, ***Farid***, ***Sofiane***, ***Omar***; the friendship and the helps given by them have been very important to me.

Finally, I am deeply indebted to my parents, ***Xiujing BAI*** and ***Laibao ZHOU***, for their infinite love and untiring support since the beginning of my life.

List of Publications

Main results of this PhD thesis have lead to the following publications.

INTERNATIONAL JOURNAL PAPERS

[1] **Z. Zhou**, F. Scuiller, J.F. Charpentier, M.E.H. Benbouzid and T. Tang, "Power control of a non-pitchable PMSG-based marine current turbine at over-rated current speed with flux-weakening strategy," *IEEE Journal of Oceanic Engineering*, pp. 1-10, 2014. (early access in IEEE Xplore)

[2] **Z. Zhou**, F. Scuiller, J.F. Charpentier, M.E.H. Benbouzid and T. Tang, "Power smoothing control in a grid-connected marine current turbine system for compensating swell effect," *IEEE Transactions on Sustainable Energy*, vol. 4, n°3, pp. 816-826, July 2013.

[3] **Z. Zhou**, M.E.H. Benbouzid, J.F. Charpentier, F. Scuiller and T. Tang, "A review of energy storage technologies for marine current energy systems," *Renewable and Sustainable Energy Reviews*, vol. 18, pp. 390-400, February 2013.

INTERNATIONAL CONFERENCE PAPERS

[1] **Z. Zhou**, F. Scuiller, J.F. Charpentier, M.E.H. Benbouzid and T. Tang, "An up-to-date review of large marine current turbine technologies," *in Proceedings of the 2014 IEEE PEAC*, Shanghai (China), pp. 1-5, November 2014.

[2] **Z. Zhou**, F. Scuiller, J.F. Charpentier, M.E.H. Benbouzid and T. Tang, "Application of flow battery in marine current turbine system for daily power management," *in Proceedings of the 2014 IEEE ICGE*, Sfax (Tunisia), pp. 8-13, March 2014.

[3] **Z. Zhou**, F. Scuiller, J.F. Charpentier, M.E.H. Benbouzid and T. Tang, "Power limitation control for a PMSG-based marine current turbine at high tidal speed and strong sea state," *in Proceedings of the 2013 IEEE IEMDC*, Chicago (USA), pp. 75-80, May 2013.

[4] **Z. Zhou**, F. Scuiller, J.F. Charpentier, M.E.H. Benbouzid and T. Tang, "Grid-connected marine current generation system power smoothing control using supercapacitors," *in Proceedings of the 2012 IEEE IECON*, Montreal (Canada), pp. 4035-4040, October 2012.

[5] **Z. Zhou**, M.E.H. Benbouzid, J.F. Charpentier, F. Scuiller and T. Tang, "Energy storage technologies for smoothing power fluctuations in marine current turbines," *in Proceedings of the 2012 IEEE ISIE*, Hangzhou (China), pp. 1425-1430, May 2012.

NATIONAL CONFERENCE PAPERS

[1] **Z. Zhou**, F. Scuiller, J.F. Charpentier et M.E.H. Benbouzid, "Intégration d'une batterie à circulation pour lisser la puissance quotidienne fournie par une hydrolienne sur un réseau îloté," *dans les Actes de Congrès SGE'14 (Symposium de Genie Electrique)*, Cachan (France), Juillet 2014.

[2] **Z. Zhou**, F. Scuiller, J.F. Charpentier et M.E.H. Benbouzid, "Lissage supercapacitif de la puissance produite par une hydrolienne connectée au réseau," *dans les Actes de Congrès SHF- Energies Marines Renouvelables 2013*, Brest (France), Octobre 2013.

[3] **Z. Zhou**, "Power smoothing and limitation control of a PMSG-based marine current turbine under swell waves," *dans les Actes de JCGE'13 (Journée des Jeunes Chercheurs en Génie Electrique)*, Saint-Nazaire (France), Juin 2013.

Earth is a gift for all life;
My life is a gift from my parents;
Love and thankfulness to our parents and the Earth.

CONTENTS

List of Figures

Introduction

The climate change due to greenhouse emissions and the depletion risk of traditional fossil energy resources are two great challenges faced by the entire human society. The share of renewable energy sources (such as wind, sunlight, geothermal heat, hydropower, modern biomass) in energy supply has been growing rapidly during the recent years. At least 30 nations around the world already have renewable energy contributing more than 20% of their national energy supplies. Renewable energy application will continue to grow fast in the coming decades as the sustainable development of the human society relies strongly on it.

As concerning the renewable marine energies, there exist various forms namely tidal energy, wave energy, marine thermal energy, marine osmosis energy, marine biomass energy and offshore wind energy. One of the most promising type is the tidal current energy. Indeed, the potential of electric power generated from marine tidal currents is very high. The worldwide tidal current power which is exploitable by existing technologies is estimated as 75 GW (11 GW in Europe and 3.5 GW in France). The identical power harnessing principle with wind power generation, the high power density resulting from the seawater property and the high predictability owning to the tidal astronomical characteristics make marine tidal currents particularly attractive and advantageous. During the last ten years, various original marine current turbines have been designed by different research and industrial communities and several prototypes are industrialized more than two

generations of systems. The achievements in megawatt-level marine current turbine systems in Europe lead to several demonstrative marine current turbine farms which are scheduled to supply electricity for coastal areas or remote islands in the next few years.

However, there are still some difficulties before commercialization of the marine current turbine system. On the one hand, the installation cost, geographical constraints and social acceptance should be considered in planning the marine current turbine projects. On the other hand, the power fluctuations both on short-time scale (caused by swell wave disturbance) and on long-time scale (caused by the periodic variations of tidal current speed) will deteriorate the power quality or result power balance difficulties between the supply and consumption.

The main objective of this *Ph.D.* thesis is to simulate the whole power chain of the marine current turbine system and to investigate the utilization of energy storage systems for improving the power quality and energy management capability. Some appropriate control strategies in case of swell disturbances and over-rated marine current speed have also been analyzed in the thesis.

The contributions of this thesis are:

- Development of a simulation platform (under Matlab/Simulink®) for the marine current generation system (including swell disturbance, turbine, PMSG, converters, grid-connection part and energy storage systems) which can be used to study both grid-connected and standalone cases.
- Proposal of using supercapacitors for compensating swell-induced short-period power fluctuations; investigation of using flow battery technology for realizing daily power/energy management of the marine current turbine system.
- Proposal of an original power limitation strategy based on flux-weakening operations for PMSG-based non-pitchable marine current turbine systems at over-rated marine current speed.

This thesis is organized as follows:

Chapter I presents the up-to-date information on the achievements in megawatt-level marine current turbine technologies; it reviews and compares various energy storage technologies concerning their applications for addressing the power fluctuation phenomena in tidal current generation systems.

Chapter II deals with the swell wave modeling and the power smoothing control strategies with supercapacitors for a grid-connected marine current turbine system.

Chapter III proposes flow battery system for daily energy management of the hybrid marine current turbine system with diesel generators.

Chapter IV analyses the flux-weakening strategy for power limitation control of the PMSG-based non-pitchable marine current turbine system at over-rated marine current speed.

Chapter

I

State of the Art Survey of Energy Storage Technologies for Marine Current Turbines

I.1 INTRODUCTION

Increasing concerns about the depletion of fossil resources and environmental issues lead to a global need for producing more clean energy from renewable sources. Ocean is appreciated as a vast source of renewable energies. Considering marine renewable energies, significant electrical powers can be extracted from marine tidal currents. However, the power harnessed from marine tidal currents could be highly fluctuant due to swell waves and the periodicity of the tidal period. To improve the power quality and make the marine turbine system produce more reliable and stable electricity to the grid/load side, energy storage systems can play a crucial role. In this chapter, a review and state of the art of energy storage technologies are presented. Various energy storage technologies are analyzed and compared. The long-period power variation due to the tide phenomenon and the short-period power fluctuation due to swell effect are both considered. The background of tidal current energy and some up-to-date information about the large current turbine technologies are also presented.

I.2 TIDAL CURRENT TURBINE BACKGROUND

Although various kinds of energy can be extracted from the sea such as tidal current energy, wave energy, thermal energy, ocean osmosis (salinity gradients) energy and biomass energy; the kinetic energy available in tidal currents can be converted to electricity using relatively mature turbine technologies. The exploitable marine current power with present technologies is estimated about 75 GW in the world and 11 GW in Europe. France has about 3.4 GW potential which places the second in European countries behind 6 GW in UK [1].

One of the main advantages of marine current energy is related to the predictability of the resource. Exploitable marine currents are mostly driven by tidal currents, which cause seawater motion twice each day with a period of approximately 12 h and 24 min (a semidiurnal tide), or once each day in about 24 h and 48 min (a diurnal tide). The astronomic nature of tides is driven by the gravitational interaction of the Earth-Moon-Sun system and makes marine tidal currents highly predictable with 98% accuracy for decades [2]. Marine current energy is in first order independent of season and weather conditions which would affect the performances of solar and wind power generation.

There are basically two ways of generating electricity from marine tidal energies: either by building a tidal barrage across an estuary or a bay, or by extracting energy from free flowing tidal currents [3]. A tidal barrage allows water to flow into a bay or river during high tide, and

releases the water back during low tide. Turbines can be placed at these sluices to capture the energy as the water flows in and out. The main drawback of this scheme is that suitable sites of constructing a dam-like structure are very limited worldwide. Moreover, large barrage systems would change the hydrology and may have negative impacts on the local ecosystem [4]. Therefore during the last few decades, developers have shifted towards technologies that capture the kinetic energy from tidal-driven marine currents. The power capture principle is quite similar to wind power generation system. In fact, various original horizontal axis and vertical axis marine current turbines (MCT) have been developed around the world in recent years [5-8]. The majority of MCT devices are horizontal axis turbines with rotation axis parallel to the current flow direction. The main disadvantages associated with vertical axis turbines are relative low self-starting capability, high torque fluctuations and generally lower efficiency than horizontal axis turbine design. Currently, only horizontal axis MCTs appear to be the most technologically and economically solution for large-scale marine current turbines with power capacity over 500 kW.

Several horizontal axis turbine technologies have been developed more than one generation of systems and have been chosen by the industrial community to realize pilot demonstrative MCT farms before the final commercial stage. These pilot MCT farm projects illustrate the up-to-date developments of MCT technologies which will provide electricity to coastal or island areas in the coming years. Table I.1 summarizes the main information about some of these pilot MCT farm projects and their planned/estimated operational dates.

OpenHydro is an open-center turbine technology; a 250 kW prototype was installed and tested at European Marine Energy Center (EMEC) off Orkney in Scotland and connected to the UK national grid in 2008. This turbine technology is then chosen by the French utility company EDF to build a demonstrative MCT farm off the coast of Paimpol-Bréhat in Brittany, France. The first 500 kW OpenHydro turbine (Fig. I.1) was tested in September 2011 in Brest. This 850 tonnes turbine has a diameter of 16 m and is supposed to be installed at a depth of 35 meters. The 4-turbine farm is reported to be in operation in 2014 [9].

The 1MW pre-commercial turbine HS1000 (Fig. I.2) was tested by Andritz Hydro Hammerfest (original Hammerfest Strøm) at EMEC tidal test site at the end of 2011. The HS1000 turbine is based on the technology of a smaller prototype HS300 (300 kW), which was installed in Norway and connected to the public grid in 2004. This turbine technology is planed to be used in a 10 MW commercial array in the Sound of Islay on the west coast of Scotland [14]. This technology is also reported to be chosen in the first phase of MeyGen tidal

current project in Inner Sound of the Pentland Firth [10]. Another candidate for the MeyGen project is the AR1000 turbine (Fig. I. 3) technology developed by Atlantis Resources

Table I.1. Pilot MCT farms in the coming years [1], [9-11].

Companies	Location	Turbine Type	Turbine Number	Total Capacity (MW)	Operational Year
DCNS, EDF	Paimpol Bréhat	OpenHydro	4	2	2014/2015
MeyGen	Pentland Firth (Scotland)	HS 1000 or AR 1000	6	6	2015/2016
MCT, Siemens	Kyle Rhea (Scotland)	SeaGen S	4	8	2015
	Anglesey (Wales)	SeaGen S	5	10	> 2015
Andritz Hydro Hammerfest	Sound of Islay (Scotland)	HS 1000	10	10	> 2015
GDF Suez, Eole Generation	Raz Blanchard	Voith Hytide	3~6	3~12	2016
	Fromveur	Sabella	> 4	> 4	2016

Fig. I.1. DCNS-OpenHydro turbine [12].

Fig. I.2. Andritz Hydro Hammerfest HS1000 turbine [13].

Fig. I.3. Atlantis AR1000 turbine [15].

Corporation [15]. The Atlantis AR1000 turbine features fixed pitch configuration and is rated at 1 MW at 2.65 m/s current velocity. The first AR1000 was successfully deployed and commissioned at the EMEC facility during the summer of 2011. A larger turbine AR1500 (1.5 MW at 3.0 m/s) is under development for future installation in the Pentland Firth in Scotland and the Bay of Fundy in Canada.

The SeaGen S turbine developed by the Marine Current Turbine Ltd (owned by Siemens since 2012) is a well-known twin rotor technology and it is the world first grid-connected megawatt-level MCT system. The 1.2 MW SeaGen S system (2×600 kW) was installed in Strangford Lough in Northern Ireland in 2008 and has generated 8 GWh electricity since the installation [16]. The new SeaGen S system planed to be installed in the two commercial arrays in UK waters (as listed in Table I.1) will be an up-scaled version with 2 MW power rating for each unit.

French energy company GDF Suez has plans to install pilot tidal energy farms at Raz Blanchard off the coast of Lower Normandy and the Fromveur passage off the coast of Finistère in Brittany. These two sites represent 80% of the marine current energy potential in France. For the Raz Blanchard project, GDF Suez has recently confirmed to use Voith Hydro HyTide turbine and Alstom tidal turbine technology [17]. Voith turbine technology (Fig. I.4) is developed by German hydropower equipment maker Voith Company. The 1 MW fixed pitch turbine has a rotor diameter of 16 m and reaches the rated power at a current velocity of 2.9 m/s. Alstom tidal turbine (Fig. I.5) is developed with Tidal Generation Ltd and also has a power rating of 1 MW. This turbine has rotor diameter of 18 m and reaches the rated power at a current velocity of 2.7 m/s. Both two turbines are now installed at EMEC tidal test site [18-19]. For the Fromveur project, the Sabella tidal turbine technology will be used. The Sabella D10 turbine will have a rotor diameter of 10 m and a power capacity of 0.5~1.1 MW for 3.0~4.0 m/s current velocities [20]. Figure I.6 illustrates the perspective Sabella turbine farm.

Fig. I.4. Voith HyTide turbine [18].

Fig. I.5. Alstom tidal turbine [19].

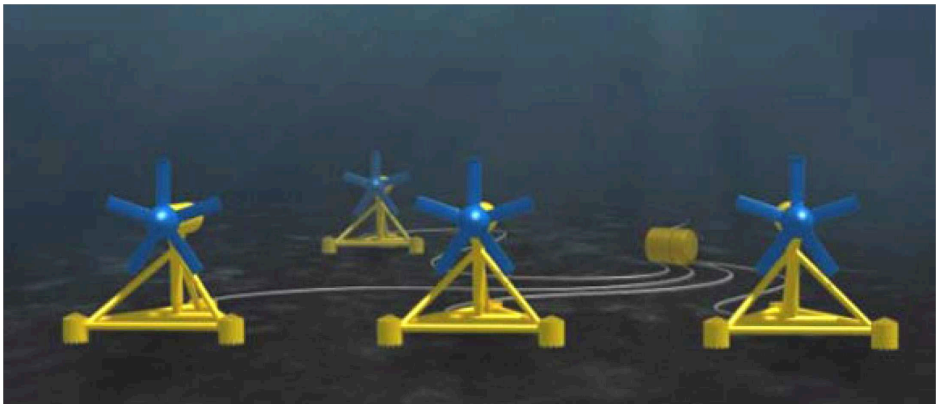

Fig. I.6. Sabella turbine farm illustration [21].

The Sabella D10 is based on the first French marine current turbine Sabella D03 (3 m rotor diameter) which was tested at Odet estuary near Brest in 2008. The prototype D10 turbine is now completing the construction and is scheduled to be installed in the Fromveur passage at the end of 2014. Larger turbines D12 and D15 with power capacities of 1~2 MW are under design for future turbine farm applications [20-21].

The turbines presented above represent the newest achievements in the megawatt-level MCT technologies. The comment point is that they are all horizontal axis turbine; and it should be noted that most of them adopt the fixed pitch solution for the turbine blades.

I.3 POWER FLUCTUATION PHENOMENA

The attraction of tidal current renewable energy lies in high energy density and high predictability of the tidal current resources. Seawater is more than 830 times denser than air and it enables a MCT to be 2~3 times smaller than a wind turbine for a same power rating. Moreover, the astronomic nature of the tides makes tidal current a very predictable energy resource on long-period scale for decades. However, the MCT is subjected to two kinds of power fluctuation phenomena.

The mechanical power harnessed by a horizontal marine current turbine can be calculated by the following equation,

$$P = \frac{1}{2}\rho C_p A V^3 \qquad \text{(I.1)}$$

In this equation, sea water density ρ and turbine blade swept area A are considered as constants; V represents the marine current velocity; C_p is the power capture coefficient and is related to the tip top speed ratio and the marine current speed when the blade pitch angle is fixed. For typical MCTs, C_p is estimated to be in the range of 0.35-0.5 [3]. When a Maximal Power Point Tracking (MPPT) strategy is used, the turbine rotor speed is able to be controlled to keep C_p at its optimal value. That means in first order, the power produced by the MCT is proportional to the cubic of current speed in the turbine cross section. It can be seen from (I.1) that the power produced by a MCT would change greatly when there are variations in the marine current speed.

Two main kinds of power fluctuations can be identified. On a daily time scale, the MCT generated power varies with a period of about 6 or 12 hours which is related to tidal astronomical phenomenon. In Europe, the semi-diurnal tide is dominant and the tidal current direction changes about every 6 hours [1]. On a much smaller time scale, the MCT power may fluctuate with a period of a few seconds caused by swell disturbances. These short-time fluctuations are mainly related to long wavelength swells which are considered as the main disturbance for the marine current turbine system.

Figure I.7 gives the measured swell waves data at Les Pierres Noires in the Fromveur passage near Brest. This correlogram of swell typical period T_p and significant height H_s is from CANDHIS (French National Archiving Center for In-situ Swell Measurements) [22]. The data are recorded during winters in the last few years (2005-2013). There are totally 46889 records in this table. If we consider that the swells corresponding to sea states of $10\ \text{s} < T_p$ and $2\ \text{m} < H_s$ can not be neglected for MCTs, it still remains about 33206 records.

Corrélogramme - Hm0/Tp - HIVERNAL

(Hauteur significative spectrales des vagues / Priode de pic barycentrique)

hm0 (m)	tp (Secondes)																				
0	1.2	2.4	3.6	4.8	6	7.2	8.4	9.6	10.8	12	13.2	14.4	15.6	16.8	18	19.2	20.4	21.6	22.8	24	Total
1			133	149	60	198	450	715	1510	1471	1025	306	111	116	41	29	5	6	8		6333
2			35	685	272	468	1130	1629	3548	3459	3397	1224	623	250	140	66	19	5	4	1	16955
3					53	269	748	1050	1924	2617	2994	911	462	143	61	45	11	7	2		11297
4						19	212	616	1243	1455	1864	781	367	138	50	24	8				6777
5							21	128	527	802	962	483	293	166	64	21	1				3468
6							2	11	127	224	386	293	140	102	38	8	2	3	2		1338
7								2	24	55	165	120	86	41	17	8	3	3			524
8									1	5	51	42	35	17	2						153
9											5	7	8	5	1						26
10											3	4	5	2							14
11													1	1	1						3
12																1					1
Total			168	834	385	954	2563	4151	8904	10088	10852	4171	2131	981	415	202	49	24	16	1	

Les valeurs du tableau sont exprimées en nombre d'éléments - Les case vides correspondent à des valeurs nulles.

Code des couleurs		
>= 10 ‰	>= 30 ‰	>= 50 ‰

Fig. I.7. Correlation diagram of swell at Les Pierres Noires [22].

It implies that non-negligible swell waves occur 71% (=33206/46889) of the time for this high potential tidal current energy site during the winter. The sea state would be relatively calmer during summer period in this site, however the swell is still considered as the main disturbance for marine current speed in this water area.

Figure I.8 gives an example of the power produced by a MCT during one day period. This calculation is based on the tidal data provided by the SHOM (French Navy Hydrographic and Oceanographic Service) for Raz de Sein. In this calculation, the C_p is set at 0.4 and the blade swept area is calculated by $\pi \cdot 8^2$. Fig. I.8a (not considering swell effect) shows the long-time power variation caused by tidal astronomic nature, which are highly predictable on hourly

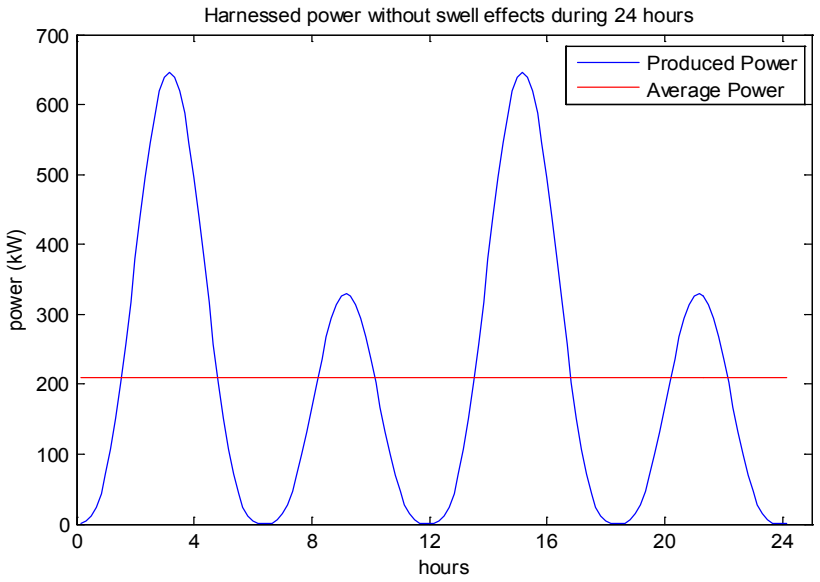

(a) without swell effect

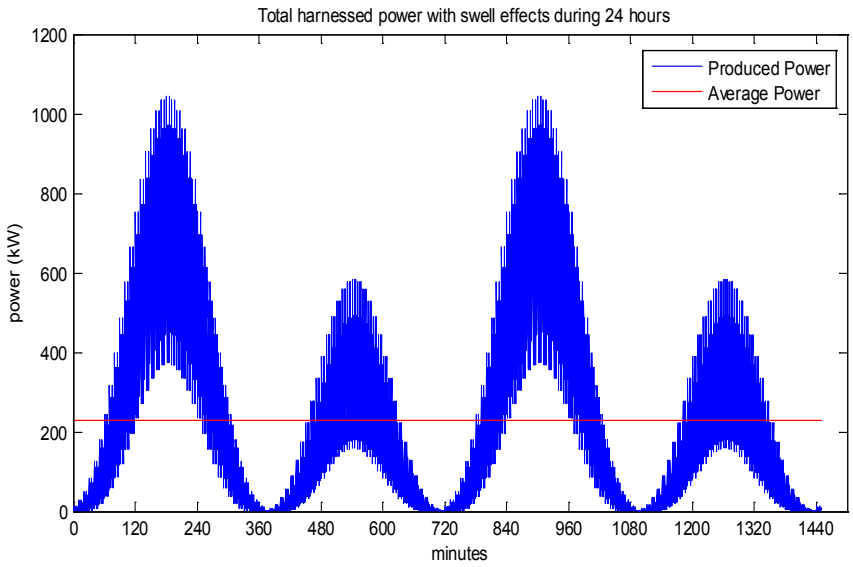

(b) with swell effect

Fig. I.8. Power produced by a MCT during one day.

periods for the given site. Fig. I.8b shows the power profile when considering swell effect which introduces short-time fluctuations in the power profile and makes the MCT harnessed power far away from the prediction.

Integration of variable and fluctuating renewable sources to the power grid increases the difficulties of stabilizing the power network and balancing the supply and demand. Energy storage systems (ESS) are assumed to be a good solution to smooth the power fluctuations, improve the system reliability and provide auxiliary services to the grid [23-24]. For marine current energy application, two different types of ESS should be considered [25]. For the slow power variation related to the tidal astronomical character, long duration and high energy capacity ESSs are expected. On the other hand, high power and quick charge/discharge ESS devices are required to deal with the fast power fluctuation caused by swell effect. In the following sections, a state of the art of various ESS technologies would be given.

I.4 BATTERY STORAGE TECHNOLOGIES

Battery is a classical solution for storing electricity in the form of chemical energy. Battery storage technologies presented here refer to rechargeable batteries which can be used as energy storage sources. A battery system usually consists of one cell or multiple cells connected in series or in parallel depending on the desired output voltage and capacity. Each battery cell comprises the cathode (positive electrode), the anode (negative electrode) and the

electrolyte which provides the medium for transfer of electrons between the two electrodes. During discharge, electrochemical reactions at the two electrodes generate a flow of electrons through an external circuit with the cathode accepting electrons and the anode providing electrons. During charging process, the electrochemical reactions are reversed and the battery absorbs electricity energy from the external circuit.

4.1 Lead-acid Batteries

Lead-acid batteries are the oldest type of rechargeable batteries. They are considered as very mature technologies. They are easy to install and have a low cost. Valve regulated lead-acid batteries require negligible maintenance. The self-discharge rates for this type of batteries are very low, around 2-5% of rated capacity per month, which make them ideal for long-term storage applications. However, disadvantages of lead-acid batteries are low energy density and short service life. The typical energy density is around 30 Wh/kg and the typical lifetime is between 1200 and 1800 cycles [26]. The cycle life would be affected by depth of discharge and they are not suitable for discharges over 20% of their rated capacity [27]. The performance of lead-acid would also be affected by temperature: higher temperature (with the upper limit of 45°C) will reduce battery lifetime and lower temperature (with the lower limit of -5°C) will reduce the efficiency.

4.2 Nickel-based Batteries

In a nickel-based battery, nickel hydroxide is used on the positive electrode but for the negative electrode different materials can be used. This fact explains the existence of various technologies. There are three kinds of nickel-based batteries namely the nickel-cadmium (NiCd) battery, the nickel-metal hydride (NiMH) battery and the nickel-zinc (NiZn) battery. The NiCd technology uses cadmium hydroxide, the NiMH uses a metal alloy and the NiZn uses zinc hydroxide. Nickel-based batteries have larger energy densities than lead-acid batteries, 50 Wh/kg for the NiCd, 80 Wh/kg for the NiMH and 60 Wh/kg for the NiZn.

NiCd batteries are now reaching the level of maturity as lead-acid batteries. NiCd batteries have a longer lifetime about 3000 cycles and can be fully discharged without damage [28]. As an example, this technology is used in the energy storage system of the Alaska Golden Valley project which provides a backup to an isolated electrical power system. This project is claimed to be the world's most powerful battery system which can produce up to 52 MW of emergency backup power for about 15 minutes [29]. However, two drawbacks limit future large-scale deployment of this technology. One is the high price, for the NiCd battery may

cost up to 10 times more than the lead-acid battery. Another is the environment concerns about cadmium toxicity and associated recycling issues [30-31].

NiMH batteries have high energy density witch is over twice than lead-acid batteries. This type of batteries can be recycled and their components are harmless to the environment. They also can be used in large temperature ranges and high voltage operation. However, repeatedly discharged at high load currents would shorten the life of NiMH batteries to about 200-300 cycles and the memory effect reduces the useful SoC (State of Charge) of the battery. NiZn batteries have the same advantages of NiMH batteries and have deep cycle capability as NiCd batteries, but they suffer from poor life cycle due to the fast growth of dendrites.

4.3 Lithium-ion Batteries

Lithium-ion batteries achieve excellent performances in portable electronics and medical devices. This technology is now typically driven by the consumer electronics market (smartphone, tablet, digital camera, etc.) and is very attractive for electric vehicle applications, because lithium-ion batteries are lighter, smaller and more powerful than other batteries. They have the highest energy density (100-250 Wh/kg) and the highest power density (800-2000 W/kg) among all the batteries [32]. Other advantages of lithium batteries include high efficiency, low memory effect and low self-discharge rate. This is the reason why lithium-ion batteries are very promising to be used in the next-generation electrical vehicles or hybrid vehicles [27, 32-33].

Some drawbacks exist in this battery technology. Lithium-ion batteries are theoretically characterized by a lifetime about 3000 cycles at 80% depth of discharge. However in actual, lithium-ion batteries are not robust and sometimes very fragile. Life cycles are affected by temperature and would be severely shortened by deep discharges [28]. Usually, lithium-ion batteries require special protection circuit to avoid overload and need sophisticated management systems to maintain safe operational conditions. Another drawback is that the cost of lithium-ion batteries, from $900/kWh to $1300/kWh. These facts would limit the use of lithium-ion batteries in large-capacity cases and applications where low SoC would be reached.

In 2011, a 32-MW lithium-ion battery system was installed adjacent to a wind farm near Elkins in West Virginia (USA) for smoothing out some of the wind's variability. This battery system is capable of discharging the rated power for about 15 minutes [29]. A recent research shows that lithium-ion batteries could be the most cost-effective solution for integrating renewable sources only when the required depth of discharge is limited around 10% [34].

4.4 Sodium-sulphur Batteries

Sodium-sulphur (NaS) is a relatively new promising high temperature battery technology, operating at over 300°C. Basic cell construction uses liquid sulphur at the positive electrode and liquid molten sodium at the negative electrode separated by a solid beta-alumina ceramic electrolyte (shown in Fig. I.9). The specific energy density of this kind of battery is 100Wh/kg and the life span is 2500 cycles at 100% depth of discharge with a high energy efficient about 89% [28].

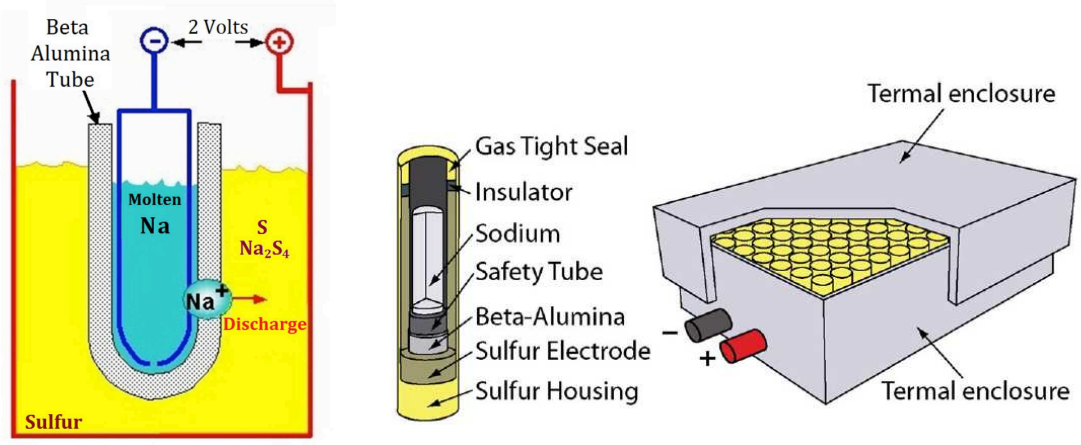

Fig. I.9. NaS battery cell and package [23],[35].

During discharge when positive Na^+ ions flow through the electrolyte and combine with the sulfur forming sodium polysulfide (Na_2S_4), electrons will flow in the external circuit of the battery. Basic cell voltage is about 2V. This process is reversible: during the charging process, the Na_2S_4 molecules release the Na^+ ions to the electrolyte where these ions are recombined as elemental sodium. In classical operating conditions, the heat produced by charging and discharging is enough to maintain running temperatures (about 300-350°C), but the battery still need to be heated in stand-by mode to keep the electrodes in molten state [36].

Sodium sulfur battery technology was brought to market in 2002 by Japanese company NGK. To date, more than 270 MW of total capacity has been set up at over 190 sites in Japan. These batteries stored energy which is suitable for 6 hours of daily peak shaving. U.S. utilities have deployed 9 MW of NaS batteries for reinforcing wind capacity and other applications. The largest NaS installation is a 34 MW, 245 MWh unit used for wind stabilization in Northern Japan [31].

On one hand, this technology has advantages such as low cost, high energy capacity, high efficiency and deep discharge tolerance. On the other hand, this battery technology is

penalized by high operating temperature and the corrosive nature of sodium. These characteristics make NaS batteries suitable for large-scale stationary applications. This technology appears attractive for marine renewable applications, being an effective solution for stabilizing energy output during periods of 3-6 hours in order to smooth the output of a marine generator farm. However the operating environment must be perfectly controlled if this solution is used. This fact implies 'a priori' a setup on an offshore platform or near the onshore transmission line for the power gird.

4.5 Flow Batteries

Flow batteries are relatively new battery technology dedicated for large energy capacity applications. This technology uses two external tanks to reserve liquid electrolytes and a pump system for circulating the electrolytes to the battery cell stack (consisting of the two electrodes and the ion exchange membrane). Figure I.10 illustrates the structure of a flow battery system. The charging and discharging processes are realized by means of a reversible electrochemical reaction between two liquid electrolyte reservoirs. Flow batteries are often called redox flow batteries (RFB), because this technology is based on the redox (reduction-oxidation) reaction between the two electrolytes in the system.

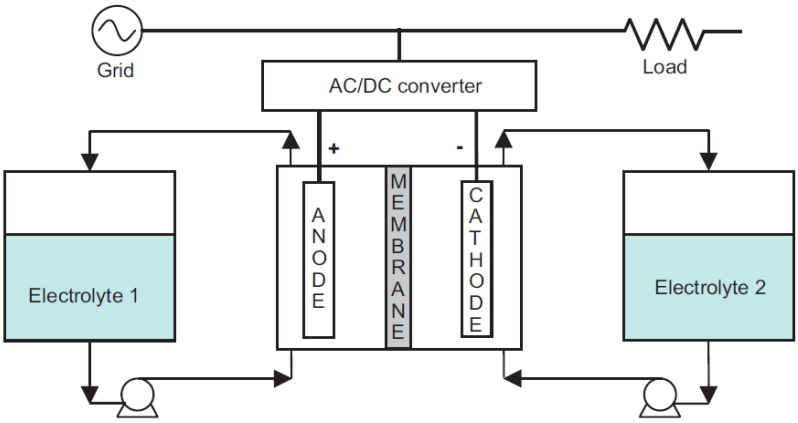

Fig. I.10. Flow battery structure [30].

The most distinguished advantage of flow battery technologies is that the power and energy ratings can be sized independently [36-38]. The power rating is determined by the design of the electrode cells and the energy capacity depends on the volume of the electrolytes which are separated from the cell stack and can be designed independently. Therefore, flow battery can be easily designed to meet specific energy capacity or power rating requirements. These characteristics make them suitable for a wider range of applications than conventional

batteries. Another significant advantage is the long service life over 10,000 cycles at 75% depth of discharge. Other advantages include high safety, negligible degradation for deep discharge and negligible self-discharge. The major disadvantages of flow batteries are that the power/energy density is relative low compared to other technologies and extra pumps systems are needed.

Over the past 20 years, four designs of flow batteries have been demonstrated: vanadium redox (VRB), zinc bromine (ZnBr), polysulphide bromide (PSB) and cerium zinc (CeZn). Major installations are in Japan and North American, using the vanadium redox and zinc bromine designs. Energy efficiency is about 85% for VRB system and 75% for ZnBr system. 5kW/20kWh Community Energy Storage units based on ZnBr batteries are now being tested. Integrated ZnBr energy storage systems have been tested on transportable trailers (1MW/3MWh), and these systems could be connected in parallel for more powerful applications [31]. VRB system of 500 kW, 10 hours (5 MWh) was installed by Sumitomo Electric Industries (SEI) in Japan for peak shaving and UPS applications in 2001. The largest VRB plant so far is the 4MW/6MWh plant in Hokkaido, Japan [38]. This VRB plant can provide a temporary overload up to 6 MW and it is intended for smoothing output power fluctuations of a nearby 30.6 MW wind power plant.

Flexibility of energy and power sizing, long lifetime, low cost and low maintenance make flow battery a very promising technology to be used for integrating fluctuant and intermittent renewable energies to the power grid. For marine current energy, flow batteries can be designed differently for compensation short-time and long-time fluctuations, and more favorably they are suitable for hours energy storage for smoothing the fluctuation due to tidal phenomenon or realizing some energy management strategies.

4.6 Battery Technologies Comparison

Table I.2 summarizes the main merits and demerits for the battery technologies discussed above. For marine energy application, these batteries are reasonable supposed to be installed underwater or on an offshore platform and they may be discharged deeply in order to achieve a required smooth effect. In the first place, low maintenance and robust long service life (deep discharge ability) should be considered as important criteria, and in that term the lead-acid and lithium-ion batteries are not favorable due to their short cycle life for deep discharge. Low cost should also be emphasized, which make lithium-ion and nickel-based batteries not attractive for megawatt-scale applications.

Table I.2. Battery Technologies Comparison.

Battery Type	Advantages	Disadvantages
Lead-acid	√Low cost √Low self-discharge (2-5%per month)	×Short cycle life (1200-1800 cycles) ×Cycle life affected by depth of charge ×Low energy density (about 40Wh/kg)
Nickel-based	√Fully charged (3000 cycles) √Higher energy density (50-80Wh/kg)	×High cost, 10 times of lead acid battery ×High self-discharge (10% per month)
Lithium-ion	√High energy density (80-190Wh/kg) √Very high efficiency 90-100% √Low self-discharge (1-3% per month)	×Very high cost (900-1300 $/kWh) ×Life severely shorten by deep discharge ×Special overcharge protection circuit
NaS	√High efficiency 85-92% √High energy density (100Wh/kg) √No degradation for deep charge √No self-discharge	×Keep heated in stand-by mode at 325℃
Flow battery	√flexible energy and power ratings √Long service life (>10,000 cycles) √No degradation for deep charge √Negligible self-discharge	×Medium energy density(40-70Wh/kg)

It can be concluded that NaS batteries and flow batteries are two best candidates among battery technologies. They are cost-effective for MW and MWh applications and they have robust service life compared with other technologies.

Compared with NaS batteries, flow batteries have a longer life span but a more complicated system set-up. Flow batteries are easier to operate because they do not need to be kept at a high temperature. With appropriate installations, flow batteries and NaS batteries seem to be two most promising battery technologies suitable for smoothing the long-term variation in marine current energy systems.

For the short-term fluctuation (caused by swell disturbance) with a period of seconds, a much shorter charge/discharge cycle time than batteries is required. Two short-term energy storage technologies with typical charge/discharge time constant about seconds to minutes are presented in the following sections.

I.5 FLYWHEEL TECHNOLOGIES

A flywheel is based on a rotating disk which can store kinetic energy. This flywheel is associated with an electrical machine and drive system which allows controlling the energy storage and discharge. According to the rotational speed, there are broadly two classes of flywheel technologies: low-speed flywheels (less than 10,000 rpm) and high-speed flywheels (more than 10,000 rpm) [39-41]. Low-speed flywheels use steel rotors and conventional bearings, and they achieve energy density of 5-30 Wh/kg. High-speed flywheels use composite rotors and low friction bearings (e.g., superconducting magnetic bearings). Composite rims are lighter and much stronger than steel, so they can be used with extremely high rotational speed and achieve high energy density up to 100 Wh/kg [26]. The amount of energy stored in a flywheel depends on the square of the rotational speed, making high-speed flywheels highly desirable for energy/mass ratio optimization.

Figure I.11 shows a typical flywheel energy storage system (FESS). It consists of a massive rotating cylinder (a rim attached to a shaft) that is supported on a stator by magnetically levitated bearings. The flywheel system is operated in a vacuum chamber to reduce friction and losses. A motor/generator is connected to the flywheel to interact with the power grid or the renewable energy sources through power electronics drive.

Conventional low-speed flywheels can be used for the uninterruptible power supply (UPS). One of the popular flywheel UPSs is the Piller's POWERBRIDGE system available in the range of 250-1300 kW. The bigger system contains a low-speed flywheel with a maximum speed of 3600 r/min and can deliver 1.1 MW during 15 seconds [39].

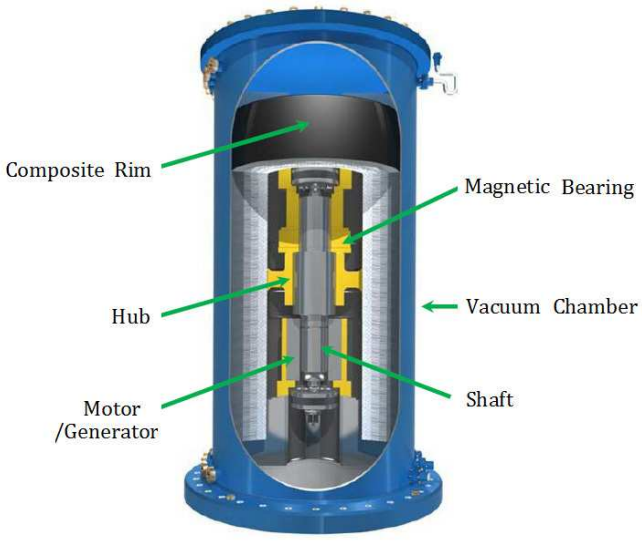

Fig. I.11. Flywheel energy storage device structure [41].

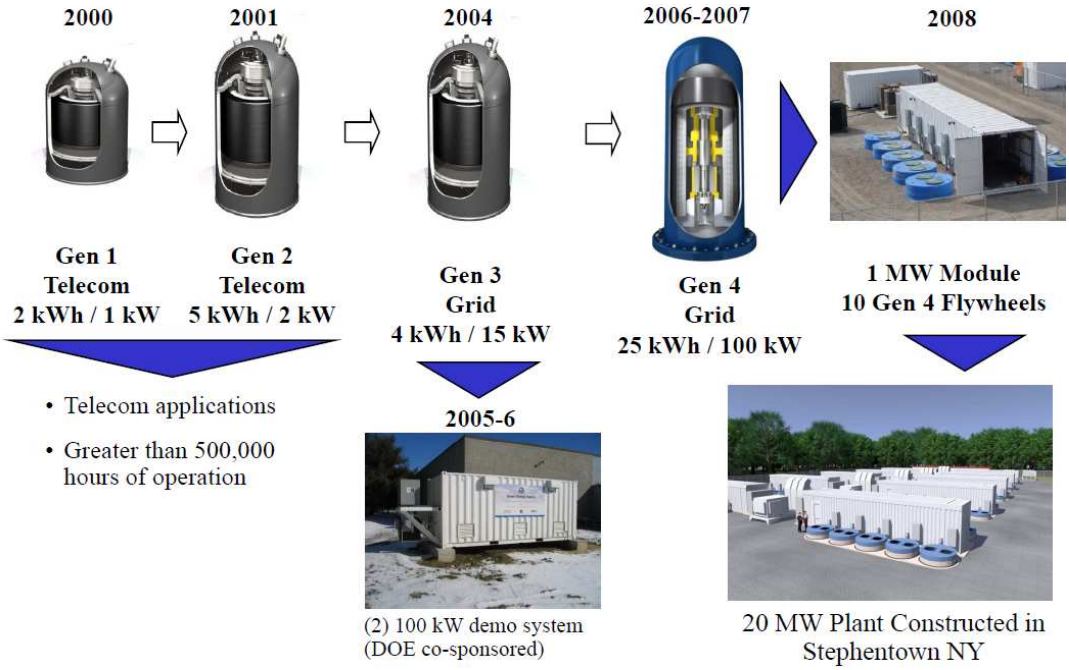

Fig. I.12. Evolution of Beacon POWER Flywheel Systems [35].

Figure I.12 illustrates the evolution of Beacon POWER FESS products and provides a clear insight into the two applications where FESS can offer. Low-power systems (several kW for hours) are used for telecommunication equipment support. High-power systems (hundreds of kW for seconds or minutes) can be used to provide power frequency regulation service for the power grid. An example of this typical grid-application is the 20 MW flywheel plant which provides frequency regulation service to the local grid in Stephentown, NY. The commercial operation of this facility started in 2011 [41]. FESSs are also being used in isolated power grid. For instance, a 350 kW / 5 kWh FESS is installed in Flores Island, Portugal, for improving frequency stability of the micro-grid on the island and a 500 kW / 5 kWh FESS is used to smooth the power fluctuations in a 3 MW wind-diesel hybrid system in Coral Bay, Australia [42].

Key advantages of flywheel energy storage system include high cyclic ability (over 10^5 cycles with deep discharge or 20 years service time), high power density (quick charge/discharge), high efficiency and low maintenance. One of the main disadvantages of flywheel energy storage system is the high self-discharge rate which is typically over 20% per hour [43]. This disadvantage makes them not suitable for long-term applications. Another challenge is to reduce the high system price due to advanced materials and limited mass production.

Based on these characters and the development trends, flywheels seem very appropriate for providing short-term ride-through power or smoothing the power fluctuations on a time scale of 15 seconds to 15 minutes. With regard to long-term energy storage, they don't have many advantages over battery systems. Therefore, for marine current energy application, flywheel systems can become a very interesting candidate to compensate short-term fluctuations related to swell effects. It should be noted that flywheel systems are not easy to be installed underwater considering the corrosion effects of sea water and the peripheral equipments such as power converters and transformers.

I.6 SUPERCAPACITOR TECHNOLOGIES

Supercapacitors, also know as ultracapacitors and electrochemical double-layer capacitors (EDLCs), store energy by the capacitance effect. Supercapacitors are working in a similar way as conventional capacitors, but they are characterized by a much higher capacitance (kilo farads) in smaller packages [23]. It must be remembered that the capacitance is proportional to the area of the plates and the permittivity of the dielectric, and inversely proportional to the distance between the plates. Supercapacitors use high-permittivity dielectric and maximize the electrode surface area by using porous active carbon, thus allowing large amount of energy to be stored at the electrode surface. The two electrodes are separated by a very thin porous separator witch is immersed in the electrolyte. The electrolyte can be either aqueous or organic. The aqueous capacitors have a lower energy density due to a lower cell voltage but are less expensive. They have a lower resistance, and work over a wider temperature range. Figure I.13 shows the structure of one individual supercapacitor cell [44]. The potential difference for one cell is around 1V and 3V with aqueous and organic electrolyte respectively.

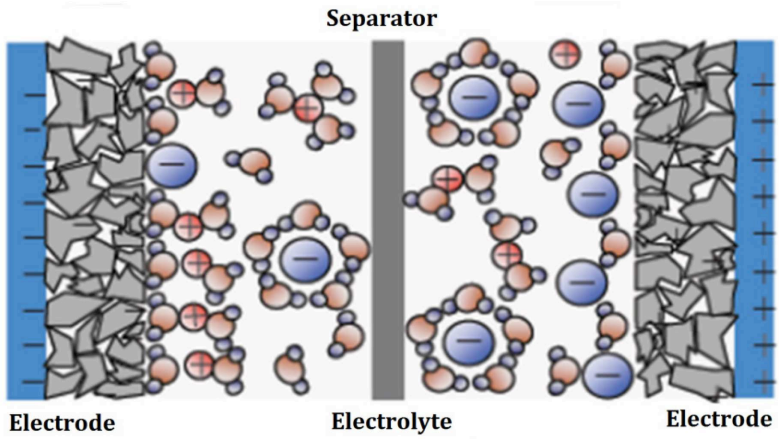

Fig. I.13. Supercapacitor cell [44].

Thanks to that the electrodes will not be chemically degraded as in batteries, supercapacitors are able to be used during hundreds of thousands cycles in deep charge/discharge operations. Supercapacitor can be cycled more than 500,000 times and have a service life of 12 years. Power density of supercapacitors is considerably higher than batteries due to that the electrical charges are physically stored on the electrodes. Supercapacitors can be easily charged and discharged in seconds, much faster than batteries. Energy efficiency is high and no heat or hazardous substances are released during operation. Although new materials for electrodes are being developed for increasing the energy density, supercapacitors are limited by the disadvantages of a very low energy density (5 Wh/kg) and a high self-discharge rate. That means supercapacitors can absorb or release high amount of power only during a very short time period. Another point is that the lifetime of supercapacitor would be affected by the variation of voltage and by the temperature, so the design of supercapacitor system should include an aging model taking into account the operation characteristics.

Common applications of supercapacitors include starting diesel trucks, railroad locomotives and actuators [45]. Another typical application for supercapacitors is hybrid electric vehicles (HEV). They are used in HEV for storing energy from electrical braking and for providing transient high load power due to their fast charge and discharge capability. Using supercapacitors in conjunction with batteries combines the high power characteristic of the supercapacitor and the high energy capacity of the battery. In a HEV, the use of supercapacitors allows extending the life of the battery (by reducing the depth of charge/discharge of the battery) and enables the battery to be downsized (by reducing the peak loads on the battery) [46-48]. A recent research shows that hybrid supercapacitor/battery design can achieve a substantial reduction in the overall ESS cost in HEV application [33].

Researches have also shown that supercapacitors can be used to absorb high-frequency power fluctuations produced from renewable energy sources, improving significantly power qualities of renewable energy generation systems. Supercapacitors for Doubly-fed Induction Generator (DFIG) and Permanent Magnet Synchronous Generator (PMSG) wind turbine applications are discussed in [49-50] and [51] respectively. In [52-54] only battery is used as the ESS, the main objection is to balance the difference between the turbine-produced power and the load (or grid) required power. If high-power fluctuations have to be smoothed, high-power density devices such as supercapacitors are therefore required. Hybrid ESS based on battery and supercapacitor for wind power application are studied in [55-57].The aim of hybrid ESS is to absorb high-frequency fluctuations by supercapacitors and let batteries dealing with low-frequency fluctuations. This will allow optimizing high-power and high-energy ESSs.

Supercapacitors used in photovoltaic applications are presented in [58-59]. In reference [60], a solution using supercapacitors for smoothing the power generated from SEAREV wave energy converter is presented; and different SoC control strategies for the supercapacitor bank are studied and compared.

For marine current energy system, both low-frequency (long-term) and high-frequency (short-term) fluctuations exist. Thanks to high power performance and high cycling capability, the supercapacitor technology appears to be one of the most appropriate solutions for smoothing the high-frequency fluctuations. But supercapacitors are not adapted for smoothing the power on a time scale larger than one minute. It means that high energy density and long-duration energy storage devices are needed to be associated with supercapacitors for a global treatment in marine current application.

I.7 PHS AND CAES TECHNOLOGIES

Megawatt-level MCTs would facilitate the tidal current energy application and increase the need of energy storage system in the near future. The energy storage technologies presented in the previous sections can easily handle the needs for a single MCT turbine or a small MCT farm with a power range of several MWs. However, larger MCT farm installation can still be envisaged in the long term development of renewable energy application. For example, the possibilities of constructing a MCT plant with 100 turbines in France and deploying a 100 MW MCT farm off the southern most tip of the Orkney Islands Scotland are mentioned in [61] and [62] respectively. Although these large MCT farm will probably be constructed around 2020, the challenge of bulk energy storage requirement for compensate long-term tidal current energy variation can not be neglected. A recent research in [63] shows that even a portfolio approach of aggregating tidal current energies from different locations can not sufficiently compensate the power variation problem caused by the tidal periodicities.

Concerning large-scale grid-level energy storage applications, pumped hydro storage (PHS) and compressed air energy storage (CAES) are two important technologies.

7.1 Pumped Hydro Storage

Pumped hydro storage is a well-known technology of storing and producing electricity by the use of pumps and turbines to transfer water between two reservoirs situated at different heights. During low electricity demand periods, excess generated energy is used to pump the

water from the lower reservoir to the upper reservoir (Fig. I.14). During the peak hours when load demand is high, the water is released back to the lower reservoir through hydro turbines, generating electricity. The round-trip efficiencies of PHS plant are over 75%. The storage capacity of PHS depends on two parameters: the height of the waterfall and the volume of the water. Sites with two natural bodies of water are favorable for this technology and the sea can be used as the lower reservoir. The low energy density of the whole system requires either very large bodies of water or a large height between the two reservoirs. Generally, the lifetime of a PHS is over 30 years with a round trip efficiency of 65-75%. The capital costs are about 650-1900 $/kW and 15-20 $/kWh [65].

Pumped hydro storage technology is the most widespread energy storage system used for electricity networks, with about 300 systems operating worldwide. Their main applications are providing energy management, frequency control, and reserve capacity. PHS is now the only energy storage technology deployed on a GW scale worldwide [66]. In the United States, about 20 GW are deployed in 39 sites, with capacities from less than 50 MW to 2,100 MW. Many of these sites are able to store the excess power during more than 10 hours, making the technology favorable for load leveling. The fast time response (switching between pumping and generating can occur within minutes) enables this technology to provide frequency control for the electricity network. However, the drawbacks for this technology are that the implementation of such a system needs an appropriate geographic site, a high cost investment, and a long construction time.

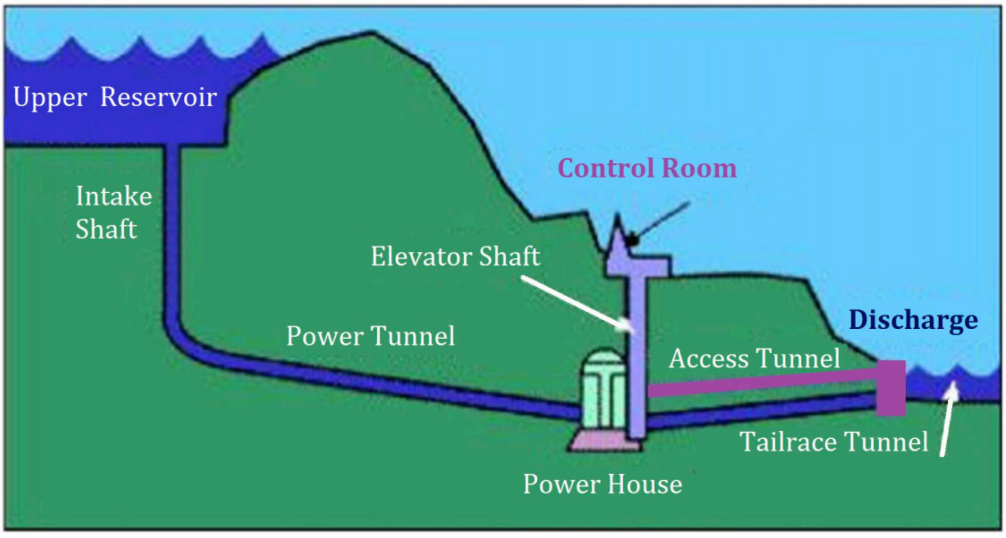

Fig. I.14. Pumped hydro storage plant illustration [64].

7.2 Compressed Air Energy Storage

In a Compressed Air Energy Storage (CAES) system, air is compressed (40-70 bars) and stored in a sealed reservoir, usually an underground cavern, during off-peak periods. During discharge at peak hours, the compressed air is released from the cavern, heated, and expanded through turbines where it is mixed with fuel and combusted to drive an electrical generator (Fig. I.15). The lifetime and efficiency of this technology are similar with PHS. The capital costs for CAES depend on the underground storage conditions, ranging typically between 400 and 800 $/kW [65]. Since the self-discharge of the system is very low, CAES is considered long term scale storage installations which can compete with PHS.

Although the conventional CAES system is not free from producing carbon footprint due to a small amount of gas needed to heat the incoming air before entering the turbine, this technology is able to produce electricity three times more than a conventional gas turbine for a given fuel consumption. Introducing advanced adiabatic concept (using thermal energy storage device to absorb and reuse the heat) in CAES design is reported to be capable of running without the added gas, and it is called AA-CAES system [67].

The cheapest solution for storing significant quantities of air at high pressures is using underground caverns as reservoirs. The air can also be compressed and stored in high-pressure pipelines or aboveground reservoir, which would eliminate the geological limitations and make the system easier to operate.

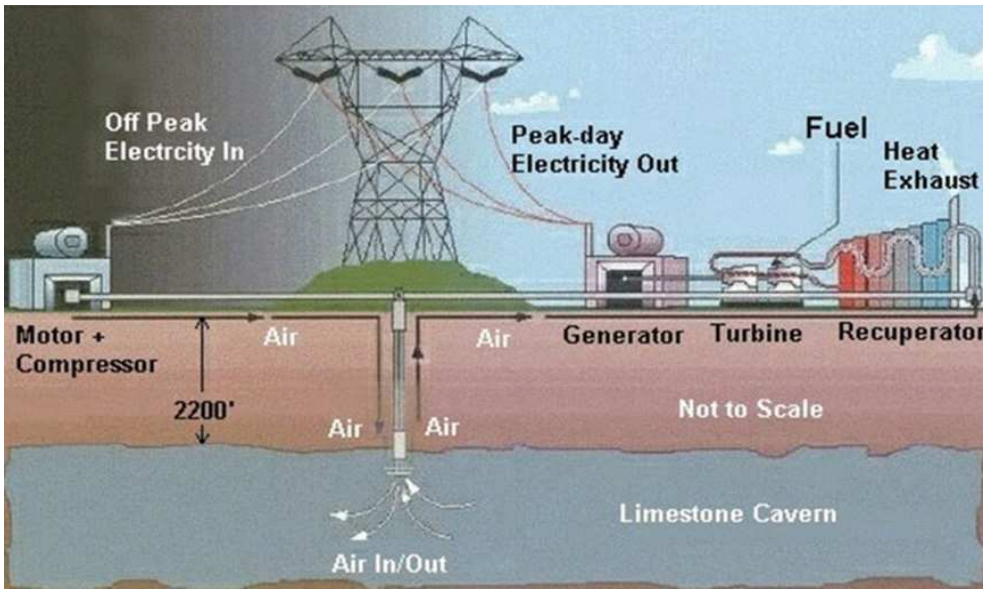

Fig. I.15. Schematic of CAES plant [24].

Another approach to compressed air storage is called CAS, compressed air in cylinders. In a CAS system, air is stored in fabricated high-pressure tanks made of carbon-fiber (up to 300 bars). CAS may become a good solution for small or medium-scale applications when a feasible manufacture cost can be achieved for ultrahigh pressure tanks.

CAES is a proven technology: the first commercial CAES to be built was a 290-MW plant built in Hundorf, Germany in 1978. The second commercial one was a 110-MW unit built in Alabama, US in 1991 [24]. Starting in late 2008, two CAES plants with advanced designs for reducing fuel consumption were constructed by several US utilities: one bulk plant uses an underground reservoir for 10 hours of storage at 300 MW capacity and another use an aboveground reservoir for 2 hours of storage at 15 MW capacity [68].

CAES is a cost-effective option for storing energy in large quantities. CAES plants can perform ramping duty and smooth the intermittent output of renewable energy sources [68]. Simulations results in [66] show that CAES is characterized by a much lower cost and generates a higher rate of return than PHS in wind farm application. Recently, ocean-based underwater compressed air energy storage (OCAES) technologies are under developing for solving the intermittency challenge for offshore renewable energy applications. OCAES utilizes the hydrostatic pressure in deep sea to keep the compressed air (in a distensible air bag/accumulator) under constant high pressure; in this way, the expensive pressure tanks or underground cavern can be avoided [134-135].

I.8 COMPARISIONS OF ENERGY STORAGE TECHNOLOGIES

To be highly efficient, storage systems need to be closely adapted to the type and the scale of applications. Energy storage applications can be generally divided into three categories based on required storage time:

(1) Power Quality: charge/discharge time is required from several seconds to minutes to ensure the quality of power delivered. Example applications are frequency regulation and transient power stability;

(2) Power Bridging: stored energy should be used for several minutes to about an hour to ensure the continuity of the power supply during the switching from one electricity source to another or during black out;

(3) Energy Management: The aim of this strategy is to decouple the synchronization between the power generation and power consumption. This kind of application requires large quantity of energy to be stored or released during several hours. Typical application are load leveling and energy arbitrage, which implies storing low-cost off-peak energy and releasing (selling) the stored energy during high-price peak hours.

Figure I.16 illustrates energy storage capacities and output power capabilities for different energy storage technologies. Figure I.17 compares energy storage technologies based on system power ratings and discharge times; and the three categories of ESS application are illustrated. Concerning the marine current energy application, the interesting ranges for smoothing long-term power variations related to tidal phenomenon and short-term power fluctuations caused by swell effect have been highlighted in Fig. I. 17. The two figures show that several technologies may be in concurrence for a given power/energy requirement. In that case, system cost would become one decisive factor for choosing the final solution.

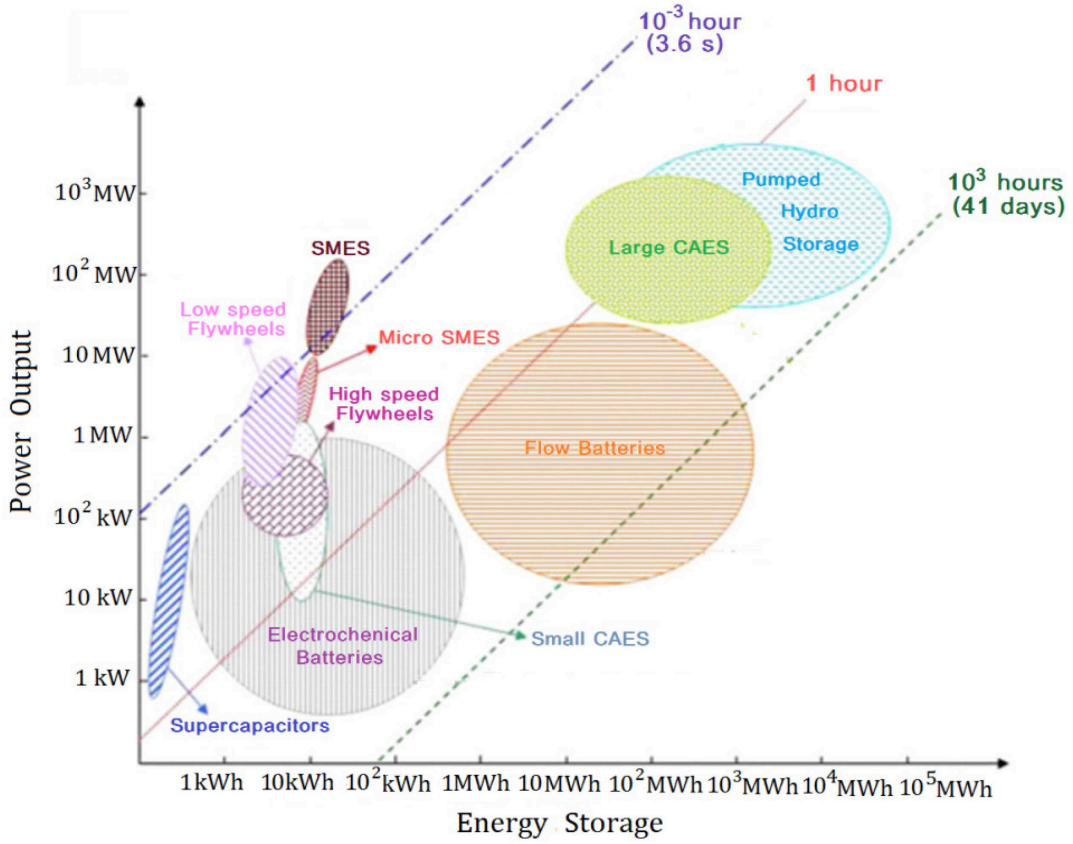

Fig. I.16. Energy storage technologies comparison [24].

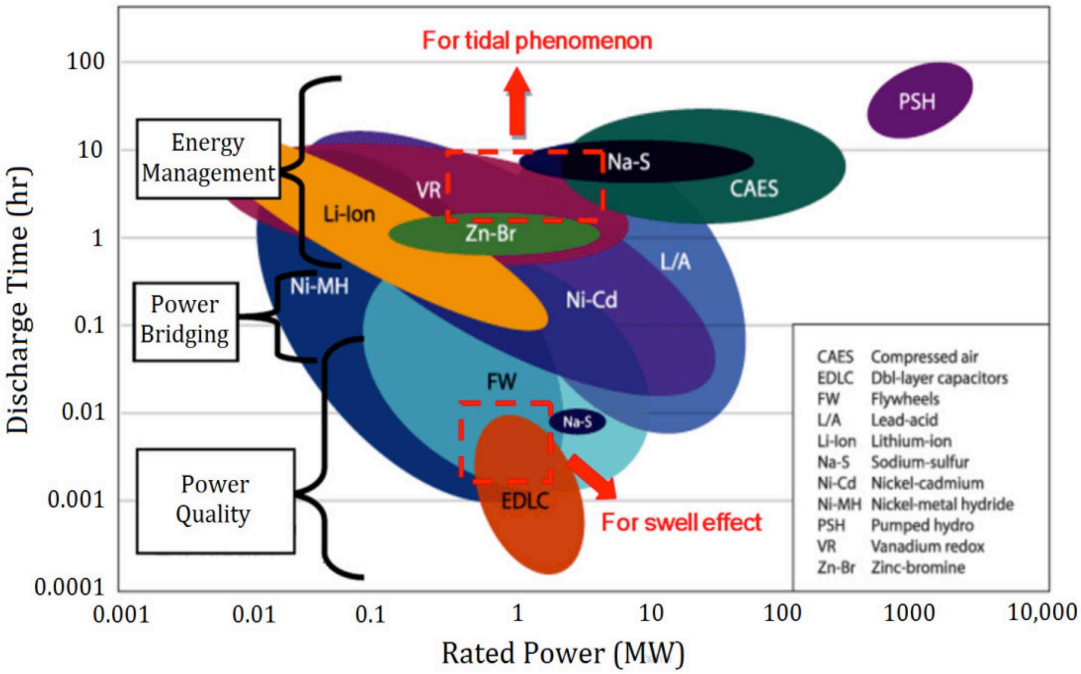

Fig. I.17. System ratings for different energy storage technologies [66].

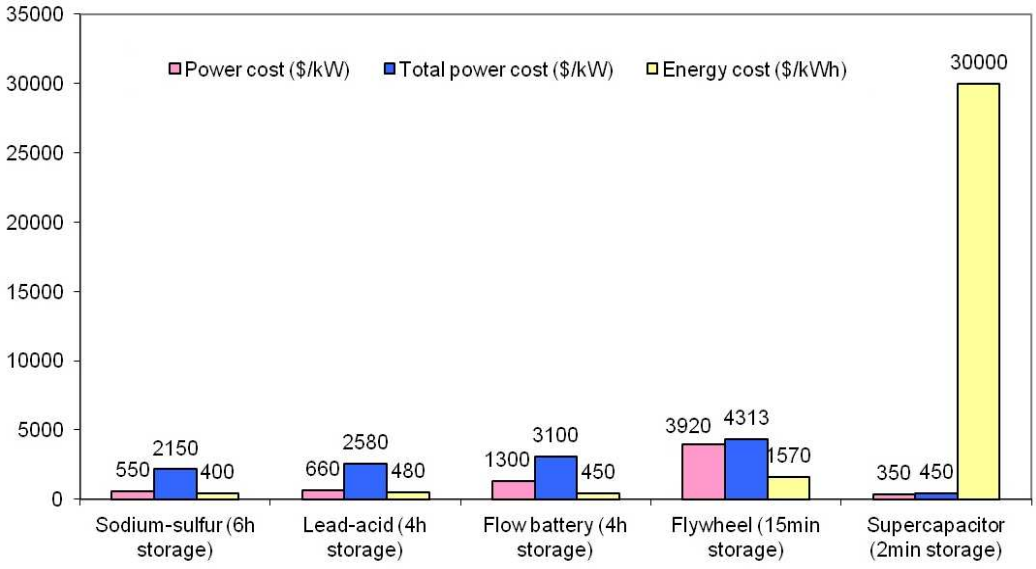

Fig. I.18. Costs for energy storage systems.

Figure I.18 (based on data from [68]) compares the costs for different energy storage technologies. The costs shown in this figure include necessary power conditioning equipments for the corresponding energy storage devices.

Based on different characteristics for each energy storage technology, and from above figures, it can be seen that for short-term energy storage (seconds to minutes), supercapacitor and flywheel technologies are ‘a priori’ the best candidates for marine current energy systems.

Flywheels are characterized by a higher cost than supercapacitors due to their higher energy capacity and higher power rating. Although both supercapacitor and flywheel technologies can be used for smoothing short-term high frequency fluctuations caused by swell effects, the former is more appropriate for single generation unit and the later seems more suitable for one generator farm.

With regard to long-term (several hours) energy storage, batteries are most suitable technologies for application under 50 MW. The flow battery is a very promising technology for its high cyclic capability and flexible power/energy sizing. NaS batteries can also be chosen but they need be kept heating during stand-by mode. Therefore, for smoothing long-term (3~6 hours) fluctuations in marine current application, high-energy batteries like flow batteries and NaS batteries are considered as good solutions. They can also be used to realize energy management strategies for marine current farm.

Other technologies like PHS and SMES (superconducting magnetic energy storage) are not very interesting in marine applications. PHS aims at GW scale for over 10 h or even days energy storage; this technology seems too large for marine current energy systems. SMES aims at MW scale for several milliseconds to 2 or 3 seconds power absorption/apply [69]. This technology does not fit the requirements of smoothing power fluctuations in marine current energy systems, and it is not economically and technologically favorable.

Although small CAES using aboveground reservoirs seems having an advantage of lower cost over batteries, such kind of systems have yet to be commercially available. Only large CAES plants (hundreds MW) are proven cost-effective in actual operations. And obviously, appropriate geographies with underground cavern for CAES are not easy to find around coastal area for potential marine current energy sites.

I.9 CONCLUSION

This chapter has introduced up-to-date large marine current turbine technologies and reviewed state of the art of energy storage technologies. The emphasis has been put on challenges of power fluctuations in marine current turbine systems. The characteristics and the strength/weakness of various energy storage system technologies have been presented for marine energy application. It has been shown that short-term energy storage devices such as supercapacitors and flywheels are favorable for compensating swell-induced power fluctuations; high-energy batteries such as flow batteries or NaS are most suitable for dealing with long-term period power variation problem related to the tidal phenomenon.

Chapter

II

Power Smoothing Control with Supercapacitors for Compensating Swell Effect on a Grid-Connected MCT System

NOMENCLATURE

A	=	Turbine blade swept area;
a_i, T_i, L_i	=	Magnitude, period and length of the swell component i;
d	=	Sea depth;
f_i, φ_i	=	Frequency and phase angle of the swell component i;
x, z	=	Horizontal and vertical point for the swell;
H_s, T_p	=	Significant height and peak period of swells;
C_{sc}, I_{sc}, V_{sc}	=	Capacitance, current and voltage of the SC;
C_p	=	Turbine power coefficient;
E_{rated}	=	Rated energy of the SC;
E_{sc}	=	Energy of the SC;
e_{abc}	=	Grid-side converter terminal voltages;
f_B	=	Friction coefficient;
g	=	Gravitational acceleration (9.8 m/s^2);
$I_{generator}$	=	Generator-side rectified current;
I_{grid}	=	Grid-side converter source current;
I_{target}	=	Grid target current;
$\overrightarrow{i_{abc}}$	=	AC-side three-phase current vector of the converter;
i_d, i_q	=	Generator d-axis and q-axis currents;
i_{dg}, i_{qg}	=	Grid d-axis and q-axis currents;
J	=	Total system inertia;
L_d, L_q	=	Generator d-axis and q-axis inductances;
L_g, R_g	=	Grid inductance and resistance;
$N_{parallel}$	=	Number of parallel branches in the SC bank;
N_{series}	=	Number of series SC cells in one branch;
n_p	=	Pole pair number of the generator;
R	=	Turbine blade radius;
R_s	=	Generator stator resistance;
R_{sc}	=	Equivalent resistance of the SC;
T	=	Filter time constant;
T_e, T_m	=	Generator and turbine torque;
T_{swell}	=	Swell wave period;

$V(t)$, V	=	Marine current speed, velocity;
V_{tide}, V_{swell}	=	Tidal current speed
V_{dc}	=	DC bus voltage;
V_{rated}	=	Rated voltage of the SC;
V_{max}, V_{min}	=	Maximum and minimum voltage setting for the SC;
$\overrightarrow{v_{abc}}$	=	AC-side three-phase voltage vector of the converter;
v_d, v_q	=	Generator *d*-axis and *q*-axis voltages;
v_{dg}, v_{qg}	=	Grid *d*-axis and *q*-axis voltages;
ΔP	=	Turbine and generator power difference;
θ, θ_g	=	Rotor position, grid voltage angle;
λ	=	Turbine tip speed ratio;
ρ	=	Sea water density;
ψ_m	=	Permanent magnet flux;
ω_e, ω_m	=	Rotor electrical and mechanical speed;
ω_g	=	Grid voltage angle speed.

GLOSSARY

ESS	=	Energy storage system;
MCT	=	Marine current turbine;
MPPT	=	Maximum power point tracking;
PMSG	=	Permanent magnet synchronous generator;
SC	=	Supercapacitor;
SHOM	=	French Navy Hydrographic and Oceanographic Service;
SoC	=	State of charge;
SVPWM	=	Space vector pulse width modulation;
TSR	=	Tip speed ratio;
VSC	=	Voltage source converter.

II.1 INTRODUCTION

This chapter focuses on the short-term power fluctuation problem in MCT system due to swell disturbances. Based on the conclusion in Chapter I, supercapacitors are chosen as the ESS for compensating the swell effect. A 1.5 MW grid-connected MCT generation system is considered. Firstly, swell effect modeling based on the Stokes model and the JONSWAP spectrum is presented. Specific location parameters and sea state are used to calculate the swell-induced power fluctuations for the given MCT. Secondly, a two-stage power smoothing control strategy is proposed. On the generator side, a modified MPPT with filter strategy is proposed to use the system inertia for reducing the generator power fluctuation in case of swells. On the grid side, supercapacitor ESS is applied to further eliminate the residual power fluctuations and realize a smoothed power injection to the grid. The models for the grid-connected MCT system and the control strategies are presented. The simulation results demonstrate that the association of the proposed MPPT strategy with the supercapacitor system achieves a smoothed power injected to the grid in case of swell disturbances.

II.2 SWELL EFFECT MODELING

Swells refer to long-length ocean waves (often over 150 m) generated from distant storms [70]. Long distance dispersion makes the swell spectrum narrower and the energy more accumulated than local wind-generated waves. These characteristics enable swells to prorogate very deep below the sea surface and therefore have a non-negligible effect on the MCT system. Figure II.1 illustrates the main parameters for describing swell characteristics including swell length L, swell height H and sea depth d.

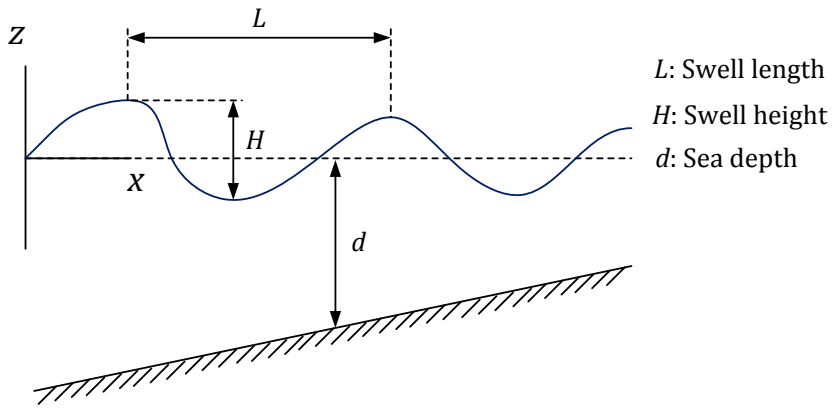

Fig. II.1. Main swell parameters.

Another important parameter is the swell period T_{swell}, which can be calculated from the sea wave dispersion relation,

$$L = \frac{g T_{swell}^2}{2\pi} \tanh\left(2\pi \frac{d}{L}\right) \tag{II.1}$$

Swell effects on the marine current speed can be estimated by Stokes models [71-72]. Stokes models calculate the swell-induced current speed by the horizontal component (in *x*-axis direction) and the vertical component (in *z*-axis direction). For a horizontal-axis MCT system, the horizontal swell-induced current speed component is considered and it can be calculated by the following equations. T_{swell} is abbreviated as T in the equations (II.2) and (II.3).

$$V_x(t) = \frac{\pi H}{T} \frac{\cosh\left(2\pi \frac{z+d}{L}\right)}{\sinh\left(2\pi \frac{d}{L}\right)} \cos 2\pi \left(\frac{t}{T} \quad \frac{x}{L}\right) \tag{II.2}$$

$$V_x(t) = \frac{\pi H}{T} \frac{\cosh\left(2\pi \frac{z+d}{L}\right)}{\sinh\left(2\pi \frac{d}{L}\right)} \cos 2\pi \left(\frac{t}{T} \quad \frac{x}{L}\right) \quad \frac{3(\pi H)^2}{4TL} \frac{\cosh\left(4\pi \frac{z+d}{L}\right)}{\sinh^4\left(2\pi \frac{d}{L}\right)} \cos 4\pi \left(\frac{t}{T} \quad \frac{x}{L}\right) \tag{II.3}$$

Equations (II.2) and (II.3) are first-order and second-order Stockes models respectively. The first-order model is suitable for relative deep sea depth and small swell height cases ($H / gT^2 \le 0.001$ and $H / d \le 0.03$), the second-order model is suitable for larger swell height and smaller sea depth ($H / gT^2 \le 0.009$ and $H / d \le 0.2$) cases. Generally, the second-order model has a wider application rang than the first-order model and satisfies the marine current application when considering a big swell effect.

However, it should be noticed that the first term of the second-order model is exactly the expression of the first-order model; and the second term can be seen as the second-order harmonics of the first-order model. The ratio of maximum values between the second term and the first term in (II.3) is illustrated in Fig. II.2 by $u_{2\max} / u_{1\max}$, and it shows that the second term becomes important only when d / L is very small.

When we consider that the typical sea depth for MCT installation is about 30-50 m and that the typical swell length is about 150-250 m, then the smallest d / L is 0.12 which corresponds to a ratio about 0.05 between the magnitudes of the second term and the first term in (II.3).

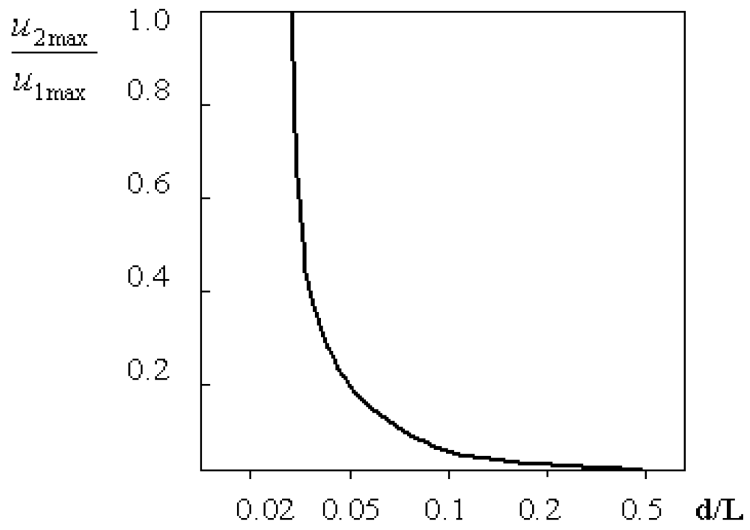

Fig. II.2. Ratio of magnitudes between the second term and the first term in the second-order Stokes model [72].

That means in this case the difference between the first-order Stokes model and the second-order Stokes model is negligible. Therefore, it is reasonable to use the first-order Stokes model for the calculation of the swell-induced speed turbulence for a MCT system installed at a sea depth over 30 m. This is the case which conforms to most potential MCT sites in French coastal areas.

More than one frequency component should be considered to model a realistic swell effect. Therefore, the total marine current speed can be calculated by

$$V(t) = V_{tide} + \sum_i \frac{2\pi a_i}{T_i} \frac{\cosh\left(2\pi \frac{z+d}{L_i}\right)}{\sinh\left(2\pi \frac{d}{L_i}\right)} \cos 2\pi \left(\frac{t}{T_i} - \frac{x}{L_i} + \varphi_i\right) \qquad \text{(II.4)}$$

It contains two parts: the first item V_{tide} represents the predictable tidal current speed, which can be regarded as a constant during a period less than half an hour; the second term represents the current speed oscillation caused by the swell. The superposition calculation in the second term of (II.4) presents that several swell frequency components should be considered. Each swell frequency component is calculated based on ocean wave theories and the swell spectrum; φ_i represents the initial phase angle of each frequency component and is given randomly.

Swells are transformed from wind waves through long-distant propagation after their

generating area. The process of dispersion (low frequency wave components propagate faster than high frequency wave components) takes place during the swell propagation. Thus, the swell observed at a fixed station has a spectrum restricted to a narrow frequency range. In this section, the JONSWAP spectrum is chosen as the swell spectrum due to its sharp peak characteristic. The JONSWAP spectrum can be written as follow.

$$S(f) = \beta_J \frac{H_s^2}{T_p^4} \frac{1}{f^5} \exp\left(-\frac{4}{5}\frac{1}{T_p^4}\frac{1}{f^5}\right)\gamma^Y \qquad \text{(II.5)}$$

where, $\beta_J = \dfrac{0.0624(1.094 - 0.0195\ln\gamma)}{0.23 + 0.0336\gamma - 0.185(1.9+\gamma)}$

$$Y = \exp\left[-\frac{(T_p f - 1)^2}{2\sigma^2}\right] \quad \text{with } \sigma \begin{cases} 0.07, & f \le 1/T_p \\ 0.09, & f \ge 1/T_p \end{cases}$$

From wave theories, the significant height H_s (or written as $H_{1/3}$) is defined as the average height of the highest one-third waves. The significant period T_s (or written as $T_{1/3}$) is defined as the average period of these highest one-third waves. These values can be calculated from wave records and have a relationship with average values about: $H_s = 1.6\overline{H}$ and $T_s \approx 1.2\overline{T}$. The peak period T_p is lightly larger than the significant period and can be estimated as $T_p \approx 1.1 T_s$.

The parameter γ is called peak enhancement factor which controls the sharpness of the spectral peak. γ = 3.3 is the mean value determined for the North Sea [73]. Larger value can be chosen to reflect the sharp peak characteristic of swell waves. The swell spectrum for engineering applications can be approximated with the peak enhancement factor being chosen between γ = 3~10, depending on the distance that the swell has traveled [70]. In this section, the peak enhancement factor is chosen as γ = 7, and the sea state of H_s = 3 m, T_p = 13.2 s is considered. This corresponds to typical sea state in the winter for the western coast of Europe. The amplitude of each frequency components can be calculated by $a_i = \sqrt{2S(f_i)\cdot\Delta f_i}$. Figure II.3 shows the calculated swell spectrum. The peak frequency in this spectrum is about 0.08 Hz which corresponds to the swell peak period T_p = 13.2 s.

It should be noticed from (II.4) that the swell effect on marine current speed also depends on the sea depth and the vertical distance between the calculation point and the sea surface. It means that the sea depth and the installation depth of the turbine must be considered to calculate the swell effect on a given MCT system.

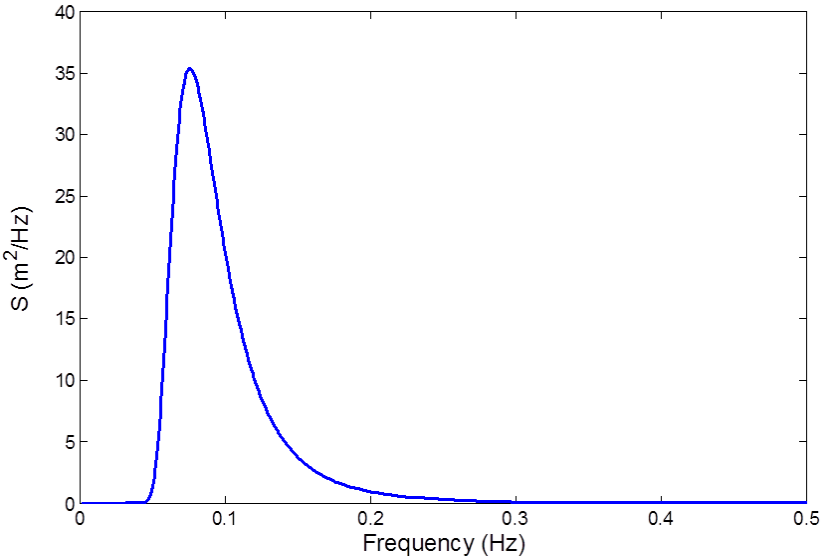

Fig. II.3. Swell spectrum based on JONSWAP spectrum.

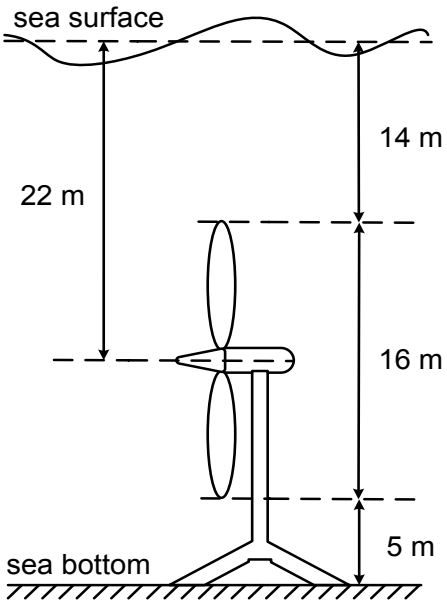

Fig. II.4. Basic dimensions and location parameters of the MCT.

Figure II.4 illustrates the main MCT installation parameters. The turbine location parameters are referenced from the industrial project OpenHydro which has been tested off the coast of Paimpol-Bréhat (France) in 2011. The turbine radius is 8 m and the system is supposed to be located at a sea depth of 35 m [12]. The equivalent marine current speed for this turbine can be calculated at a depth of 22 m below the sea surface.

Figure II.5 shows the simulation waveform of total marine current speed under the swell effect (the V_{tide} is assumed as 2m/s in the simulation). Figure II.6 shows the estimated produced power of the MCT operating at the current speed shown in Fig. II.5.

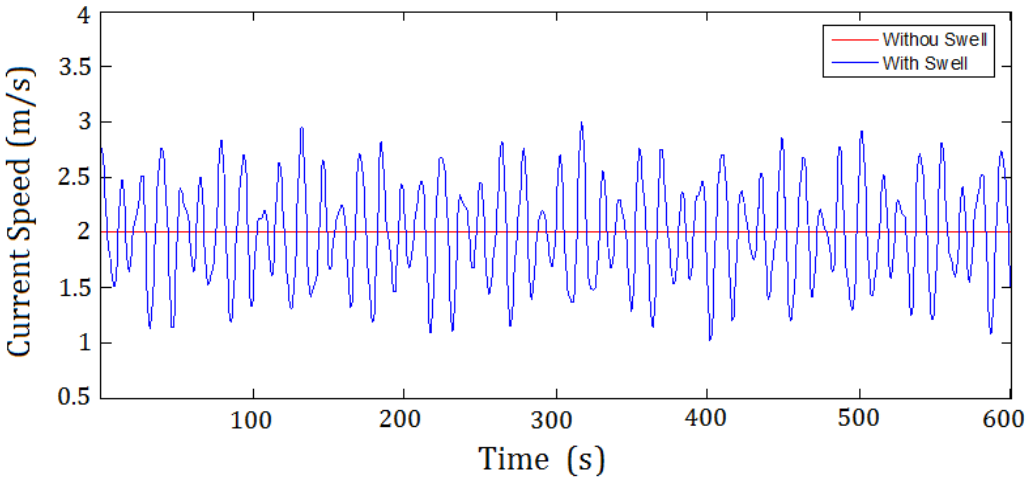

Fig. II.5. Marine current speed under swell effect.

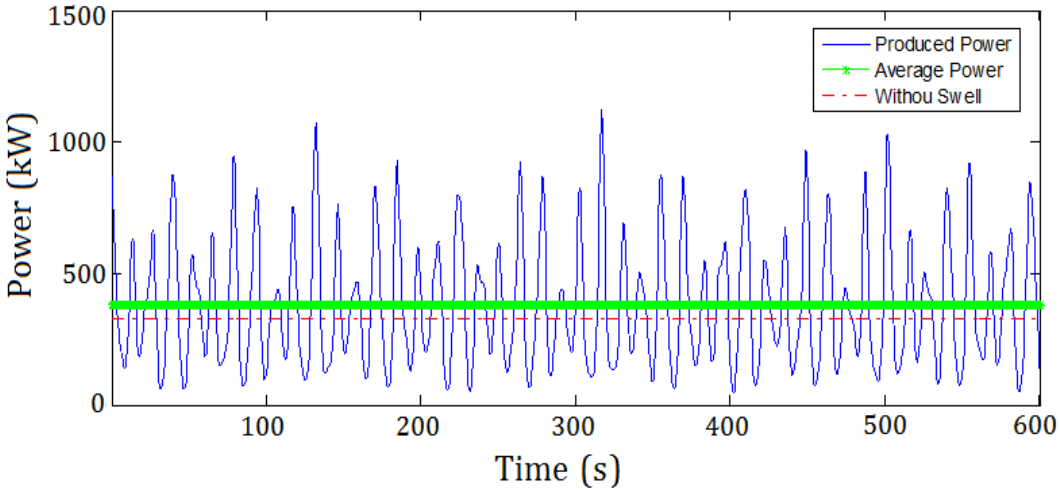

Fig. II.6. Estimated MCT power profile under the swell effect.

It can be seen that the swell effect can induce large oscillations in the marine current speed for the given depth. Figure II.5 shows that the swell can cause a 50% speed variation around the average tidal current speed and it is not surprising to see that in Fig. II.6, the MCT power could have power fluctuations over 100 % around the average power value.

Compared with normal wind-generated waves, swell-induced power fluctuations for a MCT system are much more severe. Data from experimental MCT in shallower installation cases show that the wind-generated waves can cause power fluctuations about 10 % around the average power with frequencies about 0.5 Hz [74]. Swell-induced power fluctuations have much higher magnitudes and with much lower frequencies than local wind-generated waves. Typical swells have frequency around 0.05-0.2 Hz.

One of the challenges of connecting the marine current generation system to the power grid is

to obtain a stable and smoothed power even under swell disturbances. The followed section will present the main models for a grid-connected MCT system.

II.3 MODELS FOR A GRID-CONNECTED MCT SYSTEM

In this work, one 1.5 MW grid-connected MCT generation system is studied. Figure II.7 shows the general system structure. Permanent magnet synchronous generator (PMSG) is chosen as the generator which is connected to the grid via a full sized back-to-back PWM converter. Supercapacitor (SC) is chosen as the ESS type for compensating the short-term period power fluctuations and for realizing a smoothed power to grid. The turbine power characteristic, the generator model and the three-phase power converter model will be presented in this section, while the SC and SC-side converter models will be presented in Section V.

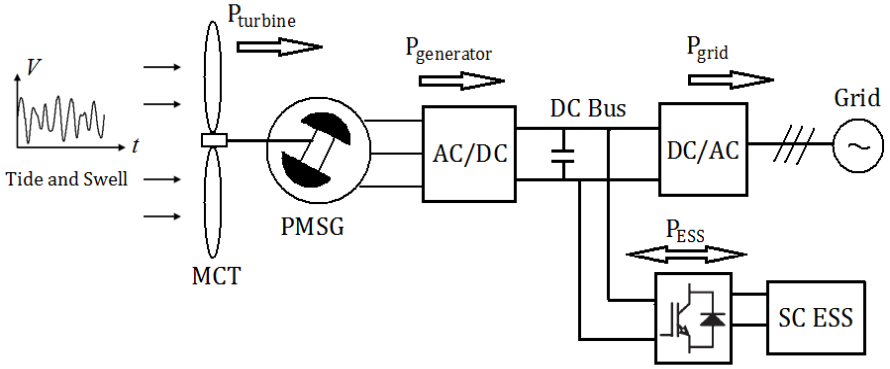

Fig. II.7. General schema for a direct-drive MCT system with ESS.

3.1 Marine Current Turbine Model

The power harnessed by a horizontal-axis MCT can be calculated by the following equation.

$$P = \frac{1}{2}\rho C_p \pi R^2 V^3 \qquad \text{(II.6)}$$

C_p is the turbine power coefficient which depends on the turbine blade structure and hydrodynamics. For typical turbine designs, the optimal C_p value for normal operation is estimated to be in the range of 0.35-0.5. For a given turbine, the C_p curve can be approximated as a function of the tip speed ratio (TSR) $\lambda=\omega_m R / V$ and the blade pitch angle β

based on experimental or numerical results [75]. The C_p curve used in this work is shown by Fig. II.8 (β = 0 for the fixed-blade case). This curve is based on the measurements of a three-blade MCT in [76] and [77]. In this case, the maximal value of C_p is reached for an optimal TSR of 6.3. In this work, a 1.5 MW-level direct-drive MCT with blade radius of 8 m is studied. The maximum rotor speed to follow MPPT is 24 rpm (2.52 rad/s) corresponding to a tidal current speed of 3.2 m/s. When the tidal current exceeds 3.2 m/s, the MCT harnessed power can be limited to 1.5 MW by appropriate power limitation strategies. Figure II.9 shows the MCT extractable powers under different marine current velocities, which are calculated based on the C_p curve and the equation (II.6).

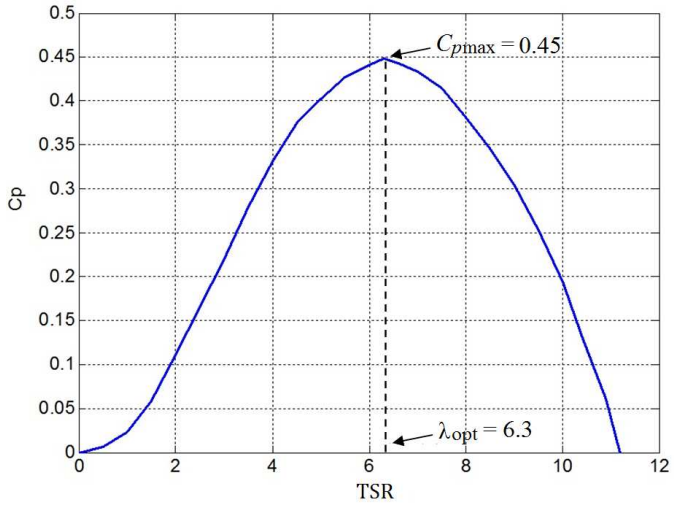

Fig. II.8. C_p curve of the MCT.

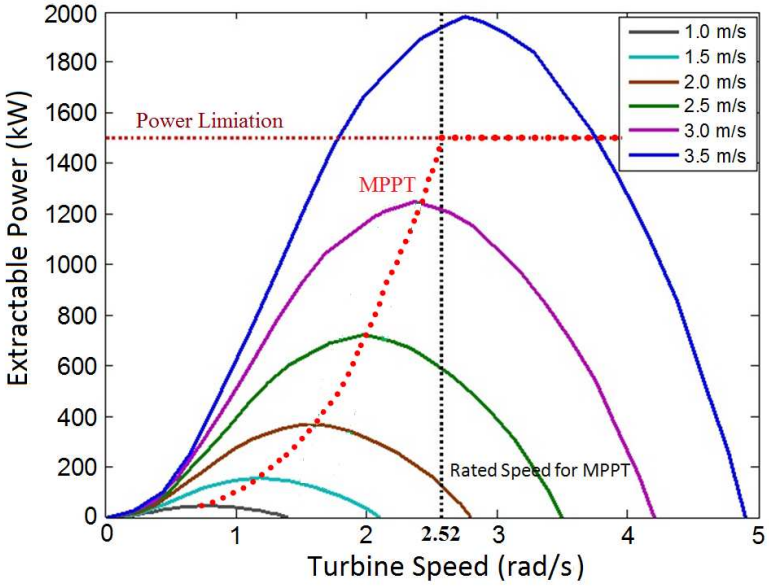

Fig. II.9. The MCT power characteristics (with power limitation operating points).

3.2 Marine Current Generator Model

The advantages of PMSG are compact structure (no excitation windings in the rotor) and the possibility of avoiding the gear box for connecting the turbine. That means a robust and low maintenance solution which is very favorable in terms of marine system application. Although doubly-fed inductive generator (DFIG) uses smaller power converters and has lower cost for large turbine application, the limited speed range would result lower energy yield than PMSG solution [78].

The PMSG dynamic model is given in a synchronous rotation *d-q* frame (shown in Fig. II.10). The Park transform used in the generator side part is given in (II.7). The *d*-axis is oriented to the rotor flux axis and θ is the electrical angle between the stator phase *a*-axis and the *d*-axis. The PMSG model in the *d-q* frame can be described by (II.8)

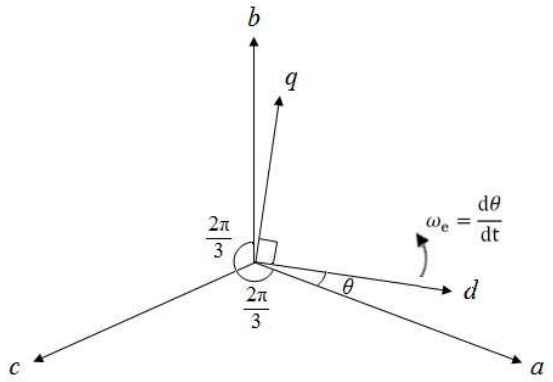

Fig. II.10. The generator-side synchronous rotation *d-q* frame.

$$\begin{bmatrix} v_d \\ v_q \end{bmatrix} = \frac{2}{3}\begin{bmatrix} \cos\theta & \cos\left(\theta-\frac{2\pi}{3}\right) & \cos\left(\theta+\frac{2\pi}{3}\right) \\ -\sin\theta & -\sin\left(\theta-\frac{2\pi}{3}\right) & -\sin\left(\theta+\frac{2\pi}{3}\right) \end{bmatrix}\begin{bmatrix} v_a \\ v_b \\ v_c \end{bmatrix} \tag{II.7}$$

$$\begin{cases} v_d = R_s i_d + L_d \dfrac{di_d}{dt} - \omega_e L_q i_q \\ v_q = R_s i_q + L_q \dfrac{di_q}{dt} + \omega_e L_d i_d + \omega_e \psi_m \\ T_e = \dfrac{3}{2} n_p \left[\psi_m i_q + (L_d - L_q) i_d i_q \right] \\ J \dfrac{d\omega_m}{dt} = T_m - T_e - f_B \omega_m \end{cases} \tag{II.8}$$

3.3 Power Converter Average-value Model

A back-to-back PWM converter should be used to interface the PMSG and the power grid. Although the generator-side converter and grid-side converter have different control aims, their circuit structures are identical. Each converter can be seen as a three-phase voltage source converter (VSC) with six fully-controllable power switches. In the simulations of this work, the three-phase VSC is simulated by an average-value model. The reason is that the average-value model can greatly reduce the computational intensity and facilitate the long-term simulation of a power system [79-80]. The space-vector PWM (SVPWM) is used to control the converter. Compared to conventional sinusoidal PWM, SVPWM has advantages such as higher utilization of DC-bus voltage and lower harmonic distortion [81-82]. The SVPWM has been widely used in electric drive systems. The maximum magnitude of the ac-side phase voltage is limited by $1/\sqrt{3}\,V_{dc}$ (= 0.577 V_{dc}) in linear SVPWM method. Supposing there is negligible loss in the converters, the converter dc-side power is equal to the ac-side power as follows,

$$V_{dc} i_{dc} = \begin{bmatrix} v_a & v_b & v_c \end{bmatrix} \begin{bmatrix} i_a \\ i_b \\ i_c \end{bmatrix} = \overrightarrow{v_{abc}} \cdot \overrightarrow{i_{abc}} \tag{II.9}$$

$$V_{dc}\left(\frac{1}{\sqrt{3}}\overrightarrow{F_m} \cdot \overrightarrow{i_{abc}}\right) = \left(\frac{V_{dc}}{\sqrt{3}}\overrightarrow{F_m}\right) \cdot \overrightarrow{i_{abc}} \tag{II.10}$$

In (II.10), $\overrightarrow{F_m}$ is the modulation function vector which can be obtained from the converter control strategy; the value is unified by the phase voltage limitation. Based on (II.9) and (II.10), the average model of the VSC is illustrated in Fig. II.11. It should be noted that in the equivalent circuit based on the average model, the power switches are substituted by the controlled current source on the dc-side and the controlled voltage sources on the ac-side. It means that the average-value model does not take into account the high frequency components of the PWM waveforms. This character is very favorable for realizing long-term simulation. For studying the performance of grid-connected MCT system under swell effect, system operation should be simulated for several minutes to include certain numbers of swell periods. In this case, detailed high frequency voltage/current harmonics (usually over kHz) generated by the power switches are not focused in this work.

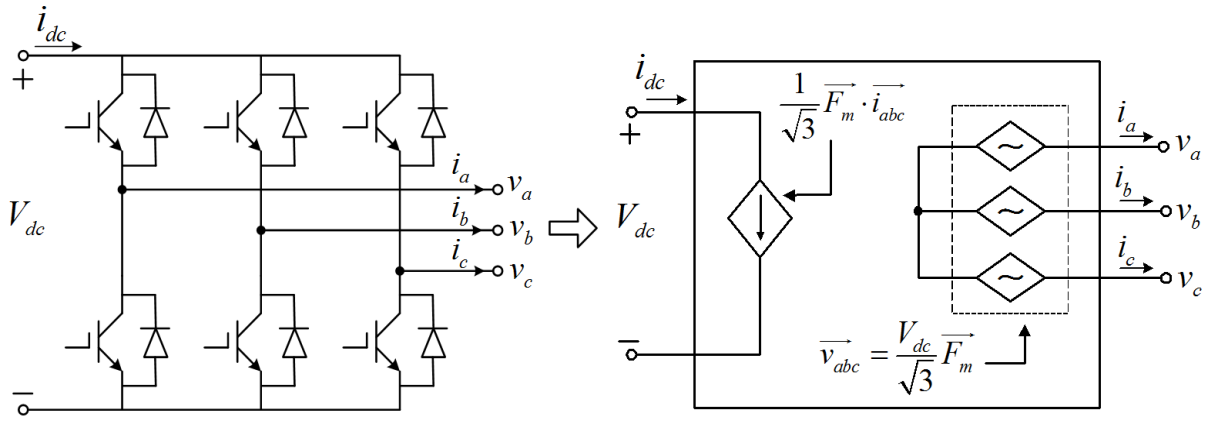

Fig. II.11. Schematic diagram and average model of a three-phase VSC.

II.4 GENERATOR–SIDE POWER SMOOTHING CONTROL

Based on the dynamic model of PMSG, the classical *d-q* decoupling vector control is applied. Stator currents are decomposed into torque component i_q and excitation component i_d. In a speed control scheme, the control of the generator aims to track the reference rotor speed to achieve the expected power extracted by the MCT.

Figure II.12 shows the control scheme for the generator-side converter. The *d*-axis current reference is set to zero under rated speed for maximizing the generator torque per ampere capability (minimization of generator Joule losses). The *q*-axis current reference can be calculated by the speed loop controller. In this work, one low pass reference filter is added to reduce the generator power fluctuation magnitude under swell effect. The tuning of the PI controllers and the speed reference filter will be discussed in the follows.

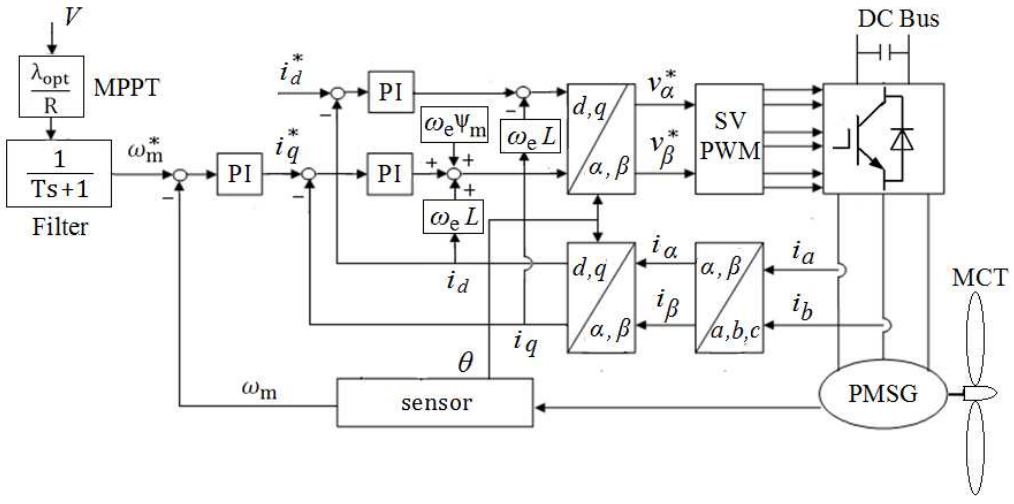

Fig. II.12. Control scheme of the generator-side converter.

4.1 PI Controllers Tuning

PI controllers are used in the speed loop and current loops. For the generator-side control scheme in Fig. II.12, the current and voltage references can be calculated by the following equations.

$$\begin{cases} i_d^* = 0 \\ i_q^* = K_{ps}\left(1+\dfrac{K_{is}}{s}\right)\left(\omega_m^* - \omega_m\right) \end{cases} \tag{II.11}$$

$$\begin{cases} v_d^* = K_{pc}\left(1+\dfrac{K_{ic}}{s}\right)\left(i_d^* - i_d\right) - \omega_e L_q i_q \\ v_q^* = K_{pc}\left(1+\dfrac{K_{ic}}{s}\right)\left(i_q^* - i_q\right) + \omega_e L_d i_d + \omega_e \psi_{\mathrm{m}} \end{cases} \tag{II.12}$$

The speed controller parameters (K_{ps}, K_{is}) and the current controller parameters (K_{pc}, K_{ic}) are tuned by the Non Symmetrical Optimum Method (NSOM) in this work. The Symmetrical Optimum Method (SOM) is very popular in the field of electrical drives; its main characteristic is to maximize the phase margin and to obtain symmetrical frequency diagrams. The NSOM is an extension of the SOM and allows setting the desired closed-loop resonant peak [83-84]. As one analytical method, the NSOM relies on a low-order approximated process model of the plant

$$G_Q = \frac{K_Q}{s\left(s/\omega_Q + 1\right)} \tag{II.13}$$

In this plant model, $T_Q = 1/\omega_Q$ is the time constant which includes all the time delays in the plant, and K_Q equals the slope rate of the open-loop step response. These two parameters can be deduced from a simple step response test in the real system. Using the NSOM, the parameters of PI controller can be calculated from the model parameters,

$$\begin{cases} K_p = \gamma_c \dfrac{\omega_Q}{K_Q\sqrt{\alpha_c}} \\ K_i = \dfrac{\omega_Q}{\alpha_c} \end{cases} \tag{II.14}$$

In (II.14), the correcting gain fact γ_c is defined in terms of the desired resonant peak value M_c and with α_c calculated by a phase advance $\Delta\varphi$ as follows

$$\begin{cases} \gamma_c = \sqrt{\dfrac{M_c^2}{M_c^2 - 1}} \\ \Delta\varphi = \arccos\left(\dfrac{1}{\gamma_c}\right) \\ \alpha_c = \left(\dfrac{1+\sin\Delta\varphi}{\cos\Delta\varphi}\right)^2 \end{cases} \tag{II.15}$$

The step response test is done in the simulation system. For current loops, *d*-axis current controller is less demanding than the *q*-axis current controller (considering $i_d^* = 0$ under rated rotor speed). Therefore, once we tune the *q*-axis current controller, the same parameters can be used for the *d*-axis current controller. The current open loop can be identified by injecting a pulse signal in the voltage reference. Figure II.13 shows the corresponding current response in *q*-axis. The parameters of approximate model can deduced from the time delay and the slope of the response.

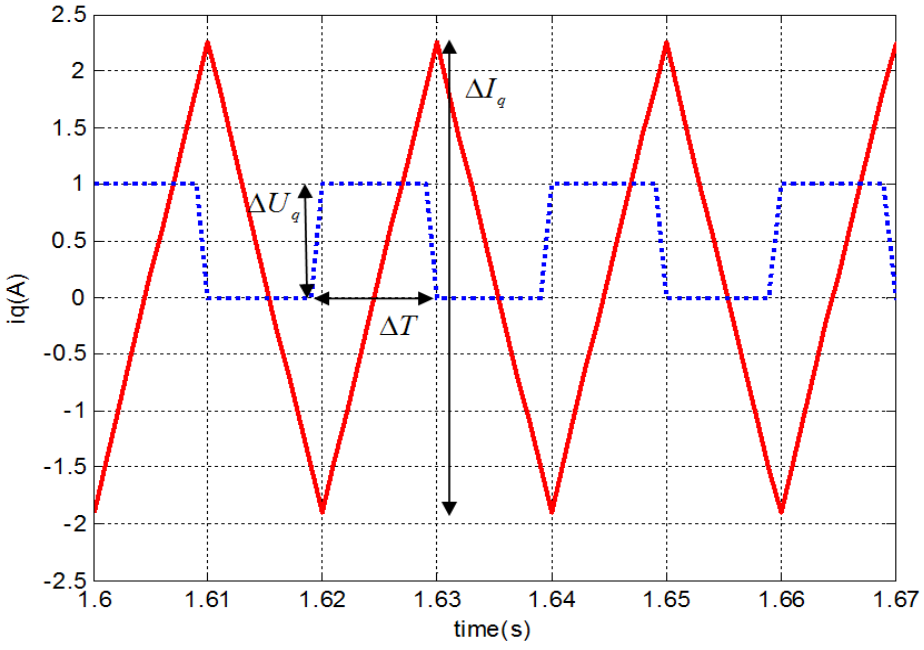

Fig. II.13. Open-loop generator current response in *q*-axis.

Since there is no current sensor module in the PMSG simulation model, the current delay is not visible in Fig.II.13. For a practical view, we suppose the delay is 0.2 ms, and we can get

$$\begin{cases} T_{Qc} = 0.2 \text{ ms} \\ K_{Qc} = \dfrac{\Delta I_q / \Delta T}{\Delta U_q / 2} = \dfrac{4 / 0.01}{0.5} = 800 \end{cases} \tag{II.16}$$

From (II.14) and (II.15), and choosing M_c = 1.2, we can obtain the parameters for current PI controllers as K_{pc} = 3.4 and K_{ic} = 455.

When the current PI controllers' parameters are fixed, we can tune the speed controller parameters. To identify the open-loop approximated model of the system speed response loop, we put a pulse signal as the q-axis reference current and observe the speed response signal.

Figure II.14 shows the speed response when the pulse amplitude of the reference q-axis reference current signal ΔI_q is 10^4 and the period ΔT is 0.25 s. It should be noticed that in this work, a 1.5 MW level MCT is studied and the total system inertia (10^6 kg·m^2 level) is considered in the PMSG model in the simulation system. Therefore, it is reasonable to see that the magnitude of the speed response signal is quite small compared with the reference current signal.

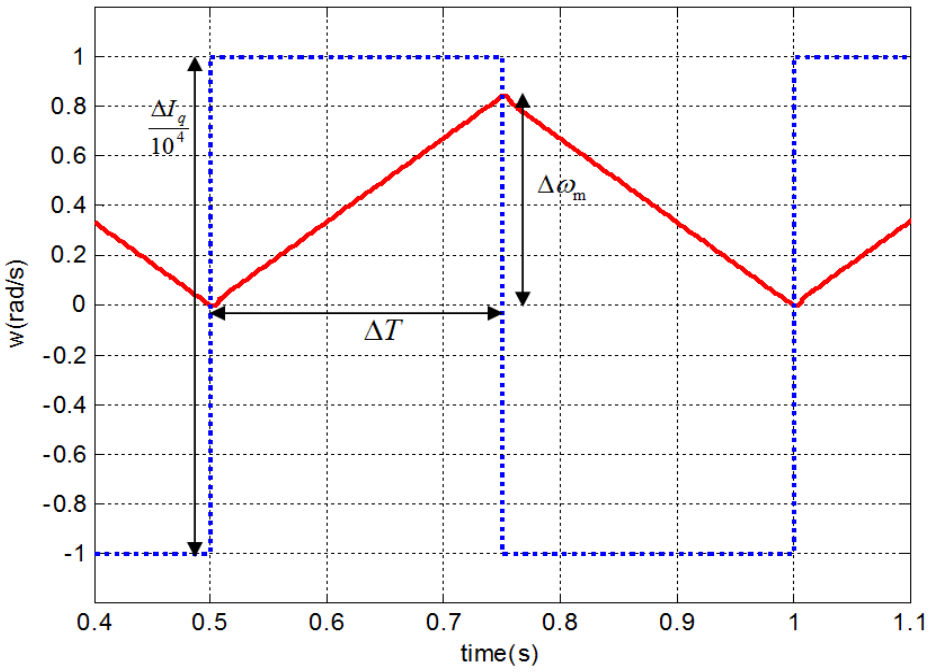

Fig. II.14. Open-loop generator speed response.

By zooming the response waveforms shown in Fig.II.14, it can be found that there is a delay of the speed response about 6 ms, which includes the delay of the current loop and the plant of the PMSG. The parameters of the approximated model for the speed loop can then be deduced as

$$\begin{cases} T_{Qs} = 6 \text{ ms} \\ K_{Qs} = \dfrac{\Delta\omega_m / \Delta T}{\Delta I_q / 2} = \dfrac{0.85 / 0.25}{5000} = 0.001 \end{cases} \tag{II.17}$$

From (II.14) and (II.15), and choosing M_c = 1.1, we can obtain the parameters for current PI controllers as K_{ps} = 8700 and K_{is} = 7.9.

4.2 Proposed MPPT for Reducing Power Fluctuation

In a speed control scheme, the generator aims to track the reference rotor speed to achieve the expected power extracted by the MCT. The rotor speed is controlled by the generator torque which is controlled by the *q*-axis current through the generator-side converter.

Basic MPPT consists in controlling the rotor speed to keep the turbine tip speed ratio λ at its optimal value, thus keeping the turbine power coefficient C_p at its maximum value. Supposing that the C_p curve is known and the marine current speed V can be obtained by flow velocity measurements, the turbine speed reference calculated by the conventional speed-based MPPT can be expressed as $\lambda_{opt} V / R$ [136].

In this paper, a low pass filter is added to modify the rotor speed reference calculated by the conventional MPPT algorithm in case of swell effect. The proposed strategy generates the speed reference as

$$\omega_m^* = \frac{1}{Ts+1} \cdot \frac{\lambda_{opt} V}{R} \tag{II.18}$$

where T is the filter time constant and it plays a significant role in reducing the generator power fluctuation in case of swell disturbances. Setting T to zero leads (II.18) to be the conventional MPPT strategy. The water velocity V is supposed to the velocity which is experienced by the whole turbine disk and its value is supposed to be known.

With the conventional MPPT, the generator power will fluctuate even more severely than the turbine power under swell effect. This can be explained as follow: when we neglect the

friction losses in the generator torque equation, we can get

$$T_m - T_e = J\frac{\mathrm{d}\omega_m}{\mathrm{dt}} \tag{II.19}$$

$$P_{turbine} - P_{generator} = \omega_m T_m - \omega_m T_e = \omega_m J\frac{\mathrm{d}\omega_m}{\mathrm{dt}} \tag{II.20}$$

Equation (II.20) can be rewritten as

$$P_{turbine} - \Delta P = P_{generator} \tag{II.21}$$

where the difference between the turbine and the generator power is $\Delta P = \omega_m J\frac{\mathrm{d}\omega_m}{\mathrm{dt}}$. This relation indicates that for the MCT, $P_{generator}$ will be lower than $P_{turbine}$ during acceleration; while during deceleration, $P_{generator}$ will be higher than $P_{turbine}$. It should be noted that for a large direct-driven MCT system, the rotor speed ω_m is very low but the total system inertia is quite high. In this case, the power difference ΔP mainly depends on the system inertia J and the rotor speed change rate $\mathrm{d}\omega_m / \mathrm{dt}$. Since the system inertia is a constant, $\mathrm{d}\omega_m / \mathrm{dt}$ becomes a decisive factor for controlling the value of ΔP.

Figure II.15 shows the simulated marine current speed under swell effect and the corresponding rotor speed reference calculated by the conventional MPPT method. The generator and turbine power responses are shown in Fig. II.16.

When the marine current speed changes rapidly under swell effect, the turbine rotor speed will have a synchronous changing rate under the conventional MPPT control; $\mathrm{d}\omega_m / \mathrm{dt}$ is then not negligible. During the acceleration, ΔP is positive and this means part of the turbine power is stored by the system inertia and the remaining mechanical power are transferring to the generator. This causes the generator output power to be smaller than the turbine power. In the extreme cases, the required power difference ΔP can be larger than $P_{turbine}$ and it could lead the generator to absorb power as in motor operation. During the deceleration, ΔP is negative which means that the system inertia will release some mechanical power and this part of power will combine with the turbine mechanical power to contribute to the generator power. This makes the generator power larger than the turbine power. Considering a system of very large inertia (system parameters are listed in [Appendix A]), ΔP can be very large as shown in Fig. II.16.

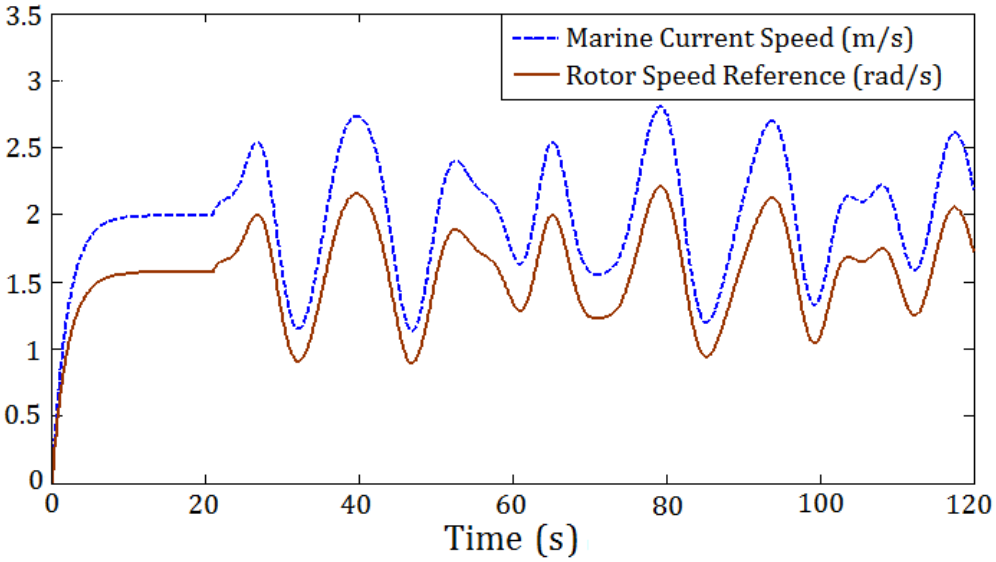

Fig. II.15. Rotor speed reference calculated by conventional MPPT.

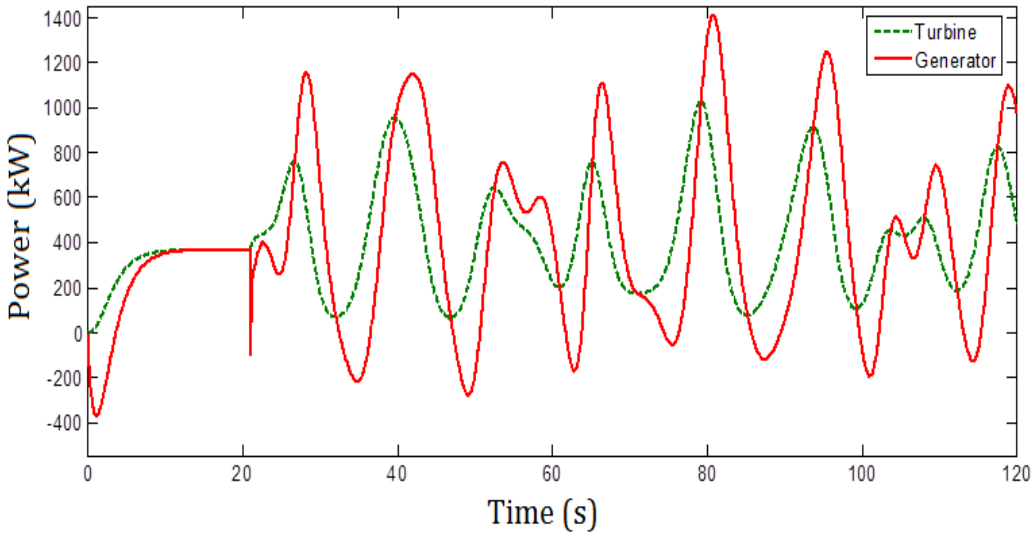

Fig. II.16. Turbine and generator powers with conventional MPPT.

In this simulation, the marine current speed starts at 0 m/s and rises to 2 m/s in the first 10 s; the swell effect is considered after 20 s. Although this is not very realistic for real marine current, it enables to study the starting stage, constant marine current stage, and the fluctuating marine current stage (under swell effect) in one simulation. In the starting stage, it is reasonable to accelerate the generator and turbine to for realizing the MPPT quickly. In Fig. II.16, at the beginning the generator output power is negative which means that the generator is operating as a motor temporarily for a fast acceleration. In the steady-state (10 to 20 s), $P_{generator}$ and $P_{turbine}$ are almost equal; while under swell effect, $P_{generator}$ fluctuates more severely than $P_{turbine}$. The reason is that the conventional speed-reference MPPT requires the turbine to be accelerated at low current speed and to be decelerated at high current speed

under swell disturbance. In other words, ΔP happens at worst moment and increases the generator output power fluctuations under swell effect.

In the proposed method, a low pass filter is added to calculate the speed reference. In this way, high $d\omega_m / dt$ can be avoided and ΔP can be reduced. And more importantly, the rotor acceleration and deceleration moments can be shifted from the conventional MPPT case to desynchronize with the turbine power change. This means that the system inertia can be utilized to reduce the generator output power fluctuation.

Figure II.17 shows the generator power profiles with different filter time constants. Figure II.18 compares the system performances based on the simulation results with different filter time constants. In Fig. II.18, "Generator Power Fluctuation" is calculated by the difference between the maximum and the minimum values of the generator power under swell effect, The "Turbine Energy" and "Generator Energy" are calculated by integrating the turbine and the generator power respectively as

$$\begin{cases} E_{turbine} = \int_0^t P_{turbine}(t) \cdot dt \\ E_{generator} = \cdot \int_0^t P_{generator}(t)\ dt \end{cases} \quad \text{(II.22)}$$

When the filter constant is $T = 0$, it means there is no filter and this is the conventional MPPT case. From Fig. II.17 and Fig. II.18, it can be seen that, by adding the filter strategy, the generator power fluctuation can be greatly reduced at a cost of slightly energy losses. The energy reduction is due to the deviation from the conventional MPPT points. When the filter time constant is chosen to be very large, the generator speed reference will have negligible changes and that will lead the system to operate as a fixed-speed turbine. This can greatly reduce ΔP, while not maximally reduce the generator power fluctuation.

In order to obtain the smallest fluctuations in the generator power, the optimal filter time constant is chosen as 7 s which equals about half of the typical swell period in the simulation. Using this optimized filter time ($T = 7$ s), the rotor speed and generator power are illustrated in Fig. II. 19 and Fig. II. 20. It can be seen that with the optimized filter, the acceleration and deceleration moments of the rotor are delayed from the conventional MPPT case in a way that the ΔP are shifted to maximally reduce the generator power fluctuations. The generator power fluctuation is reduced by 68 % with a reduction of only 7.5 % in generator-produced energy compared to the conventional MPPT case.

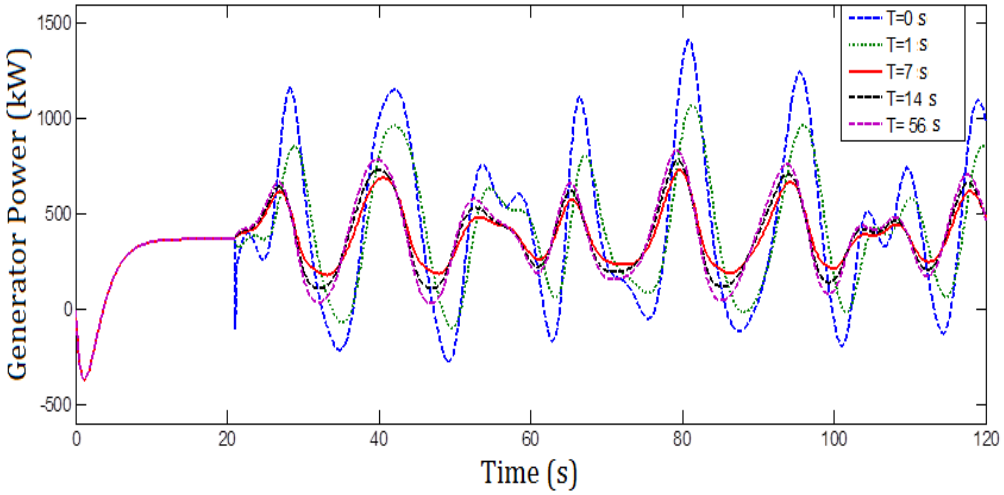

Fig. II.17. Generator powers with different filter time constants.

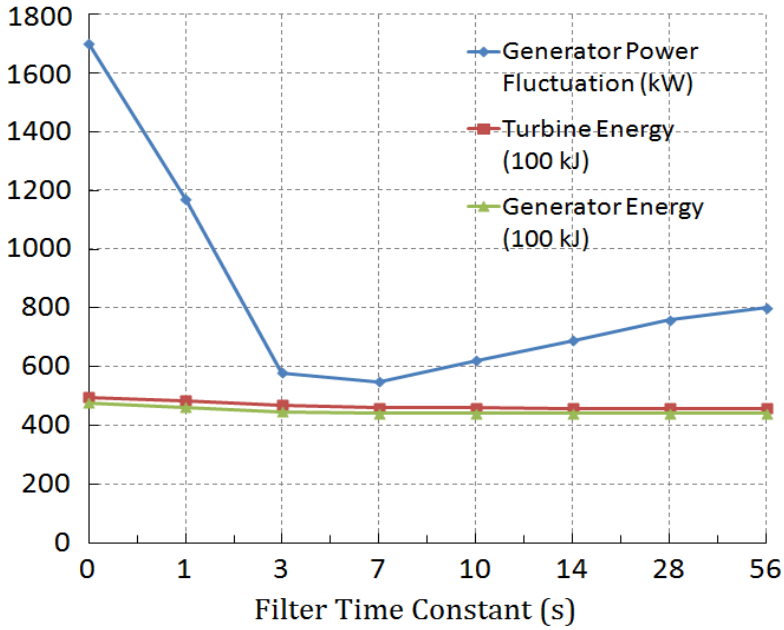

Fig. II.18. System performances with different filter time constants.

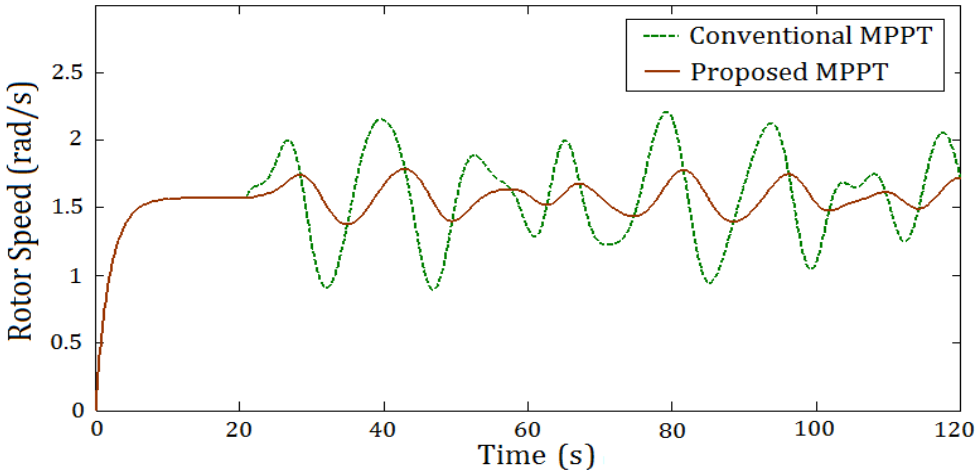

Fig. II.19. Rotor speed response.

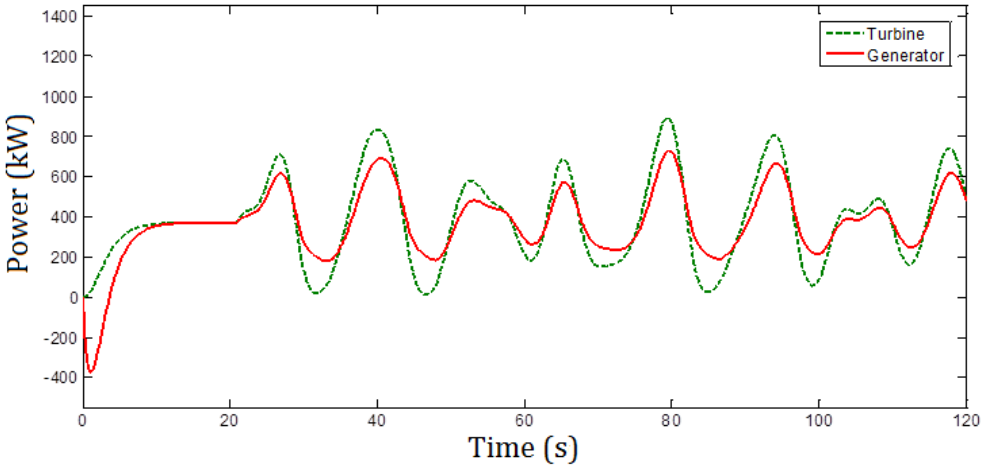

Fig. II.20. Turbine and generator power with proposed MPPT (T = 7 s).

4.3 Comparison of the Proposed MPPT with Torque-Based MPPT

The proposed MPPT is a modified tip-speed ratio MPPT. The marine current speed is supposed to be measured by flow-meters. The generator power fluctuation can be greatly reduced by filtering the current speed in the proposed MPPT. A torque reference MPPT control strategy [85-86] is assumed to have a similar effect in reducing the generator power fluctuations. The torque reference MPPT (also called optimal torque control) calculates the reference torque as

$$T_e^* = \frac{1}{2}\frac{C_{p\max}}{\lambda_{\text{opt}}^3}\rho\pi R^5\omega_m^2 \qquad \text{(II.23)}$$

This strategy does not need measuring the marine current speed. The reference torque is proportional to the square of the rotor speed and thus the generator output power will be proportional to the cubic of the rotor speed. Since the rotor speed variation is relatively low, the generator power fluctuation will be smaller than with the conventional tip-speed ratio MPPT. However, the response of the torque reference MPPT is relatively slow due to the fact that marine current speed changes are not directly reflected in the torque reference.

Figure II.21 compares the generator power using different MPPT strategies. It shows that both proposed MPPT and torque-based MPPT enable to greatly reduce the generator power fluctuation under swell disturbance. For the torque-based MPPT, there is no negative power at the starting stage and it shows the relatively long response time for the turbine to operate at the maximum power points. In some cases, a slower response can lead to reduced mechanical stress and overall cost reduction. At the swell effect stage, the torque MPPT has a similar

power fluctuation reduction performance with the proposed MPPT using the filter algorithm. Figure II.22 compares the generator energy production using different MPPT strategies. In this figure, we focus on the swell effect stage. The energy is therefore calculated by integrating the generator power after 20 s. From Fig. II.21 and Fig. II.22, it can be seen that although the conventional tip-speed ratio MPPT leads to a very high generator power fluctuation, it produces highest energy due to the fast achievement of the maximum power points. At the swell effect stage, the proposed MPPT with optimized filter results a slightly smaller power fluctuation than the torque-based MPPT and there is no significant difference in their energy productions.

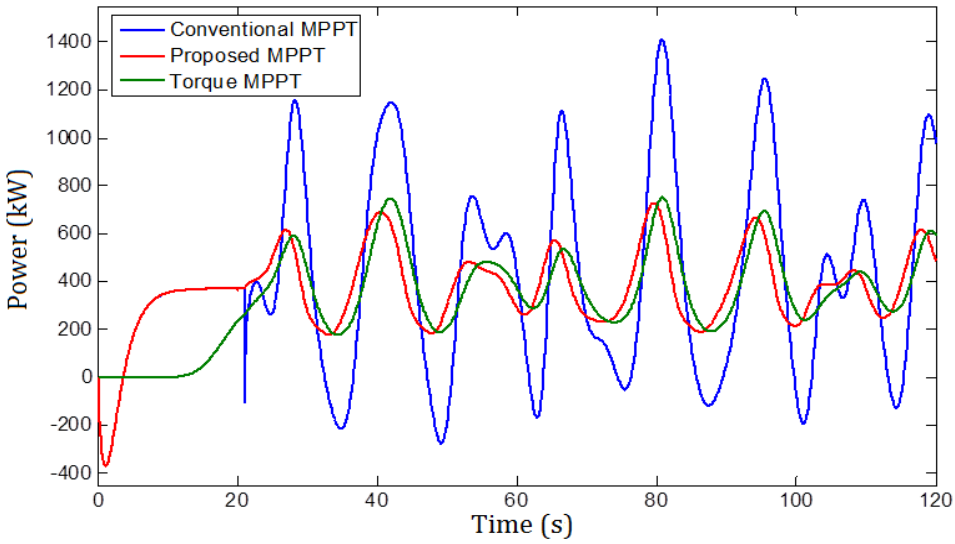

Fig. II.21. Comparison of generator-produced power.

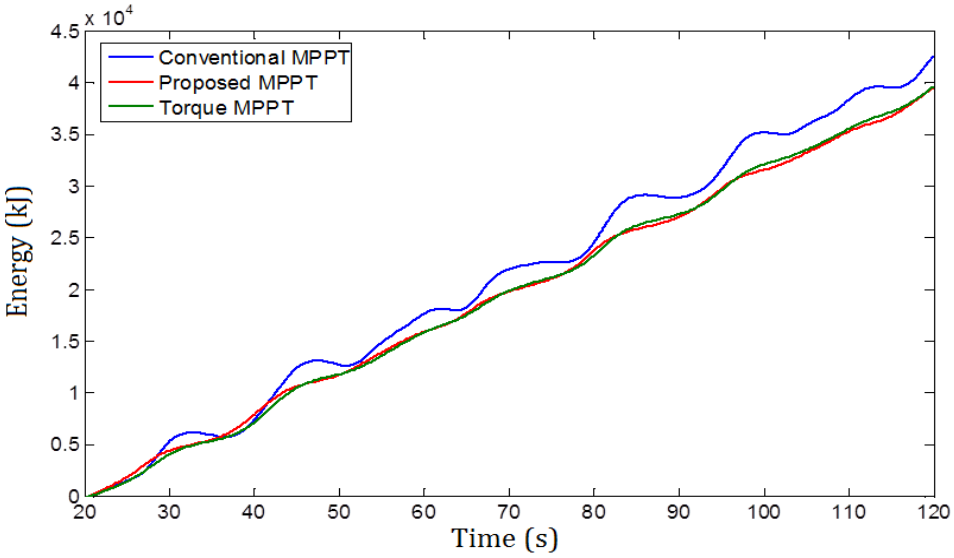

Fig. II.22. Comparison of generator-produced energy.

II.5 GRID-SIDE POWER SMOOTHING CONTROL

5.1 Grid-Side Converter Control

The main function of the grid-side converter is to keep the DC bus voltage stable and to regulate the active and reactive power injected to the grid [87-88]. Figure II.23 illustrates the circuit and the control scheme of the grid-connection part.

Based on the power flow direction, the grid-side converter mainly works as an inverter; but from the control view, the converter is supposed to keep the dc-link voltage at a constant value so that maximum available power from DC-bus can be transferred to the grid. Using vector control strategies, the grid-side converter enables to control the active and reactive powers injected to the grid [137-138]. The dynamic model for the grid-side part in *a-b-c* frame is given in (II.24). In this model, the grid current positive direction is defined as the grid output power direction.

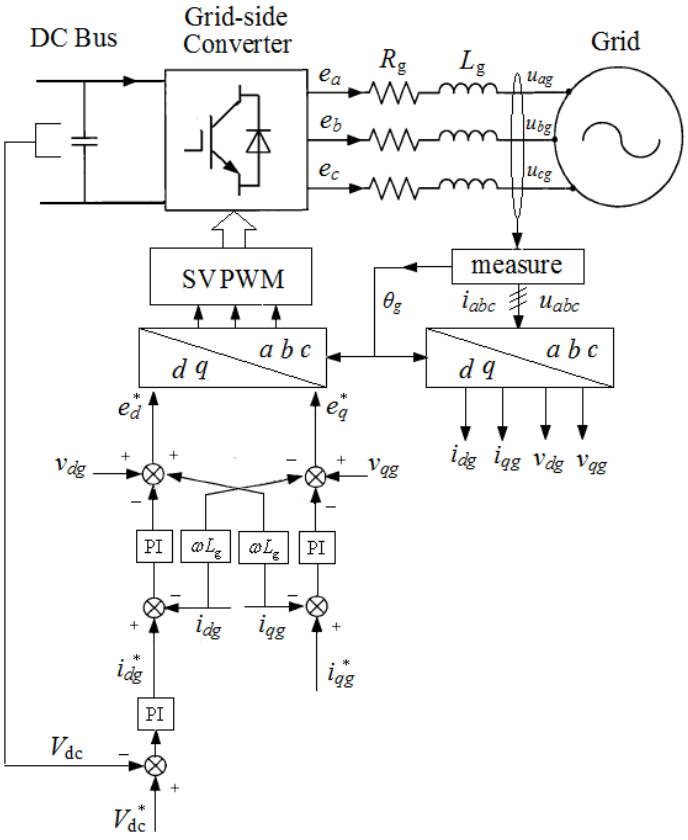

Fig. II.23. Control scheme of the grid-side converter.

$$\begin{bmatrix} e_a \\ e_b \\ e_c \end{bmatrix} = L_g \frac{\mathrm{d}}{\mathrm{dt}} \begin{bmatrix} i_{ag} \\ i_{bg} \\ i_{cg} \end{bmatrix} \begin{bmatrix} R_g & 0 & 0 \\ 0 & R_g & +0 \\ 0 & 0 & R_g \end{bmatrix} \begin{bmatrix} i_{ag} \\ i_{bg} \\ i_{cg} \end{bmatrix} \begin{bmatrix} u_{ag} \\ u_{bg} \\ u_{cg} \end{bmatrix} \quad \text{(II.24)}$$

By using the transformation matrix shown in (II.25), the *d-q* frame model of the grid side can be obtained as (II.26)

$$\begin{bmatrix} v_{dg} \\ v_{qg} \end{bmatrix} = \frac{2}{3} \begin{bmatrix} \sin\theta_g & \sin\left(\theta_g - \frac{2\pi}{3}\right) & \sin\left(\theta_g + \frac{2\pi}{3}\right) \\ \cos\theta_g & \cos\left(\theta_g - \frac{2\pi}{3}\right) & \cos\left(\theta_g + \frac{2\pi}{3}\right) \end{bmatrix} \begin{bmatrix} v_{ag} \\ v_{bg} \\ v_{cg} \end{bmatrix} \quad \text{(II.25)}$$

$$\begin{cases} e_d = -R_g i_{dg} - L_g \frac{\mathrm{d}i_{dg}}{\mathrm{dt}} + \omega_g L_g i_{qg} + v_{dg} \\ e_q = -R_g i_{qg} - L_g \frac{\mathrm{d}i_{qg}}{\mathrm{dt}} - \omega_g L_g i_{dg} + v_{qg} \end{cases} \quad \text{(II.26)}$$

For the grid part, the *d*-axis is oriented to the grid voltage synthesized vector, and the grid active power is controlled by the *d*-axis current. The *q*-axis current reference is set to zero when there is no grid reactive power requirement. The outside DC bus voltage loop aims to keep the DC bus voltage at a given value and to produce the current reference for *d*-axis.

5.2 Supercapacitor ESS for Grid Power Smoothing

5.2.1 ESS Sizing for Compensating Swell-induced Power Fluctuation

For compensating the power fluctuation caused by the swell disturbance, the ESS is supposed to absorb the difference between the MCT produced power and the power injected to the grid. In this work, the required ESS capacity is estimated based on the MCT power profile under swell during 600 s (see Fig. II.6 in § II.2); and in this power profile the average power can be regarded as the smoothed power to be injected to the grid. The energy level in the ESS (with initial value of zero) can be calculated by

$$E_{ESS}(t) = \int_0^t P_{ESS}(t)\,dt = \int_0^t \left[P_{turbine}(t) \quad P_{grid}(t) \right] dt \quad \text{(II.26)}$$

Figure II.24 shows the energy changing profile of ESS which allows eliminating the swell-induced MCT power fluctuation (shown in Fig. II. 6). The difference between the maximum and minimum value in this energy profile can serve as a primary energy rating estimation for the ESS. And the largest difference between the produced power and the grid power can be considered as the power rating of the ESS. It should be noted that in this primary estimation, the ESS losses and the SoC range limitation are not considered. A margin should be considered, therefore it is estimated that an ESS of 1.5 kWh is required in this case [25].

From the MCT power fluctuation profile (Fig. II.6), the statistical analyses of ESS charge/discharge power and period are illustrated in Fig. II. 26. Although the occurrences of the maximal charge/discharge power (800 kW) and the maximal duration (9 s) are quite low, their product gives an upper limit estimation of the required energy capacity: 2 kWh.

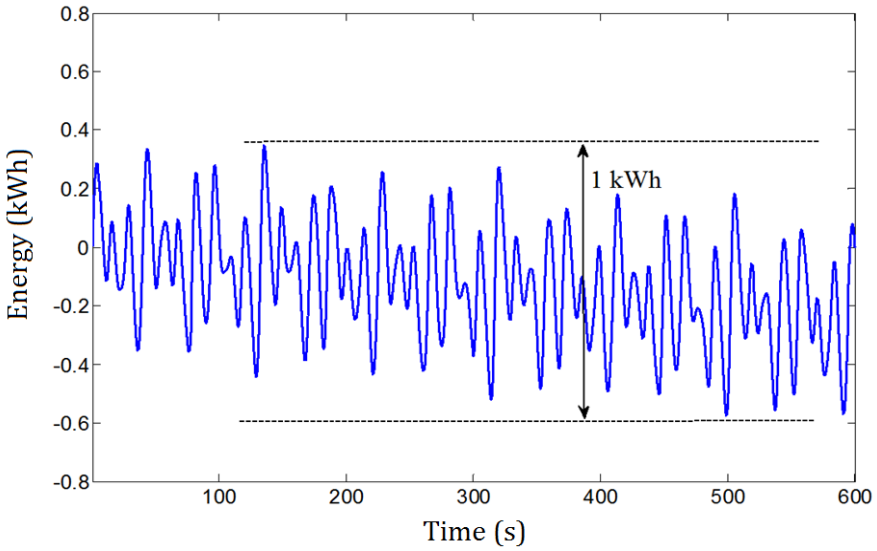

Fig. II.24. Energy changing profile of the required ESS.

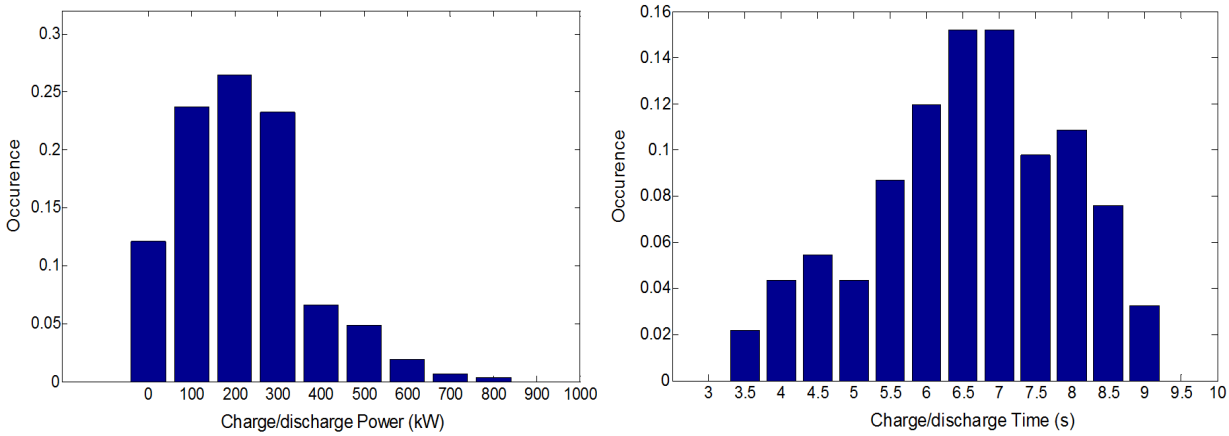

Fig. II.25. Statistical analysis of the ESS charge/discharge characteristics.

5.2.2 Supercapacitor Model and Control

Based on the ESS requirements for compensating the swell-induced power fluctuation, the SC is chosen as the ESS type for its high power capability and fast charge/discharge character. In this work, SC ESS is modeled by a capacitor in series with a resistor. Detailed models would include more RC branches to considering the temperature influence and long-term self-discharge behavior [89-90]. The first-order RC model remains as a fast and efficient way of integrating SC in dynamic power system simulation, although the main drawback is neglecting the nonlinear voltage overshot phenomenon at the end of charging and discharging [91-92].

The SC is connected to the DC bus with a bi-directional current DC/DC converter (so-called buck-boost chopper). Figure 18 shows the main structure of the SC part: the SC is modeled by a large capacitor C_{sc} in series with a small resistor R_{sc}; L_{sc} is the buffer inductor; D_1 and D_2 are the duty ratios for the two switches of the bi-directional DC/DC converter. If the converter losses are neglected, the power in the SC (positive power indicates the charge mode) should be controlled as follows

$$P_{sc}(t) = P_{generator}(t) - P_{grid}(t) \tag{II.27}$$

As average tidal current speed is predictable, the expected grid target power can be estimated based on the tidal current speed. The SC is then controlled to absorb the difference between the generator produced power and the expected smoothed power transferred to the grid.

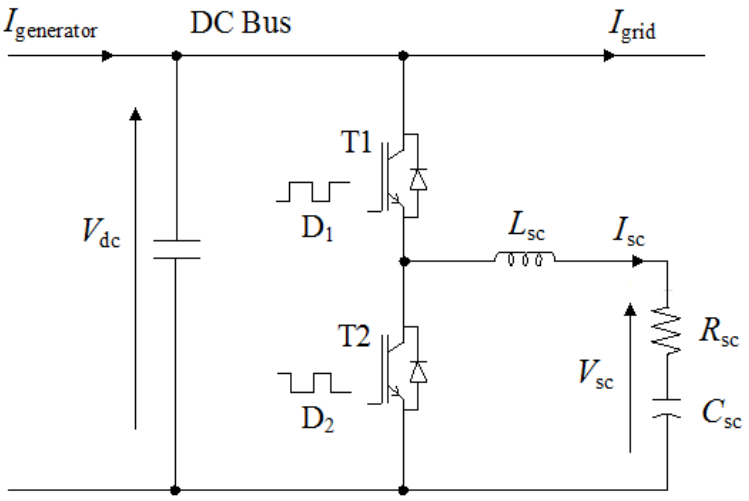

Fig. II.26. Supercapacitor and the bi-directional DC/DC converter.

Based on the buck-boost control in [44] and [93], the SC voltage can be controlled as

$$V_{sc} = \text{Đ}_1 V_{dc} = \left(\vDash\ D_2\right) V_{dc} \quad DV_{dc} \tag{II.28}$$

The State of Charge (SoC) of the SC is calculated by

$$SoC = \frac{E_{sc}}{E_{rated}} = \frac{0.5 C_{sc} V_{sc}^2}{0.5 C_{sc} V_{rated}^2} = \left(\frac{V_{sc}}{V_{rated}}\right)^2 \tag{II.29}$$

From (II.29), the relationship between the SoC and the voltage of a SC ESS can be obtained in Fig. II.27. It shows that the energy stored in the SC would drop rapidly with the decrease of the voltage. For instance, the SC will release 80% of the total energy when the voltage decreases to 44.7% of the rated value. In this work, the SoC range for the SC is limited from 0.2 to 1.

From (II.28) and (II.29), the control signal D (duty ratio) can be deduced as

$$D = \frac{V_{rated}}{V_{dc}} \sqrt{SoC} \tag{II.30}$$

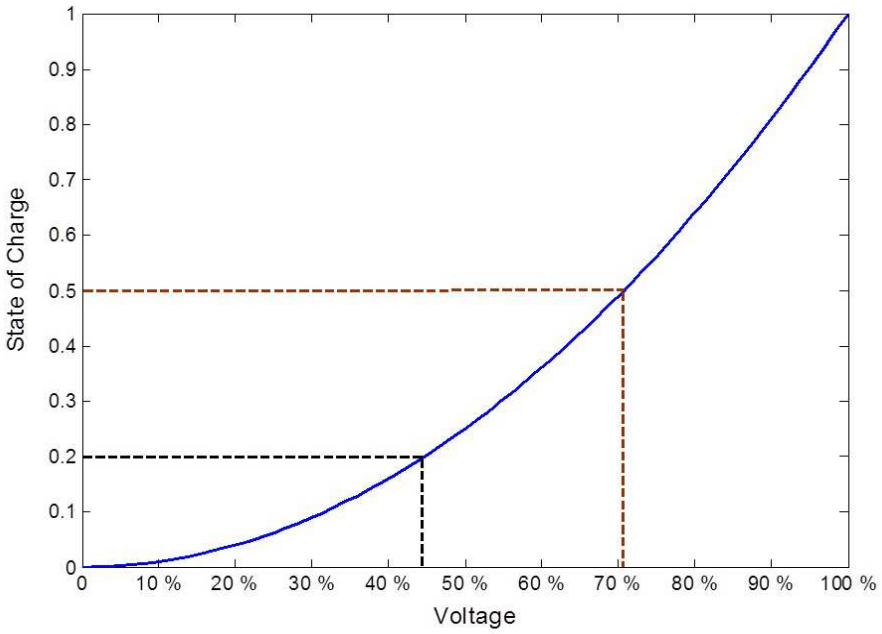

Fig. II.27. Relationship between SoC and voltage of SC ESS.

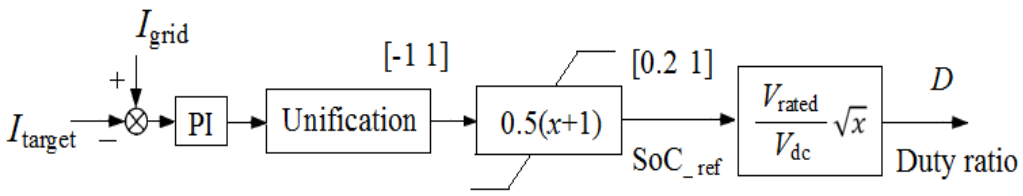

Fig. II.28. Control scheme of the bi-directional DC/DC converter.

Figure II.28 shows the duty ratio control scheme for the SC ESS. When $I_{grid} > I_{target}$, the duty ratio will rise to increase the SC voltage and make the SC absorb the power from the DC bus. When $I_{grid} < I_{target}$, the SC voltage will be decreased to make SC release the stored power. I_{target} is the current reference representing the smoothed DC current which is expected to be injected to the grid-side converter. This grid target reference can be calculated from the predicted tidal current speed when there is no swell. In case of swell disturbances, I_{target} can be obtained from filtering the generator-side rectified current ($I_{generator}$ in Fig. II.26). In Fig. II.28, the output value of the PI controller is proportional to the charge or discharge energy requirement. This value is firstly unified by $0.5V_{rated}^2$, and then the function $0.5(x+1)$ is used to transfer the range from [-1 1] to [0 1]. In this way, the charge/discharge energy requirement is transferred to SoC requirement. With a low SoC limitation of 0.2 in the SoC reference, the actual SoC variation range will be controlled in the range of [0.2 1].

5.2.3 Supercapacitor Bank Configuration

The required SC ESS is estimated to have an energy capacity of 1.5 ~ 2.0 kWh with a power rating of 800 kW. Actually, several SC cells should be used to make up a SC bank to meet such a requirement. Therefore in the SC model shown in Fig. II.26, C_{sc} and R_{sc} refer respectively to the equivalent capacitance and equivalent resistance of the SC bank (the SC for short). The parameters of C_{sc} and R_{sc} depend on the energy requirement and voltage setting of the SC, and also depend on the SC cell parameters. In the following, the details of the SC configuration are carried out. The usable energy capacity of the SC can be written as follows

$$E_{usable} = \frac{1}{2} C_{sc} (V_{\max}^2 - V_{\min}^2) \tag{II.31}$$

For the MCT system studied in this paper, the DC bus voltage is set to 1500 V, and the rated

voltage (maximum voltage) of the SC ESS is set to 750V. The SoC range is set from 0.2 to 1, and it means that the voltage rang of the SC ESS is from 335V ($V_{\min}$) to 750V ($V_{\max}$).
This required SC voltage rating is quite high, therefore we use the parameters of BMOD0063 P125 Maxwell module (63F, 128V, 18mΩ [94]) for single SC cell. Then the SC cell can be considered to have a maximum voltage of 125V. In order to obtain 750V, six cells are needed in one series branch. Therefore, $N_{series} = 6$ can be obtained. The usable energy capacity for one series branch is

$$\begin{aligned} E_{series} &= \frac{1}{2}\left(\frac{1}{6}C_{cell}\right)\left(V_{\max}^2 - V_{\min}^2\right) \\ &= \frac{1}{12}\cdot 63\cdot\left(750^2 - 335^2\right) \\ &= 0.656 \text{ kWh} \end{aligned} \tag{II.32}$$

To meet the energy capacity requirement of 1.5 kWh, three series SC branches described in (II.32) are needed. Therefore the $N_{parallel} = 3$ can be decided. Then, the parameters of the SC model in Fig. 18 can be calculated as (II.33). It results that the SC will have a usable energy capacity of 1.97 kWh. This value is higher than the original requirement of 1.5 kWh; this over-sizing enables the SC to compensate the swell-induced power fluctuations even under conventional tip-speed ratio MPPT case.

$$\begin{cases} R_{sc} = \dfrac{N_{series}}{N_{parallel}} R_{cell} & 36 \text{ m}\Omega \\ C_{sc} = \dfrac{N_{parallel}}{N_{series}} C_{cell} & 31.5 \text{ F} \end{cases} \tag{II.33}$$

5.2.4 Simulation Results

Figure II.29 and II.30 show the grid phase voltage and current simulation waveforms. The power grid is modeled by a three-phase balanced voltage source (690V, 50Hz). The grid phase voltage magnitude is assumed to be constant during the simulation ($\sqrt{2/3}\cdot 690 = 562\,\text{V}$); thereby the variations of grid current magnitude reflect directly the fluctuations of the grid-injected power (the reactive power is controlled to be zero in this simulation). Comparison of the two figures illustrates the SC's ability to eliminate the remanent power fluctuations and

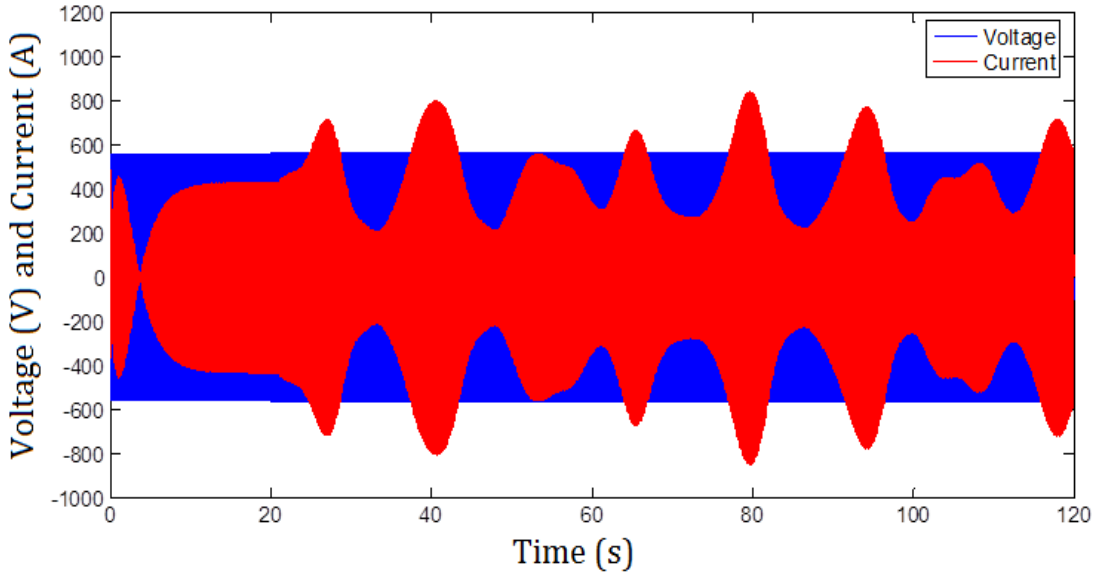

Fig. II.29. Grid phase voltage and current (without the SC).

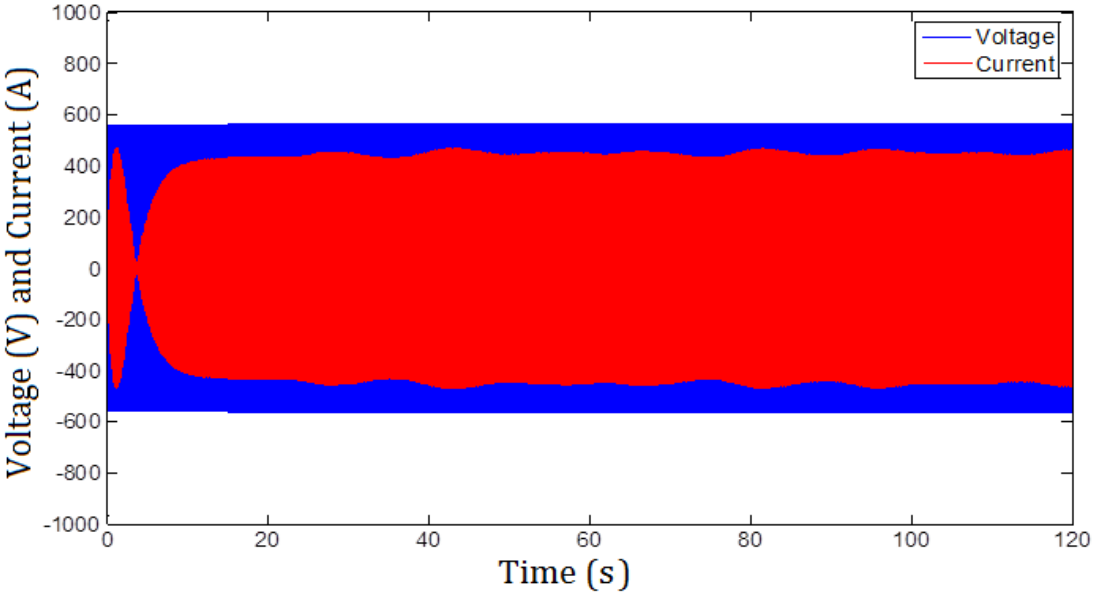

Fig. II.30. Smoothed grid phase current by the SC.

the power transferred into the grid is significantly smoothed. Figure II.31 shows voltage and current in the SC, and SoC variations in the SC are illustrated in Fig. II.32. The initial SoC is set to 0.5, and the SC is activated after 20 s (when the swell effect is introduced). From Fig. II.31, it can be seen that if the conventional MPPT is used, the SoC variation will be in the range from 0.37 to 0.8. This variation is reduced to a range from 0.48 to 0.65 when the proposed filter-based MPPT is applied. The reason is that the generator power fluctuations have been alleviated in the first stage by the proposed MPPT.

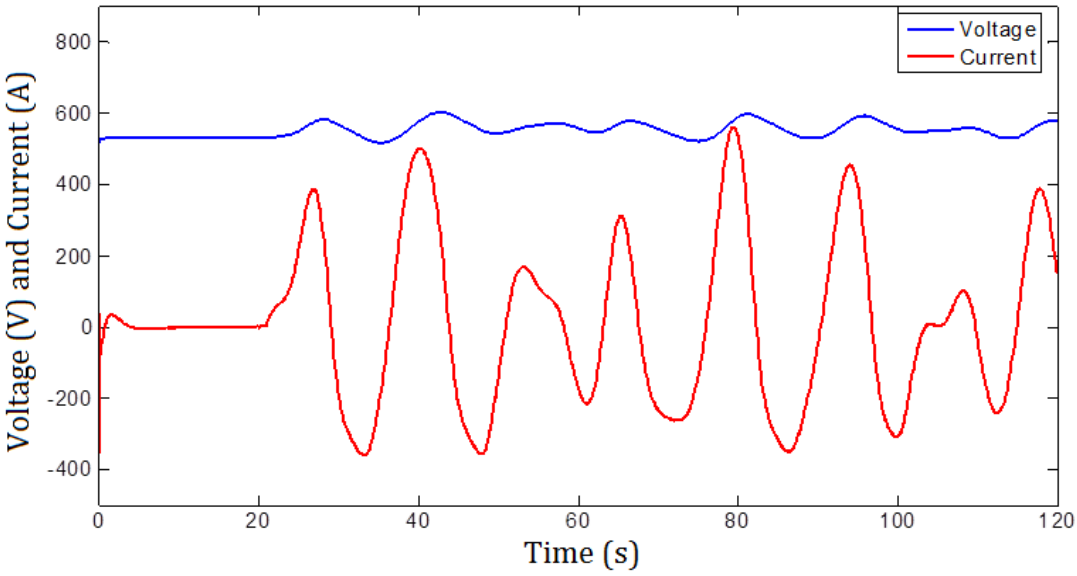

Fig. II.31. Voltage and current of the SC.

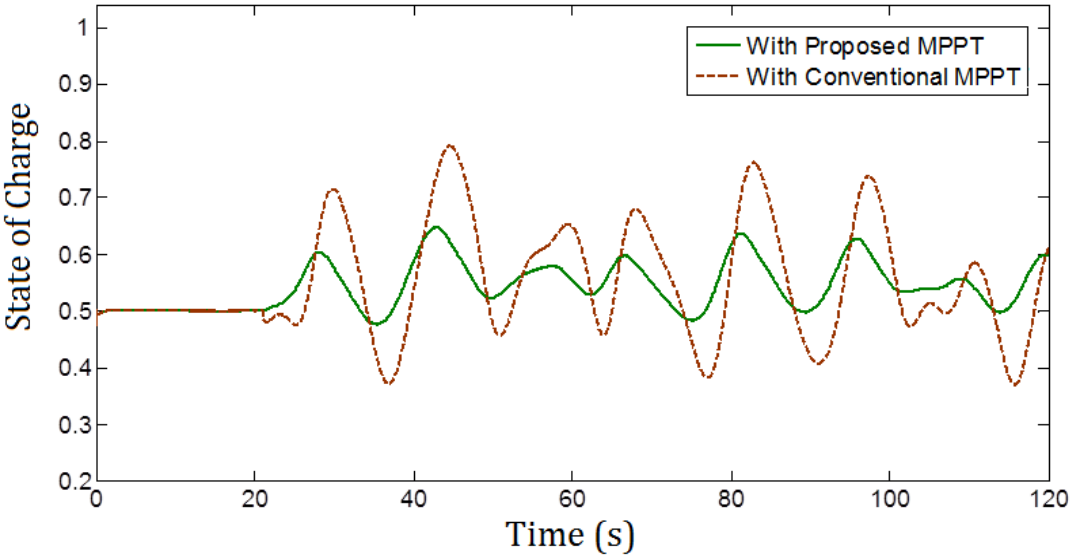

Fig. II.32. State of charge of the SC.

From the comparison shown in Fig. II.32, we can see that the proposed MPPT is able to greatly reduce the SC burden. It implies that, the proposed MPPT enables a reduction of 60% in the required energy capacity of the SC ESS compared to the conventional MPPT case.

$$\frac{\Delta E_{ess}}{E_{rate}} = \frac{\Delta SoC_1 - \Delta SoC_2}{\Delta SoC_1} \quad \frac{(0.8-0.37)-(0.65-0.48)}{0.8-0.37} \quad \frac{0.26}{0.43} \quad 60\,\% \qquad \text{(II.34)}$$

Figure II.33 illustrates the powers in different parts of the system. The active grid power is shown in this figure since the grid reactive power is controlled to zero by the grid-side converter. Figure II.34 shows the energy produced by the turbine, by the generator and the energy transmitted into the grid; it shows that about 96% of the turbine energy is transferred by the generator, and about 93% of the turbine energy is injected into the grid (at the end of the simulation). It implies that the energy captured by the turbine is efficiently transmitted to the grid without being deteriorated by the proposed power smoothing control strategy and the extra SC ESS.

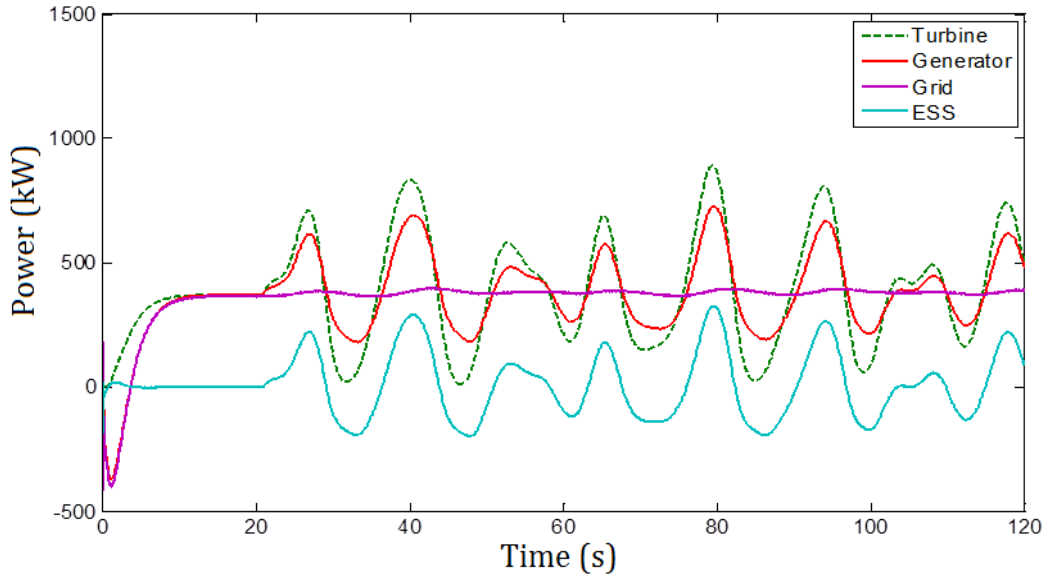

Fig. II.33. Powers in different parts of the system.

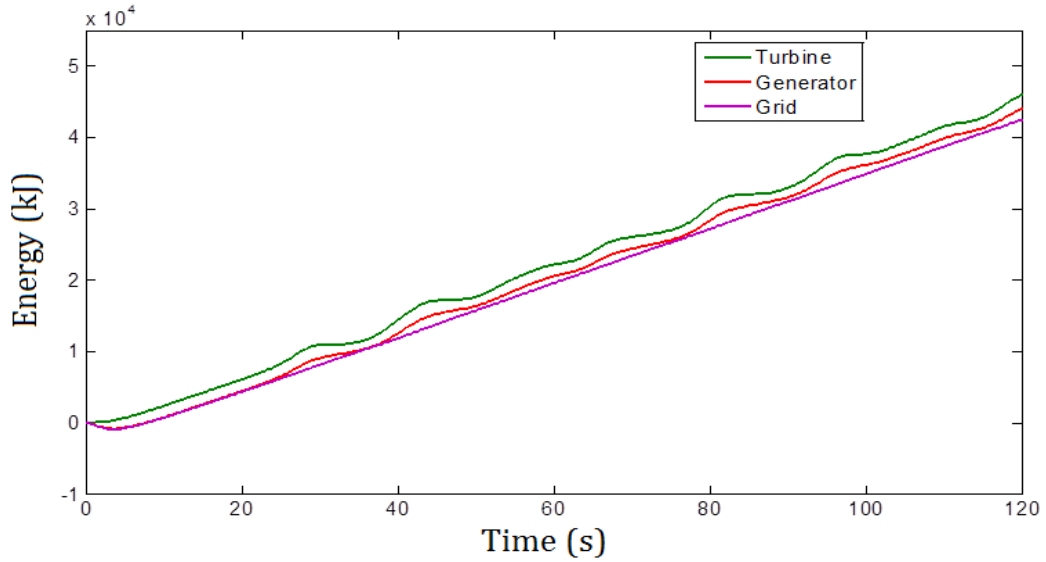

Fig. II.34. Energy comparison of the system.

II.6 COST AND LAYOUT ISSUES OF THE SC ESS

From the simulation results presented in the previous sections, it can be seen that the generator power fluctuation is controlled to be smaller than the turbine power fluctuation by applying the proposed MPPT. This makes that the 1.97 kWh SC ESS seems a little over-sized. However, this sizing is reasonable considering the dimension and the cost of a large MCT with a power rating around 1.5 MW-level MCTs are at pre-commercial stage and the market prices are still unavailable at this moment. Based on the ESS cost study in [25], the SC cost is about 20,000 $/kWh; therefore the cost for the SC ESS sized in this work is about 40,000 dollars. Current MCT prototype cost ranges from 11 to 15 million dollars per MW installed [7]. It means that the SC will only result a very fractional increase (less than 0.4 %) for the MCT system cost. Another point that should be noticed is that, in the simulation, the tidal speed (without swell) is set to be 2 m/s and a moderate sea state of H_s = 3 m, T_p = 13.2 s is used for calculating the swell effect. For higher tidal speed or with a stronger sea state (H_s may reach 5 to 6 m in some cases), the power fluctuation caused by swell effect would have a larger magnitude than that shown in the simulation. Therefore, enough margins should be considered in sizing the ESS. These points justify that the sizing of the SC ESS in this work is appropriate.

It should also be mentioned that there will be small energy losses by adding the ESS in the MCT system. A rough calculation is presented in the follows to estimate the energy profit of the MCT with and without the SC ESS. In France, the feed-in price of the marine energy is fixed at 0.173 €/kWh [95]. Considering the potential MCT sites near the French north-west coasts, the annually average marine current speed is around 1.63 m/s (at Raz de Sein), and hourly average produced power (by a 8m-radius MCT) can be estimated about 200 kW. The MCT is supposed to operate for 15 years, therefore the profit of the MCT without ESS can be calculated as

One Year Profit (k€) = 0.173 (€/kWh)×200 (kW)×8760 (h) = 303 k€

15 Years Profit (k€) =15×303 (k€) = 4545 k€

For the SC ESS used in this work, the power losses are mainly on the resistance (RI^2). The average charge/discharge current can be supposed to be about 200 A. Therefore, the power losses are 1.44 kW. The caused energy profit losses can then be calculated as follows

One Year Profit Loss (k€) = 0.173 (€/kWh)×1.44 (kW)×8760 (h) = 2.2 k€

15 Years Profit Loss (k€) =15×2.2 (k€) = 33 k€

Cost of the SC ESS (k€) = 40 k€

Total Profit Loss in 15 Years (k€) = 33 (k€) +40 (k€) = 73 k€

The above calculations show that with the SC ESS, the total profit loss in the 15 years will be only 1.6 % (=73/4545) of the energy profit of the MCT. This verifies that the use of ESS in the MCT system will only result a negligible profit loss.

The SC ESS presented in this paper is supposed to be used for one single MCT. Another possible layout of the ESS is to use a centralized ESS system for a marine turbine farm. Relative studies in wind turbine farms [96-97] show that compared to the distributed ESS configuration, a centralized ESS will have relatively smaller total power ratings due to the farm smoothing effect but it requires larger power converter equipments. In the MCT case, the farm smoothing effect may be affected by the topology of the turbine farm, the swell direction and wavelength. It is really difficult to obtain a final conclusion about which configuration is definitely better than the other one. At this stage, both configurations seem feasible for MCTs. In the future works, the aging process of the SC bank can also be considered.

II.7 CONCLUSION

This chapter shows that the tip-speed ratio MPPT may cause severe power fluctuations in the generator power under swell effect on a short-time scale. A modified MPPT with filter strategy is proposed to reduce the generator power fluctuation as the first step of power smoothing control. The effectiveness of the proposed MPPT strategy is confirmed by comparing to the tip-speed ratio MPPT and the torque-based MPPT. The achieved results have shown the ability of the proposed MPPT to greatly reduce the generator power fluctuations with the optimized filter. The second step of power smoothing control is realized by integrating supercapacitors as the ESS to compensate the remaining generator power fluctuations. The configuration of the SC is calculated by energy requirement and voltage settings. The SoC of the SC is controlled through the charge and discharge requirements to achieve a smoothed grid target power. Simulation results have shown the effectiveness of the joint operation of the proposed MPPT and the SC. In the next chapter, daily power variation challenge for the MCT system will be investigated.

Chapter

III

Daily Power Management with Flow Battery ESS

NOMENCLATURE

C_p	=	Turbine power coefficient;
E_N	=	Rated energy of the battery;
$I_{battery}$	=	Battery current (positive means charge mode);
I_{pump}	=	Battery loss current caused by the pumps;
I_{stack}	=	Battery internal stack current;
n	=	Number of battery cell;
P_{BESS}	=	Battery power (positive means charge mode);
P_{DG}	=	Diesel generator output power;
P_{Grid}	=	Power injected to the grid/load side;
P_{MCT}	=	MCT output power;
P_N	=	Rated power of the battery;
P_{stackN}	=	Rated power of the battery internal stack;
R	=	Turbine blade radius;
T_N	=	Battery rated charge/discharge time at rated power;
V_{tide}	=	Tidal current velocity;
V_{dc}	=	DC bus voltage;
$V_{battery}$	=	Battery terminal voltage;
V_{stack}	=	Battery internal stack voltage;
ρ	=	Sea water density;
ξ	=	Losses in the battery model.

GLOSSARY

BESS	=	Battery energy storage system;
DG	=	Diesel generator;
ESS	=	Energy storage system;
MCT	=	Marine current turbine;
MPPT	=	Maximum power point tracking;
PMSG	=	Permanent magnet synchronous generator;
SoC	=	State of charge;
VRB	=	Vanadium redox flow battery.

III.1 INTRODUCTION

In the previous chapter, the swell-induced short-time power fluctuation problem for the MCT system has been dealt with; and in this chapter, the power variation related to the tidal phenomenon will be focused. A semidiurnal tide causes the seawater to rise and fall with a period about 12 hours, thus resulting large variation of the MCT output power on a daily basis. On the other hand, the electricity demand from the grid side (or load side) has its own pattern during each day. Large difference between the power produced from the renewable sources and the power demanded from the grid/load side could cause power balance problem. This chapter proposes using vanadium redox flow battery (VRB) energy storage system to manage the total available power and to follow grid/load demand on a daily basis. A hybrid MCT/battery/diesel system is carried out in the simulation. The MCT dominant power supply case and the case when diesel generators as the main supply source (isolated island case) are investigated respectively. The battery modeling and control with appropriate activating rules of the diesel generator are presented in this chapter.

III.2 MCT-BASED HYBRID SYSTEM

The astronomic nature of tides causes seawater motion regularly each day with a period of approximately 12 h and 24 min for a semidiurnal tide. The tidal movement causes large variation of tide current speed and MCT output power for each day. In this chapter, one hybrid MCT generation system with battery energy storage system (BESS) and diesel generator (DG) is studied to follow a given power demand profile on a daily basis. Figure III.1 shows the general hybrid system structure.

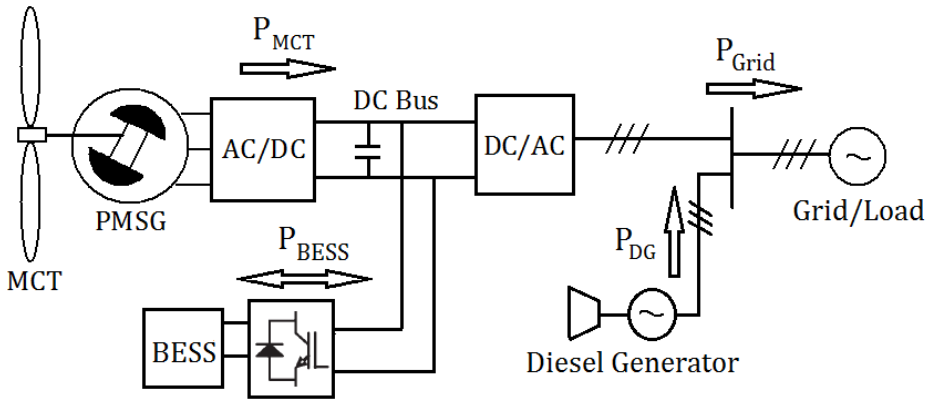

Fig. III.1. General schema for a hybrid MCT/BESS/DG system.

The BESS is connected to the DC bus of the back-to-back PWM converter which interfaces the permanent magnet synchronous generator (PMSG) and the grid/load. The diesel generator in Fig. III.1 serves as an important power supply source for enhancing the grid/load demand following ability. It should be noted that the BESS in this hybrid system aims to facilitate the power management of the MCT and to reduce the fuel consumption of the DG. Supposing that the MCT produced power has been smoothed by supercapacitors in the first place, the short-time scale power fluctuation is not very notable on a daily basis. Therefore, the MCT output power can be calculated by

$$P_{MCT} = \frac{1}{2}\rho C_{p\max}\pi R^2 V_{tide}^3 \qquad \text{(III.1)}$$

The same 1.5 WM MCT described in the previous chapter is considered. When the tidal current exceeds 3.2 m/s, the MCT harnessed power can be limited to its rated power by power limitation strategies [98]. The detailed power control strategies at over-rated marine current speed period will be presented in Chapter IV.

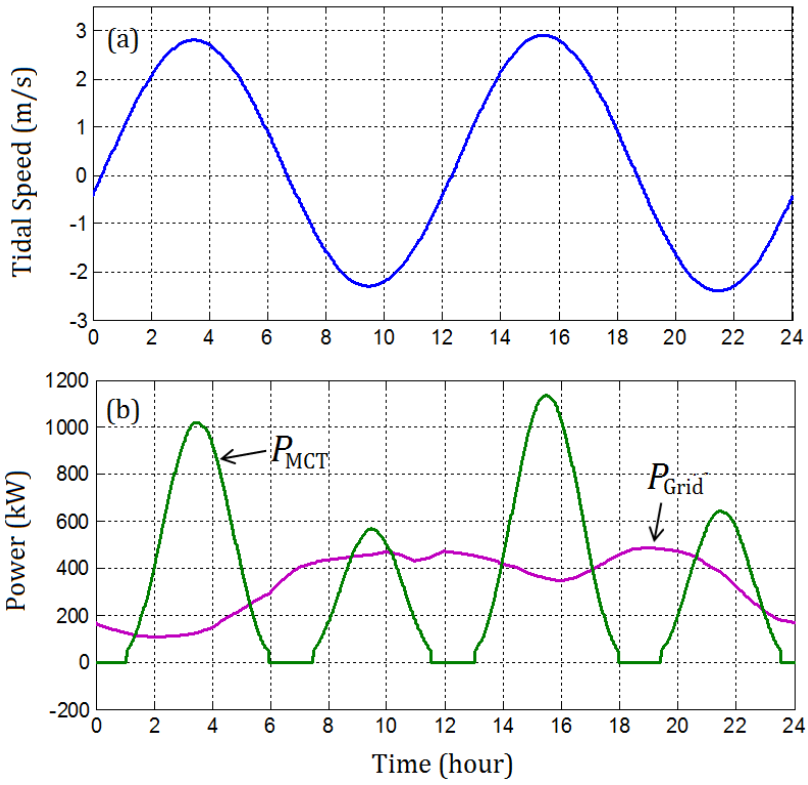

Fig. III.2. Daily profile example: (a) tidal current speed,
(b) MCT produced power and grid demand power.

Figure III.2 shows an example for tidal current speed, the corresponding MCT harnessed power, and the grid power demand profile on one day period. The cubic relationship between the tidal current velocity and the turbine power makes the MCT produce high power at both flood tide and ebb tide crests. In the middle of these tide crests, especially during the transition between flood and ebb tides, the tidal current velocity would be very low. The cut-in current velocity for MCTs should be over 0.7 m/s [99] and usually it can be considered that MCTs able to produce power efficiently for a current speed over 1 m/s due to the system inertia and mechanical losses [100]. The supposed grid/load demanded power profile (P_{Grid} in Fig. III.2b) is calculated based on typical daily load curves (per unit values can be found in [101]) and the average MCT power during one day. From Fig. III.2b, it can be seen that during the peak load periods (10h-12h and 18h-20h) the MCT produces low power or it is unable to produce power due to low tidal current velocity. In this case, large-capacity ESS can be used to store the excessive energy during MCT peak power periods and then to inject the stored energy to the grid/load side during peak load periods.

This example implies that if the MCT output power has a very high penetration level (accounts for a high percentage of the load) to maximally reduce the use and fuel consumption of the DG units, a large-capacity ESS is indispensable for storing and restoring the MCT produced energy to follow the load demand profile.

III.3 FLOW BATTERY MODELING

The VRB technology is chosen in this work. This battery technology is developed especially for high-energy capacity applications. As explained in Chapter I, this technology uses two external tanks to reserve liquid electrolytes containing vanadium salts and sulfuric acid. A pump system is needed to allow the electrolytes to circulate in the battery cell stack (consisting of the two electrodes and the ion exchange membrane) during charging and discharging. Distinguished advantages of flow batteries are flexible energy and power sizing, long service life, deep discharge ability and low maintenance. VRB has a lower generation cost compared to other battery technologies [102]. The experimental results in [37] show that VRB can be fully charged and left in discharged state for long periods without degradation.

3.1 Battery Equivalent Circuit model

Figure III.3 shows the flow battery equivalent circuit model used in this work. The equivalent circuit model is proposed in [103] and used in other papers [56] and [104]. However, some

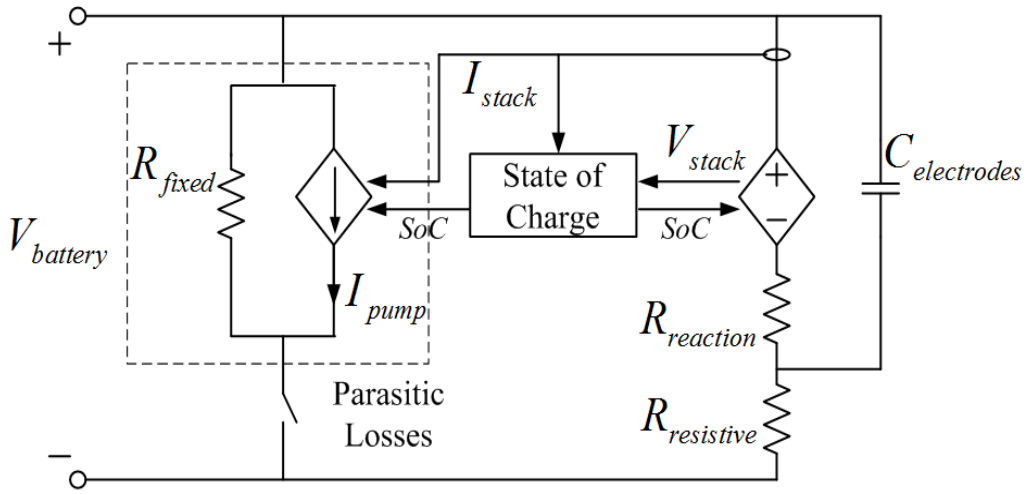

Fig. III.3. VRB equivalent circuit model [56].

parameter calculations are not detailed and the battery standby mode is not considered in these literatures. In Fig.III.3, the stack current (I_{stack}) and stack voltage (V_{stack}) represent the battery cell-stack internal current and electromotive force; and these two terms will be used to calculate the battery state of charge (SoC). The battery terminal voltage and current are expressed as $V_{battery}$ and $I_{battery}$. The internal resistances ($R_{reaction}$ and $R_{resistive}$) are modeled for reaction kinetics loss, mass transport resistance, membrane resistance, electrode resistance and bipolar plate resistance. The transient component associated with the electrode capacitance is modeled by $C_{eletrodes}$. The parasitic resistance R_{fixed} allows modeling the stack by-pass current. The power losses due to the circulation pump and the system controller are represented by the losses current I_{pump}. The switch on the parasitic branch of the equivalent circuit will be turned on when the battery is in operation (charge or discharge) and turned off when the battery is in standby mode.

3.2 Battery Parameter Calculation Process

The battery stack voltage represents the internal battery electromotive force. The value is directly related to the battery SoC as follows.

$$V_{stack} = n \cdot \left(1.4 + k \ln\left(\frac{SoC}{1 - SoC}\right)\right) \qquad \text{(III.2)}$$

In (III.2), n is number of cells in series in the battery stack; 1.4 V corresponds to the nominal battery electromotive force for one cell; k is a coefficient relating to the temperature and can take a value of 0.0514 V at 25℃.

The terminal battery voltage can be calculated from Fig. III.3 as

$$V_{battery} = V_{stack} - I_{stack}(R_{reaction} + R_{resistive}) \quad \text{(III.3)}$$

where, I_{stack} takes positive values for the charge mode and negative values for the discharge mode in this paper. The battery terminal current has the same direction as the I_{stack} and can be obtained considering the parasitic losses as

$$I_{battery} = I_{stack} + \left(\frac{V_{battery}}{R_{fixed}} + I_{pump} \right) \quad \text{(III.4)}$$

The internal resistances ($R_{reaction}$ and $R_{resistive}$) and the parasitic resistance R_{fixed} can be estimated by the power losses at the rated battery discharge current and their values are generally constant during battery operational range.

The flow battery is supposed to have a 79% efficiency at the operating point of rated discharge current I_{bmax} and 20% SoC. It can be estimated that the nominal power losses are ξ_N = 21%, with 15% accounts for internal losses (ξ_1 and ξ_2 for losses on $R_{reaction}$ and $R_{resistive}$ respectively) and 6% accounts for parasitic losses (ξ_3 and ξ_4 for losses on R_{fixed} and I_{pump} respectively) [103]. In order to enable the batter to provide the rated power P_N with a nominal losses level of ξ_N, the rated stack output power should be calculated by

$$P_{stackN} = \frac{P_N}{1 - \xi_N} \quad \text{(III.5)}$$

For the fixed parasitic loss, the R_{fixed} can be calculated by

$$R_{fixed} = \frac{V_{b\min}^2}{\xi_3 \cdot P_{stackN}} \quad \text{(III.6)}$$

where $V_{b\min}$ is the minimum battery voltage defined at the rated discharge current $I_{b\max}$ (considering as the rated battery current). The relationship with the battery rated power is $P_N = V_{b\min} \times I_{b\max}$.

For the parasitic pump loss, it is related to the stack current and SoC as shown in the following equation.

$$P_{pump} = V_{battery} \times I_{pump} = k' \left(\frac{|I_{stack}|}{SoC} \right) \tag{III.7}$$

The constant k' can be estimated at the operating point of $I_{b\max}$. If the pump loss is estimated as two times as the fixed parasitic resistance loss at $I_{b\max}$ and 20% SoC, then the k' can be calculated by

$$k' = \frac{0.2\xi_4 P_{stackN}}{I_{b\max} + 3I'} \tag{III.8}$$

where I' is the current through the fixed parasitic resistance at the operating point $I_{b\max,}$ and can be calculated by $I' = V_{b\min} / R_{fixed}$. Then the pump current I_{pump} can be calculated as follows.

$$I_{pump} = \frac{k'}{V_{b\min}} \left(\frac{|I_{stack}|}{SoC} \right) \quad \frac{0.2\xi_4 P_{stackN}}{P_N + 3\xi_3 P_{stackN}} \left(\frac{|I_{stack}|}{SoC} \right) \tag{III.9}$$

The internal resistances $R_{reaction}$ and $R_{resistive}$ can be calculated according to their losses by (III.10) and (III.11) respectively.

$$R_{reaction} = \xi_1 P_{stackN} / \left(I_{b\max} \quad 3I' \right)^2 \tag{III.10}$$

$$R_{resistive} = \xi_2 P_{stackN} / \left(I_{b\max} \quad 3I' \right)^2 \tag{III.11}$$

The SoC of the battery is calculated as follows.

$$SoC_t = SoC_{t-1} + \Delta_t SoC \tag{III.12}$$

$$\Delta_t SoC = \frac{\Delta_t E}{E_N} = \frac{V_{stack} I_{stack} \Delta t}{P_N T_N} \tag{III.13}$$

where Δt is the calculation step; E_N is the energy capacity of the battery and T_N is the time duration for which the battery can provide P_N.

3.3 Battery Size and Basic Charge-Discharge Characteristic

In this section, an example of battery sizing and a basic charge-discharge simulation are given. The required battery power/energy ratings depend strongly on the power profiles of the MCT and the grid/load demand. In the first step, the daily profile shown in Fig. III.2 is used to estimate the required battery capacity. The power rating of the battery can be estimated directly from the maximum difference of P_{MCT} and P_{Grid} (in Fig. III.2b) as

$$P_N = \max\left(P_{MCT}(t) - P_{Grid}(t)\right) \approx 1000\,\text{kW} \tag{III.14}$$

By integrating the power difference of P_{MCT} and P_{Grid} (in Fig.III.2), an energy level change profile can be obtained as shown in Fig. III.4. From this figure, the maximum energy change is $\Delta E_{\max}$ = 2040 kW. Considering battery efficiency about 80 % and an initial SoC of 0.4, the required battery energy capacity can then be calculated by equation (III.15).

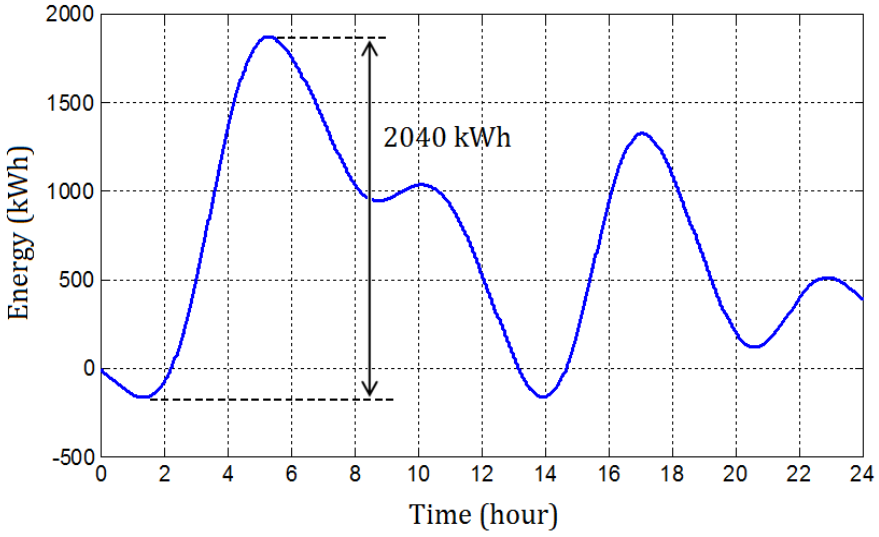

Fig. III. 4. The energy level change profile.

$$E_N = \frac{\Delta E_{\max} \times 80\%}{1-0.4} \approx 2720\,\text{kWh} \quad 3\,\text{MWh} \qquad \text{(III.15)}$$

In this case, the BESS is sized with a power rating of P_N = 1MW and energy capacity of E_N = 3MWh. The open-circuit battery voltage at 50% SoC is set as V_{b0} = 1500V. It needs n = 1072 cells in series to make up the battery stack. The VRB has an operational voltage range about 0.78~1.2 V_{b0}. Therefore, the minimum battery terminal voltage is limited at $V_{b\min}$ = 1170V and the rated discharge current is set as $I_{b\max}$ = 855A.

The power losses used to calculate the resistance and parameters in the battery model are set as : ξ_1 = 9%, ξ_2 = 6% , ξ_3 = 2% and ξ_4 = 4%. Each battery cell capacitance is about 6 F, then the equivalent electrode capacitance for 1072 cells in series is calculated by $C_{eletrodes}$ = 6F/1072. The parameters for the VRB circuit model can be found in [Appendix B].

Fig. III.5 and Fig. III.6 show the simulation results for the 3 MWh VRB on a charge-discharge cycle. The battery is charged 3 hours with a constant current of 600A and an initial

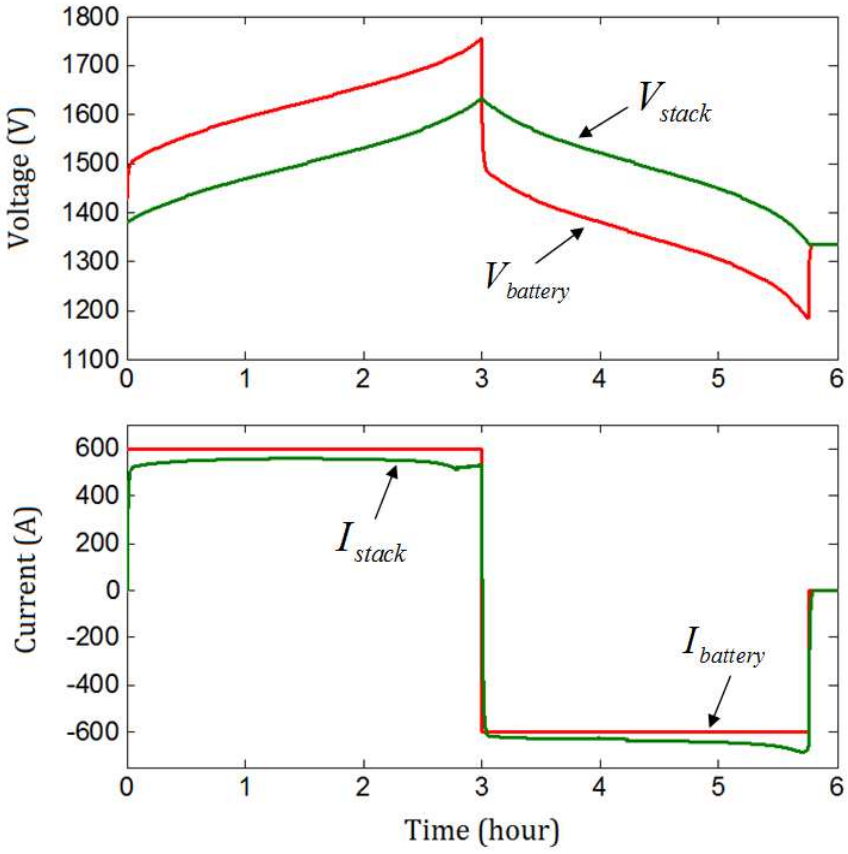

Fig. III.5. VRB voltage and current variations during a charge-discharge cycle.

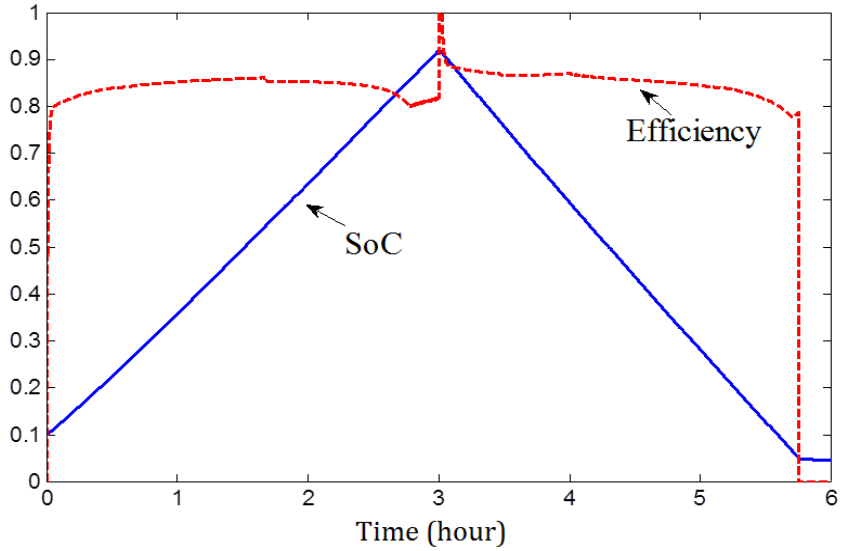

Fig. III.6. SoC and efficiency variation during a charge-discharge cycle.

SoC of 0.1, and then discharged 3 hours with the same absolute current value. From Fig. III.5, it can be seen that at the switching instant from charge mode to discharge mode, the $V_{battery}$ is discontinuous due to the sudden voltage polarity change on the internal resistances. The difference between $I_{battery}$ and I_{stack} is caused by the parasitic current losses.

In this constant current charge-discharge cycle, the discharge mode can not last up to the end of the 3 hours because of the battery losses. The battery should be turned off when the SoC is too low (at 5% SoC in Fig. III.6). Once the battery is turned off, the battery currents will return to zero and $V_{battery}$ will be equal to the battery internal electromotive force V_{stack} as shown in Fig. III.5. The battery efficiency is illustrated in Fig. III.6; this efficiency is calculated by $P_{stack} / P_{battery}$ in the charge mode and $P_{battery} / P_{stack}$ in the discharge mode. From Fig. III.6, it shows that the battery efficiency varies mainly between 80 % and 90 %. This is reasonable because the nominal power losses ξ_N = 21% (maximum power losses) are considered in the VRB model.

III.4 HYBRID SYSTEM DAILY POWER MANAGEMENT

4.1 System Configuration and BESS Control Scheme

In this section, we focus on the BESS control for enabling the MCT-based hybrid system to follow a required grid power profile. The general system structure of the MCT with BESS was shown in Fig. III.1. The MCT has a rated power of 1.5 MW and the DC bus voltage is set to V_{dc} = 1500 V.

The diesel generator shown in this section serves as a backup power source. For grid-connected case, diesel generators can be used to relieve grid burden during peak loads or provide emergency power supply during grid black out. In this section, the diesel generator is modeled by current source to provide powers when the battery SoC is too low. The DG power rating is set as 500 kW in order to cover the maximum grid demand shown in Fig. III.2b.

The BESS is connected through a bi-directional DC/DC converter to the DC bus of the back-to-back converter as shown in Fig. III.1. In the case where the battery maximum operational voltage is higher than V_{dc}, a bi-directional cascaded DC/DC converter can be used. Based on the principle of a cascaded DC/DC converter [105], the battery voltage can be controlled as

$$\frac{V_{battery}}{V_{dc}} = \frac{D_d}{1 - D_u} = D \tag{III.16}$$

D is the voltage ratio decided by the step-down duty ratio D_d and the step-up duty ratio D_u. In the step-down mode, $D_u = 0$ and D_d is controlled in the [0,1] range; while in the step-up mode, $D_d = 1$ and D_u is controlled in the [0,1] range. The corresponding switches triggered to realize the duty ratios should be determined by converter topology and power flow direction. In this work, the power converter is modeled by average-value method for facilitating long-time period simulation. Therefore, the voltage ratio D serves as the control reference for the average-value converter model.

The battery reference power (positive for charge mode) is set to compensate the difference between the available power supply and grid power demand as follows.

$$P_{BESS}^{*} = P_{MCT} + P_{DG} - P_{Grid}^{*} \tag{III.17}$$

Figure III.7 shows the BESS side DC/DC converter control scheme. In this control scheme, the voltage ratio D is limited in the range of $0.78V_{dc}$ and $1.2V_{dc}$ indicating the battery voltage is limited from 1170 V to 1790 V.

The “Battery limits” module in Fig. III.7 is used to hold the value of D when the battery is turned off. The battery is supposed to turn off once the SoC tends to exceed the range of 0.1 and 1, or the absolute value of P_{BESS} reaches the rated value of P_N.

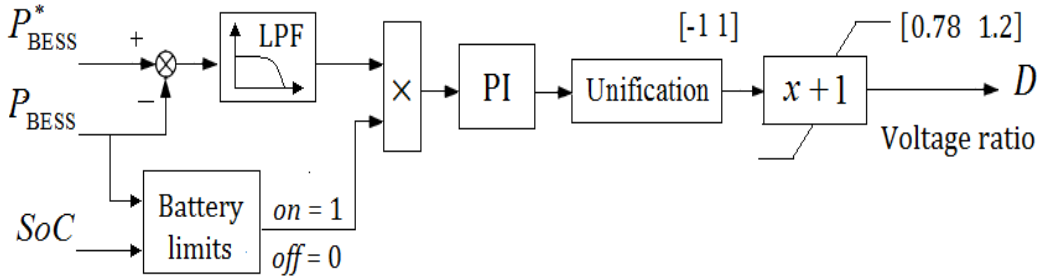

Fig. III.7. Control scheme of the BESS side DC/DC converter.

4.2 Simulation without the DG

The tidal current speed and the corresponding average MCT produced power during one day period are predictable. In this simulation, the grid demand power is set to have an average value equals to 90% of the average MCT produced power. This allows considering the system losses. The grid demand power profile (as shown in Fig. 4b) reflects the load variation during the one day period. In this section, only MCT and BESS are considered to provide grid demand power during one day. The 3MWh VRB model and the control scheme described in the previous sections are integrated into the 1.5 MW MCT system. Figure III.8 shows the MCT produced power, the power injected into the grid and the BESS power during this day. Positive BESS power indicates the battery is charging and negative BESS power indicates battery is discharging. Figures III.9 and III.10 illustrate the battery voltage/current and SoC variation curves. The initial battery SoC is set at 0.4.

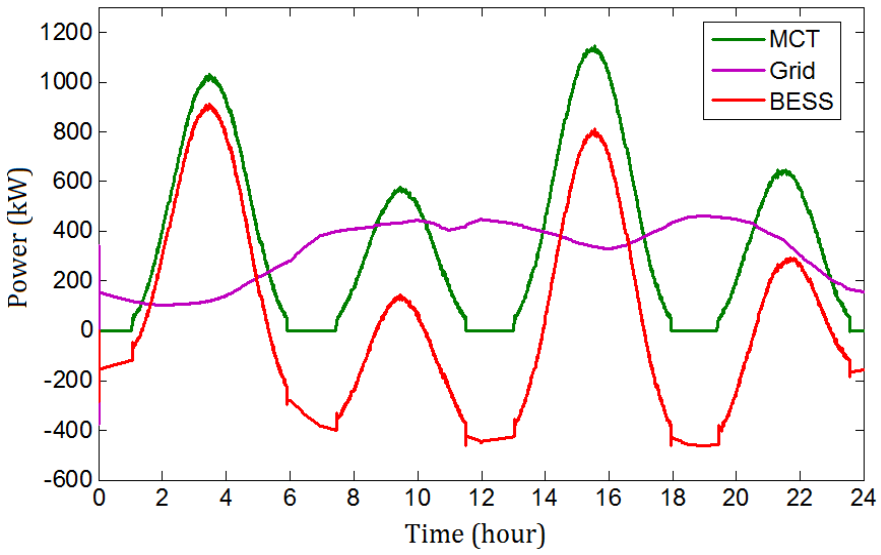

Fig. III.8. Powers of the MCT system with BESS during one day.

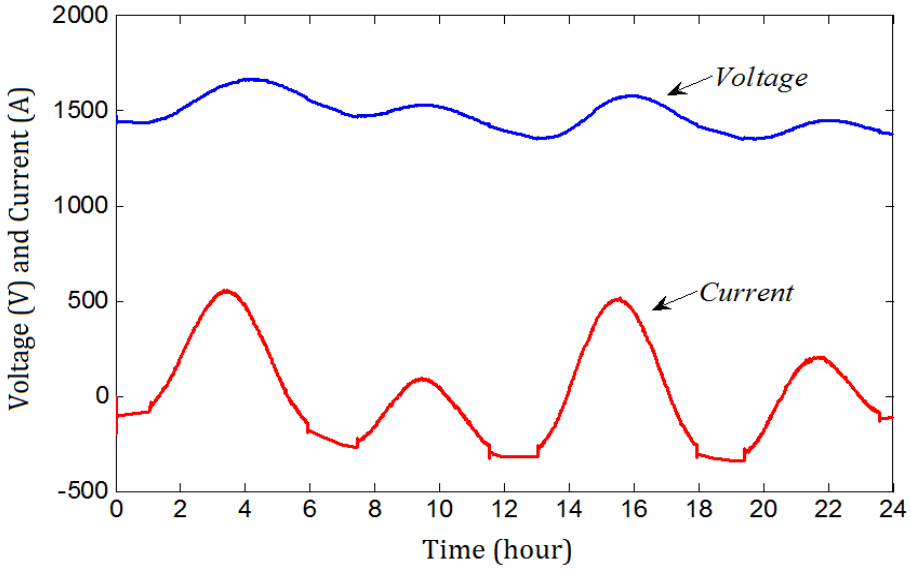

Fig. III.9. Voltage and current of the BESS.

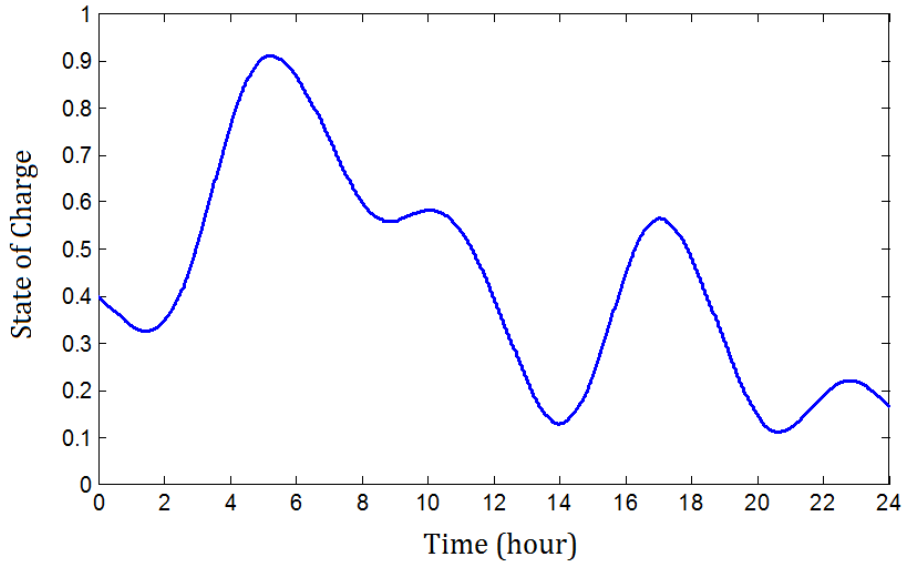

Fig. III.10. SoC of the BESS.

From Fig. III.10, it can be seen that the battery SoC varies in the range of 0.11 and 0.91. At the end of the day, the SoC will decrease below 0.2. This SoC decreasing phenomenon is mainly caused by the battery losses during the 24 hours continuous operation.

Figures III.11 to III.13 show the case when the initial SoC is set at 0.3. During 13:05-14:00 and 20:10-20:50, the SoC will reach its low limitation of 0.1 and the battery will be turned off. When the battery is off, the P_{Grid} will drop to the P_{MCT} (shown in Fig. III.11) and that means the grid power demand can not be satisfied under such situation. The battery voltage and current responses during the battery off time are highlighted in Fig. III.12.

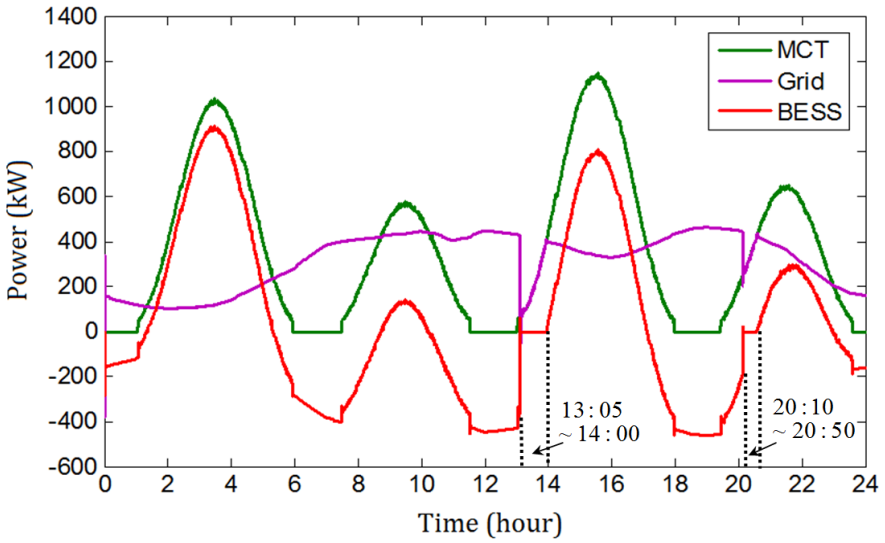

Fig. III.11. Powers of the MCT system with BESS (initial SoC = 0.3).

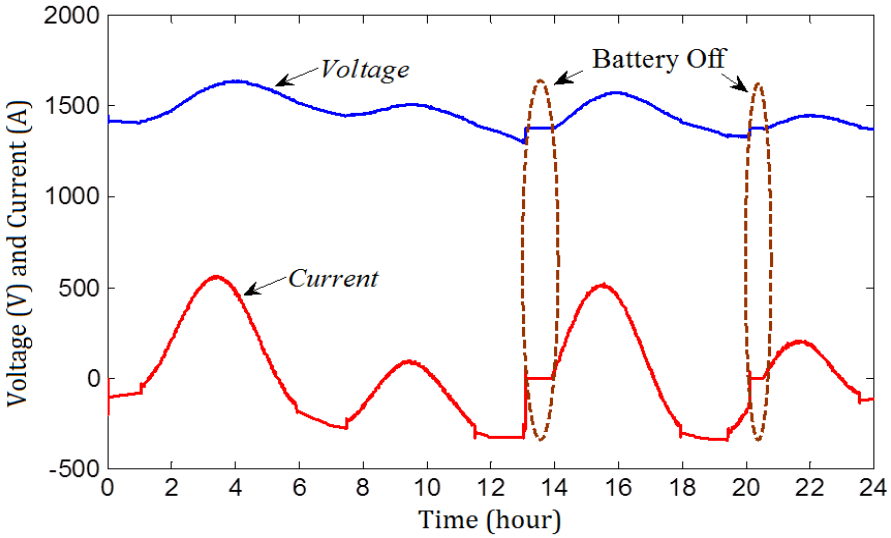

Fig. III.12. Voltage and current of the BESS (initial SoC = 0.3).

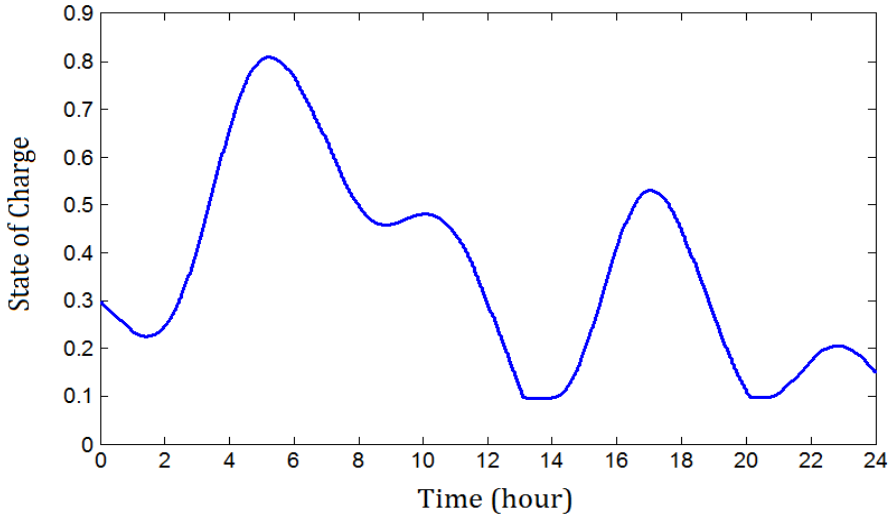

Fig. III.13. SoC of the BESS (initial SoC = 0.3).

4.3 Simulation with the DG

In order to avoid battery SoC reaching the low limitation and insure the grid demand power requirement to be satisfied at any time, the diesel generator is added to the simulation system in this section. The DG unit will be triggered when the battery SoC is near the low limitation. The DG is supposed to provide a constant power of 500kW during the operation time. This power rating is enough to cover the peak load demand (about 480 kW in the simulation).

Figure III.14 compares the powers in the different parts of the MCT-based hybrid system. Figure III.15 and III.16 show the corresponding battery voltage/current and SoC variations.

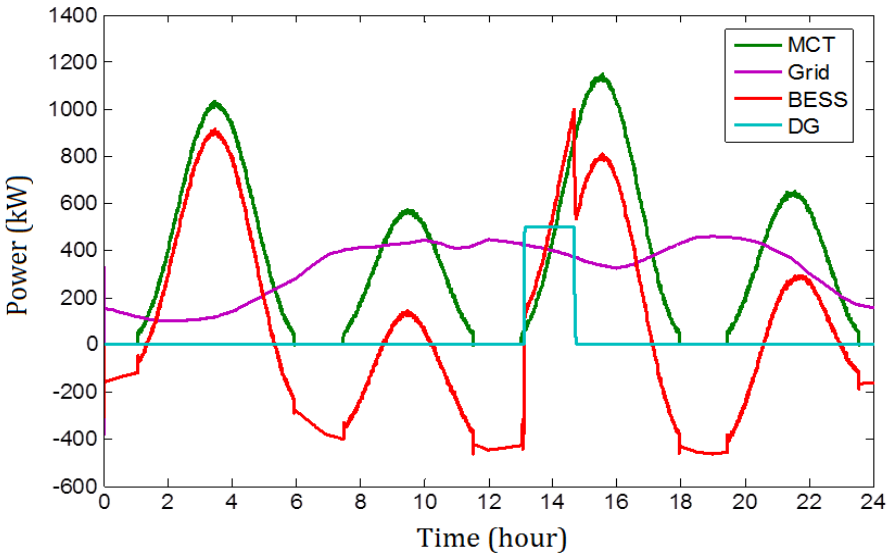

Fig. III.14. Powers of the MCT system with BESS and DG.

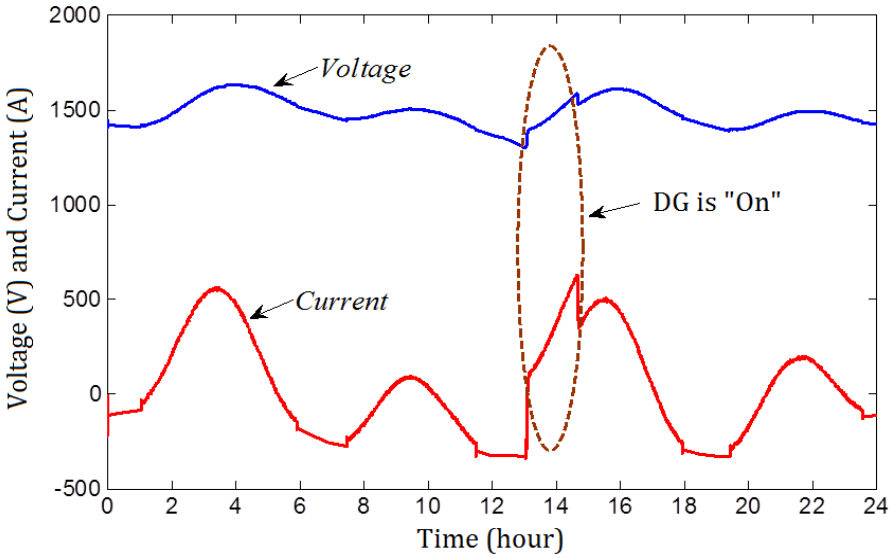

Fig. III.15. Voltage and current of the BESS.

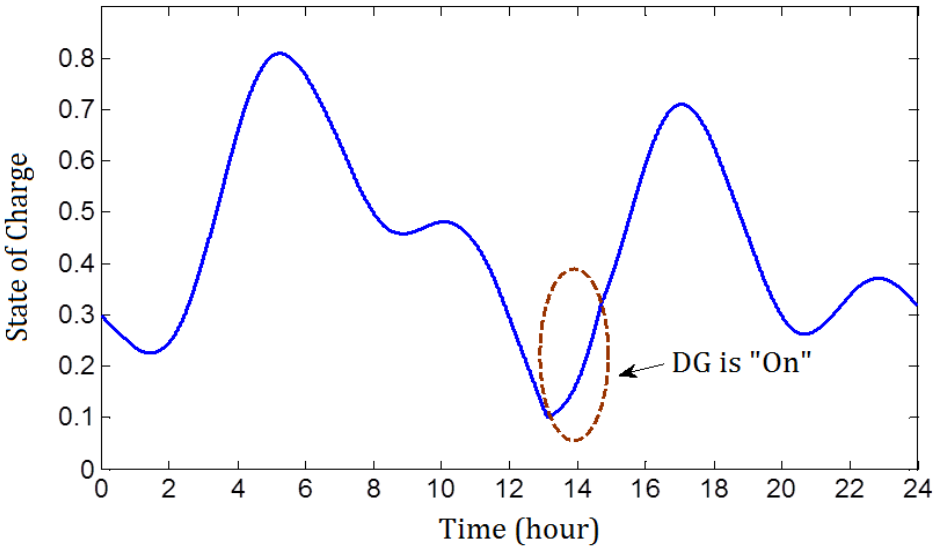

Fig. III.16. SoC of the BESS.

It can be seen that the DG is triggered at about 13:00 when the battery SoC is close to the low limitation 0.1. Then DG is providing power to maintain the grid demand and the battery is charged by both DG and MCT power. The DG is turned off when the battery power reaches the rated value at 14:40; after this point the available MCT power is high enough to charge the battery and to provide grid demand power. In the simulation, another condition for turning off the DG is when the battery SoC reaches 0.4 during the charge mode. The reasons for setting these DG turnoff rules are to avoid overcharging of the battery and to limit the fuel consumption of the DG.

4.4 Simulation with a Smaller DG

When the DG is considered as a backup power source only to restore the battery at low SoC, a smaller DG might further reduce the system cost and the fuel consumption. In this part, the simulation of a 250 kW DG case is carried out.

Figure III.17 shows the system power performance; the period of 12:00 to 16:00 is zoomed in Fig. III. 18. The corresponding battery SoC is illustrated in Fig. III.19. In this smaller DG case, the battery SoC can not be restored immediately when the DG is turned on. As shown in Fig. III.18: the battery continues to provide power (periods T_1 and T_2) for maintaining the grid demand when the smaller DG is trigged; and the battery is charged (period T_3) when the available power produced by the MCT and DG is higher than the grid demand.

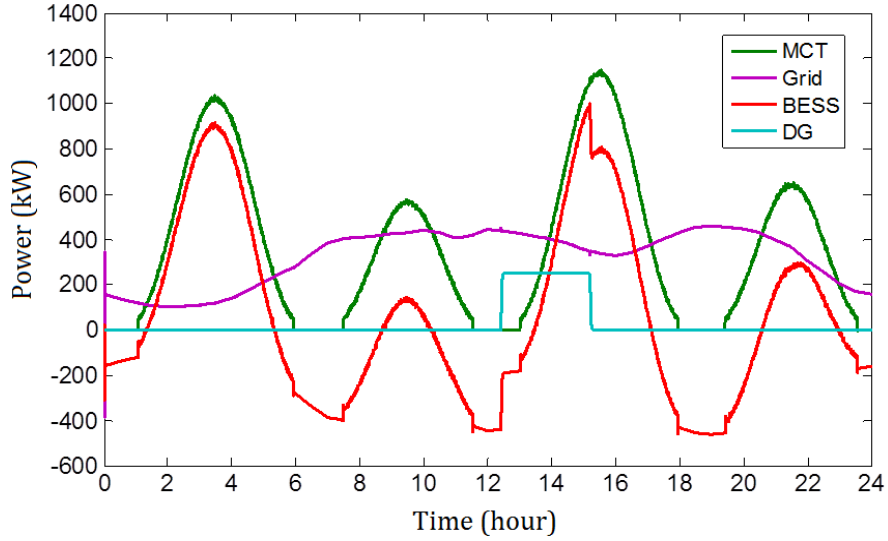

Fig. III.17. Powers of the MCT-based hybrid system with small DG.

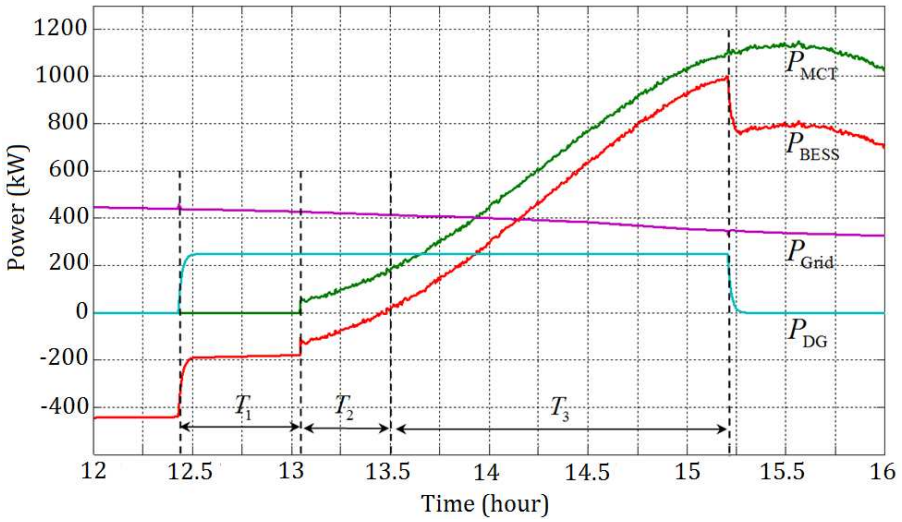

Fig. III.18. Zoom of power profiles between 12:00 and 16:00.

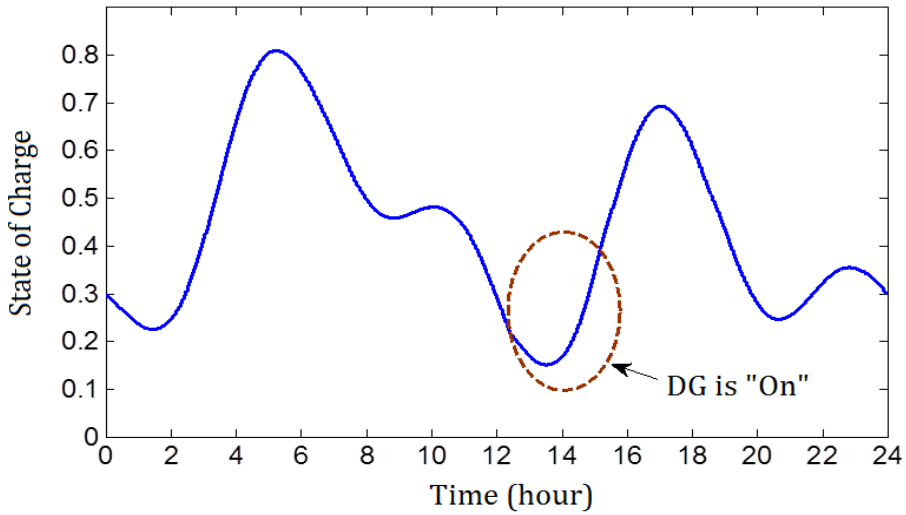

Fig. III.19. SoC of the BESS.

In the previous 500 kW DG case, the DG is in operation from 13:05 to 14:40 (Fig. III.14) and provides 790 kWh. In the 250 kW DG case, the DG is in operation from 12:26 to 15:13 and provides 695 kWh. This implies that the smaller DG case can have a possibility to further reduce diesel-fuel consumption. However, it should be noted that the small DG is incapable to cover the peak load demand; and therefore the small DG should be triggered more early than the previous case to ensure that the BESS still has a discharge margin to maintain the grid/load demand follow ability for the MCT-based hybrid system. From stability point of view for the hybrid power system, it is better to size the DG power rating enough to cover the peak demand. This point is very important for the case at neap tides when the average current speed is very low and the MCT can not produce enough powers during several days.

III.5 ISLAND POWER MANAGEMENT CASE

In the previous section, a large BESS is sized to shift large quantity of the MCT produced energy for compensating the large difference between the MCT output and grid/load demand. Actually, from the simulation of the previous section, it can be seen that large ESS is indispensable when the MCT system is supposed to be the dominant power supply source (supplying almost 100% of the load demand). It means that if we want to maximally substitute the traditional fossil fuel generation units by MCT-based renewable source, it would require a very high ESS capacity and cost to obtain the load following ability.

One of the potential MCT applications is to provide electricity for remote islands not connected to the large continental electric grid. As example, in the near future, several MCTs are planed to be installed in the Fromveur passage (near Brest) to supply 15% ~ 20% load demand of Ouessant Island [106]. Nowadays, most off-grid islands and remote area are strongly dependent on the DG sets for power supply [107]. However, considering the CO_2 emission issue and high fuel logistics cost, renewable energies will provide potential alternatives for reducing the diesel-fuel consumption. In the follows, Ouessant Island will be considered as an island power supply example for the MCT-hybrid system application.

5.1 Island Load Estimation

Ouessant Island is located 20 km off west shore of Brest. It has a surface of 15.6 km^2 and residential population about 900. During the summer, the population would be over 2000 due to a large number of tourists. The daily electric power demand peak can be estimated by the national electricity consumption data. Based on [108], the daily average peak consumption in France is about 0.86 kW per capita for summers and 1.26 kW per capita for winters.

In the case of Ouessant Island, there are very few tourists on the island in winters and the winter electricity load can be estimated around 1134 kW (= 1.26 × 900). For summers, if we consider a larger population of 2500, then the estimated peak load will be about 2150 kW (=0.86 × 2500). In fact, the island is power supplied by 4 groups of diesel generator sets with a total capacity of 5300 kVA [109]. The DG systems are usually designed with a normal power factor of 0.8, and the power ratings of the four DG sets are listed as follows.

Table III. 1. Diesel Generator Sets on Ouessant Island.

	Apparent Power (kVA)	Active Power (kW)
DG_1	1200	960
DG_2	1200	960
DG_3	1450	1160
DG_4	1450	1160
Total	5300	4240

Although there are 4 DG groups on Ouessant Island, during most time only 2 groups are in service and the rest 2 groups are out of service or for maintenance [110]. That means half of the installed DG capacities enable to serve the load demand and another half serves as a 100% backup source. It is quite reasonable to oversize the DG capacity for the off-grid island to ensure the power supply in case of emergency or DG unit's maintenance. Based on the peak load estimation, it implies that one DG of 960 kW and one DG of 1160 kW are enough for most load demands during the year on this island.

5.2 Power Management for the Island Case

5.2.1 System Configuration and Power Rules

For the island case simulation, the DG system will be the main power supply source and the MCT is supposed to provide about 20 % ~ 30 % of the load. Figure III.20 shows the daily MCT power profile and the load demands (high frequency components are neglected) used for the island case. The same current velocity and MCT power profile are used, but the load demands are different from the previous section III.4. In Fig. III.20, the low load curve (range 400~1800 kW) and high load curve (range 500~2250 kW) represent two different load cases for the island. These two load curves can also be considered as an example of the island daily load in winter and summer respectively.

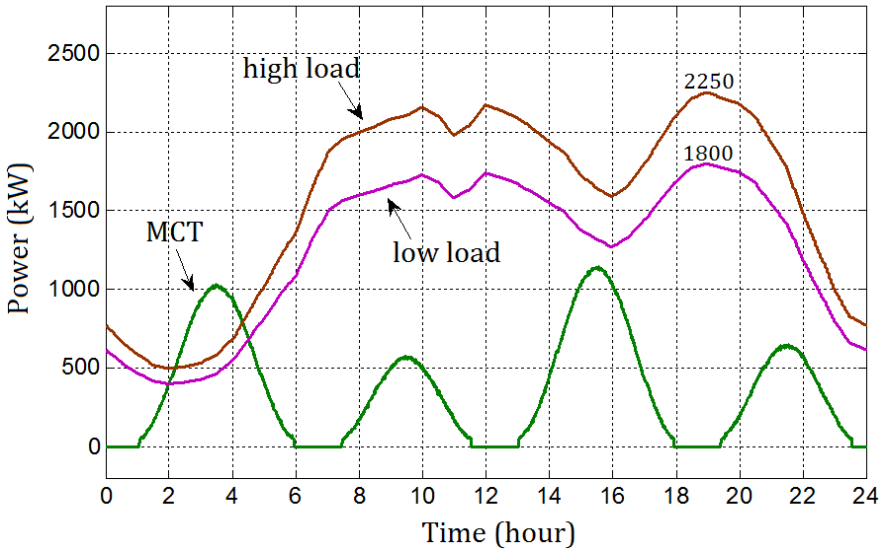

Fig. III.20. Daily power profiles of the island case.

It should be noted that: since for the island case the MCT is not supposed to provide 100 % of the load demand, therefore the BESS size can be reduced compared with the cases in the previous section. From Fig. III.20, it can be seen that the energy needed to be stored by the BESS is greatly reduced; and it also means that the BESS is no longer required to operate continuously during the 24 h of the day. In this case, the BESS burden is reduced and it can be sized smaller. Therefore, for this island case, the BESS is sized as 1.25 MWh (= 500 kW $\times$ 2.5 h). The BESS control strategy will not be changed.

For the DG system, the total available capacity is quite enough (in Table III.1). However, by using MCT and BESS, it leads to possibilities for limiting the DG utilization. In this case, we consider using two DG sets: DG_1 and DG_3. The DG should be operated over 30% of rated power for avoiding low fuel efficiency and engine damage [111]. In this island case, the low power limitation of the DG system is set to 40 % of rated power of DG_1. Therefore, the DG operational limits are given by

$$\begin{cases} P_{DG\_\max} = P_{DG\_1} + P_{DG\_3} = 2120\,\text{kW} \\ P_{DG\_\min} = 40\% \times P_{DG\_1} = 400\,\text{kW} \end{cases} \quad \text{(III.18)}$$

The battery charge/discharge strategy is the same as presented in the previous section. However, for the island case, the DG output power roles are given as follows

$$P_{DG}^{*} = P_{DG\_load}^{*} + P_{DG\_b}^{*} \quad \text{(III.19)}$$

with

$$P^*_{DG\_load} = \begin{cases} P_{load} - P_{MCT}\,, & \Delta P_1 \geq P_{DG\_\min} \\ 0\,, & \Delta P_1 < P_{DG\_\min} \end{cases}$$

$$P^*_{DG\_b} = \begin{cases} P_{DG\_\min}\,, & \textit{turn on} \\ 0\,, & \textit{turn off} \end{cases}$$

In (III.19), $P^*_{DG\_load}$ and $P^*_{DG\_b}$ represent the DG power for load demand and for battery charge demand respectively; $\Delta P_1 = \left| P_{load} - P_{MCT} \right|$ is used to respect the DG low load operation limitation; $P^*_{DG\_b}$ will be turned on when the battery SoC reaches the low limitation (0.11 in the simulation), and it will be turned off until SoC is restored to 0.5 or when the total available battery charged power (from MCT and DG) reaches the rated value of 500 kW.

5.2.2 High Load Demand Case

Figure III.21 shows the system power responses for the high load case with a initial battery SoC of 0.5. The BESS voltage/current and SoC variations are shown in Fig. III.22 and III.23. The BESS works well to store the excessive MCT produced power (2:10~4:20) and provide

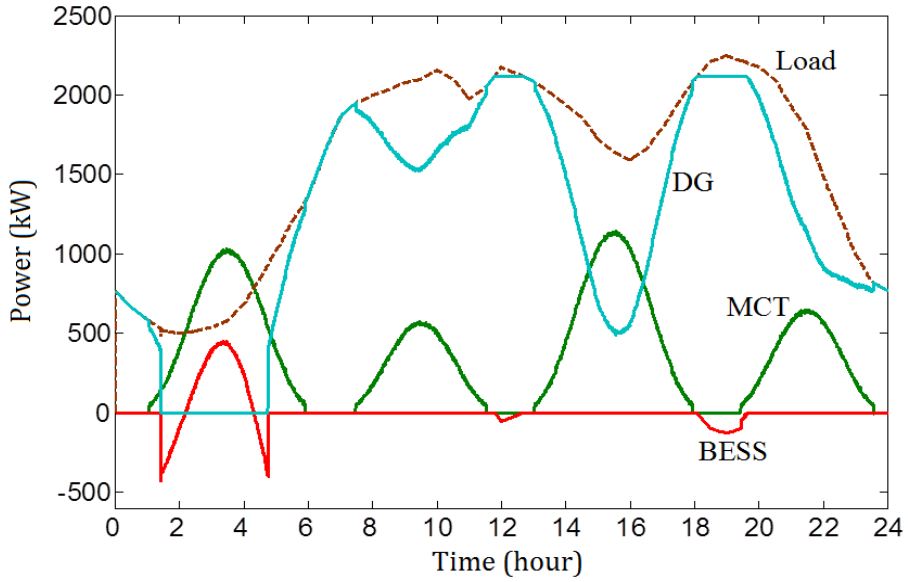

Fig. III.21. Powers of the high load demand case (initial SoC = 0.5).

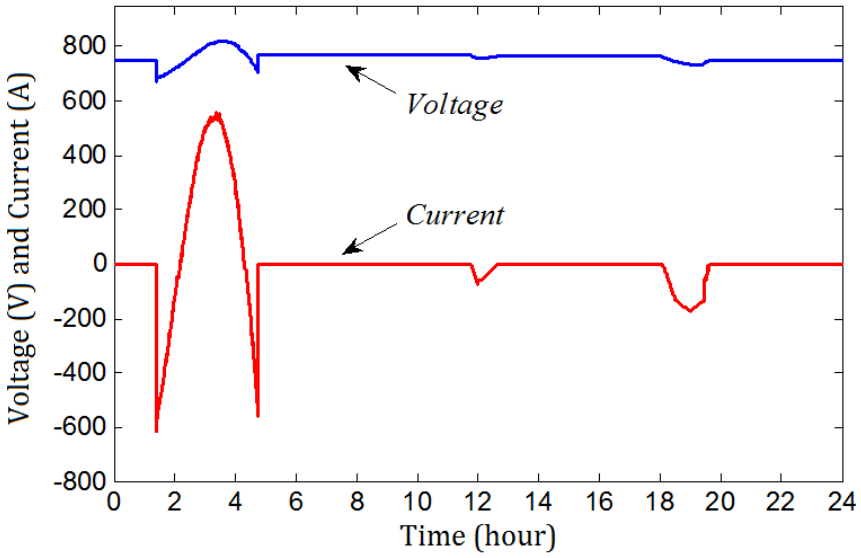

Fig. III.22. Voltage and current of the BESS (initial SoC = 0.5).

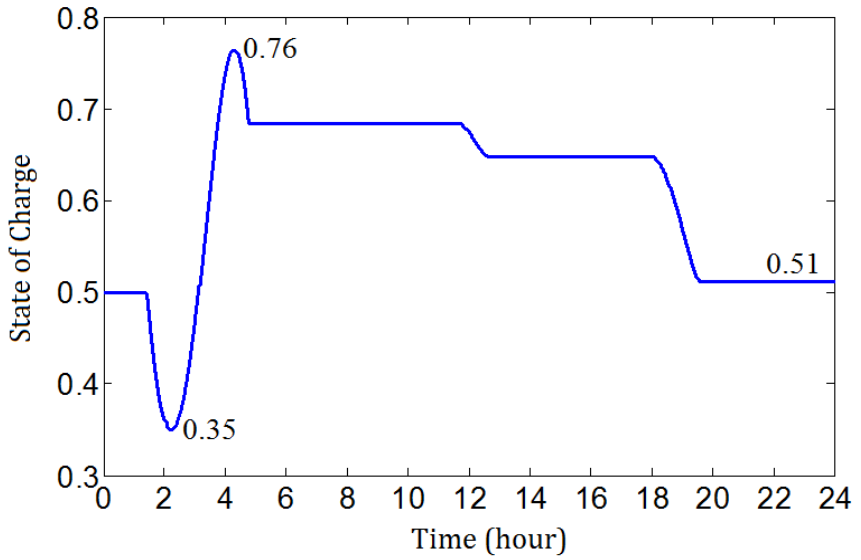

Fig. III.23. SoC of the BESS (initial SoC = 0.5).

the power during the peak load around 12:00 and 19:00 as shown in Fig. III.21. It can be imagined that if there is no BESS, a third DG would be used in these peak load periods. This illustrates the load-leveling benefit brought by the BESS in the hybrid power supply system. It should be noted that the BESS also helps to avoid the DG low power operation when the MCT power is close to the load demand. In fact, the MCT produced power is seen as a negative load for the DG; if there is no BESS, the MCT power would cause low-load DG operation in some cases. This problem is successfully handled by the BESS in the proposed power management strategy.

In case of low battery SoC, the DG will be used to charge the battery. Figure III.24 show the system power profiles and Fig.III.25 shows the battery SoC variation for the case of low BESS initial SoC. The zoomed curves on the period of 0:00~6:00 are illustrated in Fig. III.26 and Fig. III.27. From Fig. III.26, it can be seen that the BESS is discharged during 1:25~2:00 and 4:20~4:46 for avoiding the DG low load operation and saving diesel-fuel consumption. When the battery SoC reaches 0.11, the DG provides power and the BESS is charged by the DG and MCT during 2:00~2:22 until the battery attends its rated power. After this point, the DG is turned off and the BESS is charged by excessive MCT power during 2:22~4:20.

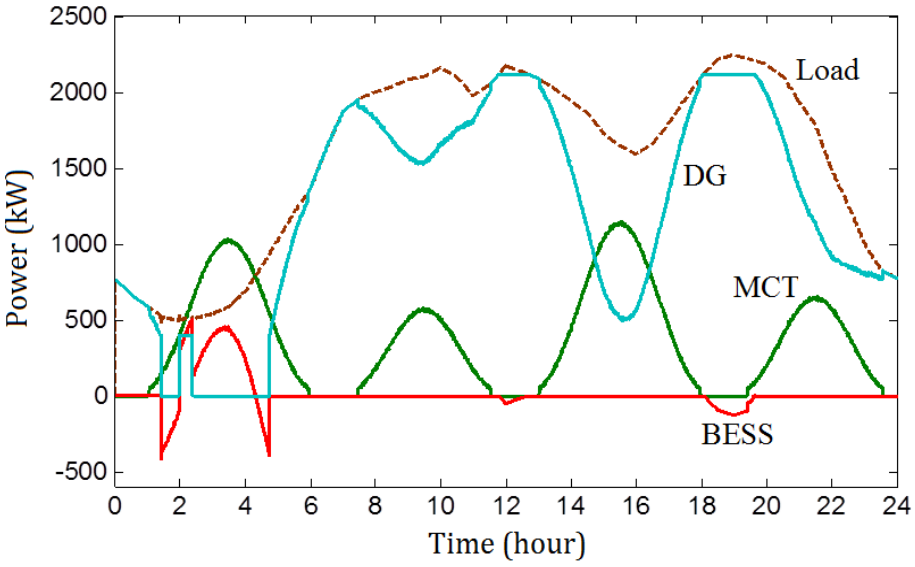

Fig. III.24. Powers of the high load demand case (initial SoC = 0.25).

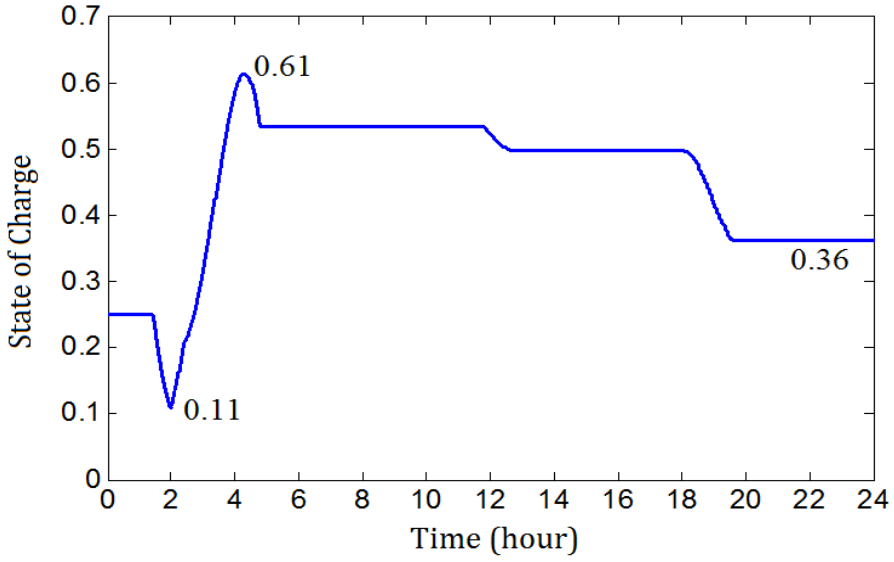

Fig. III.25. SoC of the BESS (initial SoC = 0.25).

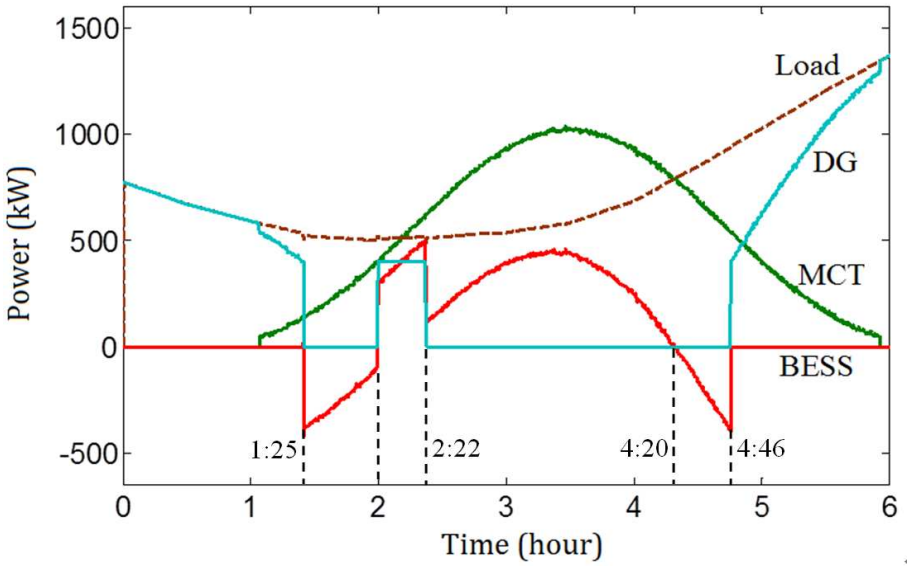

Fig. III.26. Zoomed power curves (initial SoC = 0.25).

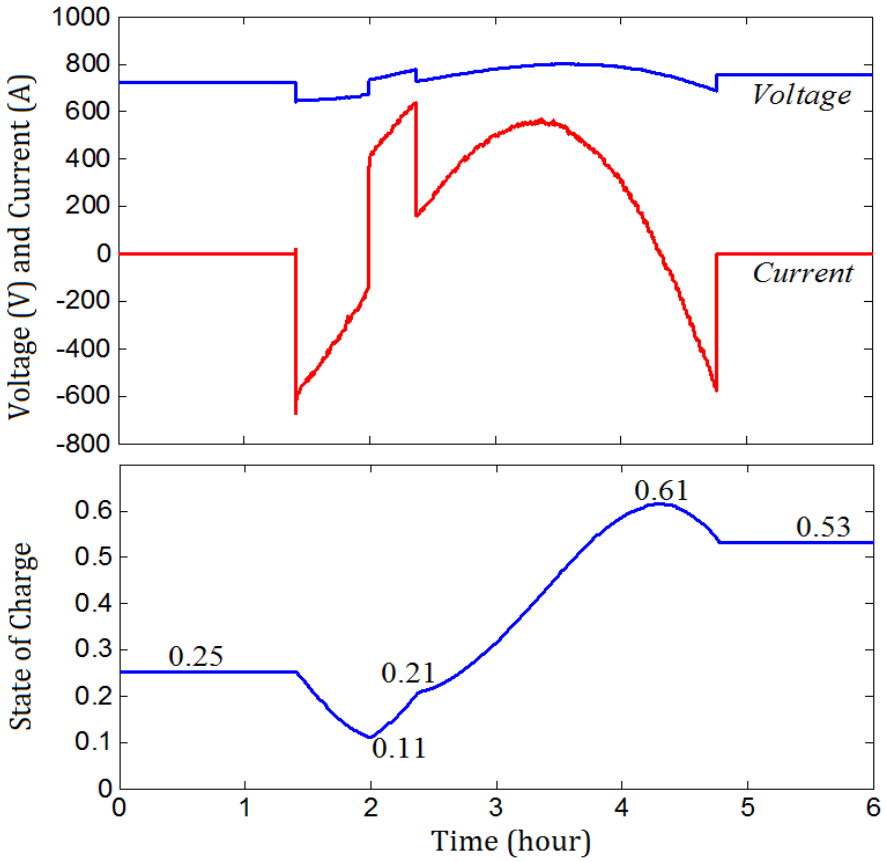

Fig. III.27. Zoomed BESS curves (initial SoC = 0.25).

5.2.3 Low Load Demand Case

For the low load demand case, the DG can easily handle the peak load but the new constrain is that the MCT power will need to be limited when the MCT power is too high.

As shown in Fig. III.28, the MCT power should be controlled to deviate from MPPT during 3:00~3:35 to limit the BESS charging power at its rated value of 500 kW. Although the BESS is charged by the MCT to a high SoC value (Fig. III.29), the BESS will be discharged during 14:55~16:15 to avoid DG low-load operation and to assistant MCT for supplying the load. It can be seen that, the DG utilization can be reduced and the battery SoC enables to maintain a same level with the initial value at the end of day by the proposed power management.

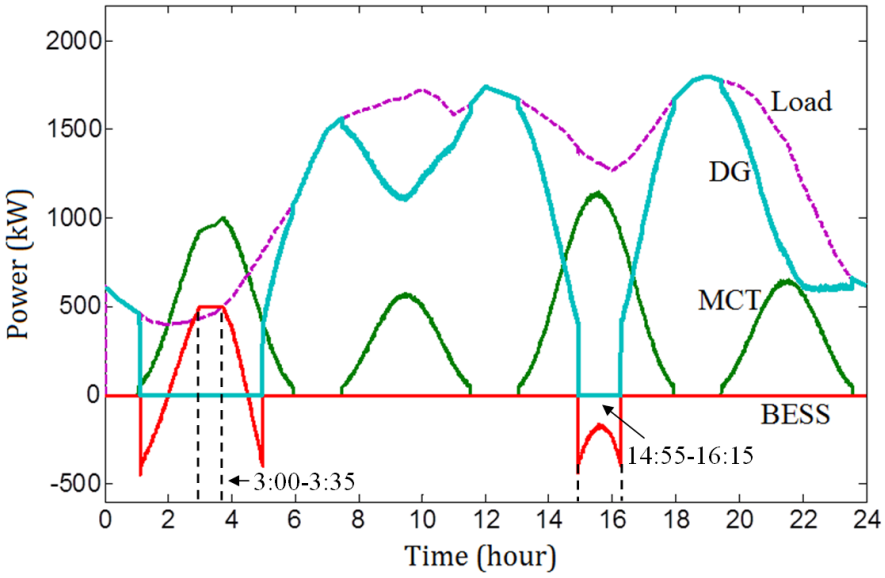

Fig. III.28. Powers of the low load demand case.

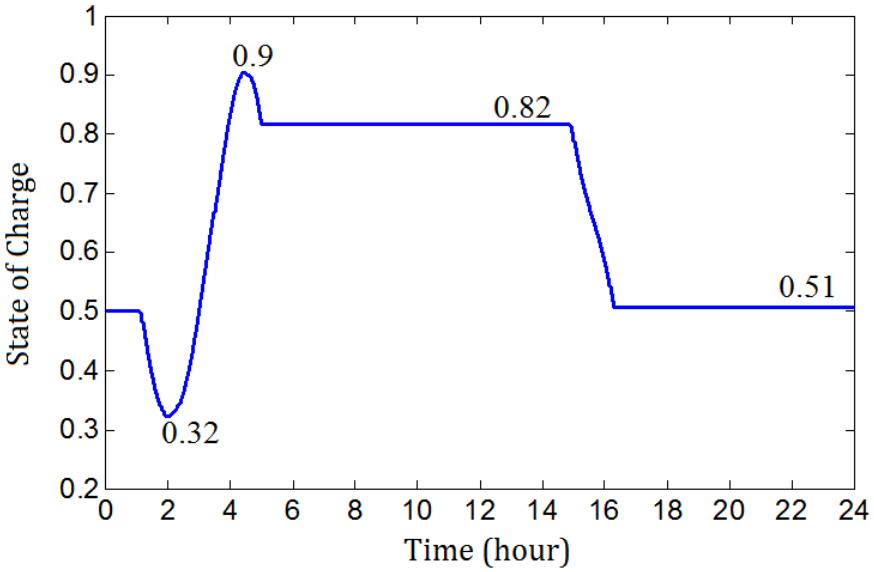

Fig. III.29. SoC of the BESS.

5.2.4 Without the BESS

It is also interesting to show what would happen if there is no available ESS. That means only MCT and DG are used to supply the load demand. In this case, the rules are given in Table III.2. The load demand should be satisfied at all moments ($P_{MCT}^{*} + P_{DG}^{*} = P_{load}$); and the required MCT output power P_{MCT}^{*} should deviate from P_{MCT_MPPT} (maximum available MCT power) during some periods according to the power balance situation.

Table III. 2. Power rules without the BESS ($\Delta P_2 = P_{load} - P_{MCT\_MPPT}$).

	$\Delta P_2 \le 0$	$0 < \Delta P_2 \le P_{DG\_\min}$	$\Delta P_2 > P_{DG\_\min}$
P_{MCT}^{*}	P_{load}	$P_{load} - P_{DG\_\min}$	P_{MCT_MPPT}
P_{DG}^{*}	0	$P_{DG\_\min}$	$P_{load} - P_{MCT\_MPPT}$

Figure III.30 shows the power curves when there is no available ESS. In this figure, the dotted green curve shows the MCT power under MPPT strategy and the solid green curve shows the real MCT output power based on the proposed rules. It can be seen that during 2:00~4:30 and 14:55~16:15, the MCT is unable to follow the MPPT due to the load demand and the DG low load power limit respectively. This not only causes the waste of the MCT power potential, but also increases the complexity of the MCT control.

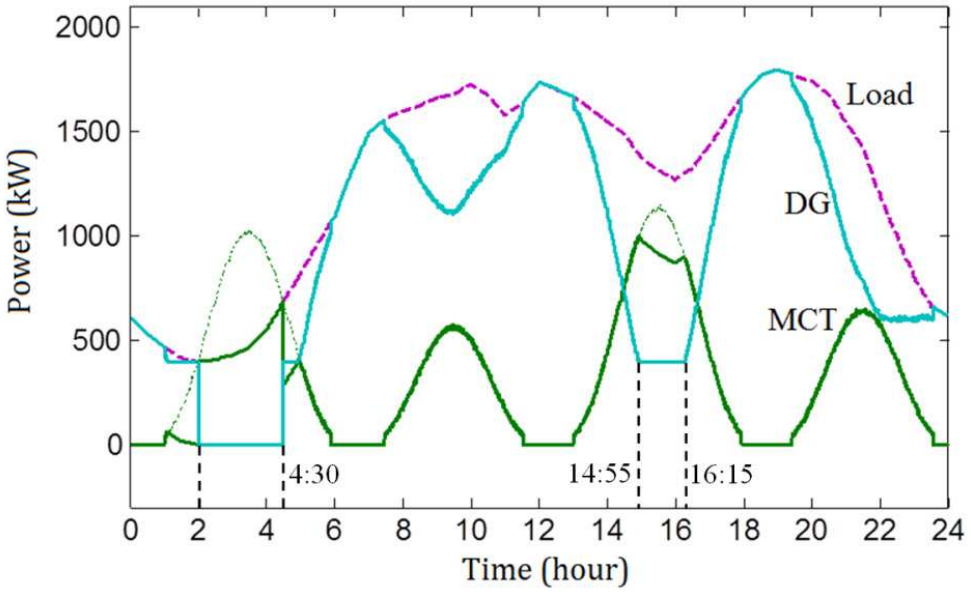

Fig. III.30. Powers curves without the BESS.

5.3 Conclusion of the Island Case

Table III.3 summarizes the energy performance for the island case and compares the DG consumption with and without the BESS. The daily load demand energy E_{load}, the MCT output energy E_{MCT} and DG provided energy E_{DG} are calculated by integration the corresponding power curves. The "with BESS" cases are based on the simulation results for the battery initial SoC of 0.5. The DG consumption saving is then calculated by (III.20); it indicates that how much DG consumption can be saved with the MCT and BESS.

$$E_{DG\_saving} = \frac{E_{load} - E_{DG}}{E_{load}} \tag{III.20}$$

Table III. 3. DG Consumption Saving During One Day.

		E_{load} (MWh)	E_{MCT} (MWh)	E_{DG} (MWh)	Consumption Saving
High Load	with BESS	37.9	8.6	29.5	22.2 %
	no BESS	37.9	7.8	30.1	20.6 %
Low Load	with BESS	30.3	8.57	21.95	27.6 %
	no BESS	30.3	7.26	23.04	24.0 %

It can be seen from Table III.3 that in both high load demand and low load demand cases, the BESS enables to increase the MCT output energy. This is because the BESS greatly facilitate to keep the MCT in MPPT mode, especially in low load demand cases (3.6% increase of the DG consumption saving compared with the case without BESS).

It also indicates that when the MCT penetration increases (about 22% in the high load case and 28% in the low load case), the importance and requirements of the BESS will increase simultaneously. From the obtained simulation results (Fig. III.23 and Fig. III.29), it can be found that the battery SoC variation is much larger in the high penetration case (the low load demand case). Therefore, the conclusion is that larger BESS is required for higher MCT penetration. Although higher MCT penetration can result lower diesel-fuel consumption, the increasing ESS need would be considered as a constraint for optimizing the total system cost.

III.6 CONCLUSION

In this chapter, the hybrid power system of MCT/BESS/DG is studied for daily power management cases. The vanadium flow battery is chosen as the BESS type and modeled by the equivalent circuit method. Two different cases are simulated: the dominant MCT supply case (MCT power covers 100% of the load) and the island power supply case (MCT power covers 20% ~ 30% of the load).

For the dominant MCT supply case, the DG consumption is maximally limited by serving as a backup source only for charging the BESS at low SoC. The load following ability is then totally realized by the BESS and this leads to a large battery system of 3 MWh.

For the island power supply case, the Ouessant Island load requirements and the existing DG capacity are considered as a study case. The high load demand and low load demand cases are studied and compared. In this case, the DG groups serve as the main power supply source and a 1.25 MWh BESS is carried out in the simulation. Simulation results show that the BESS enables to facilitate the MPPT operation of the MCT and to reduce the diesel-fuel consumption.

Chapter

IV

Control of the Non-Pitchable PMSG-Based Marine Current Turbine at Over-rated Current Speed

NOMENCLATURE

C_p	=	Turbine power coefficient;
f	=	field frequency in the generator stator;
H_S, T_p	=	Swell significant height and peak period;
i_d, i_q	=	Generator *d*- and *q*-axis currents;
I_{max}	=	Maximum phase current magnitude;
K_T	=	Generator torque constant;
L_d, L_q	=	Generator d- and q-axis inductances;
n_p	=	Pole pair number of the generator;
P_N	=	Turbine nominal power;
R	=	Turbine blade radius;
R_s	=	Generator stator resistance;
T_e, T_m	=	Generator and turbine torque;
V	=	Marine current velocity;
V_s	=	Generator phase voltage magnitude;
V_{dc}	=	DC bus voltage;
V_{max}	=	Maximum phase voltage magnitude;
v_d, v_q	=	Generator *d*- and *q*-axis voltages;
ρ	=	Sea water density;
λ	=	Turbine tip speed ratio;
φ	=	Generator power factor angle;
ψ_m	=	Permanent magnet flux;
ω_e, ω_{eb}	=	Electrical angle and base speeds;
ω_m	=	Mechanical angle speed;
ω_{mN}	=	Rotor nominal angle speed.

GLOSSARY

CAP	=	Constant active power;
CPSR	=	Constant power speed ratio;
MAP	=	Maximum active power;
MCT	=	Marine current turbine;
MPPT	=	Maximum power point tracking;
MTPA	=	Maximum torque per ampere;
PMSG	=	Permanent magnet synchronous generator;
TSR	=	Tip speed ratio.

IV.1 INTRODUCTION

The power fluctuation phenomena both on short-time period and long-time period have been studied in the previous chapters. In this chapter, the power limitation control for the non-pitchable MCT at high current speed will be focused. Difficulties of underwater accessibility make compact structure and low maintenance highly expected for MCTs. Several large industrial MCT projects such as the DCNS-OpenHydro [133], Sabella [20] and Voith Hydro turbine systems [18] adopt non-pitchable turbine blades and use permanent magnet synchronous generators (PMSG). Two advantages of these solutions can be noticed: fixed blades enable simplifying the turbine system (avoiding pitch-variable mechanism); and PMSGs enable realizing direct-drive systems (eliminating gearbox).

However, the MCT rated power will not be designed for the peak marine current speed due to the fact that the peak current speed may appear only at large spring tides and corresponds only to a very small part of the statistical resource [3]. This is why, for developing a cost effective solution, using a power limitation control strategy will greatly reduce the rated power (and the cost) of the system without reducing much of the annual energy yield. However, when the marine current speed is higher than the rated value, a fixed-pitch MCT is not able to limit the extracted power by pitch control as in large wind turbines [112-113] and some pitchable MCT turbines (such as SeaGen turbine [16]). Therefore, an appropriate generator-side control strategy should be applied to control and limit the MCT output power in this case.

In this chapter, an original solution for power limitation of the fixed-pitch MCT is proposed. This solution is based on the use of flux-weakening strategies for controlling the MCT power at high current speeds. The flux-weakening operating characteristics for the PMSG will be analyzed. The torque control and speed control schemes will be compared to show their different performance at over-rated current speed. And then, the constant power mode and maximal power mode during the flux-weakening stage will also be compared. Moreover, the influence of machine parameters on the constant power range and the influence of turbine C_p curve shape on flux-weakening operation will be discussed.

Figure IV.1 shows the general system schema of the studied system. The generator-side converter control with flux-weakening strategy will be focused in this chapter. The grid-side converter control will be the same as presented in Chapter II.

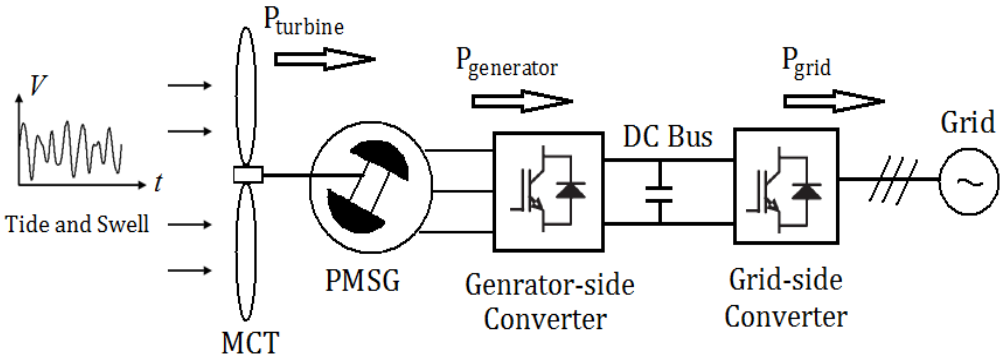

Fig. IV.1. General schema of a PMSG-based direct drive MCT system.

IV.2 GENERATOR OPERATING CHARACTERISTICS

2.1 Over-rated Speed Operation

The turbine power characteristics (shown in Fig. IV.2) presented in § II.3 show that the MCT produced power is supposed to be limited to a constant power at over-rated current speed. For the studied 1.52 MW direct-driven MCT, the maximum rotor speed to follow MPPT is 24 rpm (2.52 rad/s) for a marine current of 3.2 m/s. The PMSG nominal active power and the base speed are then designed at this point.

Based on the turbine power characteristic, one possible power limitation solution for the fixed-pitch MCT is to operate the turbine at over-rated speed during high marine current speed periods for reducing turbine power coefficient and the harnessed power. However, over-rated speed operation leads to high electromotive force (EMF) in PM machines and may cause saturations in the regulators (in fact, the AC voltage values in the PMSG windings are limited by the DC bus voltage level).

Various flux-weakening control strategies have been proposed to realize over-rated speed operations of PM machines in the literatures. In feed-forward or model-based methods [114-116], the *d*-axis current is calculated based on machine parameters and the operating speed. These methods have fast transient responses but they are sensitive to system parameter variations. Voltage regulation method in [117-118] produces *d*-axis current reference to control the output synthesized voltage of the current regulator within the inscribe circle of the voltage hexagon. This method does not depend on the machine parameter but the dc-voltage is not fully utilized. Over-modulation methods in space vector modulation are investigated in [119-120] to generate voltage vector references for maximizing output power/torque capability under flux weakening stage. Reference [121] proposes a novel anti-windup control

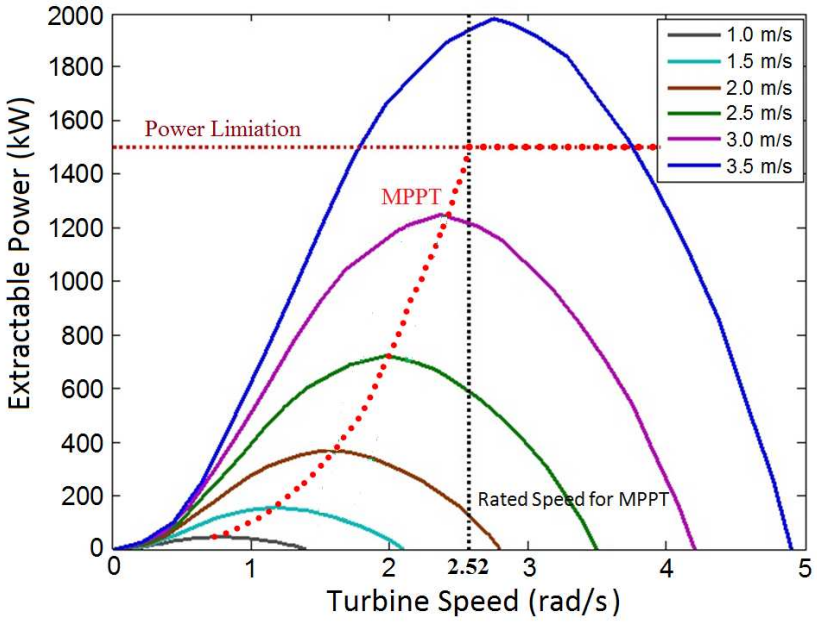

Fig. IV.2. The turbine power characteristics (§ II.3).

scheme which uses the information of the controller-output and converter-output voltages differences to modify the *d*-axis current reference current; this method is further extended to infinite constant power speed ratio (CPSR) cases in [122-123].

In the followed section, the steady-state analysis of the flux-weakening operation characteristics will be presented.

2.2 Steady-state Analysis

The PMSG *d-q* model in the synchronous rotation frame has been given in § II.3, the stator current is decomposed into a flux component i_d and a torque component i_q; and the following voltage and current limits must be guaranteed at any time.

$$v_d^2 + v_q^2 \le V_{max}^2 \tag{IV.1}$$

$$i_d^2 + i_q^2 \le I_{max}^2 \tag{IV.2}$$

It should be noted that V_{max} is limited by the available DC-bus voltage V_{dc} and the converter modulation method. $V_{max} = 1/\sqrt{3}\, V_{dc}$ for the sinusoidal wave model (linear space vector modulation) and $V_{max} = 2/\pi\, V_{dc}$ for the full six-step operation [118]. I_{max} is determined by

machine torque and converter power ratings. Smaller I_{max} will result smaller torque capability and reduce the cost of the PMSG (due to materials and weight reduction), however the machine operational area will be limited at flux-weakening stage [124-125]. In this work, the I_{max} will be designed at the generator base speed and the nominal power.

Surface-mounted PMSG (non-salient machine) is considered in this work. Although salient PM machines can have wider flux-weakening range, non-salient PM machines are usually easier to manufacture and are able of achieve a smoother electromagnetic torque [126]. For a surface-mounted PM machine, the inductances in *d-q* axes are almost equal ($L_d = L_q = L_s$). By neglecting stator resistance, the voltage limitation (IV.1) in steady-state can then be expressed by (IV.3).

Based on (IV.2) and (IV.3), the voltage and current constraints can be drawn as circles shown in Fig. IV.3. The solid-line circle indicates the current limitation and the dotted-lines circles indicate voltage constraints which have a centre of (0, $-\psi_m/L_s$) and shrink with increased operating speeds.

$$i_q^2 + \left(i_d + \frac{\psi_m}{L_s} \right)^2 \le \left(\frac{V_{max}}{\omega_e L_s} \right)^2 \qquad \text{(IV.3)}$$

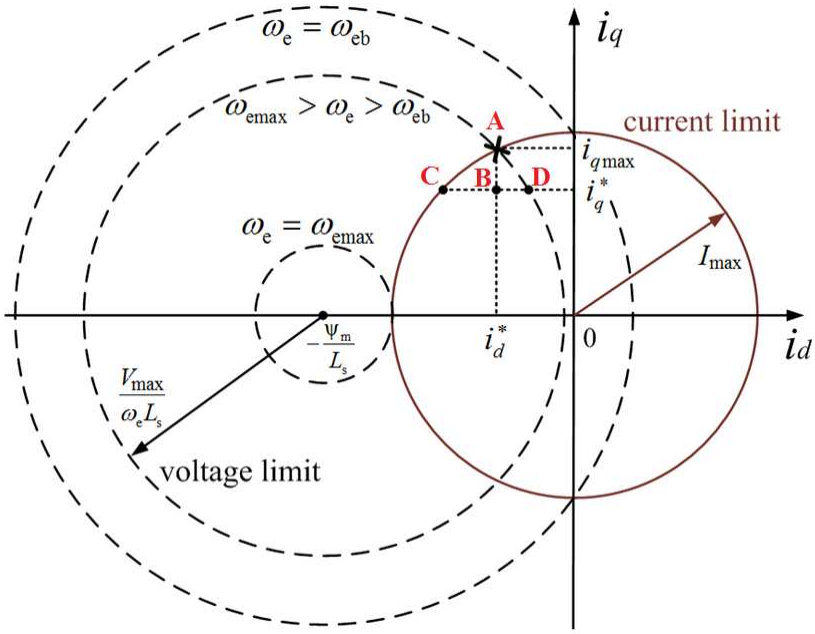

Fig. IV.3. Voltage and current limitation circles of the PM machine.

The magnetic saturation constraint should be respected to ensure the linear magnetic model; and the demagnetization constraint should also be respected to avoid permanent magnets total demagnetization. These two constraints depend on the machine design (machine geometric parameters and the used materials) [127]. In this work, the V_{max}, I_{max} are supposed to be set under the saturation and demagnetization constraints, therefore every point within the crossed area of the voltage and current limitation circles in Fig. IV.3 can be reached by the PMSG.

The generator parameters are set to match the turbine characteristics: the generator nominal speed is set at the maximum turbine speed to realize the MPPT stage (24 rpm, 2.52 rad/s); the generator nominal active power is designed as the same value of the turbine nominal one (1.52 MW); this point is considered to be the base speed for the flux weakening operations. The generator maximum torque is required at the base speed to obtain the nominal power as given by

$$P_N = T_{eN}\omega_{mN} = K_T I_{max}\frac{\omega_{eb}}{n_p} \tag{IV.4}$$

with $K_T = 1.5 n_p \psi_m$.

The typical control strategy for a non-salient PM machine under base speeds is to set $i_d = 0$ for maximizing the torque per ampere ratio (MTPA). When rotor speed is over the machine base speed, the voltage limitation circle will then shrink to the left side of the *q*-axis (as shown in Fig. IV.3). It indicates that negative *d*-axis current should be injected to decrease the total flux in the machine windings and to keep the operating points within the voltage and current limitation circles at over-base speed operations.

Finite constant power speed ratio case ($\psi_m > L_s I_{max}$) is studied in this work. In this case, the maximum torque in the flux-weakening operation area is obtained when the machine operates at the intersection points of the voltage and current limitation circles. The intersection points (like point *A* in Fig. IV.3) can be calculated when the equality sign is used in (IV.2) and (IV.3); and the corresponding i_d and the i_q can be obtained as follows.

$$i_d^* = \frac{L_s}{2\psi_m}\left[\left(\frac{V_{max}}{\omega_e L_s}\right)^2 - \left(\frac{\psi_m}{L_s}\right)^2 - I_{max}^2\right] \tag{IV.5}$$

$$i_{qmax}^{+} = \sqrt{I_{max}^2 \quad i_d^{*2}} \tag{IV.6}$$

If the generator output power is supposed to be limited to the nominal power at over-base speed operation ($\omega_e > \omega_{eb}$), the *q*-axis current reference should be calculated by

$$i_q^* = \frac{T^*}{K_T} = \frac{P_N}{K_T(\omega_e / n_p)} \quad \left(\frac{\omega_{eb}}{\omega_e}\right) I_{max} \quad \left|i_{qmax}\right| \tag{IV.7}$$

From Fig. IV.3, it can be noticed that for a given i_q^* under i_{qmax}, there exists a range for setting i_d reference values (shown as the *C*-*D* line segment). With the current constraint (for the point *C*) and the voltage constraint (for the point *D*), the i_d reference range can be calculated by

$$-I_{max}\sqrt{1-\left(\frac{\omega_{eb}}{\omega_e}\right)^2} \le i_d \le -\frac{\psi_m}{L_s}\left(1-\frac{\omega_{eb}}{\omega_e}\right) \tag{IV.8}$$

It is not obvious to determine the optimal i_d reference due to various optimization criteria. The copper loss is proportional to the square value of stator current, while the iron loss is approximately proportional to the square value of local flux density for a given speed [128]. Therefore, in the Fig. IV.3, the point *D* corresponds to the lowest copper losses while the point *C* corresponds to the lowest iron losses. If the maximum torque per ampere (MTPA) strategy is applied, then the point *D* will be chosen as the operating point for the given i_q reference.

Figure IV.4 illustrates the generator power characteristics in this work. Under the base speed, the generator is supposed to operate in MPPT mode enabling the turbine to capture maximum energy from marine currents. Over the base speed, a demagnetizing current (negative i_d current) is injected and the generator will operate in the flux weakening range. At the flux weakening stage, there exists a constant power range during which the generator power can be either over the nominal power with i_{qmax} or can be limited to the nominal power with i_q given by (IV.7). The i_d current curve shown in Fig. IV.4 is calculated by (IV.5); the two different i_q current trajectories correspond to the coordinates described by points *A* and *B* in Fig. IV.3 when the rotor speed increases. However, when the rotor speed exceeds the constant power range, i_q will be limited to i_{qmax} and the operating points of the two control modes are the same. From this step, the generator power will decrease rapidly below the nominal value with the increase of the rotor speed.

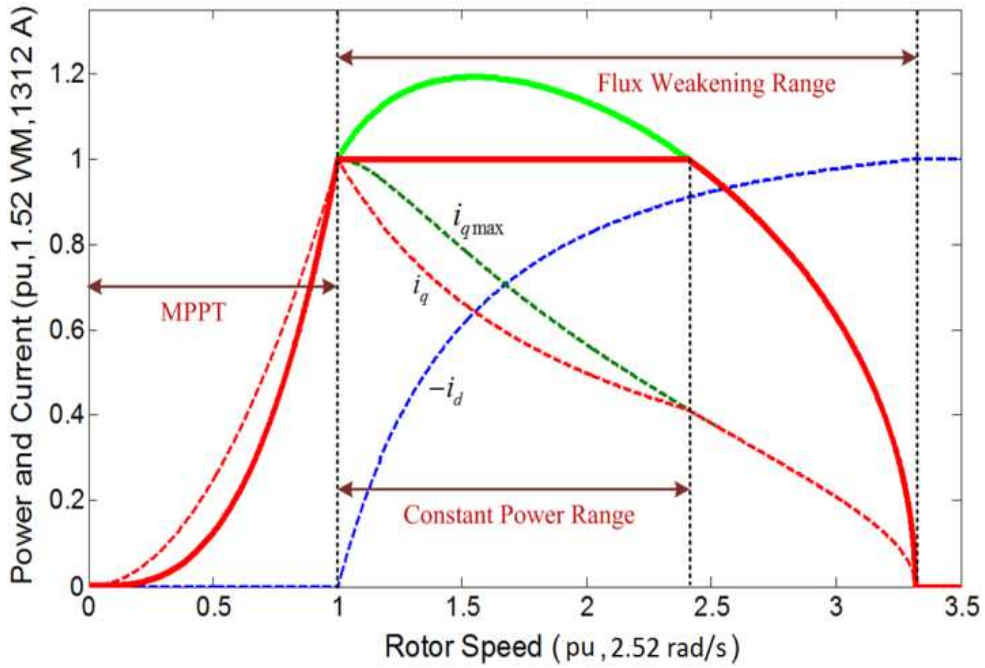

Fig. IV.4. Generator operating characteristics.

The flux-weakening range and constant power range depend on machine parameters. The maximum speed for the flux-weakening range can be obtained from Fig. IV.3 as

$$\omega_{emax} = \frac{V_{max}}{\psi_m - L_s I_{max}} \tag{IV.9}$$

The maximum speed for the constant power range can be calculated based on (IV.5) ~ (IV.7) with the equality sign in (IV.7),

$$\omega_{econ} = \frac{\omega_{eb}}{1 - 2\left(x_{pu}\right)^2} \tag{IV.10}$$

where $x_{pu} = \omega_{eb} L_s I_{max} / V_{max}$; and the parameter relationship at the base speed conforms to

$$V_{max} = \sqrt{\left(\omega_{eb}\psi_m\right)^2 + \left(\omega_{eb} L_s I_{max}\right)^2} \tag{IV.11}$$

Then, the flux-weakening range and the constant power range can be described by the ratio of their maximum operational speeds with the base speed as follows

$$Ratio\_fx = \frac{\omega_{emax}}{\omega_{eb}} = \frac{V_{max}}{\omega_{eb}\left(\psi_m - L_s I_{max}\right)} \quad \text{(IV.12)}$$

$$Ratio\_con = \frac{\omega_{econ}}{\omega_{eb}} = \frac{1}{1-2\left(x_{pu}\right)^2} \quad \text{(IV.13)}$$

In this paper, the generator (parameters illustrated in [Appendix A]) is able to have a flux-weakening range of *Ratio_fx* = 3.3 and constant power range of *Ratio_con* = 2.4 as shown in Fig. IV.4. This constant power range is sufficient for the generator to cope with the MCT power characteristics and to achieve both over-nominal power and nominal power modes during high marine current speeds.

IV.3 ROBUST FLUX-WEAKENING CONTROL

3.1 The System Control Scheme

From the steady-state calculation presented in the previous section, it can be seen that the model-based *d*-axis current reference requires accurate information about machine parameters. Actually, robust flux-weakening methods are more favorable in real applications to overcome the parameter indeterminacy and variations. For the dynamic simulation, the flux-weakening method proposed in [121-122] is chosen in this work for its robustness and high utilization of the DC-bus voltage.

Figure IV.5 illustrates the generator-side control scheme with the flux-weakening algorithm for the MCT. The difference between the current controller output (voltage reference) and the converter output voltage (real machine voltage) is used to generate the i_d reference. The low-pass filter (LPF) is able of rejecting voltage signals high-frequency components.

The MTPA strategy is embodied in this control scheme. Indeed, i_d* is generated to maintain the operating points on the voltage constraints. Therefore, this control scheme is able to achieve the maximum active power (MAP) mode as at point *A* (Fig. IV.3) and the constant active power (CAP) mode at point *D* with minimum copper losses (Fig. IV.3). In the follows, we will use MAP and CAP to represent these two different power control modes at the generator over-base speed operation area.

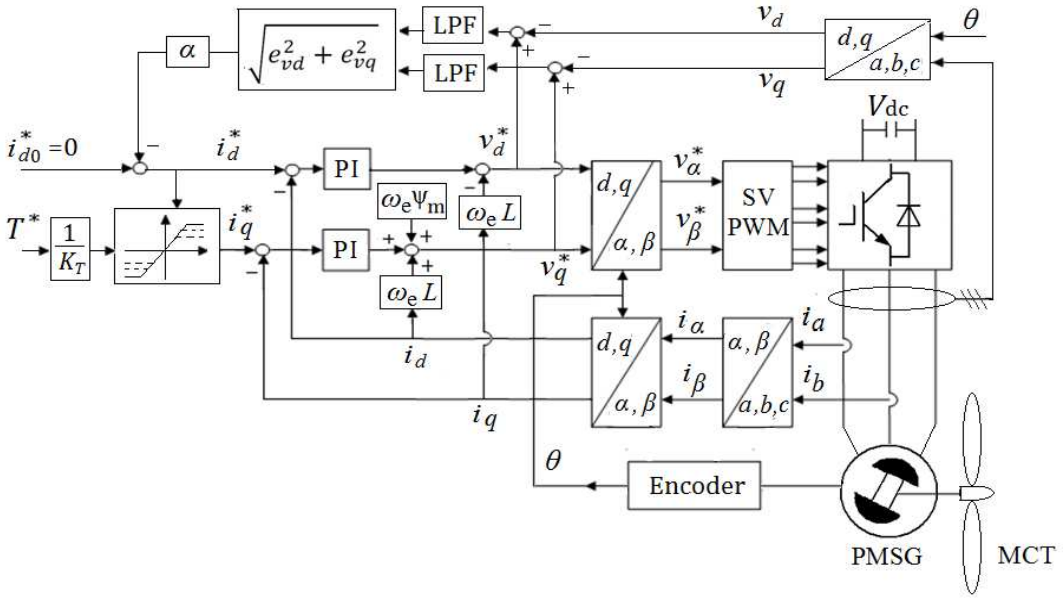

Fig. IV.5. Generator-side control scheme with flux-weakening strategy.

3.2 Speed Control and Torque Control

In this section, speed control and torque control strategies will be compared for limiting the MCT power to a constant power of 1.5 MW at over-rated marine current speed.

3.2.1 Speed Control Strategy

In speed control strategy, the rotor speed is directly controlled and the generator torque reference or the i_q reference signal is obtained from the output of speed loop controller. Supposing that the marine current velocity can be measured, the rotor speed reference can be obtained based on the C_p curve.

When the marine current speed is below the rated value, the modified MPPT with filter strategy presented in Chapter II will be used; and at the steady-state the rotor speed will be controlled to keep the turbine operating at λ_{opt}, thus keeping the turbine power coefficient C_p at the maximum value.

When the marine current speed is over the rated value, the MPPT mode must be changed to power limitation mode. In CAP mode, the generator power limitation can be fixed to a constant value (usually the generator rated power P_N). The proposed rotor speed reference at power limitation mode is shown by Fig. IV.6. In this scheme: the required C_p value is first calculated by the required power limitation (P_{limit}) and the marine current speed V based on the turbine power equation, the corresponding tip speed ratio is then obtained based on the right part of the C_p curve ($\lambda > \lambda_{opt}$). In this way, the generator power can be controlled to the

required limited value for a given over-rated marine current speed in the steady-state. The filter in this scheme is for avoiding rapid acceleration/deceleration, and it is especially necessary in case of swell disturbances as presented in Chapter II.

It should be noted that the speed control strategy relies on the information of marine current velocity and turbine power characteristics.

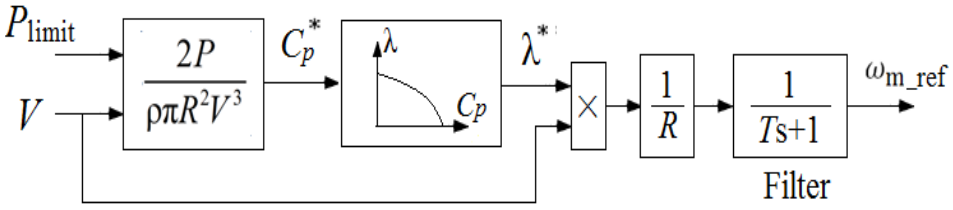

Fig. IV.6. Rotor speed reference at power limitation mode.

3.2.2 Torque Control Strategy

In order to directly control the generator power at power limitation stage, a torque control strategy can also be applied. At high current speed, the generator torque reference can be calculated with dividing the limitation power by the rotor speed ($T^* = P_{limit} / \omega_m$). In this way, the generator torque will be controlled to keep the generator power at the limitation value. Torque control strategy does not require the real-time marine current speed information and the detailed C_p curve decreasing information.

When the marine current speed is under the rated value, a torque-based MPPT strategy can also be applied. When the rotor speed is gradually driven by the high marine current speed to be over the nominal speed, the generator will be accelerated to over-base speed operation with the flux-weakening algorithm and the reference torque can be calculated by the constant power requirement. Equation (IV.14) illustrates the torque control reference used in this work.

$$T^* = \begin{cases} \frac{1}{2}\frac{C_{pmax}}{\lambda_{opt}^3}\rho\pi R^5\omega_m^2 & \text{if } \omega_m \le \omega_{mN} \\ \frac{P_{limit}}{\omega_m} & \text{if } \omega_m > \omega_{mN} \end{cases} \qquad \text{(IV.14)}$$

3.2.3 High Tidal Speed Case

The MCT is supposed to be installed at a proper depth under the sea-surface so that normal sea waves generated by local winds will have negligible influence on the MCT system. High speed marine currents would occur at large spring tides or under strong sea states (caused by swell waves or storms). In this section, the sea is supposed to be calm (without significant swell waves) and a non-disturbed high marine current speed driven by spring tides is considered. The concerned potential MCT site is supposed to have a tidal current velocity of 3.6 m/s at spring tides (for example: Raz de Sein off the coast of Brittany, France). Without power limitation control, the maximum extractable power at this peak tidal current speed would be over 2 MW for the MCT studied in this work.

In the simulations, the initial marine current speed is set at 2.8 m/s and rises to 3.6 m/s during 20 s to 70 s as shown in Fig. IV.7. After 47 s, the current speed rises over the rated value (3.2 m/s) and the power control mode with flux-weakening strategy will be applied. Although this current speed rising process is not very realistic (the tidal speed changes very slowly in reality because a tidal cycle may correspond to approximately half a day), it enables to test and compare the proposed control strategies at high spring tides. The turbine speed response, generator torque and power responses under the speed control and torque control strategies are illustrated respectively in Fig. IV.8 to IV.10. The system parameters can be found in [Appendix A] and the maximum generator torque is limited at 600 kN·m.

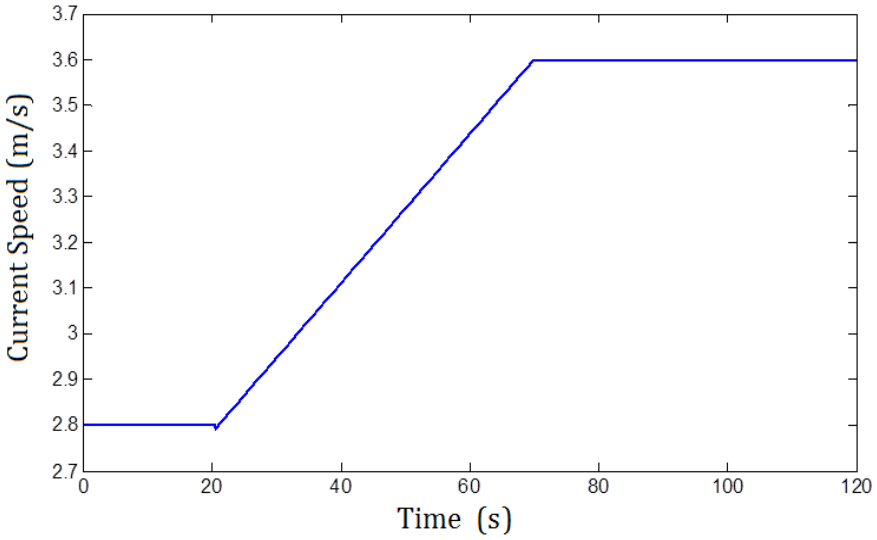

Fig. IV.7. High tidal current speed case.

It can be seen that after 45 s when the current speed rises over the rated value (3.2 m/s), the generator torque will reach to its maximum value (Fig. IV.9); and then the power limitation mode will be triggered in both speed control and torque control strategies.

The decrease of the generator torque with the rise of the rotor speed over the nominal rotor speed (24 rpm) shown in Fig. IV.8 and IV.9 indicates that the flux-weakening control works well in both power limitation control strategies.

From figures IV.9 and IV.10, the deeper drop of generator torque and power can be observed in speed control at the beginning of the over-rated current speed. This indicates that the speed control strategy tries to fast accelerate the MCT at power limitation mode based on the turbine power characteristics.

These results show that at steady-state when the marine current equals to the peak value (3.6 m/s), both control strategies can be used to limit efficiently the generator output power to the limitation value of 1.5 MW. During transient high current speed stage, only the torque control strategy enables the generator power to be well controlled at 1.5 MW; the speed control strategy fails to do that due to the generator power is not directly controlled.

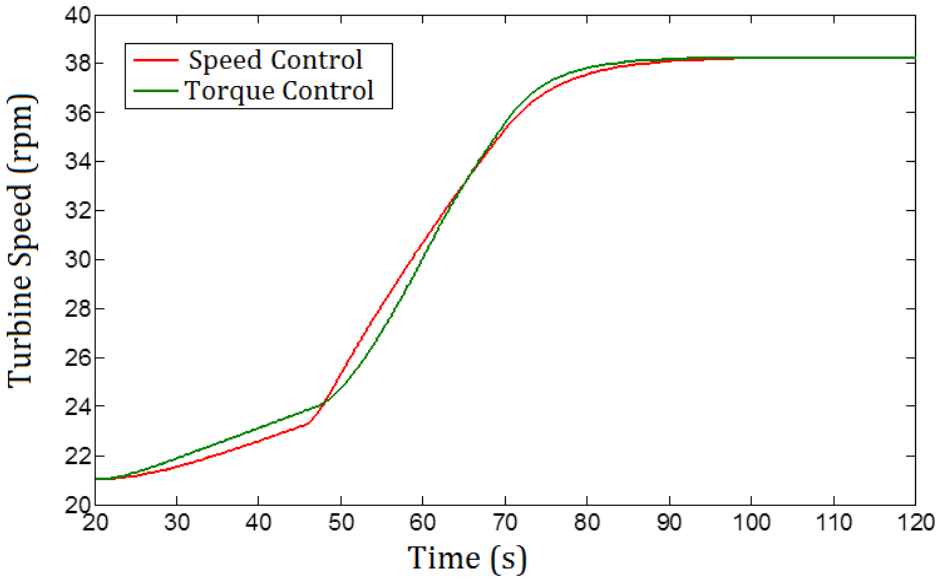

Fig. IV.8. Turbine speed responses at high tidal speed.

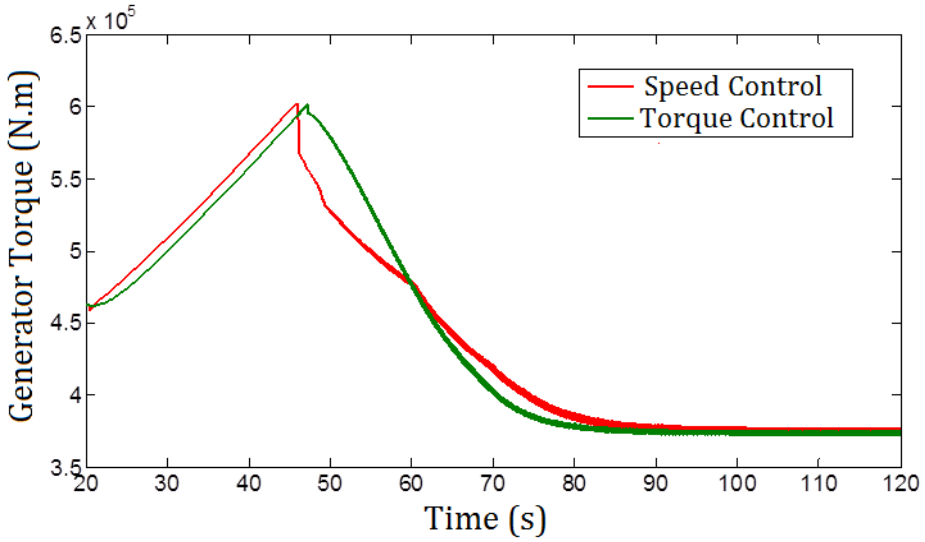

Fig. IV.9. Generator torque responses at high tidal speed.

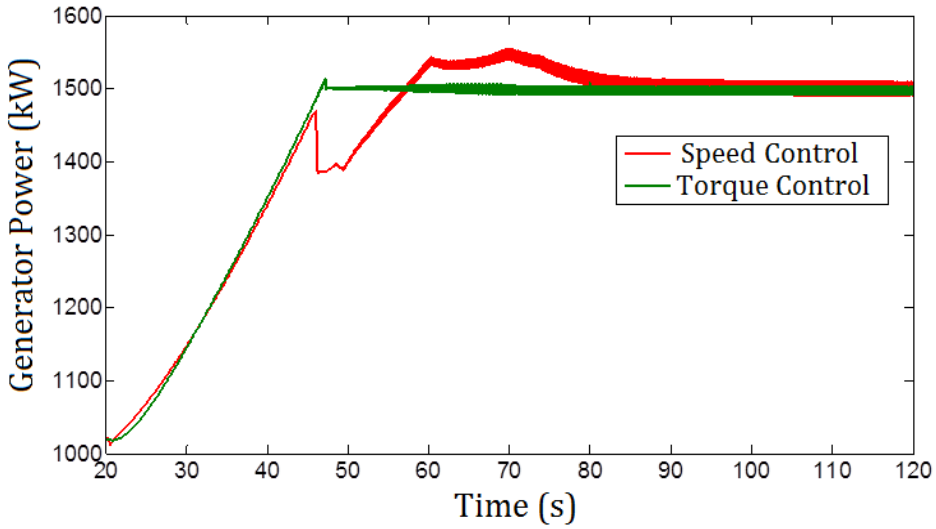

Fig. IV.10. Generator produced power responses at high tidal speed.

3.2.4 Swell Effect Case

In this part, the swell effect which may cause marine current speed to be over the rated value is taken into account. The medium-strong sea state with significant wave height H_s = 3 m and typical wave period T_p = 13.2 s is considered. This corresponds to typical sea state in the winter for the western coast of Europe [22]. The base tidal current speed is set to 2.8 m/s and the total marine current speed is calculated as the sum of the tidal current speed and the swell-induced current speed variations.

Figure IV.11 shows the marine current speed under swell effect. It can be seen that even the tidal current speed is fixed at 2.8 m/s, the total marine current speed will exceed the rated value of 3.2 m/s during some periods due to variations induced by swell effect.

Figures IV.12 and IV.13 show the turbine torque and generator torque responses with speed control and torque control respectively. The turbine torques in both control schemes seem quite similar; this indicates that the resulted turbine power coefficient is similar in the proposed speed control and torque control scheme. However, the generator torques are different due to different control algorithms: the speed control triggers the power limitation mode at every moment when the marine current speed is over the rated value regardless the real generator power, while the torque control triggers the power limitation mode only when the generator power reaches to the limited value.

Figure IV.14 compares the generator powers with the speed control and torque control strategies. It shows that torque control strategy is able to limit the PMSG power to 1.5 MW more accurately than the speed control strategy at high current speed considering swell effect.

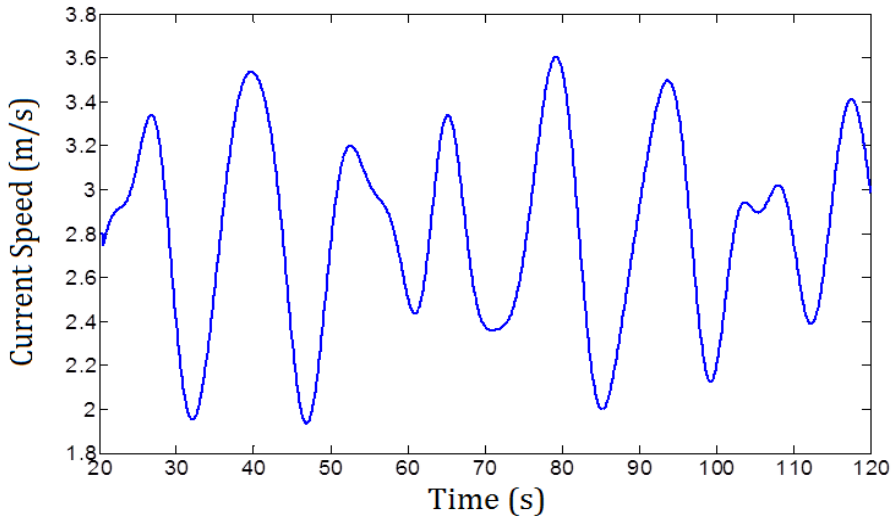

Fig. IV.11. Marine current speed under swell effect.

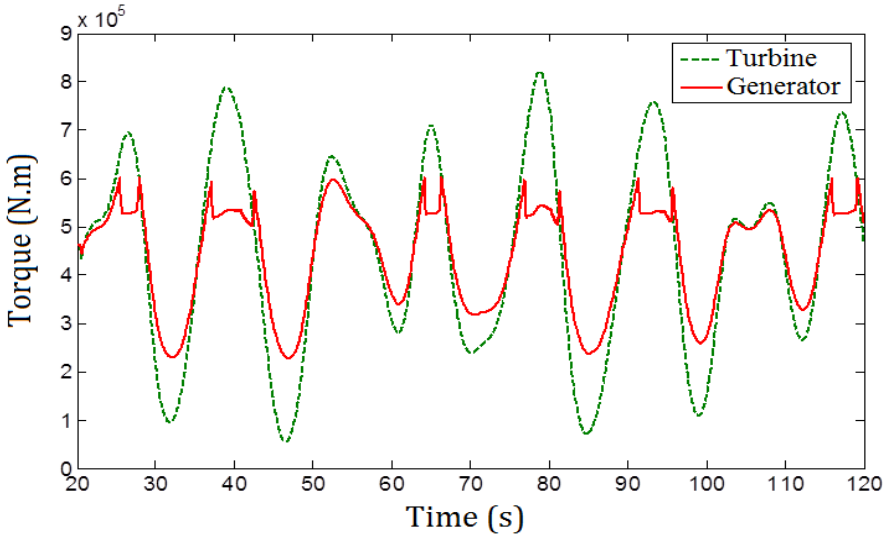

Fig. IV.12. Torque responses under swell effect with speed control strategy.

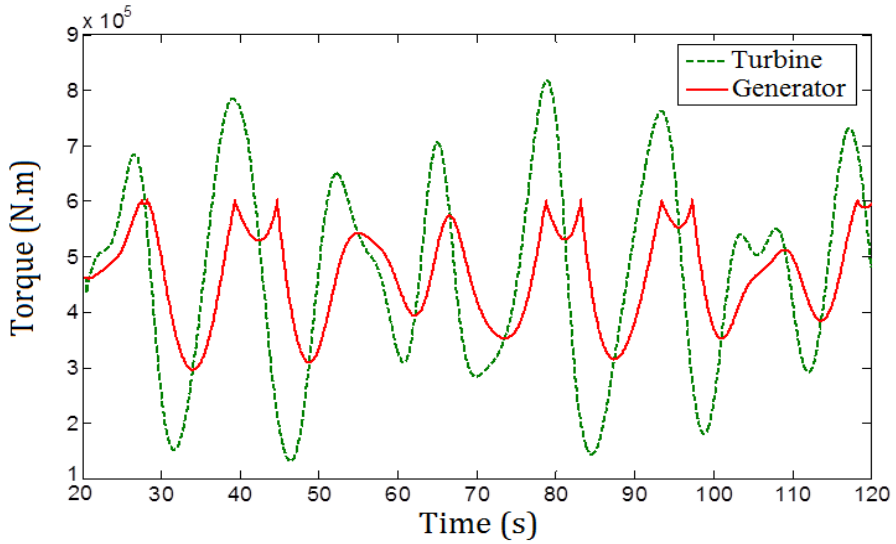

Fig. IV.13. Torque responses under swell effect with torque control strategy.

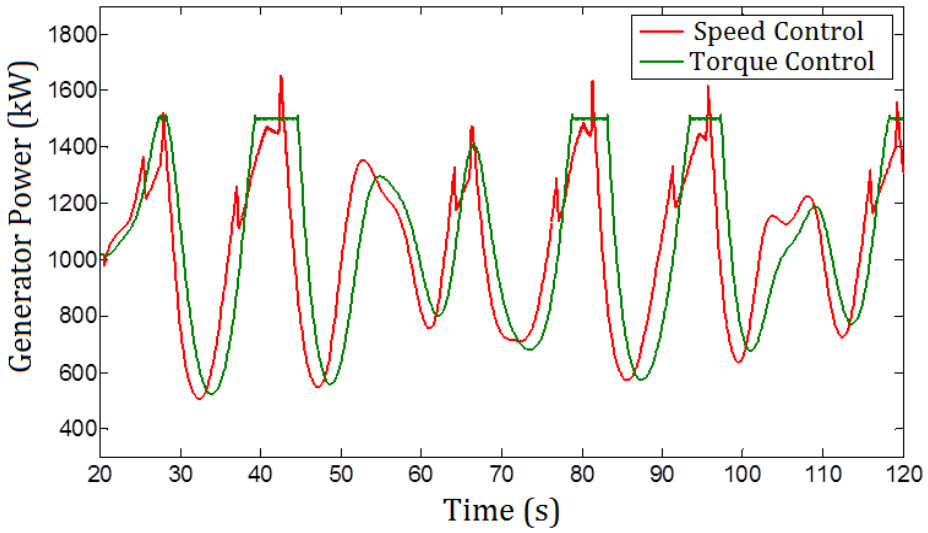

Fig. IV.14. Generator produced powers under the swell effect case.

3.3 Comparison of the CAP Mode and the MAP Mode

In the previous section, the torque control strategy has been proved more efficient to obtain a constant generator power at over-rated current speed. In this section, we will apply the torque control strategy and compare the CAP mode and the MAP mode at over-rated current speed. In § IV.2, from the generator operating characteristics steady-state analysis, it can be found that MAP mode can produce over-nominal power at the constant power range. In this section, dynamic simulations are carried out in the following to compare the two power modes in terms of speed/torque responses and system losses.

In the simulation of this section: for the CAP mode, i_q^* is calculated from the torque reference (second equation in (IV.14)) to keep the generator output power at its nominal value; and for

the MAP mode, i_q^* is set to $\sqrt{I_{max}^2 - i_d^{*2}}$ for maximizing the generator torque and output power. In both modes, i_d^* is decided by the flux-weakening control scheme to realize MTPA.

3.3.1 Under High Tidal Speed

The same high tidal current speed shown in Fig. IV.7 is used. The turbine speed response, generator torque, generator output power, and generator losses under the MAP and CAP modes are illustrated by Figs. IV.15 to IV.19 (green curve for MAP mode and red curve for CAP mode). The simulation results at 3.6 m/s are then summarized in Table IV.1.

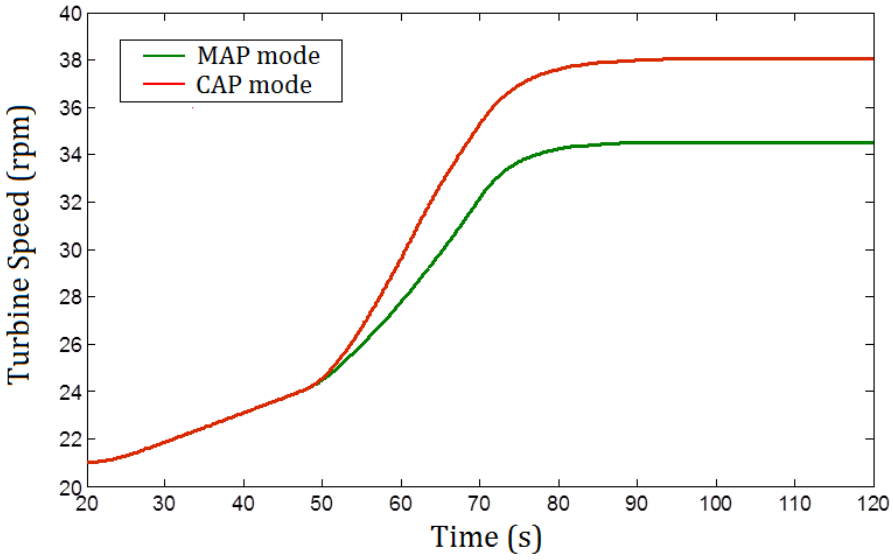

Fig. IV.15. Rotor speed responses at high tidal speed.

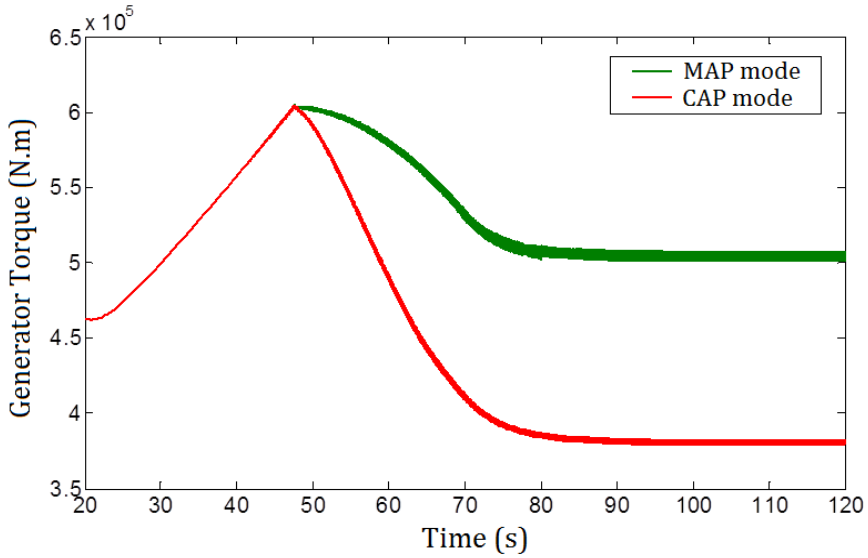

Fig. IV.16. Generator torque responses at high tidal speed.

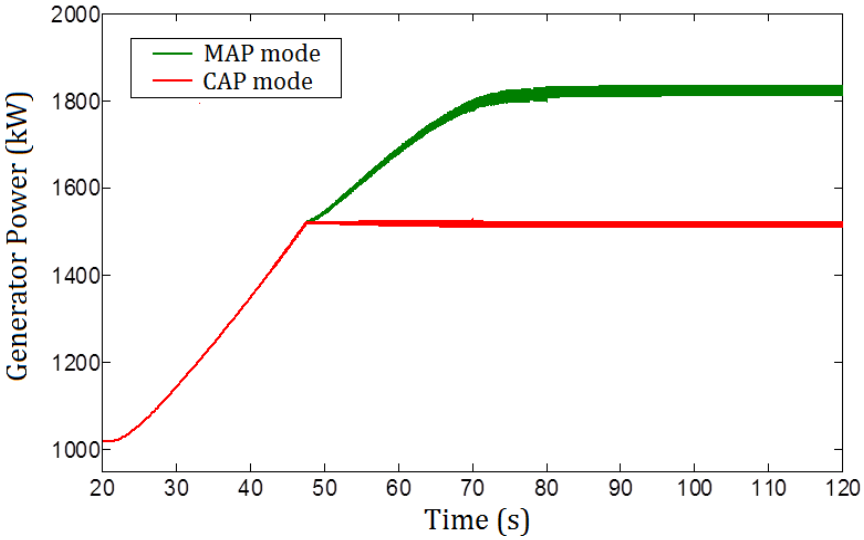

Fig. IV.17. Generator produced power at high tidal speed.

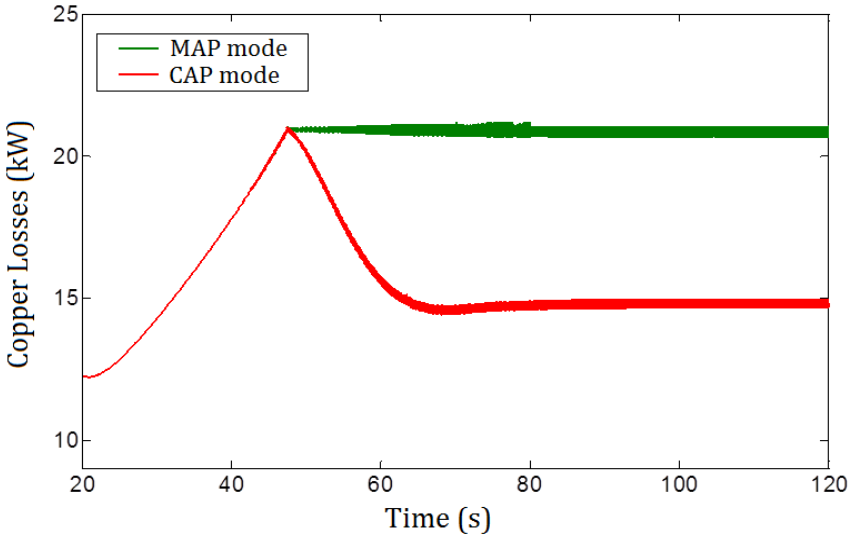

Fig. IV.18. Copper losses of the generator.

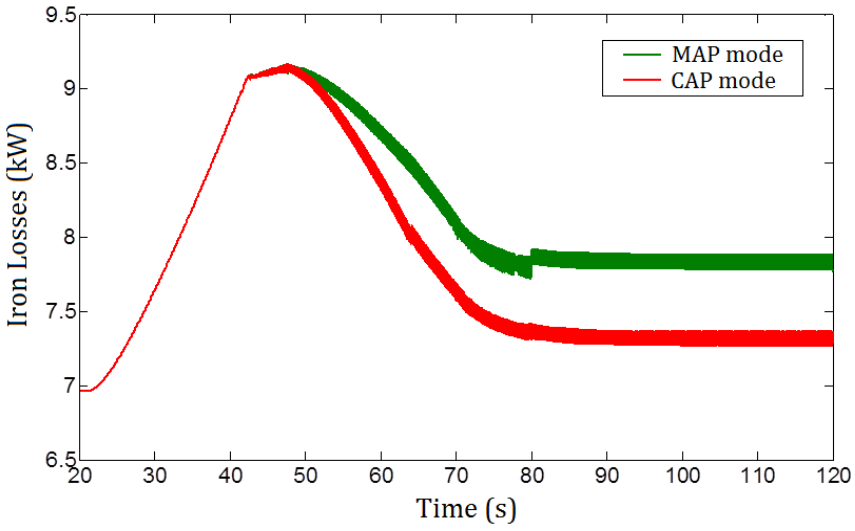

Fig. IV.19. Iron losses of the generator.

Table IV.1. Steady-State Performance at Current Speed of 3.6 m/s.

Control Mode	Rotor Speed (rpm)	Electromagnetic Torque (kN·m)	Electromagnetic Power (MW)	Copper Losses (kW)	Iron Losses (kW)
MAP	34.5	505	1.82	21	7.8
CAP	38	381	1.52	14.8	7.3

It can be seen that when the tidal current speed rises to the rated value of 3.2 m/s at about 47 s, the MCT rotor speed will reach the base value of 24 rpm (Fig. IV.15) and the generator torque will reach its maximum value about 600 kN·m. When the current speed rises over the rated value, the flux-weakening strategy will be triggered and the rotor speed will rise over the base speed. Figures IV.15 and IV.16 show that at over-rated marine current speeds, the CAP mode features lower generator torque to accelerate the turbine to a higher speed than the MAP mode. The reason is that the CAP mode requires reducing the turbine C_p value more than the MAP mode in order to keep the generator output power at the nominal value for a given over-rated current speed. While MAP mode aims to generate maximum torque and then maximize the generator output power at the over-base speed stage as shown in Fig. IV.17.

The generator copper losses (Joule losses) shown in Fig. IV.18 are calculated by

$$P_{\text{copper}} = \frac{3}{2}\left(i_d^2 + i_q^2\right) R_{\text{s}} \tag{IV.15}$$

The specific iron losses (W/kg) can be calculated based on the following common relationship

$$P_{Fe} = P_{Fe0}\left(\frac{B_{Fe}}{B_{Fe0}}\right)^a \left(\frac{f}{f_0}\right)^b \tag{IV.16}$$

where B_{Fe} and f are respectively the flux density and the field frequency in the stator iron core, and P_{Fe0} represents the iron losses per mass at the given frequency f_0 and the flux density B_{Fe0}. The typical value of a and b can be set as 2.2 and 1.5, respectively [129]. In a simplified approach, the fundamental harmonic of the flux density B_{Fe} can be considered to be proportional to V_s / f and (17) can then be rewritten as

$$P_{Fe} = P_{Fe0}\left(\frac{V_s}{V_0}\right)^{2.2}\left(\frac{f}{f_0}\right)^{-0.7} \quad \text{(IV.17)}$$

In this work, the typical point for calculating the iron losses is chosen at the base point ($V_0 = V_{max}$ and $f_0 = \omega_{eb}/2\pi$) and the corresponding P_{Fe0} is 2.5 W/kg. The total iron mass in the stator core of the 1.5 MW generator is estimated to be about 4 tons [128]. The iron losses calculation results under both CAP and MAP modes are shown in Fig. IV.19.

As analyzed in the previous section, the MAP mode operates on the intersection points of voltage-current limitation circles and maintains the stator current at its maximum magnitude I_{max}, while the CAP mode operates at a smaller stator current. The results from Fig. IV.18 confirm that the generator copper losses are kept at the maximum value by the MAP mode, and the CAP mode enables to greatly reduce the copper losses at over-rated marine currents. The iron losses difference is not very big because both modes operate at V_{max} with the MTPA strategy during the flux-weakening operation. The iron losses under MAP mode are a little higher than under CAP mode. This indicates that CAP mode reduces more flux density in the stator core (the value of V_s / f is lower) than MAP mode.

From Table IV.1, it can be seen that at steady-state with a marine current speed of 3.6 m/s, the MAP mode will accelerate the turbine to 1.45 times of the nominal speed and produce 19.7% power more than the nominal value; while the CAP mode will accelerate the turbine to 1.58 times of the nominal speed and limit the generator power to the nominal power of 1.52 MW. Compared to the MAP mode, the generator copper losses are reduced by 29.5% and the iron losses are reduced by 6.4% with the CAP mode at steady-state under a marine current speed of 3.6 m/s. Figure IV.20 shows the calculation results of the generator copper losses and iron losses under different marine current velocities. Therefore, it can be concluded that CAP mode can have smaller generator losses than MAP mode at over-rated marine current speed.

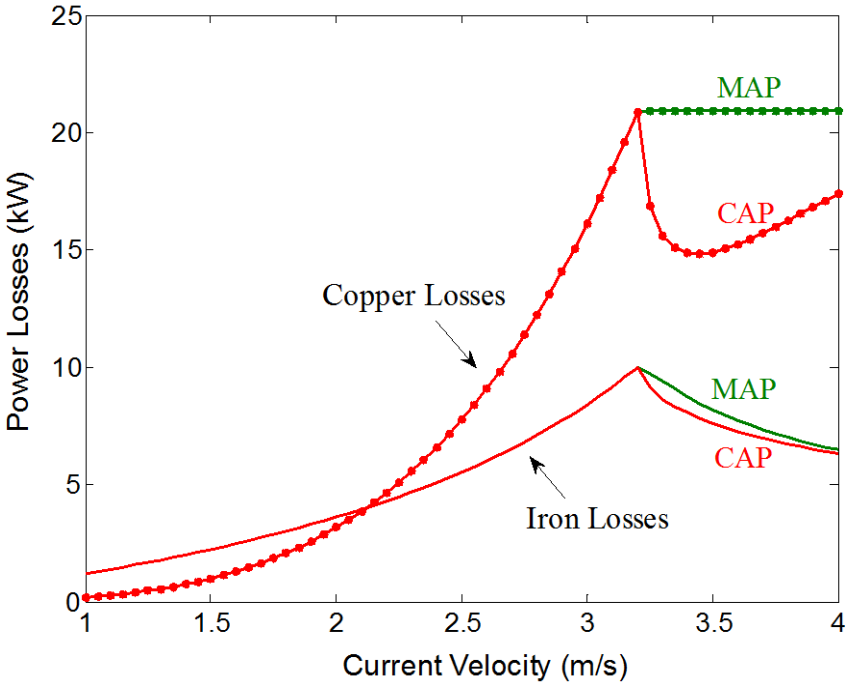

Fig. IV.20. Generator losses under different current velocities.

3.3.2 Under Swell Effect

For the over-rated current speed caused by swell effect (shown in Fig. IV.11), the rotor speed and generator power responses in MAP and CAP modes are illustrated by Fig. IV.21 and Fig. IV.22 respectively.

It can be seen that under swell effect, the marine current speed is fluctuating and there is no steady-state for the turbine. The turbine will not be accelerated to the same operating points as in steady-state cases, but the CAP mode will still accelerate the rotor speed a little higher than in the MAP mode to limit the generator power to its nominal value. In this case, the MAP can produce about 4% power more than the CAP mode during the main flux-weakening stages (40-45 s, 78-83 s and 93-98 s) as shown in Fig. IV.22.

Figure IV.23 compares the *d-q* currents with the MAP and CAP modes under swell effect. Lower i_q (and generator torque) can be noticed in the CAP mode than in the MAP mode. The difference of *d*-axis currents is very small because the CAP mode operates at a little higher speed than the MAP mode. In this case, the CAP mode has about 8% less copper losses than the MAP during the main flux-weakening stages.

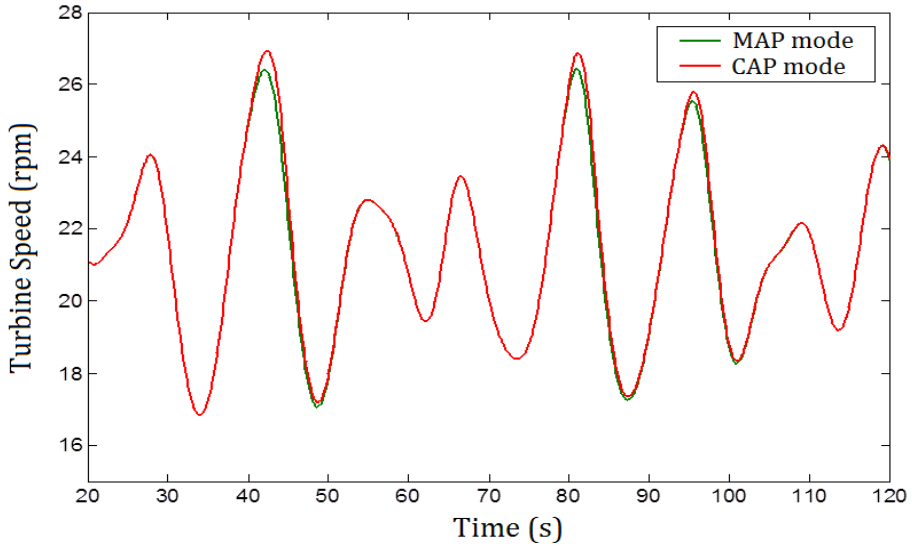

Fig. IV.21. Rotor speed responses under swell effect.

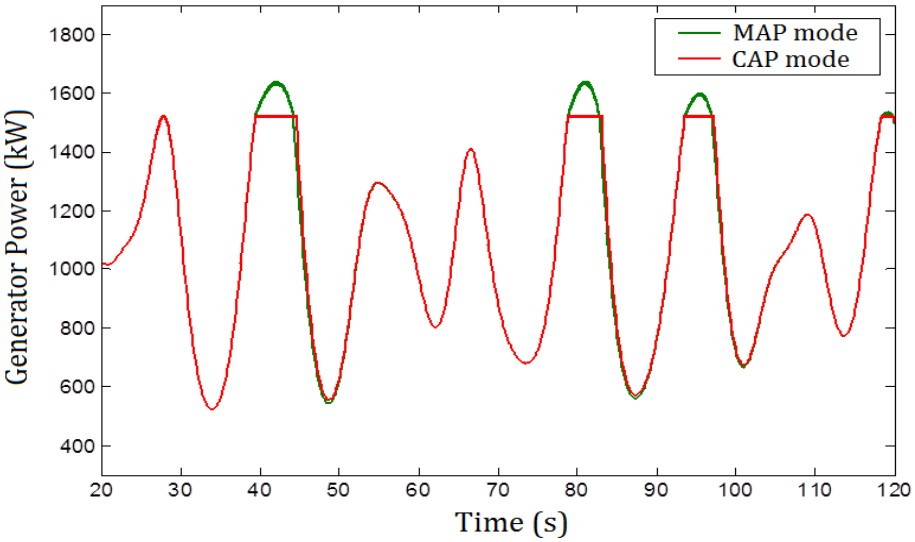

Fig. IV.22. Generator produced power under swell effect.

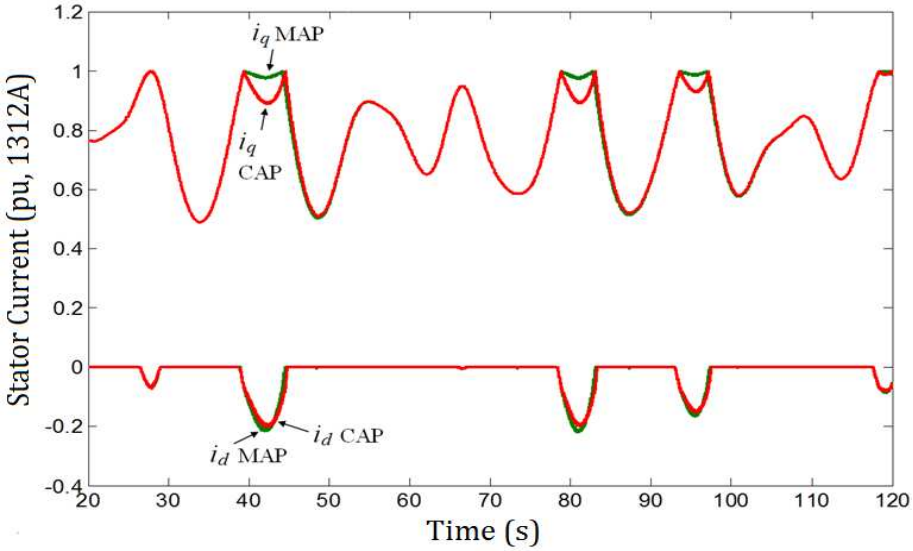

Fig. IV.23. Generator stator currents in the *d-q* axis.

IV.4 DISCUSSIONS ON GENERATOR PARAMETERS

The MAP and CAP modes are effective to operate in the constant power range; but for a rotor speed over this range the generator output power will decrease rapidly below the nominal value as analyzed in Section VI.2. Therefore, it is important to study the requirements of the generator parameters for an expected constant power range.

In this section, generator base speed ω_{eb}, nominal torque T_{eN} and the maximum stator voltage V_{max} are fixed and we therefore focus on the parameter requirements of stator inductance and rotor permanent magnet flux.

Figure IV.24 shows that the generator nominal power angle φ, defined at the base speed, is mainly decided by the ratio between L_sI_{max} and ψ_m with the MTPA strategy. From equations (IV.12) and (IV.13) in Section VI.2, it can be seen that the flux-weakening range and the constant power range strongly depend on L_sI_{max} and ψ_m. For an expected constant power speed ratio (CPSR), the required minimum values for L_sI_{max} and L_s can be calculated as follows.

$$(L_sI_{max})^* = \frac{V_{max}}{\omega_{eb}}\sqrt{\frac{Ratio\_con-1}{2Ratio\_con}} \tag{IV.18}$$

$$L_s^* = (L_sI_{max})^* \frac{3n_p\psi_m^*}{2T_{eN}} \quad \frac{3n_p(L_sI_{max})^*\sqrt{\left(V_{max}/\omega_{eb}\right)^2-\left(L_sI_{max}\right)^{*2}}}{2T_{eN}} \tag{IV.19}$$

Figure IV.25 shows the calculation results: the $(L_sI_{max})^*$ and L_s^* values are normalized by L_sI_{max} and L_s (values corresponding to [Appendix A]) respectively to illustrate the parameter change requirements according to different CPSRs. The generator parameters used in this work enable the machine to have a CPSR of 2.4 with a nominal power factor about 0.84.

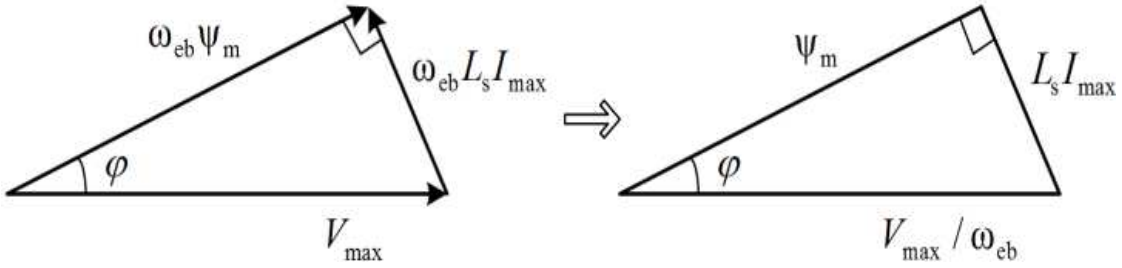

Fig. IV.24. Generator parameters at base speed (neglecting the stator resistance).

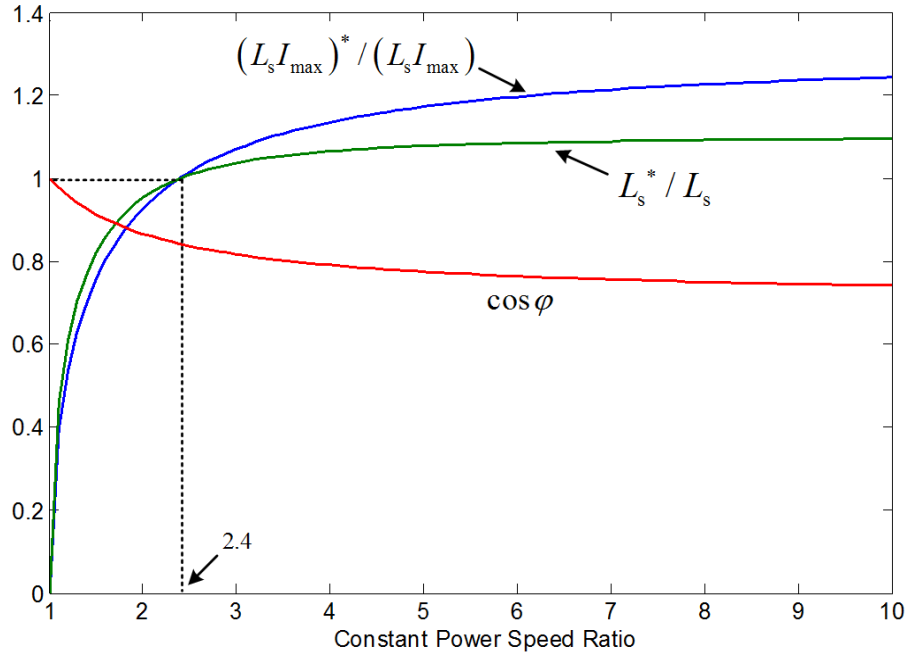

Fig. IV.25. Parameters corresponding to required CPSR.

From Fig. IV.25, it can be seen that a higher CPSR requires large stator inductance and L_sI_{max} values thus reducing the nominal power factor. For example, stator inductance value should increase by 8.3% to obtain a CPSR of 5 but the resulted nominal power factor will be reduced to 0.77.

Smaller stator inductance can improve the generator nominal power factor and then reduce the *V-I* rating of the generator-side converter, however the CPSR will also be decreased and the machine over-base speed operable area will be limited. For example, if the inductance is designed as 1.0 mH (16.7 % smaller than L_s = 1.2 mH used in this work), then the generator will have a nominal power factor of 0.9 but with a small CPSR of 1.6. Figure IV.26 shows the generator operating points with CPSR = 1.6. The dotted-lines illustrate the turbine power characteristics. In this case, both MAP and CAP modes can be applied when the marine current speed is between 3.2 m/s and 3.6 m/s. However, the MCT system can not produce power at a current speed of 4.0 m/s due to small CPSR and low flux-weakening capability of the generator.

Figure IV.27 shows the case with generator parameters set in the simulation system of this work. It can be seen that with CPSR = 2.4, the generator enables the MCT system to produce power for a wide range of over-rated marine current speeds. At a current speed of 4.0 m/s, the MCT system will still be able to produce 1.77 MW with the MAP mode or 1.52 MW with the CAP mode.

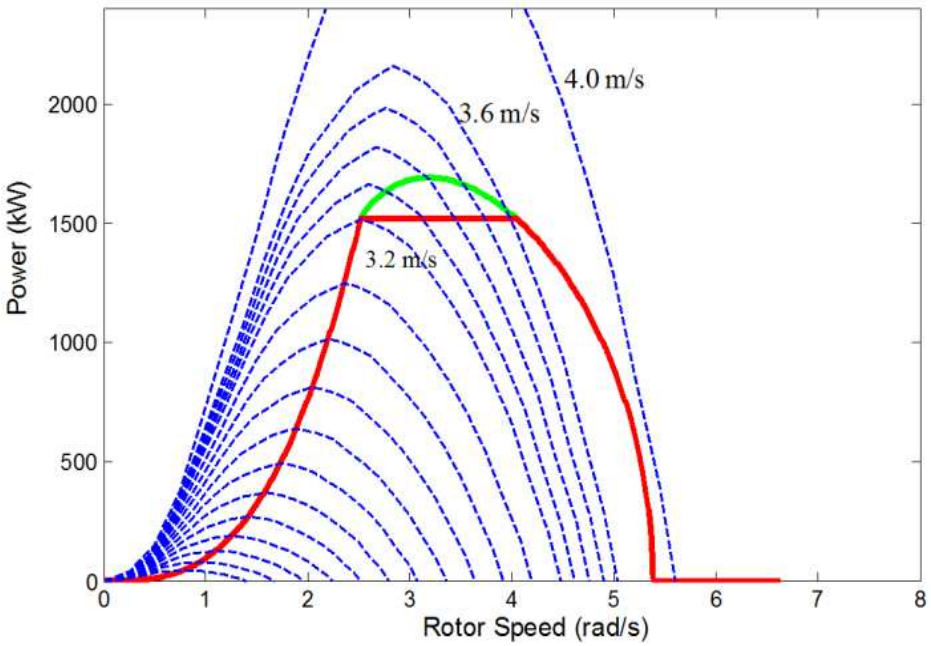

Fig. IV.26. Generator power characteristics with CPSR = 1.6.

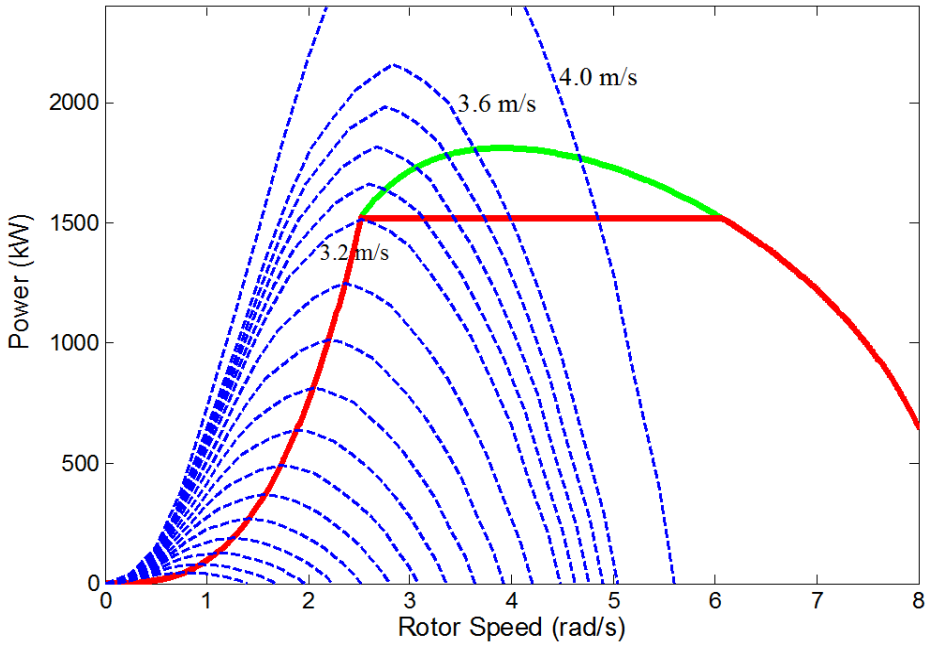

Fig. IV.27. Generator power characteristics with CPSR = 2.4.

It should be noticed that the flux-weakening operation is on the decreasing slope of the C_p ($\lambda > \lambda_{opt}$) curve to reduce the turbine power coefficient during over-rated current speeds. Therefore, the turbine C_p characteristic can also influence the expected generator CPSR for non-pitchable MCTs. The C_p curve used in this paper has a common shape for three-blade turbines [130]. Increasing turbine blade number could have sharper C_p and better performance at high current speeds. However, flatter C_p can be found in two-blade turbines or when the

blade chord and twist distribution is designed to keep high C_p value for a wide TSR range [131-132]. In this case, it would require large CPSR for the generator to cope with the turbine at over-rated marine current speed.

Figure IV.28 shows the case of a turbine with a flatter C_p (slower decreasing slope). The same generator is used for comparison. It can be seen that for a marine current speed of 3.6 m/s, the turbine should be accelerated to 6.5 rad/s (2.6 times of the nominal speed of 2.52 rad/s) at the steady-state. This speed exceeds the CPSR of the studied generator and the MCT system will produce lower power than the nominal power. If this flatter C_p turbine is supposed to be installed in a site with peak marine current speed higher than 3.6 m/s, then it seems that a generator with larger CPSR will be needed to guarantee the existence of steady-state operating points to have good transient behavior and to reduce the mechanical constraints at high operating speed.

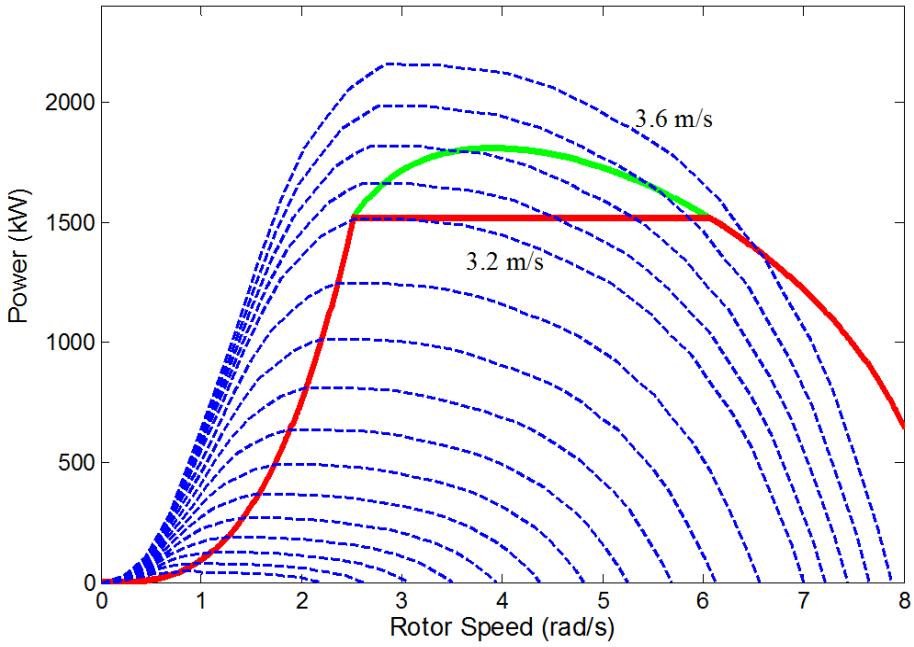

Fig. IV.28. Generator power characteristics with flatter C_p.

IV.5 CONCLUSION

This chapter has investigated power control strategies for the PMSG-based MCT system with non-pitchable blades at over-rated current speed. Flux-weakening control strategy has been proposed to accelerate the MCT over the nominal speed at high marine current speed. Two power control modes (the maximum active power mode and the constant active power mode)

on the generator constant power range have been investigated. In this context, a torque control scheme with a robust flux-weakening algorithm has been proved to be capable of controlling the MCT power efficiently at over-rated current speed. High speed marine currents caused by high tidal current speed and swell effect have been both considered.

The achieved simulation results have confirmed that at over-rated current speed, the CAP mode enables to limit the generator produced power to the nominal value with lower losses while the MAP mode enables to produce over-nominal power (better use the generator-side converter *V*-*I* rating) but with high generator losses. The parameter requirements of the non-salient PM machine for expected constant power speed ratio are provided. The compromise between high power factor and large constant power range should be noticed for appropriate generator parameter design. For turbines with flat C_p curve, wide constant power range will be required to maintain the nominal power output capability at high current speed.

Conclusions & Perspectives

This PhD thesis has focused on some important challenges which megawatt-level marine current turbine systems will face in the near future. Firstly, up-to-date information on megawatt-level marine current turbine technologies and demonstrative farm projects has been presented. Two main power fluctuation phenomena can be identified in marine current generation systems. Potential installation sites are usually with shallow sea depth (about 30-50 meters); and in this case, the swell waves can have non-negligible influence on the marine current speed and can cause short-time period power fluctuations in the MCT output power. For long-time period, the MCT power variations are related to the tidal phenomenon; and during some low current speed periods no power can be produced by the MCT. Therefore, a review of energy storage system technologies dealing with the power fluctuation phenomena has been carried out in the first chapter. This thesis has proposed to use supercapacitors for compensating swell-induced power fluctuations and to use flow battery for enabling the turbine system to follow daily load-demand even under periodic tidal current speed variations. Concerning the fact that several megawatt-level marine current turbine projects adopt fixed-pitch blade solutions, original power limitation strategies based on flux-weakening algorithm for controlling the PMSG-based turbine system at

over-rated marine current speed have also been carried out. A 1.5 MW PMSG-based MCT system has been considered. The main conclusions are listed as follows:

- The era of megawatt-level MCTs has arrived. Concerning the two identified power fluctuation phenomena in marine current generation systems, hybrid energy storage systems should be considered to improve the system power performance.
- On short-time scale, swell effect could cause large power fluctuations (with periods of 10s ~ 20s) in the generator output power under basic speed-reference MPPT control. In this case, a modified MPPT has been proposed to reduce the generator power fluctuations. In a second step, a supercapacitor bank has been integrated in the system for injecting a smoothed power into the grid-side. The simulation results have clearly shown the effectiveness of the proposed control strategy and the reasonable sizing of the supercapacitor bank.
- Flow battery can be chosen for daily power management of a hybrid MCT/battery/diesel system. For the dominant MCT power supply case, a large battery is required to balance the supply and demand and DG consumption can be limited only for charging the battery. For the Ouessant Island case (where DG is the main supply source), the battery can be reasonably reduced in size but its use is still vital important for maintaining the MCT MPPT performance and for respecting the DG operation constraints.
- For over-rated current speed, a robust flux-weakening has been proposed to control the MCT output power at the nominal value (CAP mode) or over-nominal value (MAP mode). The joint operation characteristics of the turbine and the generator have shown that a compromise between large constant power range (over the base speed) and the machine nominal power factor should be considered in the generator parameter design.

The perspectives following the above developments can be mainly divided into two aspects: fault-tolerant control strategies and turbine farm simulations. Indeed, some improvements should be considered in future works:

- Include fault-tolerant control strategies. For a grid-connected system, how to maintain a stable operation in case of grid faults (low voltage ride through, frequency distortion) is very important. The ESS can also be considered in facilitating the system fault-tolerant capability;
- Extend the single MCT case of this thesis to a MCT farm study. This could also include the comparison of distributed or centralized ESS configurations;
- Ocean compressed air energy storage system would be interesting for MCT farms over 10 MW capacities (considering the high battery cost). This point can be further investigated.

Finally, it would be interesting to apply detailed converter models for fault-tolerant study and also for verifying the limits of the average-value converter models applied in this thesis.

French Abstract

Modélisation et Commande de la Puissance d'un Système Hydrolien avec Stockage d'Energie

I. INTRODUCTION

Face au problème des émissions de gaz à effet de serre et au risque d'épuisement des sources d'énergies fossiles, les énergies renouvelables continueront à croître rapidement dans les prochaines décennies pour assurer un développement durable de la société. En ce qui concerne les énergies marines renouvelables, une des plus prometteuses est l'énergie des courants marins. Le principe est similaire à la production d'énergie éolienne. La densité de puissance élevée résultant de la masse volumique de l'eau et la prévisibilité liée aux caractéristiques astronomiques des marées font de l'énergie des courants marins une ressource particulièrement attractive et avantageuse. En Europe, les projets de générations hydroliennes (à l'échelle du mégawatt) visent la construction de plusieurs parcs hydroliens de démonstration. Ces parcs pourront fournir de l'électricité pour les zones côtières et pour les îles isolées au cours de prochaines années.

Mais les fluctuations de puissance de courte durée (liées à la houle) et de longue durée (liées aux variations périodiques de la vitesse du courant de marée) détériorent la qualité de la puissance produite et posent des problèmes d'équilibre entre production et consommation. A partir du développement d'un modèle dynamique de la chaîne de conversion hydrolienne, cette thèse a pour objectifs d'étudier l'utilisation de systèmes de stockages d'énergies visant, d'une part, à améliorer la qualité de la puissance électrique injectée au réseau et, d'autre part, à faciliter l'équilibre entre production et consommation. Le système étudié est basé sur une turbine à pas fixe et une génératrice synchrone à aimants permanents. Cette technologie est une des solutions retenues par les constructeurs pour augmenter la fiabilité du système qui est un point clé dans les applications offshores sous-marines. C'est pourquoi ce travail comporte également une étude des stratégies de commande possible pour implanter une stratégie de contrôle avec limitation de puissance pour une turbine à pas fixe.

Dans **le premier chapitre** de ce mémoire de thèse, un état de l'art sur les hydroliennes de puissance de l'ordre du mégawatt et sur les diverses technologies de stockages d'énergies est présenté.

Le deuxième chapitre de la thèse porte sur la modélisation de la houle et sur les stratégies de lissage de puissance avec supercondensateurs pour un système hydrolien connecté au réseau.

Le troisième chapitre propose d'utiliser une batterie à circulation (flow battery) pour faciliter la gestion quotidienne de la puissance de l'hydrolienne dans le contexte d'un réseau électrique isolé. Un système hybride hydrolien/batteries/diesel est étudié.

Enfin, **le quatrième chapitre** analyse la stratégie de défluxage (au niveau de la génératrice synchrone à aimants permanents) pour contrôler et limiter la puissance du système pendant les périodes de fort courant marin.

Dans ce résumé, chaque section présente d'une manière succincte les principaux éléments de chaque chapitre.

II. ETAT DE L'ART SUR LES SYSTEMES DE STOCKAGES D'ENERGIES POUVANT ETRE ASSOCIES AUX HYDROLIENNES

II.1 Problématique de l'hydrolien

La puissance des courants marins exploitables avec les technologies actuelles est estimée à environ 75 GW dans le monde et 11 GW en Europe. Avec une puissance estimée à environ 3.4 GW, la France possède le deuxième potentiel européen [1]. Le principe de récupération de l'énergie des courants marins est semblable à celui de l'énergie éolienne ce qui permet a priori de transposer un certain nombres de choix technologiques d'un contexte à l'autre. Les divers projets hydroliens ont été développés dans le monde dans les dernières années [5-8]. Actuellement, les hydroliennes à axe horizontal apparaissent comme la solution la plus utilisée pour atteindre une capacité de puissance supérieure à 500 kW.

Plusieurs technologies de turbines à axe horizontal ont été développées et choisis par les communautés industrielles pour réaliser des fermes pilotes avant la commercialisation finale. Ces projets pilotes illustrent les évolutions des technologies de grandes hydroliennes qui fourniront de l'électricité aux zones côtières ou aux îles isolées dans les prochaines années. Le Tableau I.1 résume les informations principales sur ces projets de fermes pilotes et leurs dates de mise en service prévisionnelles.

Tableau I.1. Les fermes hydroliennes pilotes [1], [9-11].

Partenaires	Localisation	Type d'hydrolienne	Nombre d'hydrolienne	Capacité Totale (MW)	Date prévisionnelle
DCNS, EDF	Paimpol Bréhat	OpenHydro	4	2	2014
MeyGen	Pentland Firth (Écosse)	HS 1000 or AR 1000	6	6	2015/2016
MCT, Siemens	Kyle Rhea (Écosse)	SeaGen S	4	8	2015

	Anglesey (Pays de Galles)	SeaGen S	5	10	> 2015
Andritz Hydro Hammerfest	Sound of Islay (Écosse)	HS 1000	10	10	> 2015
GDF Suez, Eole Generation	Raz Blanchard	Voith Hytide	3~6	3~12	2016
	Fromveur	Sabella	> 4	> 4	2016

Pour les technologies d'hydroliennes présentées dans ce tableau, le point commun est qu'elles sont toutes basées sur des turbines à axe horizontal; il apparaît également qu'un nombre significatif de projets adopte des hélices à pâles fixes pour la turbine.

L'énergie hydrolienne provient de l'énergie cinétique de l'eau de mer. En effet, pour une turbine située perpendiculairement à la direction de la vitesse des courants marins, la puissance récupérée est:

$$P = \frac{1}{2}\rho C_p A V^3 \quad (1)$$

où ρ est la densité de l'eau de mer ; C_p est le coefficient de puissance de la turbine ; A est la surface de turbine perpendiculaire à la direction du courrant marin ; V est la vitesse du courant marin. Pour des conceptions typiques d'hydrolienne, la valeur de C_p optimale pour un fonctionnement normal est estimée être de l'ordre de 0.35 à 0.5 [3]. Pour suivre la courbe de puissance maximale (MPPT), la vitesse du rotor de turbine doit être contrôlée pour maintenir C_p à sa valeur optimale. Dans ce cas, la puissance produite par l'hydrolienne est proportionnelle au cube de la vitesse du courant marin. La puissance produite par l'hydrolienne change alors considérablement lorsqu'il existe des variations non négligeables dans la vitesse du courrant marin.

Deux types principaux de fluctuations de puissance peuvent être identifiés pour l'hydrolienne. Sur une grande échelle de temps, la puissance générée varie avec une période d'environ 6 à 12 heures en fonction du phénomène de marée. En Europe, la marée semi-diurne est dominante et la direction des courants de marée change environ tous les 6 heures.

Sur une petite échelle de temps, la puissance générée peut fluctuer sur une période de 10 à 20 secondes lorsque le courant est influencé par l'état de mer à la surface (houles longues). Les

données de la houle mesurées aux *Pierres Noires* sont présentées de manière synthétique à la Fig. I.7 [22]. Elles donnent une idée des valeurs typiques de houle sur la cote occidentale française. Si l'on considère que les houles les plus perturbatrices correspondent aux états de mer tels que $10\,\mathrm{s} < T_p$ et $2\,\mathrm{m} < H_\mathrm{s}$, on peut remarquer que cela concerne environ 71% des données. La Figure I.8 donne un exemple de la puissance produite par une hydrolienne pendant une journée. Lorsque la houle est considérée (Fig. I.8b), des fluctuations de courtes périodes se manifestent dans la puissance produite par l'hydrolienne.

L'intégration des énergies renouvelables qui sont variables et fluctuantes au réseau électrique n'est pas favorable à la stabilité du réseau électrique. Les systèmes de stockages d'énergies (ESS) sont considérés comme une bonne solution pour lisser les fluctuations de puissance et améliorer la stabilité du système [23-24]. Pour la génération hydrolienne, deux types d'ESS différents peuvent être envisagés pour compenser les fluctuations lentes (marées) et rapides (houle) [25].

II.2 Etat de l'Art sur les Systèmes de Stockages d'Energies

II.2.1 Batteries

Les principaux avantages et inconvénients des technologies de batteries sont résumés (dans le Tableau I.2) ci-dessous :

Les batteries plomb-acide sont matures et ont un coût relativement bas. Cependant, la densité d'énergie est faible (typiquement 30Wh/kg) et leur durées de vie sont généralement comprises entre 1200 et 1800 cycles [26]. Le cycle de vie est également affecté par la profondeur de décharge [27]. Les batteries à base de nickel ont une durée de vie plus longue que les batteries plomb-acide, mais leur coût est beaucoup plus élevé [28].

Les batteries lithium-ion ont la puissance et la densité de l'énergie les plus élevées par rapport aux autres technologies de batteries, mais leur coût est également plus élevé [32]. Elles sont utilisées dans les applications ou l'espace est limité tels que les produits électroniques pour grand public (smartphone, tablette, etc.). Pour la demande de grande capacité (de l'ordre du mégawatt), elles ne conviennent que pour des applications à faible profondeur de décharge [34].

Les batteries de type sodium-soufre (NaS) sont basées sur une technologie relativement nouvelle de batterie à haute température, fonctionnant à plus de 300 °C. La densité de l'énergie est assez haute pour cette technologie, mais il faut chauffer les batteries même en

mode de maintien (standby) [36]. La technologie à circulation de type « flow » batterie (batterie à circulation d'électrolyte) apparaît très appropriée pour le stockage d'énergie pendant des heures en raison de sa capacité de décharge profonde, de sa longue durée de vie et de sa souplesse de dimensionnement en termes de rapport puissance/énergie. La densité d'énergie des batteries à circulation est moins élevée que les précédentes, mais le coût est très favorable en raison de la durée de vie élevée [30], [37-38].

On peut donc conclure que les batteries à circulation et les batteries NaS sont les deux meilleurs candidats parmi les technologies de batteries pour des applications à l'échelle du MW et du MWh. Par rapport aux batteries NaS, les batteries à circulation d'électrolyte ont une durée de vie plus longue, mais apparaissent plus complexes. A l'inverse, les batteries à circulation d'électrolyte sont plus faciles à utiliser, car elles n'ont pas besoin d'être maintenues à une température élevée. Avec des installations appropriées, les batteries à circulation d'électrolyte et batteries NaS semblent donc être les deux technologies de batterie les plus appropriées pour lisser les variations de puissance à long terme (dynamique des courants de marée) dans les systèmes hydroliens.

II.2.2 Volant d'Inertie et Supercondensateurs

Pour les fluctuations de court terme (dynamique de la houle, fluctuations à l'échelle de la seconde), deux technologies de stockage d'énergie apparaissent intéressantes: les volants d'inertie et les supercondensateurs.

Un volant d'inertie est basé sur un disque tournant qui permet de stocker l'énergie cinétique. La quantité d'énergie stockée dans un volant d'inertie dépend du carré de la vitesse de rotation, l'augmentation de la vitesse favorisant la densité massique [39-41]. Les principaux avantages de cette technologie sont une grande capacité de cyclage (plus de 10^5 cycles) et une densité de puissance élevée. L'un des principaux inconvénients des volants d'inertie est l'auto-décharge qui peut atteindre plus de 20% par heure [43]. Un autre point faible est le prix élevé du système à cause de l'utilisation de matériaux de haute technologie et du faible volume de production à grande échelle.

Les supercondensateurs travaillent de la même manière que les condensateurs classiques, mais ils sont caractérisés par une capacité beaucoup plus élevée (de l'ordre du kF) [23]. Cette technologie est favorable pour absorber ou injecter une forte puissance pendant une courte durée (quelques secondes). Les applications courantes des supercondensateurs sont la traction ferroviaire et certains actionneurs [45]. Cette technologie est très étudiée pour implantation

dans les véhicules électriques hybrides (HEV) pour stocker l'énergie de freinage électrique et pour fournir de la puissance transitoire en raison de leur capacité de charge et décharge rapides [46-48]. Ils peuvent également être utilisés pour lisser la puissance produite par des systèmes éoliens comme proposé dans [49-51].

II.2.3 PHS et CAES

En ce qui concerne les stockages de l'énergie au niveau d'un réseau électrique, le stockage par pompage hydraulique (PHS) et le stockage de l'énergie par air comprimé (CAES) sont les deux technologies dominantes. Leurs principales applications sont la gestion de l'énergie et le contrôle de la fréquence pour le réseau électrique. Le PHS est jusqu'à maintenant la seule technologie de stockage d'énergie déployée au niveau du gigawatt [66]. Le CAES est une technologie éprouvée pour les applications de cent mégawatts avec un coût moindre que le PHS ; son utilisation pour lisser la production intermittente des sources d'énergie renouvelables est étudiée dans [68]. Il est à noter que des versions sous-marines des CAES sont actuellement en cours de développement et pourraient être envisageable pour être associées à des systèmes de production d'énergie marine [134-135]

II.3 Comparaisons et Conclusions sur les Systèmes de Stockage d'Energie

La figure I.16 synthétise les capacités en termes d'énergie et de puissance des différentes technologies de stockages d'énergies. En ce qui concerne l'hydrolienne, les régions intéressantes pour lisser les variations de puissance à long terme liées aux phénomènes de marée et les fluctuations de puissance à court terme à cause des houles sont mises en évidence sur la Fig. I.17. Il apparaît que les supercondensateurs et les volants d'inertie sont adaptés au lissage des fluctuations de puissance de courte durée induites par des houles. Les batteries NaS et à circulation d'électrolyte sont, elles, aptes à compenser la variation de puissance liée à la marée. Les petits CAES (en particulier sous-marin) pourraient aussi être intéressants dans le cas d'une ferme hydrolienne.

III. LISSAGE DE LA PUISSANCE AVEC DES SUPER-CONDENSATEURS

Ce chapitre se concentre sur les fluctuations de la puissance dans le système hydrolien induites par la houle (fluctuation « rapide »). Un système hydrolien (1.52 MW) connecté sur le réseau électrique est considéré. Tout d'abord, la modélisation de l'effet de houle est

présentée. Ensuite, des stratégies de lissage de la puissance produite par une turbine hydrolienne à pas fixe associée à une génératrice synchrone à aimants permanents (GSAP) sont proposées. Un algorithme de MPPT modifié avec une stratégie de filtrage est proposé pour le contrôle de la génératrice. Enfin, nous étudierons l'utilisation de supercondensateurs pour réaliser une injection de puissance lissée au réseau électrique.

III.1 Modélisation de la Houle

La houle se manifeste par des trains d'onde de grande longueur (souvent plus de 150 m) générés par les tempêtes lointaines [70]. La dispersion à longue distance rend le spectre de houle plus étroit et l'énergie plus concentrée au niveau fréquentiel que celle des vagues générées par le vent local. L'effet de houle sur la vitesse du courant marin peut être estimé par les modèles de Stokes [71-72]. Les Equations (II.2) et (II.3) présentent les modèles de Stockes au premier ordre et au second ordre respectivement. Le modèle du premier ordre est adapté au cas où la profondeur de la mer est beaucoup plus importante que la longueur d'onde de la houle, tandis que le modèle du second ordre est mieux adapté aux petites profondeurs. La Figure II.2 montre que le modèle du second ordre se distingue du modèle du premier ordre uniquement lorsque le rapport entre la profondeur de la mer et la longueur d'onde de la houle est très faible. La profondeur typique pour l'installation d'une hydrolienne est de 30 à 50 m et les longueurs d'onde de la houle typique varient de 150 à 250 m, donc le modèle Stokes de premier ordre peut être utilisé avec une précision suffisante.

En effet, plusieurs composantes de différentes fréquences doivent être considérées pour modéliser les effets de la houle. Chaque composante de la houle est calculée à partir du spectre de houle. Un spectre de JONSWAP est choisi pour calculer le spectre de la houle en raison de son fort pic caractéristique [70]. La Figure II.3 montre le spectre de la houle correspondant à un état de mer de $H_s = 3m$, $T_p = 13.2s$.

Dans ce travail, on considère que le rayon de la turbine est de 8m et que le système est installé à un endroit de profondeur 35m. La vitesse du courant marin équivalent pour cette turbine peut être calculée à une profondeur de 22 m sous la surface de la mer (Fig. II.4). La Figure II.5 montre la vitesse du courant marin sous l'effet de la houle. On peut voir que la houle peut provoquer des variations de vitesse de l'ordre de 50% autour de la vitesse moyenne du courant marin et introduire ainsi de grandes fluctuations (sur une période de 10 à 20 secondes) dans la puissance produite par l'hydrolienne (Fig. II.6).

III.2 Lissage de Puissance par Action sur la Génératrice

III.2.1 Modélisation d'un Système Hydrolien Connecté au Réseau

Dans ce travail, un système hydrolien de 1.52 MW est étudié. La Figure II.7 montre la structure générale du système. Une GSAP est choisie comme générateur directement connecté au réseau par l'intermédiaire d'un convertisseur AC/DC/AC à IGBT piloté en Modulation de Largeur d'Impulsions (MLI). Un banc de supercondensateur (SC) est associé au système pour compenser les fluctuations de puissance et ainsi lisser la puissance injectée au réseau électrique.

Le modèle de la turbine est représenté par (II.6). La courbe de C_p utilisée dans ce travail est illustrée par la Fig. II.8 ($\beta = 0$ pour l'hélice à pas fixe). Cette courbe est issue de mesures effectuées pour une turbine tripale dans [76] et [77]. La Fig. II.9 montre les puissances extractibles par la turbine sous différentes vitesses des courants marins. La vitesse maximale du rotor en stratégie MPPT (stratégie de recherche d'un point maximisant l'extraction d'énergie) est de 24 tours par minute (2.52 rad/s) correspondant à une vitesse du courant marin de 3.2 m/s. Lorsque le courant marin dépasse 3.2 m/s, la puissance de la turbine peut être limitée à l'aide de stratégies décrites dans [98] et développées dans la dernière partie du document.

Le modèle de la GSAP est donné dans un repère de rotation synchrone dit de Park (*d-q)* (Fig. II.10). La transformation de Park utilisée est donnée par (II.7) et le modèle de la GSAP peut alors être décrit par (II.8). Afin de faciliter la simulation à long terme, un modèle aux valeurs moyennes du convertisseur est mis en oeuvre [79-80]. Ce modèle aux valeurs moyennes est illustré par la figure II.11.

III.2.2 Stratégie MPPT Modifiée

La figure II.12 montre le schéma de commande utilisé pour le convertisseur côté génératrice. La référence du courant d'axe *d* est maintenue à zéro pour un fonctionnement en dessous la vitesse nominale de la génératrice. La référence du courant d'axe *q* est calculée par le régulateur de vitesse (consigne en couple). Dans ce travail, la référence est filtrée par un passe-bas afin de réduire l'amplitude de fluctuation de la puissance au niveau de la génératrice sous l'effet de la houle. Les paramètres des régulateurs PI sont calculés selon la méthode de l'optimum non symétrique (NSOM [83-84]).

La stratégie MPPT basique consiste à contrôler la vitesse du rotor de la turbine pour maintenir la vitesse spécifique λ à sa valeur optimale, donc à donner une référence de vitesse de rotation

pour la machine ($\Omega = \lambda_{opt} V / R$). Les réponses en puissance de la turbine et de la génératrice sous l'effet de la houle sont montrées dans la Fig. II.16. On peut remarquer que les fluctuations de puissance de la génératrice deviennent très grandes avec la stratégie MPPT basique. En effet, cette stratégie MPPT de référence en vitesse tend à augmenter les fluctuations de puissance au niveau du générateur sous l'effet de la houle.

Dans ce travail, un filtre passe-bas est ajouté afin de modifier la référence de vitesse du rotor en cas de la houle. La stratégie proposée pour générer la référence filtrée de vitesse est montrée par (II.18). Grâce à ce filtre, l'inertie du système peut être utilisé pour décaler les moments d'accélération (ou décélération). Ainsi la fluctuation de puissance produite par la génératrice peut être réduite. La Fig. II.17 montre les profils de puissance de la génératrice avec différentes constantes de temps du filtre. La Fig. II.18 compare les performances du système pour différentes conditions de simulation. Afin d'obtenir la puissance la plus lissée possible au niveau de la génératrice, la constante du filtre est choisie à T = 7s ce qui correspond à environ la moitié de la période typique de la houle. La fluctuation de la puissance de la génératrice est alors réduite de 68% (avec une réduction de 7,5% de l'énergie) par rapport à une MPPT classique.

Cette stratégie MPPT modifiée est également comparée à une stratégie de MPPT par pilotage direct du couple [85-86]. La Fig. II.21 compare la puissance du générateur en utilisant différentes stratégies de MPPT. Elle montre que la stratégie MPPT proposée ainsi que la stratégie MPPT par pilotage direct du couple permettent de réduire considérablement les fluctuations de puissance sous l'effet de la houle.

III.3 Lissage de la Puissance Injectée Côté Réseau

La fonction principale du pont IGBT placé du côté du réseau est de maintenir une tension stable sur le bus continu du convertisseur et de réguler les puissances active et réactive injectées au réseau [87-88]. La Figure II.23 illustre le système de contrôle du convertisseur côté réseau.

La figure II.24 montre le profil d'évolution de l'énergie dans le système de stockage (ESS) qui permet l'élimination des fluctuations de la puissance induite par la houle. Une marge doit être considérée, et un ESS de 1.5 kWh est nécessaire dans ce cas [25]. Les analyses statistiques (Fig. II.25) montrent qu'une limite supérieure de l'estimation de la capacité d'énergie nécessaire est de l'ordre de 2 kWh.

La figure II.26 montre le modèle du premier ordre (un condensateur C_{sc} en série avec une résistance R_{sc}) utilisé pour modéliser le banc de supercondensateurs (SC). La Figure II.28 montre le schéma de commande du banc de SC. Lorsque $I_{Grid} > I_{Target}$, la commande tend à augmenter la tension du supercondensateur ; le supercondensateur absorbant la différence de puissance. Lorsque $I_{Grid} < I_{Target}$, la tension de SC sera diminuée ; le SC libérant alors la puissance stockée. Pour atteindre la capacité de 1.5 kWh, trois branches en série de supercondensateurs décrites par (II.32) sont nécessaires. Par conséquent, les paramètres du modèle du système de SC montré à la Fig. II.26 peuvent être calculés par (II.33) : ce SC ESS a alors une capacité d'énergie utilisable de 1.97 kWh.

Pour le même courant marin (sous l'effet de la houle), les courants électriques injectés dans le réseau avec et sans le SC sont reportés sur les figures II.29 et II.30. Les variations de l'état de charge (SoC) du SC sont présentées à la figure II.32. Nous pouvons voir que la stratégie MPPT proposée permet de réduire considérablement les contraintes sur le banc de SC. La figure II.33 montre la puissance produite par l'hydrolienne, la puissance injectée dans le réseau et la puissance fournie ou stockée par le SC. La figure II.34 montre l'énergie produite par la turbine, l'énergie produite par la génératrice et l'énergie injectée dans le réseau : elle montrent que l'énergie captée par la turbine peut être injectée efficacement dans le réseau par les stratégies de contrôle de lissage de la puissance proposées.

III.4 Discussion

Le banc de SC de 1.97 kWh semble un peu surdimensionné. Cependant, son coût représenterait environ 0.4% du coût total du système de génération hydrolien. De plus, pour une vitesse supérieure de marée ou pour un état de mer plus fort, la fluctuation de la puissance peut avoir une amplitude plus grande que celle représentée dans les simulations. Par conséquent, des marges suffisantes doivent être considérées pour dimensionner le système de stockage. Le banc de SC ici considéré est utilisé pour une seule hydrolienne ; une autre disposition possible est d'utiliser un système de stockage commun à plusieurs hydroliennes (centralisation de l'ESS sur le parc hydrolien).

IV. INTEGRATION D'UNE FLOW BATTERIE POUR LA GESTION QUOTIDIENNE DE LA PUISSANCE

En raison de la prévisibilité des courants marins, les hydroliennes apparaissent a priori très attractives en tant que source d'électricité pour les zones côtières et les îles éloignées situées à proximité de sites à forts courants comme les îles du Ponant au large du Finistère. La puissance produite par une hydrolienne varie considérablement avec la vitesse des courants marins pendant une journée. Ce chapitre propose d'utiliser une batterie à circulation ou « flow battery » pour faciliter la gestion quotidienne de la puissance d'une hydrolienne et permettre de fournir ainsi la puissance demandée par les utilisateurs d'un réseau électrique isolé. Deux configurations de système sont étudiées. Dans un premier cas l'hydrolienne sert de source principale d'alimentation et dans le deuxième cas elle vient suppléer un générateur diesel en tant que source auxiliaire.

IV.1 Modélisation de la Batterie

La figure III.1 montre la structure générale du système étudié dans ce travail (les acronymes MCT et BESS représentent respectivement la turbine et la batterie). La Fig. III.2a montre le profil théorique (sans perturbations) de la vitesse du courant marin due à une marée semi-diurne au cours d'une journée. La Fig. III.2b montre la puissance pouvant être produite par l'hydrolienne étudiée de 1.5 MW, ainsi que le profil considéré pour la puissance demandée par le réseau sur cette période. La variation d'énergie maximum (calculée par intégration de la différence de puissance représentée sur la Fig. III.2b) peut servir de base pour l'estimation de la capacité minimale requise de la batterie. Le système de batterie (BESS) étudié dans ce cas possède ainsi une puissance de 1 MW et une capacité énergétique de 3MWh.

La figure III.3 montre le modèle comportemental d'une batterie à circulation de type Vanadium Redox (VRB) [56,103]. Le courant de la pile (I_{stack}) et la tension de la pile (V_{stack}) représentent respectivement les courants des cellules de la pile et la force électromotrice interne de la batterie. Ces deux grandeurs sont utilisées pour estimer l'état de charge (SoC) de la batterie. Les différentes pertes de la batterie sont modélisées et représentées par les résistances de la Fig. III.3. Les calculs des paramètres du modèle sont détaillés par les équations (III.2) à (III.13).

Les figures III.5 et III.6 montrent les caractéristiques de charge-décharge de la batterie de 3 MWh. La batterie est chargée pendant 3 heures avec un courant constant de 600A à partir d'un état de charge (SoC) initial de 0.1. Elle est ensuite déchargée durant 3 heures avec un

courant de la même amplitude. On peut constater qu'à l'instant de commutation du mode de charge au mode de décharge, la tension $V_{battery}$ est discontinue en raison du changement de la polarité de la tension sur les résistances internes. Lorsque la batterie est désactivée, le courant de la batterie est nul et $V_{battery}$ est égal à la force électromotrice interne V_{stack}.

IV.2 Système Hybride Hydrolien/Batterie/Diesel

IV.2.1 Configuration du Système et Contrôle de la Batterie

Le travail présenté se concentre sur la modélisation et le contrôle de la batterie. L'objectif est que la puissance produite corresponde à la demande des utilisateurs du réseau sur une base quotidienne. L'hydrolienne a une puissance nominale de 1.5 MW et la tension du bus continu du convertisseur qui lui est associé est de 1500 V. Un générateur diesel (de 500 kW) est également intégré pour charger la batterie lorsque l'état de charge de la batterie est bas. Un convertisseur DC-DC bidirectionnel [105] est associé à la batterie pour la piloter et peut être modélisé par (III.16). La puissance de référence de la batterie est réglée pour compenser la différence entre la production (de l'hydrolienne) et la demande de puissance du côté du réseau. Le contrôle de la puissance de la batterie est réalisé par le convertisseur DC-DC qui augmente ou diminue la tension de batterie comme illustré par la Fig. III.7.

IV.2.2 Simulations sans Générateur Diesel

La vitesse du courant marin et la puissance moyenne produite par l'hydrolienne pendant une journée sont a priori prévisibles. Dans le cas étudié, la puissance demandée par les utilisateurs du réseau a une valeur moyenne égale de 90% de l'électricité moyenne produite. Ceci permet de prendre en compte les pertes du système. La figure III.8 montre la puissance produite par l'hydrolienne, la puissance injectée dans le réseau et la puissance fournie ou stockée au niveau de la batterie pendant une journée. Les figures III.9 et III.10 montrent la variation de la tension, du courant de batterie et de son état de charge (SoC) pour un SoC initial de 0.4 (Fig. 10). Le phénomène de diminution de l'état de charge est provoqué par les pertes de la batterie. Les figures III.11 à III.13 illustrent le cas où le SoC initial est égal à 0.3. Lorsque la batterie est désactivée (SoC trop faible), P_{Grid} va alors valoir P_{MCT}, ce qui signifie que la puissance demandée par les utilisateurs du réseau ne peut être satisfaite.

IV.2.3 Simulations avec un Générateur Diesel

Une simulation intégrant un générateur diesel (qui produit 500kW) est effectuée et les résultats sont montrés sur les Figures III.14 à III.16. On peut voir que le DG est déclenché à

13h05 lorsque le SoC de la batterie est proche de 0.1. Le DG fournit alors la puissance nécessaire pour satisfaire la demande des utilisateurs du réseau. Dans le même temps, la batterie est chargée par le DG et l'hydrolienne. Le DG est désactivé lorsque la batterie atteint sa puissance nominale (à 14h40). Après ce point, la puissance produite par l'hydrolienne est suffisante pour charger la batterie et alimenter le réseau.

Les résultats concernant un générateur diesel plus petit (qui produit 250kW) sont montrés sur les Figures III.17 à III.19. Dans le précédent cas (500 kW DG), le DG est en opération de 13:05 à 14:40 et fournit 790 kWh d'électricité. Avec de diesel de puissance réduite, le DG est en opération de 12:26 à 15:13 et fournit 695 kWh d'électricité. Il semble donc qu'un diesel de puissance plus faible permettrait de réduire la consommation de carburant diesel ; mais, il convient de noter que le petit DG exige plus de contraintes et d'anticipation sur les opérations de la batterie.

IV.3 Cas d'une Alimentation Insulaire Isolée

Aujourd'hui, la plupart des îles et régions éloignées sont fortement dépendantes des DGs pour leur alimentation électrique [107]. Plusieurs hydroliennes sont, par exemple, prévues pour être installées dans le passage du Fromveur (près de Brest) pour fournir 15% à 20% de la demande électrique de l'île d'Ouessant [106]. Ainsi dans la suite, un cas proche de l'île d'Ouessant sera considéré comme un cas d'étude pour l'utilisation d'un système hybride hydrolienne/batterie/diesel. Dans ce cas, les générateurs diesels seront les principales sources d'alimentation.

IV.3.1 Configuration Système et Les Règles d'Alimentation

Sur l'île d'Ouessant, il existe 4 groupes de groupes électrogènes diesels d'une capacité totale de 5300 kVA [109]. Les caractéristiques de ces quatre DG sont montrées dans le tableau III.1. La puissance de crête en hiver sur cette île peut être estimée à 1134 kW. En été, la puissance maximale estimée est d'environ 2150 kW (en raison du grand nombre de touristes). Cela implique que, la plupart de temps, seuls 2 groupes sont en service et les 2 groupes restants sont hors service ou pour l'entretien [110].

La figure III.20 montre le profil quotidien d'énergie produite par l'hydrolienne et les deux demandes de charge utilisées dans la simulation. La courbe de charge basse (entre 400 ~ 1800 kW) et la courbe de charge élevée (entre 500 ~ 2250 kW) représentent deux cas de charge différentes qui correspondent à des situations hivernales et estivales. Sur la Fig. III.20, on peut

voir que l'énergie devant être stockée par la batterie est considérablement réduite. Dans ce cas, la batterie est dimensionnée pour stocker seulement 1.25 MWh (= 500 kW × 2.5 h).

Un DG doit en général être utilisé à plus de 30% de sa puissance nominale afin d'assurer un fonctionnement efficace (bon rendement et réduction de l'encrassement) [111]. Dans les simulations suivantes, la limite de puissance minimum du système de DG est donc définie à 40% de la puissance nominale du DG_1. Par conséquent, les limites opérationnelles des DGs sont données par (III.18). La stratégie de charge/décharge de la batterie est identique à celle présentée dans la section précédente. Les règles de pilotage de la puissance des DG sont données par (III.19).

IV.3.2 Cas d'une Demande Utilisateur Elevée

La Figure III.21 montre les réponses du système hybride pour une demande élevée (cas typique de l'été) pendant la journée avec un SoC initial de la batterie de 0,5. Les variations de tension et de SoC de la batterie sont présentées sur les figures III.22 et III.23. La batterie permet de stocker efficacement la puissance excessive produite par l'hydrolienne (02:10 ~ 04:20) et fournit la puissance de pointe correspondants aux horaires autour de 12:00 et 19:00.

La Figure III.24 montre les profils de puissance du système et la Fig.III.25 montre la variation du SoC pour un cas de faible SoC initial. Les courbes zoomées sur la période de 00:00 à 06:00 sont données sur les figures III.26 et Fig. III.27. Lorsque le SoC de la batterie atteint 0,11, le DG fournit de la puissance; la BESS est alors chargée par le DG et l'hydrolienne pendant la période comprise entre 2:00 et 2:22 jusqu'au moment où la batterie atteint sa puissance nominale.

IV.3.3 Cas d'une Demande Utilisateur Basse

Dans le cas d'une demande basse (cas typique de l'hiver), le DG peut facilement gérer la charge maximale, mais la nouvelle contrainte est que la puissance de l'hydrolienne doit être limitée lorsque le courant de marée est élevé (Fig. III.28). Dans la Fig. III.29, on peut voir que l'utilisation du DG peut être réduite et la batterie permet de conserver un même niveau de SoC (comparé avec la valeur initiale) à la fin de la journée grâce la gestion de puissance proposée.

IV.3.4 Cas sans Batterie

Le tableau III.3 résume la performance énergétique de différentes configurations pour le cas de cette île isolée et compare la consommation du DG avec et sans la batterie. On peut voir

d'après le tableau III.3 que l'usage de la BESS permet d'augmenter la part de l'énergie quotidienne qui est produite par l'hydrolienne. La BESS permet, en effet, de maintenir l'hydrolienne en mode MPPT plus longtemps, surtout dans les cas d'un faible niveau de consommation. On constate également que lorsque le niveau de pénétration de la puissance l'hydrolienne augmente (environ 22% dans le cas de charge élevée et 28% dans le cas de charge basse), l'importance des batteries et leur sollicitation augmentent simultanément.

V. STRATEGIE DE LIMITATION DE PUISSANCE AUX VITESSES DE COURANTS MARINS ELEVEES

L'environnement sous-marin exige du système hydrolien compacité et fiabilité (en particulier les besoins en maintenance doivent être minimisés). Plusieurs grands projets d'hydroliennes industrielles telles que la DCNS-OpenHydro [133], Sabella [20] et Voith Hydro [18] adoptent les hélices à pas fixe et utilisent les génératrices synchrones à aimants permanents. Lorsque la vitesse du courant marin est supérieure à la valeur nominale, une hydrolienne munie d'une hélice à pas fixe ne peut pas mettre en œuvre une stratégie de contrôle de la puissance extraite avec limitation de puissance par changement de pas [112-113] comme c'est le cas pour les éoliennes de grandes puissances. Par conséquent, une stratégie appropriée de contrôle électrique de la génératrice doit être appliquée pour contrôler et limiter la puissance produite par l'hydrolienne.

Le chapitre IV présente ainsi une stratégie basée sur le défluxage de la génératrice pour contrôler la puissance de l'hydrolienne pour les vitesses de courants marins élevées. Une commande directe en couple et une commande de vitesse seront comparées. Le contrôle à puissance constante et le contrôle à puissance maximale au cours de l'étape de défluxage seront également comparés. La Figure IV.1 montre le schéma général du système.

V.1 Caractéristiques de Fonctionnement de la Génératrice

Les caractéristiques de puissance de la turbine (Fig. IV.2) montrent qu'il est souhaitable de limiter la puissance produite à la puissance nominale lorsque les vitesses des courants marins sont très élevées. Selon les caractéristiques de la turbine, une solution possible pour limiter la puissance est d'accélérer la turbine au-delà du TSR optimal pour réduire le coefficient de puissance au point d'utilisation. Cependant, le fonctionnement de la génératrice au-dessus de la vitesse de base conduit à une force électromotrice (FEM) élevée dans les machines à

aimants permanents et peut provoquer la saturation des régulateurs. En effet la tension pouvant être délivrée par le pont IGBT aux bornes de la machine est limitée à une valeur maximale en relation avec la valeur de la tension du bus continu. Diverses stratégies de défluxage ont été proposées dans la littérature [114-123]. Dans ce travail, nous nous concentrons sur les caractéristiques de fonctionnement communes de la turbine et la génératrice. Les impacts des paramètres de la génératrice sur la région de fonctionnement de l'hydrolienne seront également discutés.

Un GSAP à pôles lisses est considérée dans ce travail. En négligeant les résistances statoriques, la limitation de tension (IV.1) en régime permanent peut alors être exprimée par (IV.3). Selon (IV.3), les contraintes sur les tensions et les courants au niveau des bobinages de la génératrice peuvent être représentées par des cercles dans la Fig. IV.3. Le cas où $\psi_m > L_s I_{max}$ est étudié dans ce travail; le couple maximal en régime de défluxage est alors obtenu lorsque le point de fonctionnement de la machine correspond aux points d'intersection des cercles limitant la tension et du courant. Les points d'intersection (comme le point *A* sur la Fig. IV.3) peuvent être calculés par (IV.5) et (IV.6). Dans la Fig. IV.3, on peut remarquer qu'il existe un degré de liberté pour choisir la référence de i_d lorsque la référence de i_q^* est inférieure à i_{qmax} (les points de fonctionnement peuvent alors être choisis sur le segment de ligne de *C*-*D*). Le point *D* correspond aux pertes de Joule les plus faibles tandis que le point *C* correspond aux pertes de fer les plus faibles. Si une stratégie de type « couple maximal par ampère » (MPTA) est appliquée, le point *D* sera choisi comme point de fonctionnement.

La Figure IV.4 illustre les caractéristiques de puissance de la génératrice étudiée. Au dessous de la vitesse de base, la génératrice fonctionne en mode MPPT permettant à la turbine de capter l'énergie maximale des courants marins. Au dessus de la vitesse de base, un courant de démagnétisation est injecté ($i_d < 0$) et la génératrice fonctionne dans un mode de défluxage. Il convient de noter que, dans la zone de défluxage, il existe une plage de vitesse où la puissance nominale peut toujours être atteinte et maintenue constante. Dans cette plage de vitesse il est également possible de contrôler la puissance de la génératrice au-dessus de la puissance nominale afin d'extraire plus d'énergie. La plage de défluxage et la plage de vitesse où on peut maintenir la puissance constante dépendent des paramètres de la machine comme montrés dans (IV.9) et (IV.10). Dans ce travail, la génératrice (paramètres illustrés dans l'Annexe A) est en mesure d'avoir un rapport de vitesse pour la plage de défluxage valant *Ratio_fx* = 3.3 et un rapport de vitesse pour la plage ou l'on peut opérer à puissance constante valant *Ratio_con* = 2,4 comme calculés par (IV.12) et (IV.13)

V.2 Contrôle Robuste par Défluxage

Dans ce travail, la méthode de défluxage proposée dans [121-122] est choisie en raison de sa robustesse et de l'utilisation efficace de la tension du bus continu. La figure IV.5 illustre le schéma de commande du côté de la génératrice avec l'algorithme de défluxage. La différence entre les valeurs de sortie des régulateurs de courant (références de tension) et les valeurs de sortie du convertisseur (tensions réelles de la machine) sont utilisées pour générer la référence pour le courant i_d. Le filtre passe-bas (LPF) est utilisé pour rejeter des composants hautes fréquences des signaux de tension.

V.2.1 Commande en Vitesse et Commande en Couple

Dans la stratégie de commande en vitesse, lorsque la vitesse du courant marin est inférieure à la valeur nominale, le contrôle par MPPT avec la stratégie adaptée présentée dans le chapitre II est utilisé; lorsque la vitesse du courant marin est supérieure à la valeur nominale, le mode de MPPT doit être changé et remplacé par un mode de limitation de puissance. Pour le mode à puissance constante (CAP), la puissance de la génératrice peut être contrôlée à sa valeur nominale. Le calcul de la référence de la vitesse du rotor est présenté sur la figure IV.6. On peut remarquer que la stratégie de commande en vitesse repose alors sur la connaissance a priori des caractéristiques de la turbine et de la vitesse du courant marin.

Dans la stratégie de commande en couple, lorsque la vitesse du courant marin est inférieure à la valeur nominale, une stratégie MPPT qui permet un calcul direct du couple de référence peut être appliquée; lorsque la vitesse du rotor est progressivement augmentée au-dessus de la vitesse de base, la génératrice sera accélérée grâce au fonctionnement en défluxage et la référence de couple peut alors être calculée à partir de la puissance constante requise. L'équation (IV.14) illustre le calcul de la référence de couple alors utilisée.

Dans le premier cas, la mer est supposée calme (sans houles significatives) et donc la vitesse du courant marin élevée est due à la variation liée aux grandes marées. Dans la simulation considérée, la vitesse initiale du courant marin est réglée à 2.8 m/s, et puis, elle s'élève progressivement à 3.6 m/s comme montrée dans la Fig. IV.7. Lorsque la vitesse du courant augmente au-dessus de la valeur nominale (3.2 m/s), la commande à puissance constante avec la stratégie de défluxage est mise en oeuvre. La vitesse de la turbine, le couple et la puissance de la génératrice sont respectivement montrées sur les Figs. IV.8 à IV.10. Les paramètres du système hydrolien sont illustrés dans l'Annexe A et le couple maximal de la génératrice est limité à 600 kN.m. Ces résultats montrent que, lorsque le courant marin est égal à la valeur de 3.6 m/s, les deux stratégies de contrôle peuvent limiter la puissance produite par la génératrice

à la valeur requise de 1.5 MW en régime permanent. Lors de l'étape transitoire de haute vitesse de courant, la stratégie par contrôle direct du couple permet de mieux contrôler la puissance produite par la génératrice à 1.5 MW. Cette conclusion peut également être formulée dans le cas où la vitesse du courant marin est élevée en raison de la houle (Fig. IV.14).

V.2.2 Comparaison entre les Stratégies CAP et MAP

Dans la section § IV.3.3, nous comparons le mode CAP et le mode MAP en appliquant la commande par contrôle direct de couple dans la zone de fonctionnement en défluxage. Selon les caractéristiques de fonctionnement de la génératrice (§ IV.2), on constate que le mode MAP peut produire de la puissance sur-nominale dans la région de fonctionnement en survitesse. Dans la suite, les simulations dynamiques sont effectuées pour comparer les deux modes de fonctionnement en termes de réponses vitesse/couple et de pertes de la génératrice. Pour le mode CAP, la référence en couple est calculée de la façon de maintenir la puissance produite de la génératrice à sa valeur nominale. Pour le mode MAP, i_q^* vaut $\sqrt{I_{max}^2 - i_d^{*2}}$ pour maximiser le couple de la génératrice.

Dans le premier cas (élévation lente de la vitesse du courant marin sans houle), la réponse de la vitesse de la turbine, le couple et la puissance produite par la génératrice, et les pertes de la génératrice dans le cadre des modes CAP et MAP sont présentés sur les figures IV.15 à IV.19. Les résultats en régime permanent pour une vitesse du courant marin de 3.6 m/s sont ensuite présentés dans le tableau IV.1. Ces résultats montrent que le mode CAP est caractérisé par un couple de génératrice inférieur, ce qui amène la turbine à une vitesse plus élevée que dans le mode MAP. Les pertes Joule et les pertes fer sont calculées par (IV.15) et (IV.17). On peut remarquer que le mode CAP permet de réduire considérablement les pertes Joule par rapport au mode MAP. Les pertes fer pour le mode MAP sont un peu plus élevées que pour le mode CAP : ceci est lié au fait que la densité de flux dans le stator est plus réduite dans le mode CAP. La figure IV.20 montre les résultats du calcul des pertes Joule et des pertes fer sous différentes vitesses des courants marins pour la génératrice utilisée dans ce travail. On peut ainsi conclure que le mode CAP permet d'obtenir des pertes plus faibles que le mode MAP au niveau de la génératrice.

Dans le cas où la vitesse du courant marin augmente au delà de la vitesse nominale du fait de l'effet de houle, la machine accélère plus, dans le mode CAP (pour limiter la puissance à la puissance nominale), que dans le mode MAP. (Fig. IV.21). Dans ce cas, le mode MAP permet

produire environ 4% plus de puissance que le mode CAP au cours des principales étapes du fonctionnement en défluxage comme indiqué dans la Fig. IV.22.

V.3 Discussion sur les Paramètres de la Génératrice

Nous avons étudié l'influence des paramètres de la génératrice sur la plage de fonctionnement en régime de défluxage au-dessus de la vitesse de base. Dans cette discussion, la vitesse de base du générateur ω_{eb}, le couple nominal T_{eN} et la tension maximale de stator V_{max} sont fixés et nous nous ~~nous~~ concentrons donc sur les influences des valeurs de l'inductance du stator et du flux magnétique crée par le rotor. Pour un rapport de vitesse à puissance constante (CPSR) attendu, les valeurs minimales requises pour L_sI_{max} et L_s peuvent être calculées par (IV.18) et (IV.19). La figure IV.25 montre les résultats du calcul: les paramètres de la génératrice utilisés dans ce travail permettrent à la génératrice d'avoir un CPSR de 2.4 avec un facteur de puissance nominale de 0.84 environ. Selon la figure IV.25, on peut voir l'influence des changements des valeurs de L_sI_{max} et L_s pour un CPSR requis. La figure IV.26 montre les points de fonctionnement de la génératrice avec un CPSR de 1.6. Dans ce cas, le système hydrolien ne peut pas produire de la puissance à une vitesse de courant marin de 4,0 m/s en raison d'une faible capacité de défluxage de la génératrice. Dans le cas d'un CPSR de 2.4, le système hydrolien peut produire 1.77 MW avec le mode MAP ou 1.52 MW avec le mode CAP (Fig. IV.27).

Il faut remarquer que la caractéristique de la turbine (allure de la courbe de C_p) peut également influencer le CPSR requis pour une hydrolienne utilisant une hélice à pas fixe. La courbe C_p utilisée dans ce travail a la forme classique associée aux turbines à trois pales [130]. Une courbe C_p plus plate peut être associée à des turbines à deux pales ou à des turbines avec des conceptions spéciales [131-132]. Dans ce cas, l'ensemble génératrice convertisseur devrait être caractérisé par un plus grand CPSR pour que la génératrice puisse produire la puissance nominale aux vitesses de courants marins élevées (Fig. IV.28).

VI. CONCLUSIONS ET PERSPECTIVES

Cette thèse se propose d'utiliser des supercondensateurs pour compenser les fluctuations de puissance induites par la houle et d'utiliser des batteries à circulation d'électrolyte pour permettre au système hybride hydrolien/batterie/diesel de suivre les demandes de consommation quotidiennes, en compensant les variations de vitesse périodiques liées à la fluctuation du courant de marée. Du fait qu'un nombre significatif de projets d'hydroliennes

de grande puissance adoptent une solution basée des turbines à pas fixe, une stratégie de limitation de puissance par défluxage au niveau de GSAP est proposée et étudiée pour limiter la puissance pour des vitesses de courant élevée. Un système hydrolien à entraînement direct de 1.5 MW est considéré dans la thèse. Les principales conclusions de cette thèse sont répertoriées ci-dessous:

- L'effet de houle pourrait provoquer d'importantes fluctuations (avec des périodes de l'ordre de 10s à 20s) de la puissance au niveau de la génératrice en cas de contrôle MPPT basique. Dans ce cas, un algorithme de MPPT avec une stratégie de filtrage est proposé afin de réduire les fluctuations de puissance produite par la génératrice, puis un groupe de supercondensateurs est intégré dans le système pour lisser la puissance injectée au réseau électrique;
- Dans le cas où l'hydrolienne est la source dominante d'alimentation d'une installation isolée, une grande batterie est nécessaire pour équilibrer production et consommation d'électricité. Dans le cas de l'île d'Ouessant (ou DG est la principale source d'alimentation), le dimensionnement de la batterie peut être réduit, mais elle reste nécessaire pour augmenter la performance de l'hydrolienne en respectant les contraintes d'utilisation efficace des générateurs diesels;
- Pour les vitesses de courant marin élevées, une stratégie robuste de défluxage est proposée afin de contrôler la puissance produite par l'hydrolienne à sa valeur nominale (mode CAP) ou sur-nominale (mode MAP) en respectant les contraintes en tension et en courant de l'ensemble convertisseur machine. Les caractéristiques de fonctionnement conjoint de la turbine et de la GSAP sont étudiées; un compromis entre une grande plage de vitesse à puissance constante (au-dessus de la vitesse de base) et un facteur de puissance nominale acceptable de la génératrice doit être réalisé lors du dimensionnement de la génératrice et de son convertisseur.

La poursuite de cette thèse peut être principalement divisée en deux aspects: les stratégies de contrôle avec tolérance de fautes et la simulation d'un parc hydrolien. En effet, certaines améliorations doivent être prises en compte dans les travaux futurs :

- Inclure des stratégies de commande en défaut. Pour un système connecté au réseau, la façon de maintenir un fonctionnement stable en cas de fautes du réseau (LVRT ou la distorsion de fréquence) est par exemple un point crucial. Les ESSs peuvent par exemple être considérés pour faciliter la capacité du système hydrolien à opérer en mode de défaut;

- Etendre les simulations à une ferme constituées de plusieurs hydroliennes. Ceci pourrait également inclure la comparaison de différentes configuration pour les ESSs (centralisés ou décentralisés et choix technologiques);
- Considérer les systèmes de stockages d'énergies à base d'air comprimé qui pourraient intéressants pour les parcs hydroliens de plus de 10 MW.

De plus, il pourrait être très intéressant de mettre des modèles plus détaillés de convertisseurs (incluant les commutations) en particulier pour des simulations en cas de défauts. Il serait probablement intéressant d'évaluer ainsi les limites de validité des modèles à la valeur moyenne qui ont été utilisés dans cette thèse.

References

[1] H. Boye, E. Caquot, P. Clement et *al.*, "Rapport de la mission d'étude sur les énergies marines renouvelables," March 2013. (online :http://www.developpement-durable.gouv.fr/IMG/pdf/RAPPORT_ENERGIES_MARINES_2013.pdf)

[2] S. Benelghali, R. Balme, K. Le Saux, M.E.H. Benbouzid, J.F. Charpentier and F. Hauville, "A simulation model for the evaluation of the electrical power potential harnessed by a marine current turbine", *IEEE Journal of Oceanic Engineering*, vol. 32, n° 4, pp.786-797, Oct. 2007.

[3] S. Benelghali, "On multiphysics modeling and control of marine current turbine systems," *PhD Thesis*, University of Brest, Brest (France), 2009.

[4] R. Pelc and R.M. Fujita, "Renewable energy from the ocean", *Marine Policy*, vol. 26, issue 6, pp.471-479, Nov. 2002.

[5] S. Benelghali, M.E.H. Benbouzid and J.F. Charpentier, "Marine tidal current electric power generation technology: State of the art and current status," *in Proceedings of the 2007 IEEE IEMDC*, Antalya (Turkey), vol. 2, pp. 1407-1412, May 2007.

[6] F.O. Rourke, F. Boyle and A. Reynolds, "Marine current energy devices: Current status and possible future applications in Ireland," *Renewable and Sustainable Energy Reviews*, vol. 14, n°3, pp.1026-1036, Apr. 2010.

[7] A.S. Bahaj, "Generating electricity from the oceans," *Renewable and Sustainable Energy Reviews*, vol. 15, n°7, pp. 3399-3416, Sept. 2011.

[8] J. Zhang, L. Moreau, M. Machmoum and P.E. Guillerm, "State of the art in tidal current energy extracting," *in Proceedings of the 2014 IEEE ICGE*, Sfax (Tunisia), pp. 1-7, March 2014.

[9] http://www.global-et-local.eu/?Hydroliennes-les-industriels (last accessed March 2014)

[10] http://www.meygen.com/the-project/meygen-news/ (last accessed March 2014)

[11] http://www.renewableenergyfocus.com/view/26574/gdf-suez-investigates-french-tidal-potential/ (last accessed March 2014)

[12] http://cleantechnica.com/2011/11/14/worlds-largest-tidal-power-array-off-french-coast/ (last accessed March 2014)

[13] http://renews.biz/50635/andritz-back-in-action-at-emec/ (last accessed March 2014)

[14] http://www.hammerfeststrom.com/ (last accessed March 2014)

[15] http://atlantisresourcesltd.com/technology/ar-series.html (last accessed March 2014)

[16] http://www.seageneration.co.uk/ (last accessed March 2014)

[17] http://www.gdfsuez.com/en/journalists/press-releases/gdf-suez-bolsters-plans-for-marine-current-power-france-signing-partnership-agreement-alstom/ (last accessed March 2014)

[18] http://voith.com/en/products-services/hydro-power/ocean-energies-587.html(last accessed March 2014)

[19] http://www.sustainableguernsey.info/blog/2013/01/alstom-completes-purchase-of-tidal-generation-ltd-from-rolls-royce/ (last accessed March 2014)

[20] http://www.sabella.fr/ (last accessed March 2014)

[21] http://www.enerzine.com/7/17093+sabella-implante-la-premiere-hydrolienne-francaise-connectee-au-reseau+.html (last accessed March 2014)

[22] http://candhis.cetmef.developpement-durable.gouv.fr/ (last accessed March 2014)

[23] S. Vazquez, S.M. Lukic, E. Galvan, L.G. Franquelo and J.M. Carrasco, "Energy storage systems for transport and grid applications," *IEEE Trans. Industrial Electronics*, vol. 57, n°12, pp. 3881-3895, Dec. 2010.

[24] H. Ibrahim, A. Ilinca and J. Perron, "Energy storage systems-Characteristics and comparisons," *Renewable and Sustainable Energy Reviews*, vol. 12, pp.1221-1250, Jun. 2008.

[25] Z. Zhou, M.E.H. Benbouzid, J.F. Charpentier, F. Scuiller and T. Tang, "A review of energy storage technologies for marine current energy systems," *Renewable and Sustainable Energy Reviews*, vol. 18, pp. 390-400, Feb. 2013.

[26] I. Hadjipaschalis, A. Poullikkas and V. Efthimiou, "Overview of current and future energy storage technologies for electric power applications," *Renewable and Sustainable Energy Reviews*, vol. 13, pp.1513-1522, 2009.

[27] A. Khaligh and Z. Li, "Battery, ultracapacitor, fuel cell, and hybrid energy storage systems for electric, hybrid electric, fuel cell, and plug-in hybrid electric vehicles: State of the art," *IEEE Trans. Vehicular Technology*, vol. 59, n°6, pp.2806-2814, Jul. 2010.

[28] K.C. Divya and J. Østergaard, "Battery energy storage technology for power systems—An overview," *Electric Power Systems Research*, vol. 79, pp.511-520, 2009.

[29] J. Kumagai, "A battery as big as the grid," *IEEE Spectrum*, vol. 49, n°1, pp.45-46, Jan. 2012.

[30] J. Baker, "New technology and possible advances in energy storage," *Energy Policy*, vol. 36, pp.4368-4373, 2008.

[31] http://energystorage.org/energy-storage/energy-storage-technologies (last accessed March 2014)

[32] C. Alaoui, "Solid-State thermal management for lithium-Ion EV batteries," *IEEE Trans. Vehicular Technology*, vol. 62, n°1, pp.98-107, Jan. 2013.

[33] J. Wu, J. Wang, K. Li, H. Zhou et *al.*, "Large-scale energy storage system design and optimization for emerging electric-drive vehicles," *IEEE Trans. Computer-Aided Design of Integrated Circuits and Systems*, vol. 32, n°3, pp.325-338, March 2013.

[34] M. Świerczyński, D.I. Stroe, A.I. Stan et *al.*, "Selection and performance-degradation modeling of $LiMO_2/Li_4Ti_5O_{12}$ and $LiFePO_4/C$ battery cells as suitable energy storage systems for grid integration with wind power plants: an example for the primary frequency regulation service," *IEEE Trans. Sustainable Energy*, vol. 5, n°1, pp.90-101, Jan. 2014.

[35] Z. Zhou, M.E.H. Benbouzid, J.F. Charpentier, F. Scuiller and T. Tang, "Energy storage technologies for smoothing power fluctuations in marine current turbines," *in Proceedings of the 2012 IEEE ISIE*, Hangzhou (China), pp. 1425-1430, May 2012.

[36] P.J. Hall and E.J. Bain, "Energy-storage technologies and electricity generation," *Energy Policy*, vol. 36, pp.4352-4355, 2008.

[37] B.E. Muhando, R.W. Wies, T.H. Johnson and G. Holdmann, "Grid-Scale rampable dispatchable storage: cascaded use of advanced battery technology to increase energy security in Alaska," *in Proceedings of the IEEE PES General Meeting*, San Diego (USA), pp. 1-8, Jul. 2012.

[38] P. Alotto, M. Guarnieri and F. Moro, "Redox flow batteries for the storage of renewable energy: A review," *Renewable and Sustainable Energy Reviews*, vol. 29, pp.325-335, 2014.

[39] G.O. Cimuca, C. Saudemont, B. Robyns and M.M. Radulescu, "Control and performance evaluation of a flywheel energy-storage system associated to a variable-speed wind generator," *IEEE Trans. Industrial Electronics*, vol. 53, n°4, pp.1047-1085, Aug. 2006.

[40] J.M. Carrasco, L.G. Franquelo, J.T. Bialasiewicz et *al.*, "Power-electronic systems for the grid integration of renewable energy sources: A survey," *IEEE Trans. Industrial Electronics*, vol. 53, n°4, pp.1002-1016, Aug. 2006.

[41] http://beaconpower.com/ (last accessed March 2014)

[42] R. Sebastian and R.P. Alzola, "Flywheel energy storage systems: Review and simulation for an isolated wind power system," *Renewable and Sustainable Energy Reviews*, vol. 16, pp.6803-6813, 2012.

[43] R.T. Doucette and M.D. McCulloch, "A comparison of high-speed flywheels, batteries, and ultracapacitors on the bases of cost and fuel economy as the energy storage system in

a fuel cell based hybrid electric vehicle," *Journal of Power Sources*, vol. 196, pp.1163-1170, 2011.

[44] W. Chen, A.K. Ådnanses, J.F. Hansen, J.O. Lindtjørn and T.Tang, "Super-capacitors based hybrid converter in marine electric propulsion system," *in Proceedings of the 2010 ICEM*, Rome (Italy), pp.1-6, Sept. 2010.

[45] C. Naish, I. McCubbin, O. Edberg and M. Harfoot, "Outlook of energy storage technologies," *Policy Department Economic and Scientific Policy*, Brussels, Feb. 2008.

[46] http://www.nrel.gov/vehiclesandfuels/energystorage/ultracapacitors.html (last accessed March 2014)

[47] P. Thounthong, V. Chunkag, P. Sethakul, B. Davat and M. Hinaje, "Comparative study of fuel-cell vehicle hybridization with battery or supercapacitor storage device," *IEEE Trans. Vehicular Technology*, vol. 58, n°8, pp.3892-3904, Oct. 2009.

[48] E. Schaltz, A. Khaligh and P.O. Rasmussen, "Influence of battery/ultracapacitor energy-storage sizing on battery lifetime in a fuel cell hybrid electric vehicle," *IEEE Trans. Vehicular Technology*, vol. 58, n°8, pp. 3882-3891, Oct. 2009.

[49] C. Abbey and G. Joos, "Supercapacitor energy storage for wind energy applications," *IEEE Trans. Industry Applications*, vol. 43, n°3, pp.769-776, May/Jun. 2007.

[50] L. Qu and W. Qiao, "Constant power control of DFIG wind turbines with supercapacitor energy storage," *IEEE Trans. Industry Applications*, vol. 47, n°1, pp.359-367, Jan./Feb. 2011.

[51] S.M. Muyeen, R. Takahashi, T. Murata and J. Tamura, "Integration of an energy capacitor system with a variable-speed wind generator," *IEEE Trans. Energy Conversion*, vol. 24, n°3, pp. 740-749, Sept. 2009.

[52] P.K. Goel, B. Singh, S.S. Murthy and N. Kishore, "Isolated wind–hydro hybrid system using cage generators and battery storage," *IEEE Trans. Industrial Electronics*, vol. 58, n°4, pp. 1141-1153, April 2011.

[53] A. Abedini and H. Nikkhajoei, "Dynamic model and control of a wind-turbine generator with energy storage," *IET Renewable Power Generation*, vol. 5, n°1, pp. 67-78, Jan. 2011.

[54] M. Bragard, N. Soltau, S. Thomas and R.W. De Doncker, "The balance of renewable sources and user demands in grids: power electronics for modular battery energy storage systems," *IEEE Trans. Power Electronics*, vol. 25, n°12, pp. 3049-3056, Dec. 2010.

[55] W. Li and G. Joós, "A power electronic interface for a battery supercapacitor hybrid energy storage system for wind applications," *in Proceedings of the 2008 IEEE PESC*, Rhodes (Greece), pp.1762-1768, Jun. 2008.

[56] W. Li, G. Joós and J. Bélanger, "Real-time simulation of a wind turbine generator coupled with a battery supercapacitor energy storage system," *IEEE Trans. Industrial Electronics*, vol. 57, n°4, pp.1137-1145, Apr. 2010.

[57] H. Jia, Y. Fu, Y. Zhang and W. He, "Design of hybrid energy storage control system for wind farms based on flow battery and electric double-layer capacitor," *in Proceedings of the 2010 IEEE APPEEC*, Chengdu (China), pp.1-6, March 2010.

[58] H. Zhou, T. Bhattacharya, D. Tran, T.S.T. Siew and A.M. Khambadkone, "Composite energy storage system involving battery and ultracapacitor with dynamic energy management in microgrid applications," *IEEE Trans. Power Electronics*, vol. 26, n°3, pp. 923-930, March 2011.

[59] Y. Cheng, "Super Capacitor Applications for Renewable Energy Generation and Control in Smart Grids," *in Proceedings of the 2010 IEEE ISIE*, Gdansk (Poland), pp.1131-1136, Jun. 2011.

[60] J. Aubry, P. Bydlowski, B. Multon, H. Ben Ahmed and B. Borgarino, "Energy storage system sizing for smoothing power generation of direct wave energy converters, " *in Proceedings of 3rd Int. Ocean Energy Conf.*, Bilbao (Spain), pp.1-7, Oct. 2010.

[61] www.gdfsuez.com/wp-content/uploads/2012/06/GDF-SUEZ-announces-its-tidal-power-ambitions-for-France.pdf (last accessed March 2014)

[62] http://www.marineturbines.com/3/news/article/53/siemens_increases_stake_in_marine_current_turbines (last accessed March 2014)

[63] A.S. Iyer, S.J. Couch, G.P. Harrison and A.R. Wallace, "Variability and phasing of tidal current energy around the United Kingdom," *Renewable Energy*, vol. 51, pp. 343-357, March 2013.

[64] M. Hessami and D.R. Bowly, "Economic feasibility and optimisation of an energy storage system for Portland Wind Farm (Victoria, Australia)," *Applied Energy*, vol. 88, pp. 2755-2763, Aug. 2011.

[65] T. Kousksou, P. Bruel, A. Jamil, T. Elrhafiki and Y. Zeraouli, "Energy storage: applications and challenges," *Solar Energy Materials & Solar Cells*, vol. 120, pp.59-80, Jan. 2014.

[66] P. Denholm, E. Ela, B. Kirby and M. Milligan, "The role of energy storage with renewable electricity generation," Technical Report of National Renewable Energy Laboratory, U.S., Jan. 2010. (http:// www.nrel.gov/docs/fy10osti/47187.pdf)

[67] T.M.I. Mahlia, T.J. Saktisahdan, A. Jannifar, M.H. Hasan and H.S.C. Matseelar, "A review of available methods and development on energy storage; technology update," *Renewable and Sustainable Energy Reviews*, vol. 33, pp.532-545, May 2014.

[68] D. Raster, "New demand for energy storage," *Electric Perspectives*, pp.30-47, Sept./Oct. 2008. (www.jointventure.org/images/stories/pdf/2008-09-01-energystorage_drastler.pdf)

[69] F. Diaz-Gonzalez, A. Sumper, O. Gomis-Bellmunt and R. Villafafila-Robles, "A review of energy storage technologies for wind power applications," *Renewable and Sustainable Energy Reviews*, vol. 16, pp. 2154-2171, May 2012.

[70] Y. Goda, *Random Seas and Design of Maritime Structures*. Advanced Series on Ocean Engineering, vol.33, World Scientific: Singapore, 2010.

[71] R. Bonnefille, *Mouvements de la Mer (in French)*. *Techniques de l'Ingénieur*, C4610, pp.1-19, 2010.

[72] http://hmf.enseeiht.fr/travaux/CD0001/travaux/optsee/hym/7/rapport.htm (last accessed March 2014).

[73] British Standard BS 6349-1:2000 "Maritime structures. Part 1. Code of practice for general criteria", Jul. 2003.

[74] T. Thiringer, J. MacEnri and M. Reed, "Flicker evaluation of the SeaGen tidal power plant," *IEEE Trans. Sustainable Energy,* vol. 2, n°4, pp.414-422, Oct. 2011.

[75] J.G. Slootweg, S.W.H. de Haan, H. Polinder and W.L. Kling, "General model for representing variable speed wind turbines in power system dynamics simulations," *IEEE Trans. Power Systems*, vol. 18, n°1, pp.144-151, Feb. 2003.

[76] A.S. Bahaj, A.F. Molland, J.R. Chaplin and W.M.J. Batten, "Power and thrust measurements of marine current turbines under various hydrodynamic flow conditions in a cavitation tunnel and a towing tank," *Renewable Energy*, vol. 32, n°3, pp. 407-426, March 2007.

[77] W.M.J. Batten, A.S. Bahaj, A.F. Molland and J.R. Chaplin, "The prediction of the hydrodynamic performance of marine current turbines," *Renewable Energy*, vol. 33, n°5, pp.1085-1096, May 2008.

[78] S. Benelghali, M.E.H. Benbouzid and J.F. Charpentier, "Generator systems for marine current turbine applications: a comparative study," *IEEE Journal on Oceanic Engineering*, vol. 37, n°3, pp. 554-563, Jul. 2012.

[79] S. Chiniforoosh, J. Jatskevich, A. Yazdani et *al.*, "Definitions and applications of dynamic average models for analysis of power systems," *IEEE Trans. Power Delivery*, vol. 25, n°4, pp. 2655-2669, Oct. 2010.

[80] E. Tara, S. Filizadeh, J. Jatskevich et *al.*, "Dynamic average-value modeling of hybrid-electric vehicular power systems," *IEEE Trans. Power Delivery*, vol. 27, n°1, pp. 430-438, Jan. 2012.

[81] S.R. Bowes and Y.S. Lai, "The relationship between space-vector modulation and regular-sampled PWM," *IEEE Trans. Industrial Electronics*, vol. 44, n°5, pp. 670-679, Oct. 1997.

[82] D.C. Lee and G.M. Lee, "A novel overmodulation technique for space-vector PWM inverters," *IEEE Trans. Power Electronics*, vol. 13, n°6, pp. 1144-1151, Nov. 1998.

[83] L. Loron, "Tuning of PID controllers by the non-symmetrical optimum method," *Automatica*, vol. 33, n°1, pp. 103-107, Jan. 1997.

[84] T. Ane and L. Loron, "Easy and efficient tuning of PI controllers for electrical drives," *in Proceedings of the 2006 IEEE IECON*, Paris (France), pp.5131-5136, Nov. 2006.

[85] S. Morimoto, H. Nakayama, M. Sanada and Y. Takeda, "Sensorless output maximization control for variable-speed wind generation system using IPMSG," *IEEE Trans. Industry Applications*, vol. 41, n°1, pp. 60-67, Jan./Feb. 2005.

[86] K.H. Kim, D.C. Lee and J.M. Kim, "Fast tracking control for maximum output power in wind turbine systems," *in Proceedings of the 2010 IEEE AUPEC*, Christchurch (New Zealand), pp.1-5, Dec. 2010.

[87] F. Blaabjerg, R. Teodorescu, M. Liserre and A.V. Timbus, "Overview of control and grid synchronization for distributed power generation systems," *IEEE Trans. Industrial Electronics*, vol. 53, n°5, pp. 1398-1409, Oct. 2006.

[88] F. Deng and Z. Chen, "Power control of permanent magnet generator based variable speed wind turbines," *in Proceedings of the 2009 IEEE ICEMS*, Tokyo (Japan), pp.1-6, Nov. 2009.

[89] C.H. Wua, Y.H. Hung and C.W. Hong, "On-line supercapacitor dynamic models for energy conversion and management," *Energy Conversion and Management*, vol. 53, pp.337-345, 2012.

[90] Y. Diab, P. Venet, H. Gualous and G. Rojat, "Self-discharge characterization and modeling of electrochemical capacitor used for power electronics applications," *IEEE Trans. Power Electronics*, vol. 24, n°2, pp. 510-517, Feb. 2009.

[91] L. Shi and M.L. Crow, "Comparison of ultracapacitor electric circuit models," *in Proceedings of the 2008 IEEE Power and Energy Society General Meeting*, Pittsburgh (USA), pp.1-6, Jul. 2008.

[92] F. Scuiller, "Study of a supercapacitor energy storage system designed to reduce frequency modulation on shipboard electric power system," *in Proceedings of the 2012 IEEE IECON*, Montreal (Canada), pp. 4054-4059, Oct. 2012.

[93] M. Ortuzar, J. Dixon and J. Moreno, "Design, construction and performance of a buck-boost converter for an ultracapacitor-based auxiliary energy system for electric vehicles," *in Proceedings of the 2003 IEEE IECON*, Roanoke (USA), pp. 2889-2894, Nov. 2003.

[94] http://www.maxwell.com/ (last accessed April 2014)

[95] http://www.enerzine.com/7/16313+les-hydroliennes-representent-la-formule-la-plus-prometteuse+.html (last accessed April 2014)

[96] W. Li and G. Joos, "Comparison of energy storage system technologies and configurations in a wind farm," *in Proceedings of the 2007 IEEE PESC*, Orlando (USA), pp.1280-1285, Jun. 2007.

[97] W. Li, G. Joos and C. Abbey, "Wind power impact on system frequency deviation and an ESS based power filtering algorithm solution," *in Proceedings of the 2006 IEEE PSCE*, Atlanta (USA), pp.2077-2084, Oct./Nov. 2006.

[98] Z. Zhou, F. Scuiller, J.F. Charpentier, M.E.H. Benbouzid and T. Tang, "Power limitation control for a PMSG-based marine current turbine at high tidal speed and strong sea state," *in Proceedings of the 2013 IEEE IEMDC*, Chicago (USA), pp. 75-80, May 2013.

[99] C.T. Pham and V.A. Martin, "Tidal current turbine demonstration farm in Paimpol-Bréhat (Brittany): tidal characterisation and energy yield evaluation with Telemac," *in Proceedings of the 8th European Wave and Tidal Energy Conference*, Uppsala (Sweden), pp. 181-188, 2009.

[100] http://www.verdantpower.com/kinetic-hydropower-system.html (last accessed May 2014)

[101] B. Wu, B. Zhang, J. Wang, J. Li *et al.* "Theoretical research for the application of flow storage battery in demand side management," *in Proceedings of the 2010 IEEE POWERCON*, Hangzhou (China), pp. 1-7, Oct. 2010.

[102] D.D. Banham-Hall, G.A. Taylor, C.A. Smith and M.R. Irving, "Flow batteries for enhancing wind power integration," *IEEE Trans. Power Systems*, vol. 27, n°3, pp. 1690-1697, Aug. 2012.

[103] J. Chahwan, C. Abbey and G. Joos, "VRB modeling for the study of output terminal voltages, internal losses and performance," *in Proceedings of the 2007 IEEE EPC*, Montreal (Canada), pp. 387-392, Oct. 2007.

[104] W. Wang, B. Ge, D. Bi and D. Sun, "Grid-connect wind farm power control using VRB-based energy storage system," *in Proceedings of the 2010 IEEE ECCE*, Atlanta (USA), pp. 3772-3777, Sept. 2010.

[105] F. Caricchi, F. Crescimbini, F. Giulii Capponi and L. Solero, "Study of bi-directional buck-boost converter topologies for application in electrical vehicle motor drives," *in Proceedings of the 1998 IEEE APEC*, Anaheim (USA), vol. 1, pp. 287-293, Feb. 1998.

[106] http://www.letelegramme.fr/local/finistere-nord/brest/ville/hydrolien-sabella-prete-pour-l-immersion-05-04-2013-2059467.php (last accessed May 2014)

[107] M. Arriaga, C.A. Canizares and M. Kazerani, "Renewable energy alternatives for remote communities in northern Ontario, Cannada," *IEEE Trans. Sustainable Energy*, vol. 4, n°3, pp. 661-669, Jul. 2013.

[108] http://www.rte-france.com/fr/developpement-durable/eco2mix/consommation-d-electricite (last accessed May 2014)

[109] http://www.sysenr.com/actualites/maitrise-energie-production-energies-renouvelables-ouessant-molene.html (last accessed May 2014)

[110] http://www.lefigaro.fr/flash-actu/2013/01/13/97001-20130113FILWWW00152-panne-d-electricite-a-ouessant.php (last accessed May 2014)

[111] K. Kusakana and H.J. Vermaak, "Hybrid diesel generator - battery systems for off-grid rural applications," *in Proceedings of the 2013 IEEE ICIT*, Cape Town (South Africa), pp. 839-844, Feb. 2013.

[112] H. Polinder, "Overview of and trends in wind turbine generator systems," *in Proceedings of the 2011 IEEE Power and Energy Society General Meeting*, San Diego (USA), pp. 1-8, Jul. 2011.

[113] H. Polinder, J.A. Ferreira, B.B. Jensen et *al.*, "Trends in wind turbine generator systems," *IEEE Journal of Emerging and Selected Topics in Power Electronics*, vol. 1, n°3, pp. 174-185, Sep. 2013.

[114] S. Morimoto, M. Sanada and Y. Takeda, "Effects and compensation of magnetic saturation in flux-weakening controlled permanent magnet synchronous motor drives," *IEEE Trans. Industry Applications*, vol. 30, n°6, pp. 1632-1637, Nov./Dec. 1994.

[115] D. Lu and N.C. Kar, "A review of flux-weakening control in permanent magnet synchronous machines," *in Proceedings of the 2010 IEEE VPPC*, Lille (France), pp. 1-6, Sept. 2010.

[116] M. Tursini, E. Chiricozzi and R. Petrella, "Feedforward flux-weakening control of surface-mounted permanent-magnet synchronous motors accounting for resistive voltage drop," *IEEE Trans. Industrial Electronics*, vol. 57, n°1, pp. 440-448, Jan. 2010.

[117] J.H. Song, J.M. Kim and S.K. Sul, "A new robust SPMSM control to parameter variations in flux weakening region," *in Proceedings of the 1996 IEEE IECON*, Taipei (China), vol. 2, pp. 1193–1198, Aug. 1996.

[118] D.S. Maric, S. Hiti, C.C. Stancu, J.M. Nagashima and D.B. Rutledge "Two flux weakening schemes for surface-mounted permanent-magnet synchronous drives - Design and transient response considerations", *in Proceedings of the 1999 IEEE ISIE*, Bled (Slovenia), vol. 2, pp. 673-678, Jul. 1999.

[119] H. Liu, Z.Q. Zhu, E. Mohamed, Y. Fu and X. Qi, "Comparison of drive performance of PM synchronous machine fed by inverters with different PWM strategies in constant torque and constant power regions," *in Proceedings of the 2011 IEEE IEMDC*, Niagara Falls (Canada), pp. 1334-1339, May 2011.

[120] P.Y. Lin and Y.S. Lai, "Voltage control technique for the extension of dc-link voltage utilization of finite-speed SPMSM drives," *IEEE Trans. Industrial Electronics*, vol. 59, n°9, pp.3392-3402, Sept. 2012.

[121] T.S. Kwon and S.K. Sul, "Novel antiwindup of a current regulator of a surface-mounted permanent-magnet motor for flux-weakening control," *IEEE Trans. Industry Applications*, vol. 42, n°5, pp.1293-1300, Sep./Oct. 2006.

[122] T.S. Kwon and S.K. Sul, "A novel flux weakening algorithm for surface mounted permanent magnet synchronous machines with infinite constant power speed ratio," *in Proceedings of the 2007 IEEE ICEMS*, Seoul (Korea), pp. 440-445, Oct. 2007.

[123] H. Liu, Z.Q. Zhu, E. Mohamed, Y. Fu and X. Qi, "Flux-weakening control of nonsalient pole PMSM having large winding inductance, accounting for resistive voltage drop and inverter nonlinearities ," *IEEE Trans. Power Electronics*, vol. 27, n°2, pp.942-952, Feb. 2012.

[124] M. Morandin, E. Fornasiero, S. Bolognani and N. Bianchi, "Torque and power rating of a wind-power PM generator drive for maximum profit-to-cost ratio," *IEEE Trans. Industrial Applications*, vol. 49, n°2, pp.866-872, Mar./Apr. 2013.

[125] R.H. Moncada, R.A. Rodrigue, J.A. Tapia and T.M. Jahns "Axial flux permanent-magnet machine under optimum control strategy for wind power generation," *in Proceedings of the 2009 IEEE IEMDC*, Miami (USA), pp. 1065-1071, May 2009.

[126] S. Chaithongsuk, B. Nahid-Mobarakeh, J.P. Caron, N. Takorabet and F. Meibody-Tabar, "Optimal design of permanent magnet motors to improve field-weakening performances in variable speed drives," *IEEE Trans. Industrial Electronics*, vol. 59, n°6, pp. 2484-2494, Jun. 2012.

[127] J. Aubry, H.B. Ahmed and B. Multon, "Sizing optimization methodology of a surface permanent magnet machine-converter system over a torque-speed operating profile: application to a wave energy converter," *IEEE Trans. Industrial Electronics*, vol. 59, n°5, pp. 2116-2125, May 2012.

[128] H. Li, Z. Chen and H. Polinder, "Optimization of multibrid permanent-magnet wind generator systems," *IEEE Trans. Energy Conversion*, vol. 24, n°1, pp. 82-92, Mar. 2009.

[129] L. Drouen, J.F. Charpentier, E. Semail and S. Clenet, "Study of an innovative electrical machine fitted to marine current turbine," *in Proceedings of the 2007 IEEE OCEANS*, Aberdeen (UK), pp. 1-6, Jun. 2007.

[130] A.M. Eltamaly, "Modeling of wind turbine driving permanent magnet generator with maximum power point tracking system," *J. King Saud Univ.*, vol. 19, *Eng. Sci.* (2), pp. 223-237, 2007.

[131] D.P. Coiro, F. Scherillo, R. Familio, U. Maisto and G. Troise, "Experimental test campaign on an innovative device to harness clean energy from tidal and river current," *in Proceedings of the 2009 IEEE ICCEP*, Capri (Italy), pp. 87-92, Jun. 2009.

[132] F. Scherillo, U. Maisto, G. Troise, D.P. Coiro and S. Miranda, "Numerical and experimental analysis of a shrouded hydroturbine," *in Proceedings of the 2011 IEEE ICCEP*, Ischia (Italy), pp. 216-222, Jun. 2011.

[133] http://www.openhydro.com/techOCT.html (last accessed May 2014)

[134] http://www.theengineer.co.uk/in-depth/the-big-story/compressed-air-energy-storage-has-bags-of-potential/1008374.article (last accessed May 2014)

[135] A.J. Pimm, S.D. Garvey and M. de Jong, "Design and testing of energy bags for underwater compressed air energy storage," *Energy*, vol. 66, pp. 496-508, March 2014.

[136] L. Belhadji, S. Bacha, I. Munteanu, A. Rumeau and D. Roye, "Adaptive MPPT applied to variable-speed microhydropower plant," *IEEE Trans. Energy Conversion*, vol. 28, n°1, pp. 34-43, March 2013.

[137] M. Andreica, S. Bacha, D. Roye, I. Exteberria-Otadui and I. Munteanu, "Micro-hydro water current turbine control for grid connected or islanding operation," *in Proceedings of the 2008 IEEE PESC*, Rhodes (Greece), pp. 957-962, Jun. 2008.

[138] M.A. Vallet, S. Bacha, I. Munteanu, A.I. Bratcu and D. Roye, "Management and control of operating regimes of cross-flow water turbines," *IEEE Trans. Industrial Electronics*, vol. 58, n°5, pp. 1866-1876, May 2011.

Appendices

Appendix A: Grid-Connected MCT System Parameters

A.1. MCT System Parameters

TABLE A.1. PARAMETERS OF THE MCT SYSTEM.

Sea depth	35 m
Sea water density	1027 kg/m^3
Turbine blade radius	8 m
System total inertia	1.3131×10^6 kg·m^2
Maximum C_p value	0.45
Optimal TSR for MPPT	6.3
Rated marine current speed	3.2 m/s
MCT nominal power	1.52 MW
Generator nominal phase voltage	649 V (RMS)
Generator nominal phase current	928 A (RMS)
DC-bus voltage	1500 V
DC-bus resistance	0.2 mΩ
DC-bus capacitor	13 mF
Rotor nominal speed	24 rpm
Pole pair number	125
Permanent magnet flux	2.458 Wb
Generator stator resistance	0.0081Ω
Generator *d-q* axis inductance	1.2 mH
Grid-side resistance	0.1 mΩ
Grid-side inductance	1.5 mH
Grid frequency	50 Hz
Grid phase voltage	690 (RMS)

A.1. Supercapacitor ESS Parameters

TABLE A.2. PARAMETERS OF THE SUPERCAPACITOR ESS.

SC-side buffer inductor	1.0 mH
SC rated voltage	750 V
SC equivalent capacitance	31.5 F
SC equivalent resistance	36 mΩ

Appendix B: Flow Battery Equivalent Circuit Parameters

B.1. The 3 MWh (=1MW×3h) Battery (MCT Dominant Supply Case)

TABLE B.1. PARAMETERS FOR THE VRB EQUIVALENT CIRCUIT.

R_{fixed}	54.071 Ω
$R_{reaction}$	0.135 Ω
$R_{resistive}$	0.09 Ω
$C_{electrodes}$	0.0056 F
I_{pump} coefficient	0.0094

B.2. The 1.25 MWh (=0.5MW×2.5h) Battery (Island Supply Case)

TABLE B.2. PARAMETERS FOR THE VRB EQUIVALENT CIRCUIT.

R_{fixed}	27.036 Ω
$R_{reaction}$	0.067 Ω
$R_{resistive}$	0.045 Ω
$C_{electrodes}$	0.0011 F
I_{pump} coefficient	0.0094

Appendix C: Control Parameters

C.1. PI Controllers

TABLE B.1. PARAMETERS FOR PI CONTROLLERS.

Generator speed loop	K_p = 87000, K_i = 7.9
Generator *d*-axis current loop	K_p = 3.4, K_i = 455
Generator *q*-axis current loop	K_p = 3.4, K_i = 455
DC-bus voltage loop	K_p = 3, K_i = 25
Grid *d*-axis current loop	K_p = 0.2, K_i = 50
Grid *q*-axis current loop	K_p = 0.2, K_i = 50
SC ESS current loop	K_p = 70, K_i = 130
3MWh BESS power loop	K_p = 0.5, K_i = 0.7
1.25MWh BESS power loop	K_p = 0.05, K_i = 0.3

C.2. Flux-Weakening Control loop (in Fig.IV.5)

TABLE B.2. PARAMETERS FOR THE FLUX-WEAKENING CONTROL LOOP.

LPF time constant	0.03 s
Gain α	30

Modélisation et Commande de la Puissance d'un Système Hydrolien avec Stockage d'Energie

***Résumé*—**Ces travaux de thèse concernent l'étude de l'ensemble de la chaîne de puissance d'un système hydrolien utilisant des systèmes de stockage d'énergie pour améliorer la qualité de la puissance produite et la capacité de gestion des échanges d'énergie. Dans un premier temps, les différentes technologies de stockage d'énergie et leurs applications pour lisser les fluctuations de la puissance produite par le système hydrolien sont étudiées et comparées. Ensuite, une stratégie de lissage des fluctuations de la puissance, dues à l'effet de houle (fluctuations de courte durée), est proposée: elle associe une stratégie MPPT avec filtrage (au niveau de la génératrice) à l'utilisation de supercondensateurs pour lisser la puissance injectée au réseau. Puis il est proposé d'utiliser des batteries à circulation d'électrolyte pour la gestion quotidienne de la puissance d'une hydrolienne dans le contexte d'un réseau électrique isolé. Un système hybride hydrolien/batteries/diesel est étudié pour deux configurations simples : le cas d'une alimentation avec une hydrolienne comme sources principales et le cas où les générateurs diesels sont considérés comme sources dominantes. Enfin, des stratégies de limitation de puissance basées sur le défluxage de la génératrice pour contrôler la puissance de l'hydrolienne dans le cas de vitesses de courants marins élevées sont proposées. Dans ce contexte, le contrôle à puissance constante et à puissance maximale en cours de défluxage sont comparés. L'influence des paramètres de la génératrice sur les caractéristiques de fonctionnement commun de la turbine et la génératrice est également etudiée.

Modeling and Power Control of a Marine Current Turbine System with Energy Storage Devices

***Abstract*—**This PhD thesis models the whole power chain of a marine current turbine (MCT) system and investigates the use of energy storage devices to improve power quality and energy management capability. First, various energy storage technologies concerning their applications to address the power fluctuation phenomena in tidal current generation system are reviewed and compared. Then, a two-stage power smoothing control strategy for compensating swell-induced short-time fluctuations is proposed. The proposed control strategy uses a modified MPPT with filter strategy on the generator-side and supercapacitors on the grid-side for injecting a smoothed power to the grid. Afterwards, a flow battery system for daily energy management of a hybrid MCT/battery/diesel system is proposed. The MCT dominant power supply case and an island power supply (with diesel generators as the main source) are investigated. Finally, power limitation controls with a robust flux-weakening strategy for a PMSG-based non-pitchable MCT system are proposed for over-rated marine current speed periods. In this context, the constant power control and maximum power control modes at the flux-weakening stage are compared; and the influence of the generator parameters on the joint operating characteristics of the turbine and generator are also discussed.